Structural and functional characterisation of the fungal plasma membrane proton pump, Pma1, and related P-Type ATPases



Maxwell Maria Gabriël Geurts
Merton College
University of Oxford

A thesis submitted for the degree of
Doctor of Philosophy

October 2022

Abstract

P-type ATPases are a large family of ubiquitous ion pumps that carry out fundamental biological processes, ranging from generating membrane potentials to muscle contraction.

Part I of this thesis focuses on the fungal plasma membrane proton pump, Pma1. Pma1 is responsible for generating the proton-motive force that drives nutrient import into the cell via secondary active transporters. Uniquely, Pma1 forms ring shaped hexamers in the plasma membrane and is regulated through C- and N-terminal extensions. Due to its critical role in the cell, it poses as a target for novel antifungals against invasive mycoses. To date, the structure of Pma1 from *Neurospora crassa* has been determined in an autoinhibited state, and the structure from *Saccharomyces cerevisiae* has been determined in both an activated and autoinhibited state. However, whilst the structures have elucidated the molecular basis for function and regulation, they did not provide an understanding of the role of the surrounding lipids. In this thesis, *N. crassa* Pma1 was studied in a native-like membrane using coarse-grained molecular dynamic (MD) simulations. The results explain Pma1's dependency on anionic lipids such as phosphatidylserine and phosphatidylinositol ceramide but also reveal a further understanding of how Pma1 cooperatively interacts with the membrane: it induces a membrane deformation that could play a critical role in the mechanism and energetics of proton pumping. In addition to computational studies, the expression and purification of Pma1 was optimised, leading to inhibitory assays and preliminary cryo electron microscopy. Finally, first steps toward a recombinant expression system for purification of *N. crassa* Pma1 from yeast have been made.

Part II of this thesis addresses the sarco(endo)plasmic reticulum Ca^{2+}-ATPase (SERCA). SERCA is the most widely studied and well-characterised member of the family, forming the basis of understanding other P-Type ATPases. Whilst being well characterised, the central residue, Glu340 and its mutant, E340A, have not been understood until now. Previous functional studies of the mutant showed that the mutation impacts the Ca^{2+}-binding kinetics, but a E340A crystal structure did not explain this effect. By studying the wild-type, E340A and an *in silico* E340A structure of SERCA in a lipid membrane using all-atom MD, we found that the mutant has altered dynamics around both the Ca^{2+}- and the ATP-binding sites. Altogether, the work allowed us to propose that E340A stabilises a more substrate-occluded state in SERCA. Conversely, the conserved Glu340 ensures a highly dynamic and coupled mechanism of action by aiding inter-domain communication between the head piece and transmembrane domain of SERCA.

Acknowledgements

First and foremost, I would like to express my sincere gratitude to Dr. Maike Bublitz for her patience and incredible knowledge, and sharing her enthusiasm for P-type ATPases with me. I would also like to extend thanks to my co-supervisor Prof. Mark Sansom for sparking my interest in molecular dynamics and Dr. David Sauer for providing support in the final few months of my DPhil.

The work in this thesis was only possible due to the constant day-to-day support of the MBU lab. In particular, I would like to extend a massive thanks to Dr. Robin Corey for sharing his vast knowledge and without whom learning MD would have been impossible. A thank you also Dr. Margaret Young for mentoring me in the lab, giving me a crash-course into cryo-EM and for our frequent thought-provoking conversations on Pma1. You all have provided an immense amount of encouragement and pushed me to be a better scientist.

I would also like to thank Merton College, the boat club and all of my friends. You all have made my life more interesting and have provided a real sense of home and a family to be a part of in Oxford. Finally, I would like to conclude with a major thank you to my parents, Ton and Karin, my sister, Daan, and to Charlotte - without you I would not have got where I am today.

Authorship declaration

This dissertation, entitled “Structural and functional characterisation of the fungal plasma membrane proton pump, Pma1, and related P-type ATPases” is the result of my own work and includes nothing which is the outcome of work done in collaboration except as declared in the text.

This work was carried out Department of Biochemistry, University of Oxford, between October 2018 and August 2022, under the supervision of Dr. Maike Bublitz. Information and data derived from other sources have been referenced and attributed accordingly.

Publications resulting from this work

Heit, S., Geurts, M.M.G. Murphy, B.J., Corey, R.A., Mills, D.J., Kühlbrandt, W., Bublitz, M. (2021) “Structure of the hexameric fungal plasma membrane proton pump in its autoinhibited state” Science Advances, vol 7, no. 46. https://doi.org/10.1126/sciadv.abj5255

Some material from this publication is reproduced in Chapter 3 of this thesis. Contributions from other authors are clearly described in text.

Geurts, M.M.G., Clausen, J.D., Arnou, B., Montigny, C., Lenoir, G., Corey, R.A., Jaxel, C., Møller, J.V., Nissen, P., Andersen, J.P., le Maire, M., Bublitz, M. (2020) “The SERCA residue Glu340 mediates interdomain communication that guides Ca^{2+} transport” PNAS, vol. 117, no. 49. https://doi.org/10.1073/pnas.2014896117

Some material from this publication is reproduced in Chapter 8 of this thesis. Contributions from other authors are clearly described in text.

Covid Statement

The closure of laboratories due to the Covid-19 pandemic caused a delay to the work presented in Chapters 4 to 6. However, I was able to access computing facilities remotely that allowed me to learn molecular dynamics simulations from home and I was able to conduct the research presented in Chapter 3 and 8.

Table of Contents

Abstract ..... *i*

Acknowledgements ..... *iii*

Authorship declaration ..... *iv*

Publications resulting from this work ..... *v*

Covid Statement ..... *vi*

Table of Contents ..... *vii*

List of Abbreviations ..... *x*

Chapter 1: Introduction *1*

1.1 The fungal plasma membrane **1**

1.1.1 The fungal plasma membrane lipid composition 1

1.1.2 Fungal membrane microdomains 4

1.2 The P-type ATPase superfamily **6**

1.2.1 Conserved structure of the P-Type ATPase superfamily 9

1.2.2 The conserved mechanism of catalysis in the P-type ATPase family 11

1.2.2.1 Studying the P-type ATPase catalytic cycle 14

1.2.3 Lipid interactions with P-type ATPases 15

1.3 Plasma membrane H^+-ATPases **17**

1.3.1.1 Plasma membrane H^+-ATPases: Introduction 17

1.3.1.2 Fungal H^+-ATPase isoforms 19

1.3.1.3 H^+-ATPase Oligomerisation 19

1.3.1.4 N- and C-terminal autoregulation 20

1.3.1.5 Microdomain association and surface transport 22

1.3.2 Structure of the plasma membrane H+-ATPase from *N. crassa* **24**

1.4 The Sarco-Endoplasmic Reticulum Calcium ATPase (SERCA) **29**

1.4.1 General structure and function 29

1.4.1.1 Studying Ca^{2+} occlusion in SERCA with ADP-AlF_4^- and E309Q 30

1.4.1.2 The functional role of Loop 6-7 32

1.4.1.3 The P1-helix and E340A 34

Chapter 2: Materials and Methods *36*

2.1 Molecular dynamics simulations - Background **36**

2.1.1 Molecular mechanics 37

2.1.1.1 Potential energy function 37

2.1.1.2 Choice of Force Field 42

2.1.1.3 Laws of Motion 43

2.1.1.4 Time steps 43

2.1.1.5 Statistical ensembles 44

2.1.1.6 Periodic boundary conditions 46

2.1.2 -Coarse-grained MD simulations 47

2.1.2.1 The Martini force field 47

2.1.2.2 The elastic network 50

2.2 Methods specific to Pma1 ..... **50**

2.2.1 Coarse-grained simulations of Pma1 50

2.2.2 Molecular Biology 52

2.2.2.1 Cloning of construct *Nc*Pma1-7 52

2.2.3 Protein Biochemistry 54
2.2.3.1 SDS-PAGE 54
2.2.3.2 Western Blot 54
2.2.3.3 Protein quantification 55
2.2.3.4 Baginski ATPase assay 55
2.2.3.5 Inhibitor dose-response curves 56
2.2.4 Native *Neurospora crassa* Pma1 Purification 57
2.2.4.1 Cell culture 57
2.2.4.2 Membrane preparation 58
2.2.4.3 Membrane solubilisation screen 59
2.2.4.4 Purification in DDM 59
2.2.4.5 Purification in LMNG 61
2.2.5 Recombinant expression and purification of *Nc*Pma1 in *Saccharomyces cerevisiae* 62
2.2.5.1 Yeast transformation 62
2.2.5.2 Small scale expression 63
2.2.5.3 Large scale recombinant expression 64
2.2.5.4 Yeast membrane preparation 65
2.2.5.5 Recombinant Pma1 purification 66
2.2.6 Electron Microscopy 66
2.2.6.1 Negative stain electron microscopy 66
2.2.6.2 CryoEM sample and grid preparation 67
2.2.6.3 CryoEM data acquisition 67
2.2.6.4 CryoEM data processing 67

2.3 Methods specific to SERCA 69
2.3.1 All-atom MD simulation setup 69

Results Part I 70

Chapter 3: Coarse-grained simulations of Pma1 in a native-like membrane 70

3.1 Chapter 3 Introduction 70

3.2 Setting up simulations of Pma1 71

3.3 Pma1 preferentially interacts with double-unsaturated phospholipids 74

3.4 Local lipid accumulation at the Pma1 monomer interface suggest a role for anionic lipids 75

3.5 Pma1 induces a considerable membrane deformation to create a cation funnel 79

3.6 The Chute-like membrane deformation attracts cations 83

3.7 Simulations of Pma1 with a phosphatidylinositol ceramide 84

3.8 A conserved set of Arginine residues in the Pma1 A-domain are important for supporting the membrane deformation 88

3.9 Chapter 3 discussion 92

Chapter 4: Optimising native source purification of Neurospora crassa Pma1 94

4.1 Chapter 4 Introduction 94

4.2 Purification of Pma1 in LMNG 95

4.3 Improving the AEX purification by greater fractionation volume and a systematic approach to pooling 99

4.4 Expression and purification of glucose-activated Pma1 for functional and structural studies 104

4.5 Chapter 4 discussion 109

Chapter 5: Structural and functional studies of glucose-activated Pma1 111

5.1 Chapter 5 Introduction 111

5.2 Establishing optimal ATPase conditions for inhibitor studies at pH 7 112

5.3 Inhibition studies with a proposed antifungal 114

5.4 Inhibition studies with metal fluorides that mimic phospho-intermediate states 116

5.5 CryoEM screening of Pma1-GA 119

5.5.1 CryoEM screening of MgF_x-inhibited Pma1-GA 119

5.5.2 CryoEM screening of BeF_x-inhibited Pma1-Ga 127

5.6 Chapter 5 discussion 133

Chapter 6: Establishing a recombinant expression system for Neurospora crassa Pma1 137

6.1 Chapter 6 Introduction 137

6.2 Small scale expression of *Nc*Pma1-6 138

6.3 Large-scale expression and purification of *Nc*Pma1-6 140

6.4 Negative stain electron microscopy of *Nc*Pma1-6 143

6.5 Redesigning and restriction cloning of *Nc*Pma1-7 145

6.6 Expression testing of *Nc*Pma1-7 145

6.7 Chapter 6 discussion 147

Chapter 7: Discussion and conclusion Part I 150

Results Part II 157

Chapter 8: The role of E340 in SERCA 157

8.1 Chapter 8 Introduction 157

8.2 Structure of SERCA E340A and Functional assay 159

8.3 The structural deviations of E340A from WT are stable in MD simulations 163

8.4 E340A stabilises occluding behaviour in Loop 6-7 and M3 167

8.5 E340A rigidifies the mobility of the M1 kink 171

8.6 E340A stabilises the phosphorylation site in a more occluded state 173

Chapter 9: Discussion and conclusion Part II 176

References 183

Appendices 200

List of Abbreviations

Lipid names

PO-	palmitoyl-oleoyl (C16:0/18:1)
PI-	palmitoyl-linoleoyl (C16:0/18:2)
DI-	di-linoleoyl (C16:2/18:2)
DP-	C(d18:1/18:0)
PN-	C(d18:1/24:1)
PV-	C(d18:1/18:1(11c))
XN-	C(d24:1/24:1)
CIP	phosphatidylinositol ceramide
CE	ceramide
ERGO	Ergosterol
MIPC	mannosyl-inositolphosphoryl ceramide
$M(IP)_2C$	mannosyl-di-(inositolphosphoryl) ceramide
PA	phosphatidic acid
PC	phosphatidylcholine
PE	phosphatidylethanolamine
PI	phosphatidylinositol
PICE	phosphatidylinositol ceramide coarse grain model
PIP_2	phosphatidylinositol biphosphate
PS	phosphatidylserine
SM	sphingomyelin
AEX	anion exchange
AMP-PCP	adenosine 5′-(β,γ-methylene)triphosphate

AMP-PNP	adenylyl-imidodiphosphate
ATP/ADP/AMP	adenosine tri/di/mono phosphate
CG	coarse grained
Cryo-EM	cryo-electron microscopy
DDM	n-dodecyl-β-D-maltopyranoside
DMSO	dimethyl sulfoxide
DNA	deoxyribonucleic acid
DTT	dithiothreitol
EDTA	ethylenediaminetetraacetic acid
ER/SR	endoplasmic reticulum/sarcoplasmic reticulum
GSFSC	gold standard fourier shell correlation
LMNG	Lauryl Maltose Neopentyl Glycol
LPC16	LysoFos Choline 16
MCP	membrane compartment containing Pma1
MD	molecular dynamics
MM	molecular mechanics
OD	optical density
PCR	polymerase chain reaction
PDB	protein data bank
Pi	inorganic phosphate
PM	plasma membrane
RE	restriction enzyme
RNA	ribonucleid acid
RT	room temperature
SDS	sodium dodecyl sulphate

SDS-PAGE	sodium dodecyl sulphate polyacrylamide gel electrophoresis
SEC	size exclusion chromatography
TM	transmembrane

Chapter 1: Introduction

1.1 The fungal plasma membrane

All living cells are surrounded by a semi-permeable, biological plasma membrane (PM) that carries out a multitude of functions. It protects cells and their contents from the harmful outside world that contains foreign agents and allows cells to accumulate valuable molecules inside. The membrane barrier also provides a means to interact with other cells and conduct cell signalling as well as allowing cells to generate ion gradients whose potential energy can be used to pay for the import and export of ions, molecules, proteins and nutrients through secondary active transport. Regarding the basic structure of biological membranes, after years of debate and controversy, in 1972 the structure was described by the fluid mosaic model, which is now widely accepted. The model consists of a two-dimensional fluid formed by a bilayer of lipids that proteins sit in, both free to diffuse laterally (Singer & Nicolson, 1972).

Since the conception of the fluid mosaic model, it has become increasingly evident that whilst the model generally remains relevant, membranes contain further complexity and nuances. They host an incredibly diverse range of lipids and proteins that can compartmentalise into various structured domains referred to as microdomains. These microdomains can serve as a sorting platform to segregate particular protein machinery in aid of their function.

1.1.1 The fungal plasma membrane lipid composition

Generally, eukaryotic plasma membranes are composed of a complex lipid mixture of glycerophospholipids, sphingolipids and a sterol. Glycerophospholipids

are composed of glycerol-3-phosphate containing two fatty acyl chains along with various substituent head groups including ethanolamine, choline, serine and inositol. Sphingolipids on the other hand have an *N*-acylated phytosphingosine base and are often linked to a fatty acid via an amide bond. The process of lipid synthesis is closely linked to the metabolic state of cells and creates greater diversity by modulating the acyl chain length of the glycerophospholipids and sphingolipids (Klose et al., 2012). Moreover, the fluidity of a membrane is in part regulated by the degree of saturation present in the lipid tails. Unlike sphingolipids and glycerophospholipids, sterols do not contain extended acyl chains attached to polar head groups. They are amphipathic lipids containing an aromatic steroid ring structure that plays a crucial role in contributing to the biophysical properties of membrane fluidity, thickness, permeability, microdomain formation and protein function (de Meyer & Smit, 2009; Kaiser et al., 2011). Whereas mammalian cells contain cholesterol as the membrane sterol, fungal membranes predominantly contain ergosterol (Dupont et al., 2012). Compared to cholesterol, ergosterol has a greater propensity to promote domain formation (described below) and packs more tightly against saturated acyl chains (Athanasopoulos et al., 2019).

The lipid composition of the PM varies between kingdoms all the way down to species. Additionally, numerous external factors such as temperature, external stresses and metabolic state can influence the biosynthesis of lipids and result in different acyl-chain lengths and saturations as well as distributions of lipid head groups. Due to the variability of membrane composition and limited techniques to study them exist, only a few studies have tried to elucidate the overall membrane composition of fungi. Initial studies of the *Neurospora crassa* PM report that it consists mostly of PC and PE phospholipids up to 30-50% each, as well as

phosphatidylinositol (PI), phosphatidylserine (PS) and phosphatidic acid (PA), however, this study is limited to the analysis of the glycerophospholipids (Friedman & Glick, 1980). The acyl chains typically consist of 16:0 and 18:2 length and saturation. Since then, techniques have evolved significantly and now mass spectrometry-based shotgun lipidomics has made it possible to quantify the complete set of lipids from isolated membranes in a single experiment. This technique was used more recently to analyse the *S. cerevisiae* PM. Its composition consists of 70% glycerophospholipids, 15% sphingolipids and 15% sterols (Klose et al., 2012). Phosphatidylinositol ceramides (CIPs) make up over 40% of the sphingolipids class, whilst mannosyl-inositolphosphoryl ceramide (MIPC), and mannosyl-di-(inositolphosphoryl) ceramide ($M(IP)_2C$) mostly make up the rest. They also report that the majority of these were found to have the α-hydroxylated C26:0 chain linked to the sphingosine long base chain. The glycerophospholipid distribution matched that of *N. crassa*, with phosphatidylcholine (PC), phosphatidylethanolamine (PE) and PI each making up around 20% of the total composition, followed by PA and PS. The acyl chain composition of these classes mostly consisted of palmitic (C16:0), palmitoleic (C16:1) and oleic acid (C18:1). Klose *et al* tested the impact of various external factors on lipid composition and concluded that the carbon source had a marked effect. When grown on glucose, the concentration of both CIP and PS lipids increased significantly compared to raffinose or glycerol. Whilst there are differences in the membrane composition of *S. cerevisiae* and *N. crassa* (including that yeast are uniquely limited to monounsaturated acyl chains), this information will function as a useful reference until new studies of *N. crassa* are conducted.

1.1.2 Fungal membrane microdomains

The notion of microdomains, originally referred to as the ‘raft hypothesis’, was first introduced by Kai Simons and Elina Ikonen in their seminal paper published in 1997 (Simons & Ikonen, 1997). They postulate that preferential interactions between lipids and sterols can induce the formation of tightly packed membrane domains with distinct compositions of lipid and protein and exhibit distinct biophysical properties from their surrounding membranes. Rafts would allow cells to concentrate specific proteins and reactants and exclude others. The basic physical chemistry underlying the domain formation is straightforward; whilst all lipids preferentially interact with each other compared to water, forming the self-assembling membrane, certain lipids interact more favourably with each other than other lipids. Specifically in the proposed rafts, long-chain, saturated phospholipids and sphingolipids and sterols preferentially interact to form a thicker, compartmentalised domain. This state of matter is referred to as the ‘liquid ordered (Lo) phase’ which is fluid and like the basic liquid-disordered (Ld) phase allows for molecular motion and flexibility (Figure 1.1). The Ld phase, on the other hand, consists mostly of unsaturated phospholipids. What sets the Lo phase apart is the arrangement and physical properties governing lipid packing, rigidity and permeability. Experiments on protein incorporation illustrated that the ordered domains tend to exclude most transmembrane proteins and so a small set of proteins evolved to sort into microdomains as it's features uniquely benefit its function (Levental et al., 2011). Despite this compelling theory and the plethora of supporting data, after decades, their existence is still being heavily debated in the field (Levental et al., 2020).

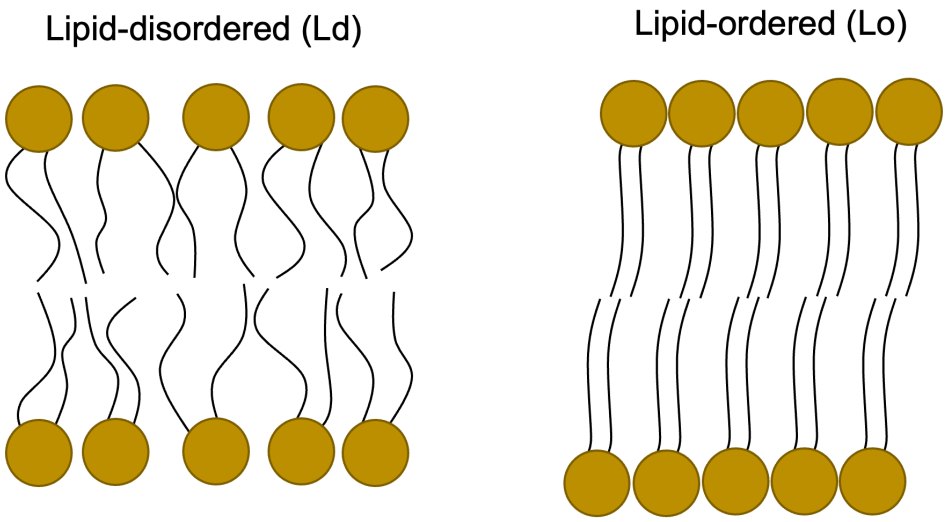

Figure 1.1: Lipid phases. *Individual lipids are represented by yellow head groups and black acyl tails. The greater order in the acyl tails of the ordered phase results in smaller spacing between the head groups and an overall thicker bilayer.*

In fungi, the existence of microdomains first became apparent by early freeze-etching studies on yeast. Electron microscopy was used to visualise various surfaces within yeast cells and illustrated that the plasma membrane is composed of a complex structure of microdomains. Regions of smooth, particle-free membranes were noted by having straight lines of furrow-like invaginations whilst other regions of the membrane contained honeycomb-like areas of repetitive crystalline patterns (Moor & Muhlethaler, 1963). Since then, fungal studies have focussed on deciphering the various microdomains and their composition.

Microdomains of *S. cerevisiae* have been particularly well studied and are generally divided into five non-overlapping domains: the Membrane Compartment containing arginine permease Can1 (MCC), the H^+-ATPase Pma1 (MCP), the TORC2 kinase (MCT), the sterol transporters Ltc3/4 (MCL), and the cell wall stress mechanosensory Wsc1 (MCW). These microdomains typically contain sphingolipids and ergosterol together with a mix of proteins, including the one they

are named after. However, they range from static patches to more dynamic network-like domains, varying in size, dynamics, composition and mechanism of formation (Athanasopoulos et al., 2019) (Figure 1.2). The same compartments are believed to exist in *N. crassa* and other fungi, however, to date, only the MCC has been shown to exist (Q. Yang & Kempken, 2020).

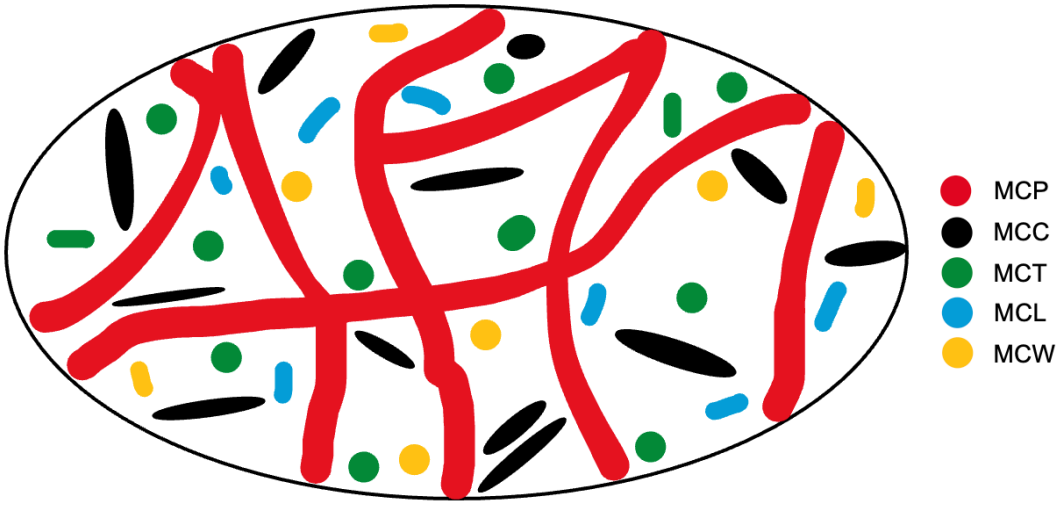

Figure 1.2: Compartmentalisation of microdomains in the fungal plasma membrane. *Figure based on Athanasopoulos et al. 2019 and Santos et al, 2020. Scale not provided as microdomain sizes can vary per species.*

1.2 The P-type ATPase superfamily

P-type ATPases form a large and varied family of membrane proteins, found across all domains of life. Generally, the role of P-type ATPases is to establish and maintain steep electrochemical gradients across cellular membranes by transporting an array of cations, heavy metals and, in a few cases, alternative substrates such as lipids. This endergonic reaction is fuelled by harnessing the energy released from ATP hydrolysis. Unlike other well-known membrane ATPases like the F- and V-type ATPase and ATP-binding cassette (ABC) transporters, P-type ATPases form a phosphorylated intermediate during the process of ATP hydrolysis (P. L. Pedersen & Carafoli, 1987).

In 1957, Jens Skou discovered the first P-type ATPase when studying the effect of various cations on leg nerves from crabs. He proposed that the membrane potential is generated by a K^+-driven ATPase now known as the Na^+/K^+-ATPase that transports Na^+ and K^+ across axonal membranes (Skou, 1957). Well-studied examples of P-type ATPases include: 1) the Na^+/K^+-ATPase and plasma membrane H^+-ATPase that maintain essential potentials that energize the membranes for numerous cellular processes like signalling and secondary-active transport (Skulachev, 1994), 2) the sarco(endo)plasmic reticulum Ca^{2+}-ATPase responsible for restoring Ca^{2+} levels after muscle contraction and Ca^{2+}-mediated signalling and 3) heavy metal ATPases that ensure trace metal homeostasis and detoxification in eukaryotes and prokaryotes (Bublitz et al., 2011).

Phylogenetic studies conducted by Axelsen and Palmgren suggested that the P-type ATPase family can be grouped into five subfamilies (P_I-P_V) (Axelsen & Palmgren, 1998). The 159 sequences used were grouped together based on known and predicted substrate specificity and not based on the evolutionary relationship of the parental species. This finding indicated that the invention of new substrate specificities is due to abrupt changes in the rate of sequence evolution. The five families are described below:

P_I-type ATPases are possibly the most ancient and are generally classed into two subgroups, type IA and IB. Type IA is a small class that contains bacterial ion pumps, the *E. coli* Kdp K^+-pump is the most studied example (Axelsen & Palmgren, 1998). The larger subgroup, type IB, is an evolutionarily distant group that transports heavy metals. They are typically involved in the homeostasis of trace elements (Nelson, 1999) or responsible for removing toxic ions such as Cu^+, Ag^+, Zn^{2+}, $Cd2^+$ or Pb^{2+} from the cell (Rosen, 2002).

P_{II}-type ATPases split into several subgroups. Most are believed to transport Ca^{2+} and are divided into two relatively distant families: type IIA for SR-based ATPases and type IIB for PM-based ATPases. Type IIC include the axonal Na^+/K^+-ATPases and their closely related gastric H^+/K^+-ATPases responsible for acidifying the stomach lumen. Type IID consists of a small group of fungal Na^+-ATPases.

P_{III}-type ATPases are classified into two groups. Plasma membrane H^+-ATPases found almost exclusively in fungi and plants form group IIIA and a small set of bacterial Mg^{2+} ATPases make up group IIIB.

P_{IV}-type ATPases consist of a unique group that so far has only been identified in eukaryotes and is responsible for maintenance of bilayer asymmetry. These flippases are thought to translocate phospholipids from the outer to the inner leaflet of the plasma membrane.

P_V-type ATPases are a group of poorly understood proteins that until recently were completely uncharacterised. Phylogenetic analysis distinguished two groups, type VA conserved in all eukaryotes and type VB which is lost in a few eukaryotic species including the entire plant kingdom (A. B. Møller et al., 2008). The yeast P_{VA}-ATPase Spf1 was recently determined to be a helix dislocase required for the removal of mis-inserted hydrophobic helices from the ER membrane (McKenna et al., 2020). The function of P_{VB}-ATPases ATP13A2-5 varies. For example, ATP13A2 resides in the lysosome (Schröder et al., 2007) and its malfunction leads to cell death (Dehay et al., 2012). The protein was recently shown to transport polyamines such as spermine from the lysosomal lumen to the cytosol, as ATP13A2 deficiency leads to lysosomal spermine accumulation (van Veen et al., 2020). This suggests it plays a fundamental role in lysosomal health.

1.2.1 Conserved structure of the P-Type ATPase superfamily

All P-type ATPases contain three cytoplasmic domains: the N (nucleotide binding), P (phosphorylation) and A (actuator) domain (Toyoshima et al., 2001), and a transmembrane domain consisting of at least 6 α-helices. The soluble domains bind ATP and phosphorylate a conserved aspartate residue in the P-domain during the catalytic cycle. Meanwhile, the membrane helices are responsible for substrate binding and transport.

Aside from the core conserved structure, P-type ATPases can contain an array of additional subunits either on the same chain or as a binding partner to form a heterocomplex, adding to the variety and complexity of the family (Figure 1.3). Typically, P_{II-V}-ATPases contain an additional four helices (M7-10) that form a support domain that tightly pack against M5 and 6. P_{III}-ATPases contain both N- and C-terminal extensions that are involved in autoregulating the enzyme. The majority of P_V-ATPases contain an N-terminal domain consisting of a β-barrel, and P_{VA}s contain an α-helical 'arm'-domain between the P-domain and M5 (Li et al., 2021; McKenna et al., 2020). P-type ATPases will also form heterocomplexes with either soluble or membrane-bound additional subunits. For example, plant proton pumps are activated by a small soluble protein, 14-3-3, that binds at their C-terminal domain (Jahn et al., 1997), and P_{IV}-flippases form a heterodimer with CDC50 (Dieudonné et al., 2022). Examples of membrane-bound regulators include phospholamban which is involved in regulating SERCA activity (Traaseth et al., 2008) and additional β- and γ-subunits that modulate the activity of the Na^+/K^+ ATPase (W.-K. Yang et al., 2016).

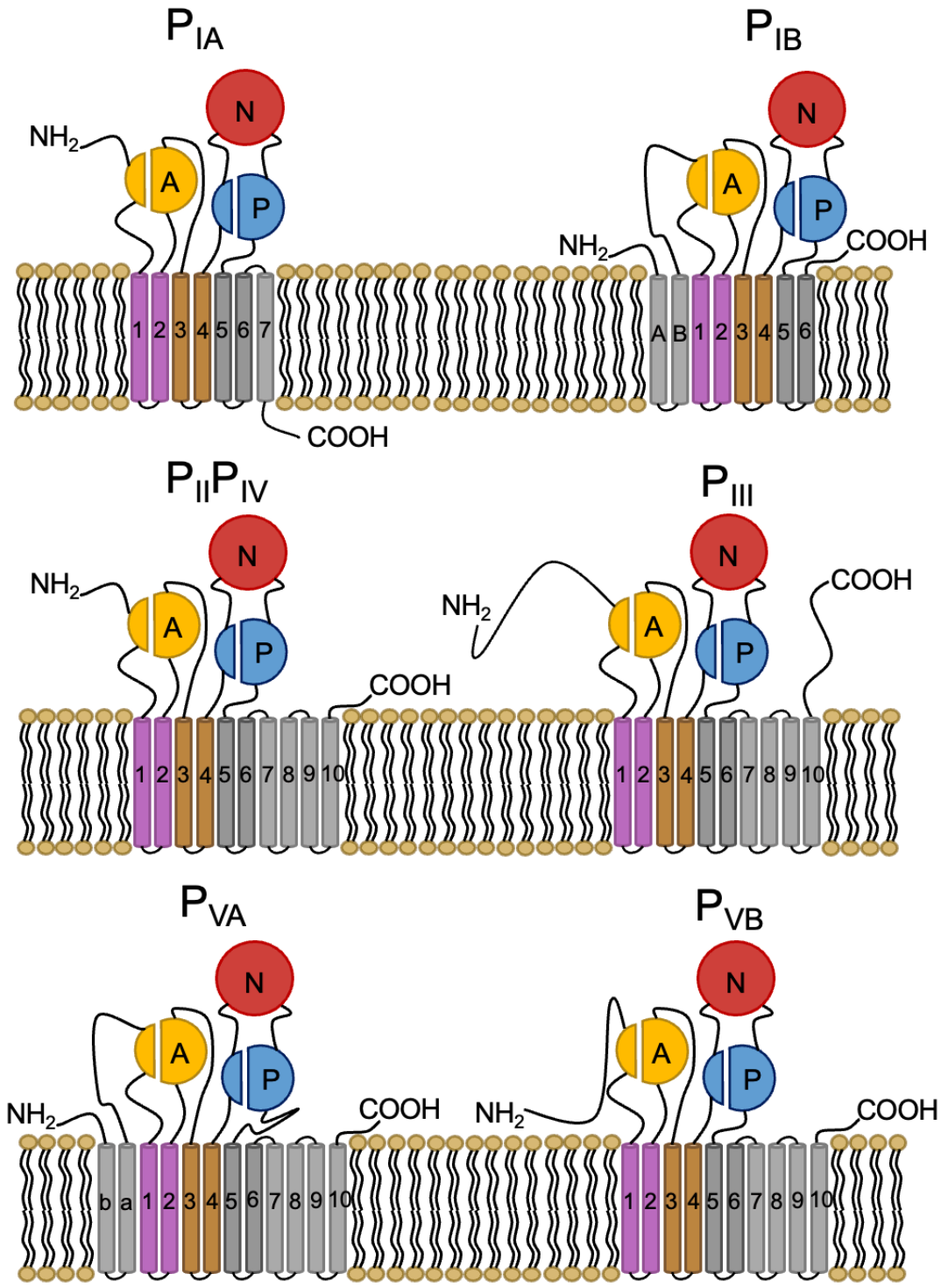

Figure 1.3: Overview of the P-type ATPases comprising of classes P_I-P_V *that all contain a core of 6 transmembrane helices and soluble actuator (A), phosphorylation (P) and nucleotide binding (N) domains. Various families contain addition transmembrane helices and N- and C-terminal extensions in addition to the core P-type ATPase fold.*

1.2.2 The conserved mechanism of catalysis in the P-type ATPase family

Over 50 years ago, it was discovered that P-type ATPases undergo large conformational changes to translocate ions. The described alternating-access model would prevent back-flow of ions against the steep gradients they create. Moreover, two distinct conformational states were distinguished, the so-called E1 and E2 states (enzyme-1 and enzyme-2) (Albers, 1967; Jardetzky, 1966; Post et al., 1969). The states were distinguished by their different affinity for nucleotide and substrate. E1 states are associated with autophosphorylation activity and increased affinity for substrate on the cytosolic side whereas the E2 states are associated with autodephosphorylation and lower affinity for cytosolic substrate. Since its discovery, the nomenclature of the E1 and E2 state enzymes is still in use and the cycle of P-type ATPase transport to this date is referred to as the Post-Albers cycle (Figure 1.4) (Kühlbrandt, 2004).

An abundance of structural and functional studies on the two archetypical P-type ATPases, SERCA and Na^+/K^+-ATPase, has generated an in-depth structural understanding of the catalytic mechanism. Structural studies of many other P-type ATPases have also shown that this molecular mechanism is remarkably well-conserved across the family. The molecular mechanism is depicted in Figure 1.4, using structures of SERCA as a model.

In the E1 state, upon binding of ATP and substrate, autophosphorylation of a perfectly conserved aspartate residue occurs in the P-domain through a nucleophilic attack on the Pγ of ATP. This phosphorylation forms a short-lived state, E1P · ADP. Because the bond with Pγ is broken, the N-domain, bound to the adenosine group of ADP, releases and moves out the way for the A-domain to rotate in by almost 120°. Movement of the A-domain transmits through the linkers to M1-

3 and induces subsequent conformational changes to open an extra-cytoplasmic exit pathway, distorting the substrate binding site and releasing ADP and substrate (Bublitz et al., 2010; Kühlbrandt, 2004).

Following the release of the substrate and ADP, the charge on the protein is neutralised by the binding of counterions in a fast, short-lived transition state which remains poorly understood. This state, in which the phosphate is still covalently bound and the substrate has been released, is the E2P state (Bublitz et al., 2010; Kühlbrandt, 2004).

Whilst the N-domain is released and the A-domain closely interacts with the P-domain, a modulatory ATP binds the N-domain through the adenosine group. The modulatory ATP binds to the same site as the functional ATP, however, its P_γ is about 9 Å away from the phosphorylation site (Jensen et al., 2006). The binding of counterions induces occlusion by the transmembrane helices. Transmitted through the linkers connecting the α-helices to the A-domain, the highly conserved Thr-Gly-Glu-Ser (TGES) loop in the A-domain dephosphorylates the P-domain aspartate through a condensation reaction with a water molecule, forming the E2 · P_i (ATP) state.

After the release of the inorganic phosphate, the protein cycles through the short-lived E2 (ATP), in which affinity for the A-domain is lost, the cytoplasmic side of the transmembrane helices becomes accessible to substrate again and the modulatory ATP bound to the N-domain transitions to the co-factor bound E1 · ATP state, associated with the release of counterions on the cytoplasmic side. The role of the modulatory ATP is to accelerate the transition from E2 to E1, as well as the transition from E2P to E2 and E1P to E2P (Champeil et al., 1988; Lund & Møller, 1988; Mintz et al., 1995), perhaps by stabilising the activity of the N-domain.

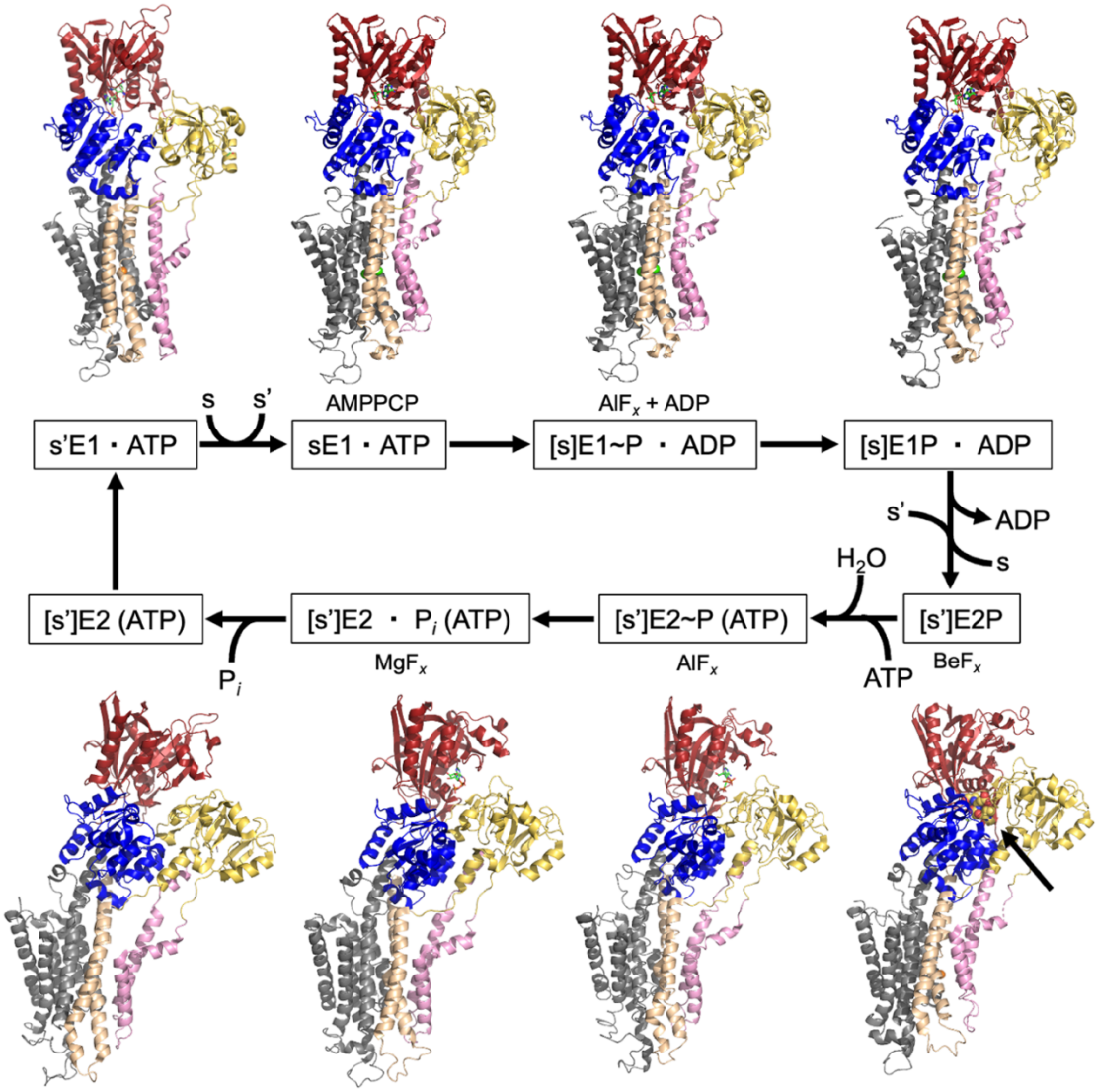

Figure 1.4: The Post-Albers cycle representing the general ion-translocation scheme of P-type ATPases *based on SERCA. s represents the cytosolic substrate, s' the counter-transported substrate, [s] is occluded substrate and (ATP) refers to modulatory ATP. Inhibitors are shown beside the state they stabilise. The structural basis for transport is based on structures: s'E1 · ATP (PDB 3W5A), sE1 · ATP (PDB 3N8G), [s]E1~P · ADP (PDB 1T5T), [s]E1P · ADP (PDB 3BA6), [s']E2P (PDB 3B9B), [s']E2~P (ATP) (PDB 3B9R), [s']E2 · Pi (ATP) (PDB 1WPG), [s']E2 (ATP) (PDB 3W5C), s'E1 · ATP (PDB 3W5A). Arrow for [s']E2P points towards the conserved TGES loop in the A-domain, shown as spheres. Note these structures most closely match the state however for 3W5A a temporary ion is bound in transition between s' and s for 3B9B the structure is open without s' bound yet. Colours represent domain colouring shown for P$_{II}$-type ATPases in Figure 1.3.*

1.2.2.1 Studying the P-type ATPase catalytic cycle

To access the energy stored in ATP, P-type ATPases hydrolyse the phospho-anhydride bond between the β and the terminal γ phosphate of ATP to release ADP and inorganic phosphate P_i, as is described above. Due to the reversibility of the hydrolysis, ADP and P_i can be condensed back to form ATP by other proteins in the cell, allowing a continual cycle between the two states to exist and the energetic currency available in the cell to be renewed.

The cyclical nature of ATP hydrolysis and regeneration can be harnessed to structurally investigate the catalytic cycle of P-type ATPase by inhibiting the enzyme with a series of analogues that resemble the molecule and its derivatives (Bagshaw, 2001). Analogues of ATP have been designed to alter the nature of the γ-end of the phosphate chain. Relevant examples to this thesis include AMP-PCP and AMP-PNP which are non-hydrolysable analogues where the oxygen in the anhydride bond has been changed for carbon or nitrogen, respectively. With the use of AMP-PCP, the E1-ATP state was solved (T. L. M. Sørensen et al., 2004; Toyoshima & Mizutani, 2004) and with AMP-PNP (a low turnover ATP mimic) the high-energy E1P state was solved (Olesen et al., 2007).

A series of heavy metal fluorides (AlF_x, MgF_x and BeF_x) have been used to capture the phosphoryl-transfer states. The theory behind the heavy metal fluorides is that they adopt slightly different stereochemistry that relates to a different state of phosphate during hydrolysis. Biochemical evidence for the inhibition of E2 states with these fluorides was pioneered by Danko *et al.* They demonstrated that beryllium, aluminium and magnesium fluorides in fact do stabilise the specific states they were hypothesised to inhibit (Daiho et al., 2010; Danko et al., 2004). Structural work using the metal fluorides further corroborated this understanding. The E1

transition state of SERCA was captured with ADP and AlF_4^- which mimics the geometry of planar pentavalent phosphate during transfer (T. L. M. Sørensen et al., 2004). Covalently phosphorylated SERCA E2P was captured by inhibition with BeF_3^- and the P_i-bound E2 · Pi after dephosphorylation was solved with MgF_4^{2-} (Olesen et al., 2004, 2007). Together, these series of studies present a comprehensive overview of how ATP and P_i analogues can be used to study the mechanism of phosphorylation, dephosphorylation and substrate transport in all P-type ATPases.

1.2.3 Lipid interactions with P-type ATPases

Lipids have long been suggested to play a crucial role in mediating the activity of P-type ATPases, yet few studies have shed light on the exact mechanism of where they bind or how they might influence function.

In the P_{II}-ATPase family, studies predominantly focussed on the Na^+/K^+-ATPase and SERCA. For the Na^+/K^+-ATPase, a combination of the structural and functional studies showed that PS and cholesterol stabilise the protein and support activity, and PC and PE specifically stimulate the activity (Habeck et al., 2017). A study on detergent-solubilised SERCA crystallised with PC lipids containing different acyl chain lengths and saturation reported a total of four recurring binding sites (Drachmann et al., 2014). Two of the binding sites were specific to a certain conformation, suggesting that there is variable interaction between P-type ATPases and lipids depending on the conformation, and that the binding must be transient. In the site that PS bound to the Na^+/K^+-ATPase, one of the two conformation-independent sites bound a lipid as well. This highlights the potential for overlap of lipid-binding site functionality among P-type ATPases. The studies on SERCA

modelled the lipid densities as either PC or PE and no further analysis was conducted to identify them. Coarse-grained (CG) molecular dynamics (MD) simulations of SERCA demonstrated that cholesterol primarily influences activity through a more general impact of the bilayer properties (Autzen et al., 2015). Stimulation of the plasma membrane Ca^{2+}-ATPase (PMCA) activity by PI and PS has also been observed, and the lipids are believed to compete with the auto-inhibitory domain from a calmodulin binding site (Pinto & Adamo, 2002). Aside from lipid-specific interactions, membrane deformation has been proposed for the Na^+/K^+-ATPase as the hydrophobic stretch of the TM helices does not match the membrane thickness (Cornelius et al., 2015).

The more recently characterised P_V-type ATPases require anionic lipids for function, as studies of the P_{VA}-ATPase Spf1 indicate the protein is stimulated by phosphatidylinositol-4-phosphate (D. M. Sørensen et al., 2019). The study also shows that ceramides and ergosterol increase activity compared to the baseline. The recent structure of the P_{VB}-ATPase found a putative rod-shaped density that was defined as an unassigned lipid binding between M1, M3 and M4; a site critical to substrate binding and a site that frequently pops up in crystallographic data (Li et al., 2021). Three further densities in the structure were found between unlabelled helices and are assigned to PC, PA and PIP_2.

Of greatest relevance to this thesis is the interaction of lipids with P_{III}-type ATPases. The *in vitro* fungal H^+-ATPase activity requires anionic lipids from Folch Fraction I (Addison & Scarborough, 1981a), and proper oligomerisation and trafficking are dependent on CIPs (see section 1.3) (Gaigg et al., 2005). Lysophospholipids activate the plant PM H^+-ATPases (AHA2) by interaction with the C-terminal domain. This interaction is dependent on the glycerol backbone and

increased with the acyl chain length of the lipid whilst the head group had little effect (Wielandt et al., 2015).

All in all, the literature to date demonstrates lipids play an important role in the regulation, stability, biosynthesis and function of P-type ATPases. Yet, there is no comprehensive understanding of how lipids fulfil this role. One of the challenges in these studies is linking the functional data to obtaining a spatiotemporal understanding of the function, especially in a complex membrane setting.

1.3 Plasma membrane H^+-ATPases

1.3.1.1 Plasma membrane H^+-ATPases: Introduction

Plasma membrane H^+-ATPases of the P-type ATPase family are members of the P_{IIIA}-type ATPases found exclusively in fungi and plants. They are entirely unrelated to the better known and well-studied F_oF_1-ATPases which is also capable of pumping protons across biological membranes. H^+-ATPases have been researched as one of the model P-type ATPases for a long time, with biochemical studies dating back to the 1960s. Seen as the discoverer of the H^+-ATPase, Clifford Slayman found that *N. crassa* has a substantial plasma membrane potential (often exceeding -200 mV) and inhibitors of ATP synthesis caused membrane depolarization (Slayman, 1965; Slayman et al., 1973). The theory, therefore, became that plants and fungi could generate a proton-based plasma membrane potential through ATP consumption, which at the time stood contradictory to the chemiosmotic hypothesis from Peter Mitchell proposing that the proton gradient could be used to condense ADP and P_i into ATP (which also happens in the mitochondria of plants and fungi) (Mitchell, 1961). Researchers have since established that the proton gradient produced by H^+-ATPases serves as the main

energy source for nutrient uptake by secondary active importers (Palmgren, 2002) and when H^+-ATPases are knocked out, cells do not survive. Because of this, H^+-ATPases have long been identified as a potential drug target for novel antifungals. The secondary active transporters couple transport of nutrients and waste in and out of the cell to the import of protons along their gradient. H^+-ATPases have been reported to use up to 20% of cellular ATP (Morsomme et al., 2000) and are capable of maintaining an intracellular pH of 6.6 against an extracellular pH of 3.5, corresponding to a membrane potential of -180 mV (Eraso & Gancedo, 1987). In fungi, the major H^+-ATPases is called Pma1. For the purpose of this thesis, the introduction will focus on the fungal H^+-ATPase, and where relevant, reference will be made to the plant H^+-ATPase.

The isolation of Pma1 was critical to its early characterisation as purification of all membranes included the F_oF_1-ATPase as a contaminant, which interfered with the research questions being addressed at the time. Gene Scarborough developed a solution by using a wall-less mutant of *N. crassa* that could be agglutinated with concanavalin A. The concanavalin A binds to carbohydrates on the surface and cells agglutinate due to the multimerization of concanavalin A. Upon cell disruption, the concanavalin A-bound membranes could be harvested separately by centrifugation at lower speeds than for normal membranes (Scarborough, 1975). This forms the basis of membrane preparation described in section 2.2.4.2. By developing this protocol, Scarborough and subsequent researchers discovered that Pma1 is the most abundant membrane protein in the plasma membrane and constitutes up to 10% of the total membrane proteins in *N. crassa* and 25% in *S. cerevisiae* (Fajardo-Somera et al., 2013).

1.3.1.2 Fungal H^+-ATPase isoforms

Fungi contain two isoforms of the PM H^+-ATPase, Pma1 and Pma2. Pma2 shares 89% sequence identity with Pma1 and is functionally interchangeable with Pma1 (Schlesser et al., 1988). Pma1 and Pma2 vary in their response to glucose and ethanol activation and Pma2 has a higher apparent affinity for ATP and Mg^{2+} (Monteiro & Sá-Correia, 1998; Supply et al., 1993). More recently, Fernandes and Sá-Correia investigated the pattern of Pma1 and Pma2 expression in *S. cerevisiae* under various growth conditions and found that Pma1 is the predominant H^+-ATPase present in the fungal PM, with negligible amounts of Pma2 (Fernandes & Sá-Correia, 2003). Under respiratory metabolism in ethanol-based medium or after diauxic shift, both genes expressed 2.5-4.5-fold more compared to fermentative growth. In diauxic growth after ethanol depletion, an eight-fold activation of Pma2 gene transcription is observed, suggesting Pma2 plays a role during carbon starvation (Fernandes & Sá-Correia, 2003).

1.3.1.3 H^+-ATPase Oligomerisation

In contrast to the majority of P-type ATPases that function as monomers, the fungal H^+-ATPase oligomerises (Chadwick et al., 1987; Cyrklaff et al., 1995; Rhee et al., 2002). Until recently, there has been some debate regarding what the functional oligomerisation state of the enzyme is. Studies have shown that monomeric H^+-ATPase has both ATPase and proton-pumping activity (Goormaghtigh et al., 1986). However, radiation inactivation experiments have predicted the size of the protein to correspond to a functional dimer (Ferreira et al., 2001) and for maturation, surface delivery and glucose activation, the oligomeric state is crucial (Bagnat et al., 2001; M. C. S. Lee et al., 2002; Permyakov et al.,

2012). Detergent-solubilised Pma1 from *N. crassa* exists as a hexamer as seen by cryoEM of two-dimensional crystals (Cyrklaff et al., 1995) as well as single particle cryoEM (Rhee et al., 2002). Freeze-fracture studies of *S. cerevisiae* PMs by electron microscopy showed the existence of tightly packed lattices of a hexagonal protein (Gross et al., 1978) now believed to be the H^+-ATPase and suggest that the H^+-ATPase does exist as a hexamer in the fungal PM. The oligomerisation state of H^+-ATPases might however vary per species. Whilst *N. crassa* and *S. cerevisiae* H^+-ATPases form hexamers, Dufour and Goffeau found that 8-10 H^+-ATPase monomers oligomerise in *S. pombe* (Dufour & Goffeau, 1980).

1.3.1.4 N- and C-terminal autoregulation

Fungal H^+-ATPases contain both C-terminal and N-terminal extensions and both regulate the activity. The ScPma1 N-terminal extension is proposed to serve as a voltage sensor based on a high propensity of negatively charged residues (Kühlbrandt et al., 2002) and could be involved in intracellular pH regulation. Removal of the first 27 residues of ScPma1 did not affect the activity or its response to glucose metabolism (Mason et al., 1998). In contrast, deletion of the C-terminal 18 residues in the same study generated an enzyme insensitive to glucose metabolism and significantly lowered the K_m for ATP. Dual truncation caused the K_m to lower even further, suggesting the N-terminus does play a role in regulating activity. Recent advances in the high-resolution structure have resolved the α-helical R-domain and proposed a mechanism of function (discussed below), however, the N-terminus was not resolved, likely due to it being predicted to be a disordered region. This disorder is also found in the AlphaFold structure, which predicts a long, unfolded region covering the first 40 residues, and an α-helix that

folds against the A-domain from residues 41-61, with a low confidence score (Jumper et al., 2021).

The R-domain is believed to regulate Pma1 via both *cis*- and *trans* acting effects. Under starving conditions, the R-domain is bound across the P-domain and tethers the P-domains of two adjacent monomers (Heit et al., 2021). Binding to the P-domains restricts the motions necessary for catalysis and limits the activity of Pma1 – this is referred to as the basal state. Under metabolic conditions, i.e. in the presence of glucose, a signalling cascade induces the expression of kinases that phosphorylate the R-domain at specific serine and threonine sites. Specifically, in *Sc*Pma1, release of autoinhibition has been linked to phosphorylation of Ser899 (Ser901 in *N.* crassa) by Ptk2 and phosphorylation of Ser911 and Thre912 (Ser913/Thr914 in *N. crassa*) by an unknown kinase (Eraso et al., 2006; Lecchi et al., 2005, 2007; Mazón et al., 2015). Calcium signalling, inositol trisphosphate signalling and membrane protease Lpx1 are also involved in glucose activation (Mazón et al., 2015). Whilst glucose-activated Pma1 has not been structurally resolved, based on the autoinhibited structure, phosphorylation would block interaction with one of two adjacent P-domains to alleviate inhibition, further supporting the relevance of the hexamer as the functional unit (Heit et al., 2021). Zhao *et al.* recently published a structure of *Sc*Pma1 described as an E2P BeF_x state that they activated by pH 6. In the structure, the helix is proposed to release completely, induced by the pH, suggesting there might be alternative mechanisms for R-domain activation other than phosphorylation, although any physiological relevance of such suggestions remain to be demonstrated (P. Zhao et al., 2021).

1.3.1.5 Microdomain association and surface transport

Over two decades ago, Pma1 delivery to the PM was shown to require microdomain association (Bagnat et al., 2001). This domain has since been termed the MCP. An interesting feature of the MCP, unlike most other microdomains, is that its formation occurs in the ER. The consensus, however, states that the secretory pathway contains a gradient of lipid compositions, with the ER membranes being poor in domain-forming lipids such as sterols and sphingolipids (van Meer et al., 2008). Once formed, the MCP network spans across the cell and has a long half-life (Malinska et al., 2004). Whilst microdomains are generally considered to be rigid, Pma1 laterally diffuses within them (Malínská et al., 2003), yet it can form a hexagonal honeycomb-like packing (Malinsky et al., 2016). The physiological purpose of the MCP remains unknown. Two studies have shown reduced function for H^+-driven arginine permease, Can1, and methionine permease, Mup1, when tethered to the MCP, causing authors to propose that the proton symporters need to occupy domains distinct from the MCP to maintain the proton gradient and membrane potential (Malinska et al., 2004; Spira et al., 2012).

The temperature-sensitive double mutant P434A, G789S of Pma1 exhibits defective MCP association and is targeted for vacuolar degradation (Bagnat et al., 2001). They discovered that whilst its function is unknown, multicopy overexpression of Ast1p can restore correct raft association of the mutant. The original raft hypothesis states that associated proteins may not spontaneously partition into them but instead there are proteins that drive them into the sphingolipid/sterol-rich regions (Simons & Ikonen, 1997). Ast1p could therefore fulfil the role of ensuring Pma1 associates with the MCP (Bagnat et al., 2001). The same study also shows that Pma1 oligomers require the presence of functional

microdomains and they conclude that the oligomerisation event is not isolated but part of the formation of microdomains.

Whilst Pma1 is thought to be the sole protein component, a few studies have tried to elucidate the lipid composition of the MCP. It depends on very long-chain fatty acids of 26+ C-atoms, as shortening to C22 induces rapid Pma1 degradation (Gaigg et al., 2005, 2006). A major fungal PM component is ceramides and so their impact on Pma1 biogenesis was tested using a series of inhibitors; Myriocin to block long chain synthesis, fumonisin B1 to block ceramide production and aureobasidin to block the conversion of ceramide to phosphoinositol ceramide. Pma1 degraded in cells treated with each of these inhibitors and so it was concluded that ceramide synthesis up to inositol addition, forming CIP, is required for stable Pma1 production. A follow-up study by Gaigg *et al.* found that by substituting C26 sphingolipids for C26 glycerophospholipids, the former are dispensable for microdomain association and that successful surface delivery of Pma1 relies on C26 fatty acids (Gaigg et al., 2006). One other study also showed that cells devoid of ceramides contain monomeric Pma1 only (M. C. S. Lee et al., 2002). Moreover, the presence of phosphoinositol ceramides in the ER is crucial for oligomer formation and not in downstream processes of packaging into COPII vesicles or Golgi trafficking. COPII vesicles containing monomeric Pma1, whilst able to leave the ER, are redirected to the vacuole (M. C. S. Lee et al., 2002). Aside from long-chain ceramides, studies with a fluorescent sterol-binding compound, Filipin, suggests the MCP also contains low levels of ergosterol (Grossmann et al., 2007), however blocking the production of ergosterol does not impact Pma1 biogenesis (Gaigg et al., 2005). Contradictory to this finding, another study isolated the *S. cerevisiae* MCP using styrene-maleic-acid-lipid-particles (SMALPs) and report the

MCP is enriched for sphingolipids and PS, however, ergosterol is depleted (van 't Klooster et al., 2020). The exact composition of the MCP is therefore still under debate.

Once sorted into the MCP, Pma1 is transported via the secretory pathway from the ER to the Golgi and via secretory vesicles to the PM. Several studies have shed light on the nature of Pma1 transport. Lst1, for example, is a specialised Sec24 isoform that is required for the packaging of Pma1 into COPII-coated vesicles (Ferreira et al., 2001). Deletion of the ER-resident protein Exp1 leads to ER retention of Pma1 and has therefore been identified as a cargo receptor for Pma1 (Geva et al., 2017).

1.3.2 Structure of the plasma membrane H+-ATPase from *N. crassa*

The fungal H^+-ATPase is a ~600 kDa hexamer consisting of six identical 100 kDa monomers. Until recently, structural understanding of Pma1 was limited to an 8 Å electron microscopy map (Kühlbrandt et al., 2002). Now, high resolution structures of Pma1 from *N. crassa* and *S. cerevisiae* have been published (Heit et al., 2021; P. Zhao et al., 2021). The publication of *N. crassa* Pma1 by Heit *et al* includes work presented in Chapter 3. The structural description below will primarily refer to *N. crassa* Pma1 and clearly states when referring to *S. cerevisiae* Pma1.

Pma1 adopts the canonical P-type ATPase fold (Figure 1.5C). It consists of the N-, P- and A- soluble domains along with 10 TM helices. Additionally, the structure contains a C-terminal extension involved in its regulation. In the structures of both *Sc*Pma1 and *Nc*Pma1, an N-terminal extension was not resolved. In the autoinhibited states of both, however, the R-domain forms an α-helix that folds against the P-domain. Zhao *et al.* report an additional short α-helix for *Sc*Pma1 that

lies horizontal to the membrane and lies before the functional α-helix of the C-terminus.

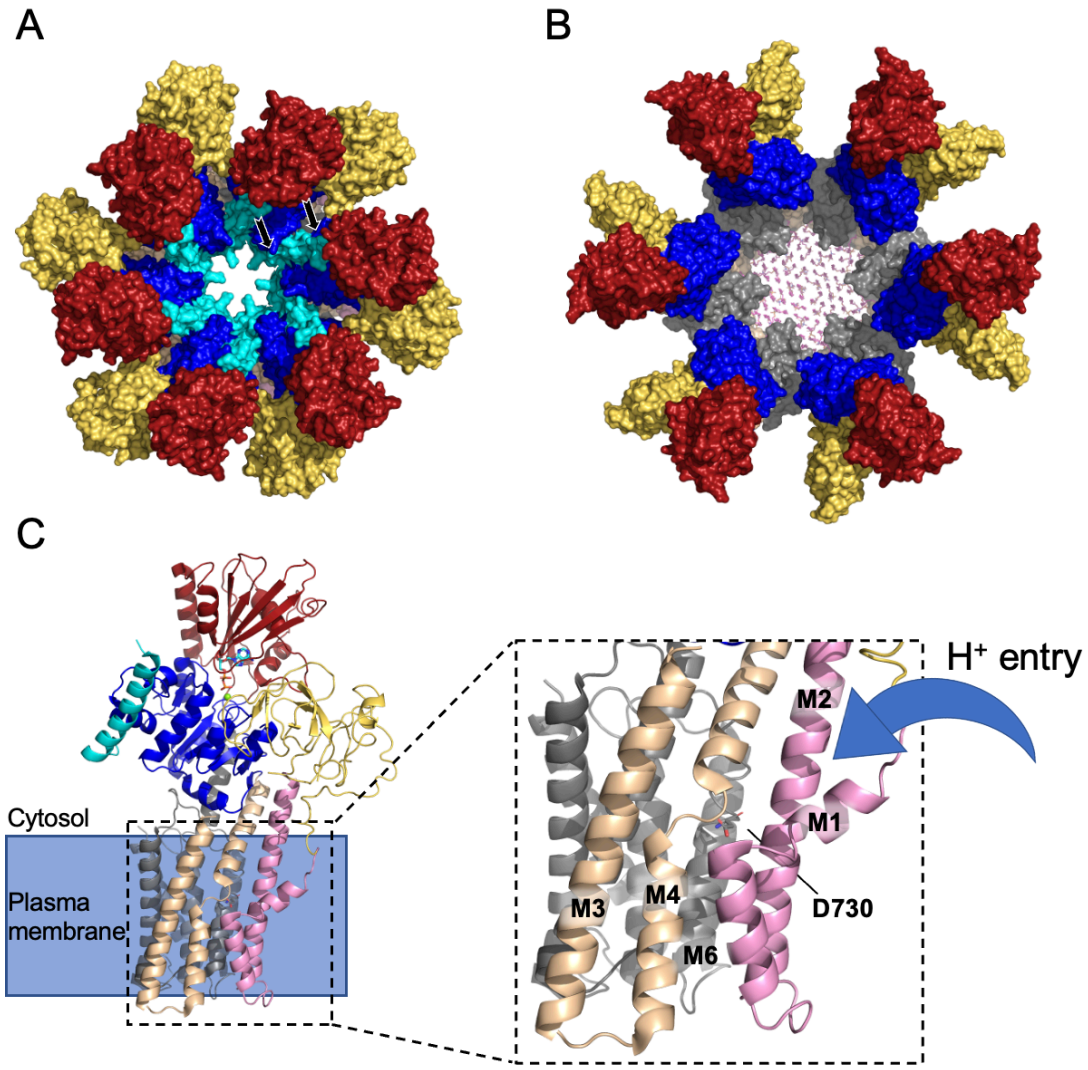

***Figure 1.5: CryoEM structure of Pma1**. Domains are coloured as follows; N-domain: red, P-domain: blue, A-domain: yellow, R-domain: cyan, M1/2: pink, M3/4: wheat, M5-10: grey. A) Surface view of the N. crassa Pma1 hexamer (PDB 7NY1), in the autoinhibited state, bound by ADP AlF_4^-. Arrows point to the intermonomer contacts with the R-domain. B) Surface view of the S. cerevisiae Pma1 hexamer in the pH-activated state, bound to BeF_x (PDB 7VH6). Lipids are shown as sticks. C) N. crassa Pma1 monomer structure from (A) illustrating the overall P-type ATPase fold. ADP shown as sticks. Inset highlights the proton binding site at Asp730 and the predicted proton entry path.*

Six monomers come together in a symmetric ring (Figure 1.5A). Whilst Pma1 adopts the same fold as other P-type ATPases, it uniquely makes intermonomer contacts that are crucial to the structural integrity of the protein. Monomer contacts are mediated by both the soluble domains and the TM domains. The soluble domains contact via the R-domain spanning two adjacent P-domains on the inside of the hexamer. Additionally, in the E1-inhibited *N. crassa* structure, the highly conserved TGES loop of the A-domain makes a contact with two α-helix termini in the P-domain on the outside of the hexamer. The transmembrane regions interact in a V-shape manner, predominantly connecting in the outer leaflet-half of the TMs (Figure 1.6). Specifically, residues in M3 of one monomer make polar contacts with residues in M7 and M10 of the neighbouring monomer. Hydrophobic residues in these TM helices also interact and are functionally conserved. Additionally, M3, 5 and 7 line the interior of the Pma1 hexameric ring whilst M1, 2, 6 and 9 face the outside.

The E1-inhibited structure of *Nc*Pma1 was bound by ADP, but clear density for AlF_x was not resolved. Therefore, the structure is proposed to represent a basal, pre-hydrolysis state. In this state, the M1 helix exhibits a characteristic kink. In Heit *et al.*, we propose that access to the proton-binding site within the TM domain is open and the M1 helix forms an anionic funnel-shaped access channel towards M6 that binds H^+. The proton acceptor/donor residue in Pma1 is conserved Asp730 on M6 and is essential for proton transport (Miranda et al., 2011). Upon proton-binding, it is proposed to make an H-bond with the adjacent Asn154 on M2. Proton release upon transition to E2 is believed to be driven by conformational changes that break this hydrogen bond as Asp730 forms a salt bridge with Arg695. This occurs with a concomitant closing of the entry funnel and opening of the exit pathway between

M1, M4 and M6, a model based on the research on the plant PM H^+-ATPase, AHA2 (Focht et al., 2017).

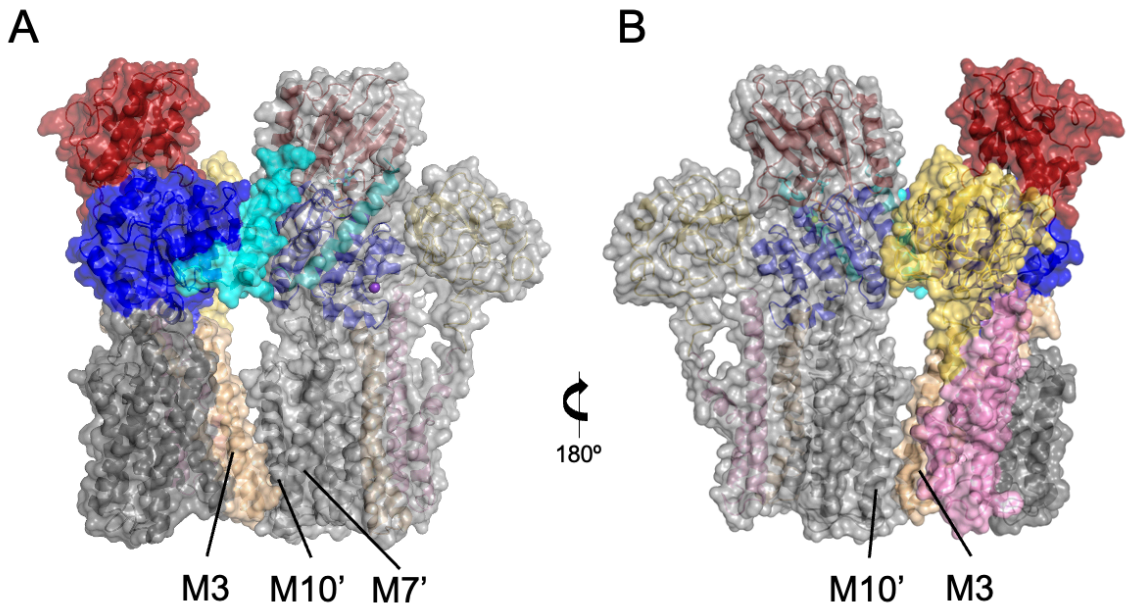

Figure 1.6: Interaction interface between the M-domains of NcPma1*, looking from the inside of the hexamer (A) and the outside of the hexamer (B). (PDB 7NY1)*

Evidence for lipid binding in the Pma1 structure was found by Zhao *et al* in the structure from *S. cerevisiae.* In the map of the C1-refined structure, 115 well-resolved, straight rod-like densities are located in the outer leaflet of the core of the protein (Figure 1.7). The rods are each 21 Å long and pack into a hexagonal lattice. At an inter-rod distance of 4.8 Å, this packing is consistent with a crystalline lipid monolayer. Zhao *et al* propose that this endogenous, co-purified lipid plug is a tightly packed microdomain of 57 fully saturated sphingolipids and one randomly distributed cavity. Moreover, they found 18 discernible lipid densities between the 115 rods and Pma1 hexamer. Zhao *et al.* state that the tight packing of the outer leaflet core could play an important role in maintaining the large potential across the membrane by preventing back leakage. The earlier mentioned V-shape

arrangement of the monomers in the hexamer is proposed to allow diffusion of lipids into and out of the core of Pma1 in the inner leaflet.

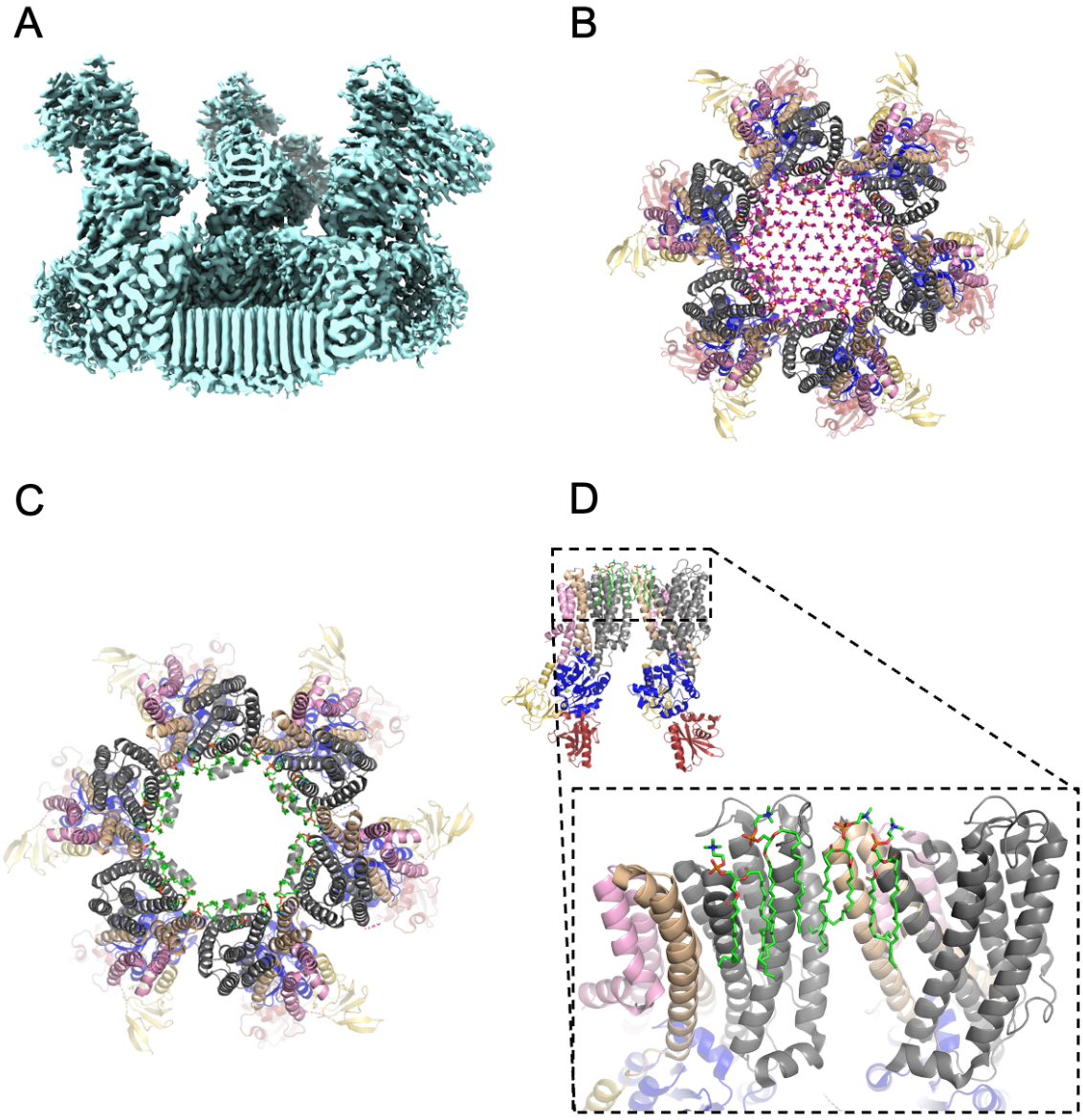

Figure 1.7: ScPma1 lipid densities from cryoEM*. A) CryoEM map showing the lipid plug consisting of 57 ordered lipids in the outer leaflet. B) Bottom view of the fitted model with the built in lipids (PDB 7VH6). C) Identified lipids binding to the inner ring of Pma1 (shown as green sticks). D) Zoom of (C) to show the binding of these lipids at the interface between monomers.*

1.4 The Sarco-Endoplasmic Reticulum Calcium ATPase (SERCA)

SERCA is a 110 kDa, Ca^{2+}-translocating ATPase that belongs to the P_{IIA}-type ATPase subfamily that pumps cytosolic Ca^{2+} ions across the sarco(endo)plasmic reticulum membrane and is vital in all eukaryotic cells. In particular, the pumping of Ca^{2+} back into the ER is relevant in the case of muscle contraction, Ca^{2+} signalling and cell survival (J. v. Møller et al., 2010).

In mammals, SERCA exists in three distinct genes, coding for SERCA1, 2, and 3. These 3 genes can be spliced to produce more than 10 isoforms through alternative splicing (Periasamy & Kalyanasundaram, 2007). SERCA1 is expressed in fast-twitch skeletal muscle and is responsible for Ca^{2+} uptake into the SR/ER during muscle relaxation and cellular Ca^{2+} homeostasis. SERCA1 is alternatively spliced to produce either SERCA1a (994 amino acids) expressed in adult mammals and SERCA1b (1001 amino acids) in neonatal mammals. The isoforms are distinguished by a hydrophilic amino acid segment at the C-terminus (Y. Zhao et al., 2015). SERCA1a is the most widely studied isoform with regards to structure and mechanism and is the isoform studied in this thesis. SERCA2 is the most widely distributed isoform and plays a critical role in Ca^{2+} homeostasis in cardiovascular tissue. SERCA3 encodes six isoforms that are expressed in several non-muscle tissues and appear in small quantities in muscle tissue (Anger et al., 1993).

1.4.1 General structure and function

SERCA1a (from here on referred to as SERCA), consists of the canonical N-, P- and A- cytosolic domains, the 6 core transmembrane transporter helices, TM1-6, as well as an additional 4 support helices, TM7-10. There are two Ca^{2+}-binding sites within the TM domain of SERCA, denoted as sites I and II based on a

sequential order of Ca^{2+} binding (Toyoshima et al., 2001). Ca^{2+}-coordination in site I is mediated by helices M5, 6 and 8 and site II coordinates Ca^{2+} between M4 and 6. Asp351 in the P-domain gets phosphorylated during the transition from Ca_2E1-ATP to Ca_2E1P-ADP.

1.4.1.1 Studying Ca^{2+} occlusion in SERCA with ADP-AlF_4^- and E309Q

A key aspect relating to substrate transport in P-type ATPases is the process of substrate occlusion during E1-ATP to E2P transition, a process that is particularly pertinent to this thesis. Occlusion of substrate entails blocking the exchange of Ca^{2+} with solvent to both the cytosolic and luminal sides of the membrane, preventing the formation of an open channel that would break the gradient during transport. The structural understanding of Ca^{2+} occlusion has come about through the investigation of an occlusion-deficient mutant and studies with ADP-AlF_4^- inhibition (Figure 1.8). The SERCA mutant E309Q (Glu309 coordinates Ca^{2+} at site II) has been demonstrated to bind two ions of Ca^{2+}, yet it is unable to occlude the ions (Clausen et al., 2013). The crystal structure portrays several features believed to be involved in Ca^{2+} occlusion. Firstly, the M1 helix is straight and shifted downwards, compared to the WT structure, creating an opening for Ca^{2+}-access to the cytosol (Figure 1.8B). This straight helix has also been reported in the nucleotide-free structure of SERCA with Ca^{2+} bound (Toyoshima et al., 2001). The M3 helix relaxes from the helical bundle, seen as an outward motion away from the P1-helix (see below for more information). Therefore, in an unoccluded state, M1 is believed to be flexible and capable of switching between a straight and kinked confirmation, thereby allowing Ca^{2+} to bind and unbind. Upon occlusion, the M3 helix

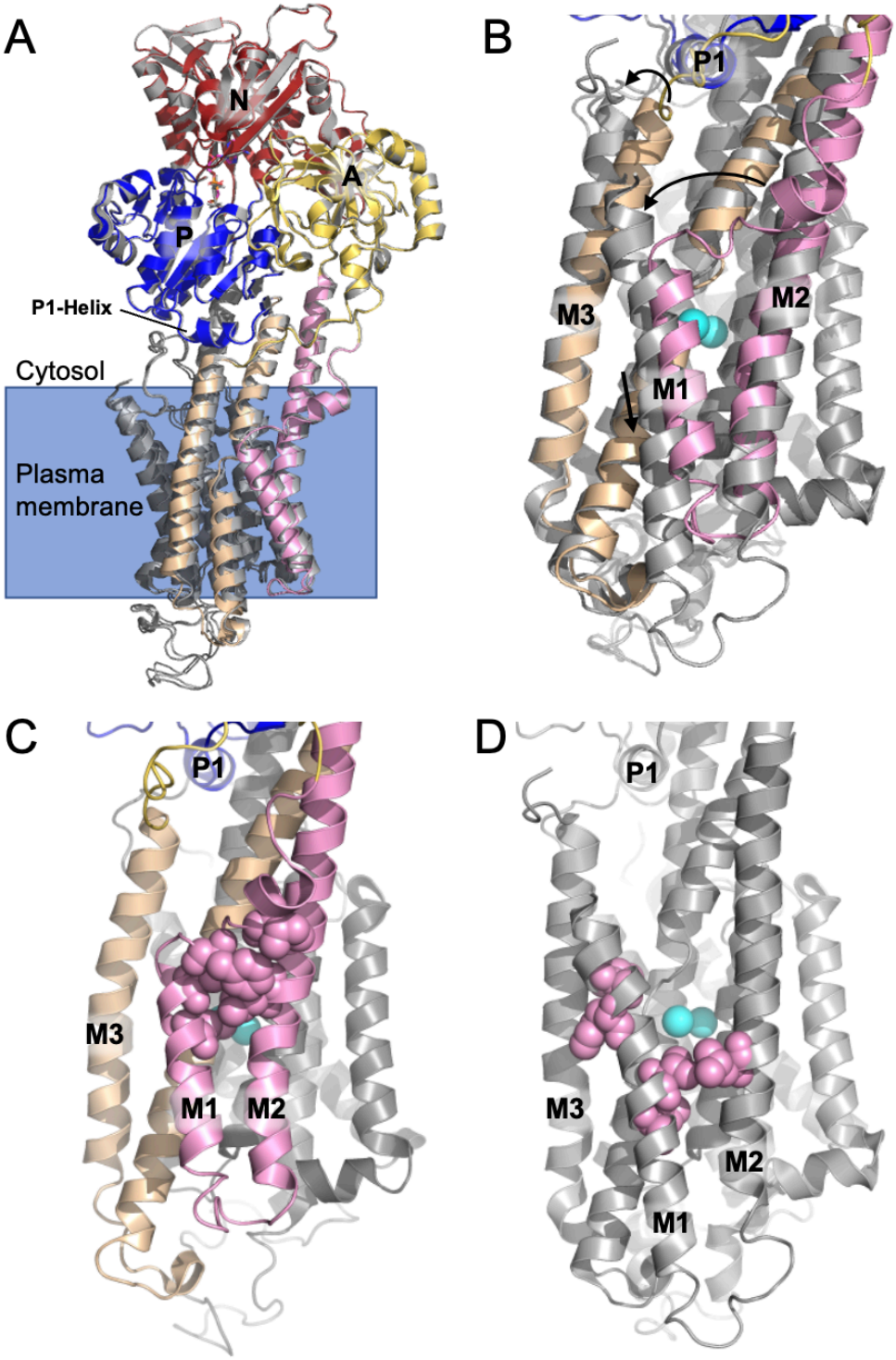

***Figure 1.8: Calcium occlusion in SERCA**. Alignments are made across M7-10. A) Alignment of E1 AMP-PCP (PDB 3N8G) to the transition state ADP AlF_x^- structure (PDB 1T5T). B) Alignment of E309Q occlusion-deficient mutant (PDB 4NAB:grey) to WT SERCA (PDB 3N8G: coloured) marking a straightening of M1 and outward motion of M3. The M1 hydrophobic lock is formed by a cluster of residues (shown as spheres) in WT E1 AMP-PCP (C) and are disengaged in E309Q (D). Ca^{2+} is shown as cyan spheres.*

tightens inward on the helical bundle and makes a closer association with P1 and the M1 helix is predicted to remain in a kinked confirmation. To further support this, when SERCA is inhibited with the ADP-AlF_4^- transition state mimic, it is locked in an occluded state that is marked by a loss in calcium exchange with the bulk solvent (T. L. M. Sørensen et al., 2004). By comparison, Ca_2E1-ATP, the state prior in the catalytic mechanism, exhibits free exchange of calcium with the bulk solution. The ADP-AlF_4^- crystal structure depicts an almost identical overall fold compared to the AMP-PCP inhibited structure (0.26 Å RMSD for all C_α atoms) (Figure 1.8A), which doesn't explain the observed functional differences. Therefore, there must be a link between the state of the ATPase site and the calcium-binding dynamics. Moreover, in the comparison with Ca_2E1 (no nucleotide), Sørensen *et al.* propose the kink in M1 establishes the formation of a hydrophobic lock between residues in M1 and M2 (Figure 1.8C). In the E309Q structure, these residues are disengaged (Figure 1.8D). Since this lock is engaged in both AMP-PCP and the ADP-AlF_4^- structure, Sørensen *et al.* propose that the difference induced by the phosphoryl-transfer transition state lies in the dynamics of the two states rather than the inhibited lowest energy state.

1.4.1.2 The functional role of Loop 6-7

The cytosolic loop (L6-7 spanning residues Gly808-Ser830) that connects M6 to M7 contains a series of residues that are well conserved among P-type ATPases and have been implicated in the process of calcium binding and transport (Figure 1.9) (Lenoir et al., 2004; Menguy et al., 2002). Initially, limited proteolysis studies of SERCA showed changes in the electrophoretic migration of a C-terminal proteolytic peptide (corresponding to L6-7) in the presence of Ca^{2+}, suggesting that L6-7 interacts directly with Ca^{2+} (Falson et al., 1997). Mutation of the conserved

Asp813 and 818 (Figure 1.9 – bottom panel) to alanine (referred to as the ADA mutant, with Asp815 unchanged) showed a reduced ATPase activity and was rationalised by a loss of affinity for Ca^{2+} (Menguy et al., 1998). However, structural elucidation of SERCA showed the aspartate residues were not in a conformation expected to coordinate Ca^{2+}, suggesting the L6-7 is involved differently in Ca^{2+} binding. In light of the structure, Menguy *et al* proposed that the mutation of Asp813-818 to alanine has an indirect, allosteric effect on calcium occlusion through the loss of hydrogen bonds to TM helices that coordinate calcium (Menguy et al., 2002). It should also be noted that investigations of L6-7 in both SERCA and the Na^+/K^+-ATPase have suggested that the loop may be part of the ion binding pathway instead of via the M1 helix (Or et al., 1993; Shainskaya et al., 2000), however, the consensus currently is the M1-pathway described above. Further studies by Lenoir *et al.* on the ADA mutant demonstrated an effect on the affinity for ATP and has therefore also led to the proposal that the loop has a long-range functional role in the ATPase activity (Lenoir et al., 2004), altogether suggesting that the loop plays an allosteric role in calcium binding and ATPase activity – something that Chapter 8 sheds further light on. Finally, mutational studies on Arg822 (Figure 1.9 – bottom panel) have shown that, when mutated to alanine, a marked slowing down of Ca^{2+} binding and unbinding is observed (Clausen & Andersen, 2004). Interestingly, in the same study, mutation of Arg819 to alanine caused a 2-fold decrease in the rate of Ca^{2+} binding, but there was no recorded change in Ca^{2+} dissociation. The role of Arg822 is of particular relevance in the work presented in this thesis as it directly interacts with the P1 helix.

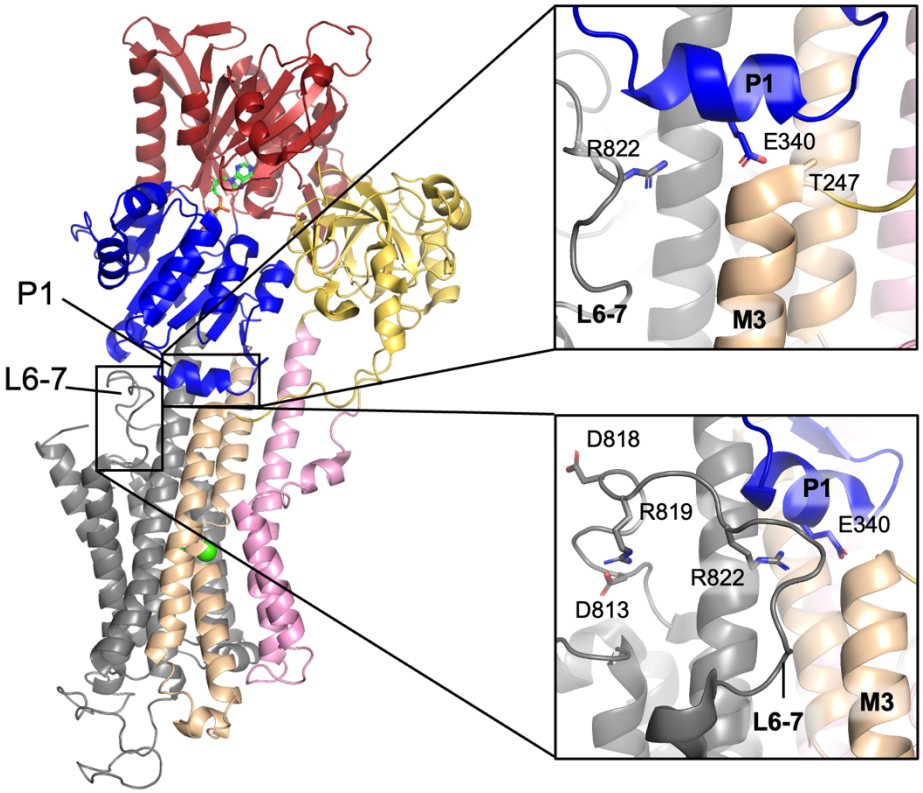

Figure 1.9: SERCA L6-7 and P1. Zoom in of the SERCA (PDB 3N8G) P1-helix is shown in the top panel, with residues 247, 340 and 822 shown as sticks. Zoom in of loop 6-7 is shown in the bottom panel with key residues shown as sticks.

1.4.1.3 The P1-helix and E340A

The P1-helix (Pro337-Cys344) in the P-domain of SERCA is an α-helix that runs parallel to the surface of the membrane and perfectly bisects the soluble and transmembrane domains (Figure 1.9 – top panel). The helix is directly connected to the β-strand that contains Asp351, and it contacts the cytosolic end of M3 and L6-7. Due to its positioning and interaction with key elements involved in both ATPase activity and Ca^{2+}-transport, P1 may play a key role in inter-domain communication. Within P1 lies a highly conserved residue, Glu340. The residue was first studied by Clausen and Andersen in 2004 when examining the relevance of the network connecting the P1-helix to M3 and L6-7 (Clausen & Andersen, 2004), they found that R822A in L6-7, T247A in M3 and E340A in P1 all cause a slowing in Ca^{2+}

binding and unbinding as well as reduced overall ATPase activity. Moreover, the mutation of Glu340 leads to the greatest measured difference in activity compared to T247A and R822A, explained by the fact that Glu340 engages in hydrogen bonds to both Thr247 and Arg822 and its loss disrupts the entire H-bond network whilst the other two mutations only cause partial loss.

Chapter 2: Materials and Methods

2.1 Molecular dynamics simulations - Background

Structural biology has continuously evolved our perception of the structure of proteins. Understanding these structures lies at the basis of almost all key processes in biology. With the advances made in cryoEM methodology, membrane proteins previously not resolvable by x-ray crystallography are now pushing our understanding even further. However, whilst these experimental techniques have allowed investigation of particular properties of these proteins, including their structure and function, their preferred bilayer orientation, lipid annulus, and dynamics have remained a mystery. With the development of computational molecular dynamics simulations, it is possible to look beyond the static structures and consider folding, self-assembly and interactions with the surrounding lipid membrane by placing solved protein coordinates into a native-like environment containing solvent and possibly a lipid membrane (Bond et al., 2007; Ingólfsson et al., 2016; Kandt et al., 2007; Lindahl & Sansom, 2008; Marrink & Tieleman, 2013). Molecular dynamics methods allow stepwise trajectories of such an environment to be calculated, identifying dynamic interactions that occur at sub-nanosecond and sub-nanometer spatiotemporal scales that are beyond that observable with traditional experimental techniques (Jefferies & Khalid, 2021). Two such cases are discussed in this thesis: the unique protein-lipid interactions of Pma1, and the intricate structural dynamics of SERCA. This chapter gives a background on the computational molecular dynamics simulation method.

2.1.1 Molecular mechanics

Firstly, a system in a given state needs to be described computationally. For this, a traditional approach is to use molecular mechanics (MM). Here, atoms are typically treated as individual particles with a given radius, and bonds between atoms treated as springs. MM relies on the computation of the potential energy of a system in a given state, as a product of the interactions between all atoms in the system. This is calculated using a potential energy function, and is described in more detail below.

2.1.1.1 Potential energy function

MM relies on the computation of the potential energy of a system in a given state. This is typically calculated as a sum of the forces acting between atoms forming either bonded or non-bonded interactions, as follows:

$$V = V^{bond} + V^{angle} + V^{dihedral} + V^{electrostatic} + V^{van\ der\ Waals} \quad (2\text{-}1)$$

This equation of potential energy (V) represents the potential energies resulting from bonds ($V^{bond} + V^{angle} + V^{dihedral}$) and the non-bonded energies ($V^{electrostatic} + V^{van\ der\ Waals}$).

Bonded interactions

Bonded interactions terms constitute bond length, angle and dihedral. The bond length between two covalently bound atoms is often modelled by a harmonic potential with a force constant derived from Hooke's law, which increases the potential energy as the distance between the bonded atoms deviates from the reference value, r_{eq} (equation 2-2). This however does not allow bond breakage.

$$V^{bond} = \sum_{bond} k_r(r - r_{eq})^2$$

(2-2)

The bond angle term is described by a formula that equates potential energy with the result from angle distortion based on a spring force constant and a reference angle (equation 2-3). Reference angles are a particular example where experimental data is used to inform the system. Both bonds and their angles are resisted by a force constant (k_r and k_θ respectively) since they require a lot of energy to change and are chemically more fixed.

$$V^{angle} = \sum_{angle} k_\theta(\theta - \theta_{eq})^2$$

(2-3)

Finally, the dihedral potential energy consists of a proper dihedral and improper dihedral component. Dihedral angle changes require significantly less energy than bond stretching and angle bending and are defined by their angle and the number of energy minima that exist between 0 and 2π (defined as *n* in equation 2-4). The term essentially restricts the rotation of atoms around bonds to a certain extent. The improper dihedral is often included to maintain planar configurations and prevent the opposite chirality and is related to the difference between the out-of-plane angle and the equilibrium angle, kept by the associated improper dihedral force constant. The rotation about chemical bonds is perhaps one of the major components in structural biology that allow for conformational changes and are therefore a key aspect in molecular dynamics simulations.

$$V^{dihedral} = \sum_{\substack{improper \\ dihedral}} k_\varphi(\varphi - \varphi_{eq})^2 + \sum_{\substack{proper \\ dihedral}} k_\phi[1 + cos(n\phi - \phi_{eq})]$$

(2-4)

Non-bonded interactions

The second part of the potential energy that describes the simulated system (equation 2-1) refers to the non-bonded interactions between atoms, including electrostatic interactions (attractive and repulsive) and van der Waals interactions. Often, these interactions are harder to model and computationally outweigh the bonded interactions due to the much greater plausible number of interactions possible. Several methods therefore exist to model these interactions.

Lennard-Jones Potential

The Lennard-Jones potential is a simple function that defines the potential energy of interaction between uncharged atoms and is a function of the distance between these two atoms (Jones, 1924; Rahman, 1964). Van der Waals interactions are often modelled with this Lennard-Jones potential. This function can be written as:

$$V_{LJ} = 4\varepsilon\left[\left(\frac{\sigma}{r}\right)^{12} - \left(\frac{\sigma}{r}\right)^{6}\right] \tag{2-5}$$

ε is a measure of how strong the molecules interact, referred to as the dispersion energy, σ is the distance at which the inter-particle potential energy is zero, often referred to as the size of the particle, and r is the distance between two interacting particles. The r^{-12} term describes the rapid increase in energy when two particles come closer and therefore represents the interatomic repulsion and the r^{-6} term represents the favourable interaction energy at long-range resulting from dispersion forces. When the distance becomes too short, the $\left(\frac{\sigma}{r}\right)^{12}$ magnifies and overpowers $\left(\frac{\sigma}{r}\right)^{6}$, causing the potential energy (V_{LJ}) to be very high. When the particles move

apart, the long-range energy can dominate and make the potential energy favourable until the particles move far enough apart for the interactions to cancel each other out and the potential energy decays towards zero, with Coulombic contributions dominating. For computational efficiency, a cut-off distance is usually applied to reduce the number of calculations so that interaction energy between atoms that are apart beyond a certain distance is reduced to zero.

Electrostatics

Electrostatic interactions play a critical role in molecular dynamics simulations and can attract two objects across greater distances. Their calculation is therefore important to model the potential energy of the system accurately. Several methods have been developed to approximate the potential energy, all aimed at describing Coulomb's law for interacting particles:

$$V^{electrostatic} = \frac{q_i q_j}{4\pi r_{ji} \epsilon} \tag{2-6}$$

where, q is the charge magnitude of particle i and j respectively and r_{ji} is the distance between the two particles. The equation describes the potential energy between two particles as proportional to the interaction between two point charges of a given size of charge and inversely proportional to the square of the distance between them.

The simplest technique to solve for Coulomb's law would be to calculate the direct sum of the equation, however this method is slow and computationally expensive. Therefore, alternative methods were developed that apply cut-offs that define once two atoms are a certain distance apart, their interaction is considered

trivial and no longer accounted for, thereby significantly reducing the number of particles to solve Coulomb's law for. Example methods include Ewald summation (Ewald, 1921), particle-mesh Ewald summation (Darden et al., 1993), and the Reaction Field method (Onsager, 1936).

Limitations of MM

There are several limitations of MM. Firstly, the electrons are assumed to adapt their motions instantly when the nucleus of an atom changes position and remain in the ground state. The Born-Oppenheimer approximation allows the motion of atomic nuclei and electrons to be treated separately, therefore the energy of the system can be considered as a function of the positions of nuclei only.

Additionally, due to this assumption, force fields (which describe the potential energy function of a system) are incapable of describing the properties that involve electronic distribution such as electron transfer (i.e. the process of chemical bond formation or breaking) and transition states with excited electrons (Monticelli & Tieleman, 2013). Put into context, this means that whilst the structural dynamics of P-Type ATPases can be studied, it is limited to its crystallised starting position and cannot cycle through the catalytic states, since the process of phosphorylation and dephosphorylation cannot be simulated.

As a result, force fields are simplified models of the true system's potential energy and need to strike the balance between modelling in as much detail as possible and computing costs. Parameterisation of the force field is based on empirical, experimentally derived data on the behaviour of atoms, including NMR, neutron diffraction and spectroscopy and quantum mechanical calculations. Various

force fields have been developed, each optimised to represent the nature of a particular type of system.

2.1.1.2 Choice of Force Field

There are different approaches for computing the underlying potential energy of a given system. Class I force fields have been developed to solve the harmonic functional form for bonded interactions shown in equation 2-1 and are used in this thesis. Class II force fields, on the other hand, have been developed to simulate nanoscopic molecular properties and do so by, for example, modelling bonded interactions by anharmonic functions (Jefferies & Khalid, 2021). Several class I force fields (such as CHARMM) have been optimised towards simulating biomolecular systems by combining quantum chemical calculations with thermophysical and phase coexistence data.

Class I force fields contain editable parameter files with values for calculating each component of equation 2-1 (including sizes of force constants). These empirically-derived parameters describe the physical properties of each atom, such as size and mass, as well as the nature of the bonded ($V^{bond} + V^{angle} + V^{dihedral}$) and the non-bonded ($V^{electrostatic} + V^{van\ der\ Waals}$) interactions.

Having described the energy of a system using MM, the power of molecular dynamics allows us to analyse a system that samples additional states and evolves over time, leading to potentially useful observations based on the dynamics of the system.

2.1.1.3 Laws of Motion

The generation of successive frames in molecular dynamics trajectories is based on the calculation, for a system of N atoms, of Newton's second law:

$$\overrightarrow{F_i} = m_i \overrightarrow{a_i} = \frac{d^2 r_i}{dt^2}, \forall i = 1 \dots N \tag{2-7}$$

where the instantaneous force ($\overrightarrow{F_i}$) acting on a particle of mass m_i at position r_i produces an acceleration $\overrightarrow{a_i}$ and moves the atom i in space (Leach, 2001). The force for each atom in the system can be derived from the potential energy function (V), which depends on the complete set of particles in the system.

$$\overrightarrow{F_i} = -\frac{dV}{dr_i}, \tag{2-8}$$

By defining the initial potential energy of the system, the forces acting on each of the atoms can be resolved, which causes the resulting positions, accelerations, velocities etc. to be calculated and updated.

2.1.1.4 Time steps

To solve for Newton's second law, (equation 2-7), the equation is solved across all atoms and can calculate the force acting on each atom at a given time point, generating a time dependent trajectory as the atomic positions are updated. However, since the motion of each particle is affected by the position and velocity of nearby particles, a finite difference approach needs to be used to overcome the computational burden. Whilst molecular dynamics simulations typically model systems in the nanosecond to microsecond time scale, the positions of atoms are

updated over small time steps, Δt, to make it computationally affordable and obtain greater resolution in the data. The most widely used method in Gromacs (the MD simulation package used in this thesis) is the leap-frog algorithm (van Gunsteren & Berendsen, 1988). This algorithm calculates the first velocities at half the defined time step ($t + \frac{1}{2}\Delta t$), followed by the updated positions of the atoms at the full time step ($t + \Delta t$), with approximated velocities for time step $t + \Delta t$. The time step selected needs to be small enough to capture the high frequency motions and bond oscillations whilst also accommodating realistic computational times. Since the leap-frog algorithm relies on the velocities from the prior step, a simulation requires random starting velocities to solve the first timestep and these are generally obtained from a Maxwell-Boltzmann distribution at a defined temperature.

2.1.1.5 Statistical ensembles

A molecular dynamics simulation deals with a constant particle number (N), constant volume (V) and constant energy (E), referred to as the NVE ensemble. However, in biological systems, the energy can fluctuate and typically the temperature (T) and pressure (P) are the constants instead. Systems are therefore described by the NPT (isothermal-isobaric) and NVT (canonical) ensemble.

Temperature Coupling

The NVT canonical ensemble aims to regulate the system at thermal equilibrium with a heat bath fixed at a constant temperature, derived from the kinetic energy of the system (H. C. Andersen, 1980). To maintain a temperature, the canonical system needs to exchange with the heat bath using a thermostat. A range of thermostats have been developed to accommodate this. The Berendsen scheme

is a weak-coupling algorithm that uses exponential relaxation to correct for deviations from the defined temperature of the system. It does so by scaling the velocities per time step in accordance with the temperature term to suppress fluctuations in kinetic energy (Berendsen et al., 1984). The velocity-rescaling thermostat is a modified version of the Berendsen thermostat with an additional stochastic term that ensures a correct kinetic energy distribution throughout the system, producing a correct canonical ensemble (Bussi et al., 2007). Another commonly used thermostat to simulate the canonical ensemble is the Nosé-Hoover chain method (Hoover, 1985), which introduces a thermal reservoir and a friction term to the equations of motion that is proportional to the particle's velocity. The friction term is a dynamic quantity, where its own momentum is dependent on the difference between the kinetic energy of the system and the set temperature.

Pressure Coupling

On top of coupling a system to a heat bath to maintain the temperature, ensembles can be coupled to a pressure bath to generate the isothermal-isobaric ensemble. This ensemble maintains a constant temperature, pressure and number of particles. Generally, two algorithms have been created to deal with the issue, the Berendsen barostat (Berendsen et al., 1984) and the Parrinello-Rahman barostat (Parrinello & Rahman, 1981). The Berendsen barostat rescales atomic coordinates at each simulation step to provide first-order kinetic relaxation towards the set pressure of the system. Whilst this algorithm produces a correct average pressure, the weak-coupling induced fluctuations do not modulate an isothermal-isobaric ensemble well. The Parrinello-Rahman barostat uses a constant-pressure algorithm, whereby the coordinates and box vectors obey the equations of motion

and the coupling strength is linked to the mass of the system, closely matching the NPT ensemble. The only drawback to the algorithm is that the system can become unstable in the case of large pressure fluctuations. As such, the Berendsen barostat is sometimes used for equilibrating the pressure of a system before simulation.

Additionally, in the case of simulating biological lipid membranes, the isotropy of the pressure coupling needs to be considered. Typically, biological simulations use an isotropic coupling that have uniform pressure scaling in all dimensions, as this responds best to pressure fluctuations. However, for lipid bilayers, better behaviour is seen when using semi-isotropic pressure coupling which scale in the x-y membrane plane independently from the z-axis (Sansom & Biggin, 2010).

2.1.1.6 Periodic boundary conditions

In molecular dynamics simulations, systems are limited to a box with a relatively small number of particles compared to the *in vivo* system and are drastically simplified to make it computationally achievable. For this reason, the treatment of molecules at the boundaries needs to be carefully considered. If the boundaries were to be treated as rigid walls, the particles would interact with the wall, which would lead to artefacts. Periodic boundary conditions alleviate this issue by replicating the box infinitely in all dimensions around itself such that a particle can diffuse across one barrier and appear on the opposite side. Due to this, it is important to select a box that is large enough to ensure that a particle cannot interact with its own image across the boundary.

2.1.2 -Coarse-grained MD simulations

For biological simulations, achievable time- and length-scales are still a limiting factor when studying the properties of atomistic systems such as a complex lipid membrane or slow processes. To partially circumvent this limitation, coarse grained simulations can be employed. By combining several atoms into one particle, the size of the system shrinks considerably, reducing the degrees of freedom. The dynamics of the system can then be computed, as described above but using much longer time steps (20-40 fs) and with fewer interaction calculations per time step, allowing considerable speeding up of the simulations.(Marrink et al., 2007).

This method is particularly applicable to membrane proteins, as this allows for larger systems that can accommodate complex membranes more accurately and equilibrate well. CG simulations as a result also achieve greater lipid diffusivity than atomistic simulations (Camley et al., 2015) and are therefore ideal for the study of protein-lipid interactions.

2.1.2.1 The Martini force field

A commonly used force field for CG simulations (and used in this thesis) is the Martini 2.2 force field (de Jong et al., 2013; Marrink et al., 2007). The force field was originally developed to study CG lipids (Marrink et al., 2004), and has been extended to proteins (Monticelli et al., 2008), carbohydrates (López et al., 2009) and nucleic acids (Uusitalo et al., 2015). The CG Martini force field parameters for non-bonded interactions are derived from experimental partitioning free energies. Specifically, this was achieved by calibration of the building blocks (discussed below) against thermodynamic data of the oil/water partitioning coefficients. To do so, a given coarse grained molecule is simulated in a system with both water and a

number of organic phases and the partitioning free energies are calculated and compared to the thermodynamic data.

With the building blocks parameterised, a shifted Lennard-Jones 12-6 potential energy function (equation 2-5) is used to describe the non-bonded interactions. For σ, the same effective bead size is assumed for each interaction pair. One exception to this is in the case of interactions between charged and the most apolar types, where the range of repulsion is extended, making it more favourable for charged particles to keep their hydration shell when dragged into an apolar medium (SJ et al., 2007). The Lennard-Jones interactions are divided into ten levels of interaction strength (ε) that are summarised by an interaction matrix, defining all possible combinations between the different bead types (described below) (SJ et al., 2007). Typically, non-bonded interactions are cut off once they reach a distance of 1.2 nm and the shift force is added in CG simulations to allow the force to decay smoothly to zero once a predefined shift distance is reached. For Martini CG simulations, parameterisation has set this shift distance to 0.9 nm. Additionally, charged group interactions are calculated by Coulombic potential energy with a shift distance of 0.0 nm and cut-off distance of 1.2nm. The extensive calibration of non-bonded interactions of the building blocks allow a system to be constructed with a mixture of these building blocks without the need for re-parameterisation. Bonded interaction parameters on the other hand are derived from all-atom and united-atom simulations.

The Martini force field employs a mapping scheme that on average simplifies four heavy atoms to one CG bead particle, with hydrogen atoms being neglected. These beads are then parameterised to have chemical properties closely matching the combined properties of the four heavy atoms. The Martini force field can be

generalised to four main families of particles, representing different chemical natures:

- Polar (P) particles represent neutral, hydrophilic atoms.
- Non-polar (N) particles represent mixed atom groups containing both polar and apolar features.
- Apolar (C) particles represent hydrophobic atoms.
- Charged (Q) particles represent ionised atoms.

P and C particles are both subdivided into five subgroups, ranging from low polarity (1) to high polarity (5). N and Q particles are subdivided into four subgroups, defined on the basis of their hydrogen-bonding capabilities (d for donor, a for acceptor, da for donor and acceptor and 0 for neither donor nor acceptor). By subdividing the particle groups into finer detail, the atomistic chemical variety can be more closely matched. For proteins, all backbone atoms are converted to a single polar particle with the degree of polarity depending on the local secondary structure.

New molecules can be parameterised to work with the Martini force field. Developers of the force field describe this process as follows. Firstly, a mapping of the atomistic molecule to the CG model needs to be decided. Then, bonded interactions need to be determined. Most molecules will use a standard bond length of 0.47 nm and a force constant of 1250 kJ mol^{-1} nm^{-2}. If the atomistic structure requires different values, such as describing a carbon-carbon double bond, then these values can be adjusted accordingly. Finally, the coarse grained model can then be compared to atomistic simulations. This structural comparison can be particularly useful to adjust the bonded parameters for the molecule.

Since hydrogen bonding is not possible in CG simulations, higher order structures need to be maintained in some way. For CG proteins, the secondary

structure is maintained by assigning it to each of the particles using DSSP (Kabsch & Sander, 1983).

2.1.2.2 The elastic network

Whilst the protein secondary structure is maintained by defining it in the particles using DSSP, the tertiary structure is preserved through creating an elastic network. In this thesis, the ElNeDyn network was used (Periole et al., 2009). The ElNeDyn network applies harmonic potentials between the backbone particles of a given three dimensional coarse grained structure within a given cut-off distance. This process creates a network of harmonic bonds that conserves the structure of the protein in a rigid manner. As a result of the rigidification of the protein structure, the dynamics of confirmational changes is lost, however it is particularly useful for the study of protein-lipid interactions for a given solved protein state.

2.2 Methods specific to Pma1

2.2.1 Coarse-grained simulations of Pma1

The atomistic hexamer model of *N. crassa* Pma1 (PDB 7NY1) was taken and one of the monomers was deleted to generate a model of Pma1 as a pentamer. Coordinates for all ligands were removed – which due to the use of the ElNeDyn network will not impact the structure of Pma1 during simulation. The pentamer structure coordinates were converted to coarse-grained MARTINI representation using the publicly available martinize.py script and the monomer chains were merged (de Jong et al., 2013). Their tertiary structures were constrained using the ElNeDyn elastic network (Periole et al., 2009) with a force constant of 500 kJ/mol/nm^2 and a cut-off of 0.9 nm.

The CG protein coordinates were positioned in the centre of a simulation box of size 23 x 23 x 23 nm^3 with its principal transmembrane axis aligned parallel to the z-axis and embedded in a complex asymmetric membrane bilayer comprised of 14 lipid species using the insane script (Wassenaar et al., 2015), the composition of which is described in Chapter 3. To investigate the role of lipid saturation, additional simulations were set up of pentameric Pma1 in a 50% C16:0/18:2 PC (PIPC): 50% C16:2/18:2 (DIPC) symmetric membrane. NaCl was added to the solvated system to 0.15 M.

The Martini coarse-grained force field version 2.2 (de Jong et al., 2013) was used for protein and version 2.0 for lipids. All the simulations were performed using Gromacs 2019.1 (Abraham et al., 2015). The systems were energy minimised using the steepest descents method, equilibrated for 50 ns using 20 fs timesteps in the isothermal-isobaric (NPT) ensemble at 323 K using the V-rescale thermostat (Bussi et al., 2007) and at 1 bar using a semi-isotropic Berendsen barostat (Berendsen et al., 1995). Five production simulations were run to 10 μs using the Parrinello-Rahman barostat (Parrinello & Rahman, 1981). Data were analysed using VMD (Humphrey et al., 1996), Gromacs tools (Berendsen et al., 1995) and in-house scripts. A weighted atomic density for Na^+ at each grid point was calculated using the VMD VolMap tool over 50 μs of simulation with default settings. Plots were made using MDAnalysis (Michaud-Agrawal et al., 2011) and Microsoft Excel.

2.2.2 Molecular Biology

2.2.2.1 Cloning of construct *Nc*Pma1-7

For recombinant expression of Strep-tagged Pma1 in S. cerevisiae, I modified a previously existing construct (*Nc*Pma1-1 - see Chapter 6) by inserting a Twin-STREPPII tag at position 850 and removing the existing N-terminal STREPII-TEV-tag using PCR cloning.

To create the Twin-STREPII insertion primers, the *in silico* *Nc*Pma1-1 construct was aligned to *Nc*Pma1-7 using NEBaseChanger to generate forward and reverse primers that would anneal at position 850. The Twin-STREPII amino acid sequence optimised for *S. cerevisiae* using the tool found at http://www.molbiol.ru/eng/scripts/01_19.html and inserted between the forward and reverse primers. Restriction sites for BspEI were engineered into the primers to create the following two primers: Forward (5'-ggtggttccggaggtggttctggtggttctgc ttggtctcatccacaatttgaaaaatctgct**gacacctccatcgtcgccg**-3') and reverse (5'-**ggttgg ttcgagcactcc**gcttcttggtctcatccacaatttgaaaaaggtggtggttccggaggtggt-3'). The bold letters refer to the annealing section of the primer, the rest is overhang.

The second set of primers were designed to remove the N-terminal STREPII-TEV tag from the vector. A Kozak sequence was inserted into the forward primer across the start codon of Pma1 on the vector. The following two primers were designed: forward (5'-cagggcggatccaaaaaaatggctgaccactcgg-3') and reverse (5'-cgccatggatccccggtaatttagtgtgtgtatttgtgtttgcg–3').

The forward primer of the Twin-STREPII insert with the reverse primer of the N-terminus created a 9 kB amplicon by PCR and the reverse primer of the Twin-STREPII insert and the forward primer of the N-terminus created a 2.6 kB amplicon by PCR. Triplicate reactions for both amplifications were run by PCR as follows.

Reactions were set up in PCR tubes: 0.5 µM forward primer, 0.5 µM reverse primer, 0.4 ng/µl *Nc*Pma1-1 template, 200 µM dNTPs, 1X NEB reaction buffer and 0.02 U/ml Q5 Polymerase HotStart. For the 2.6 kB fragment, the annealing temperature was 72 °C with an elongation time of 79 sec. For the 9 kB fragment, the annealing temperature was 71.5 °C with an elongation time of 406 seconds. Both reactions ran for 25 cycles. Reactions were checked for successful amplification by Agarose gel and fragments were purified by PCR Cleanup (Sigma Aldrich). The two fragments were restriction digested at 37 °C for four hours with BamHI-HF and BspeI in a 50 µl set up with the following final concentrations: 0.02 µg/µl PCR fragment, 1X buffer NEB3.1, 0.4 U/µl of either RE. After restriction digestion, quick CIP phosphatase was added to 0.2 U/µl to the 2.6 kB reaction mixture for 10 minutes. The fragments were ligated together with a 1:10 ratio of insert (2.6 kB fragment) to vector (9 kB fragment), calculated using the following formula:

$$insert\ (ng) = \frac{Insert\ (kB) \times\ vector\ (ng) \times\ ratio}{vector\ (kB)}$$

The reaction setup was as follows: 5 ng/µl of 9 kB fragment, 14.5 ng/µl of 2.6 kB fragment, 1X ligase buffer, 0.25 U/µl T4 Ligase (Thermo Fisher). The ligation reaction ran for 1 hour at 22 °C and was transformed into *E. coli* XL10 Gold ultracompetent cells (Aligent) according to the accompanying protocol and selected for on LB Agar Ampicillin (100 µg/ml) plates. Successfully transformed colonies were grown up in LB media overnight at 37 °C and plasmids were purified using NEB Miniprep kit. A standard restriction digest test on plasmids was performed using BamHI-HF and XbaI and plasmids displaying the expected digestion pattern were sent for sequencing (Source Bioscience).

2.2.3 Protein Biochemistry

2.2.3.1 SDS-PAGE

All gels presented in this thesis contain 10% polyacrylamide. In-house gels were made using BioRad gel casts. The resolving gel was composed of 375 mM Tris-HCl pH 8.8, 9.74% v/v acrylamide/0.26% v/v bisacrylamide, 0.1% w/v SDS, 0.08% w/v ammonium persulfate (APS) and 0.13% v/v tetramethylethylenediamine (TEMED). The stacking gel was composed of 125 mM Tris-HCl pH 6.8, 4.5% v/v acrylamide/0.12% v/v bisacrylamide, 0.1% w/v SDS, 0.12% w/v APS and 0.2% TEMED. Protein samples were incubated with 4X sample buffer (120 mM Tris-HCl pH8, 20% v/v glycerol, 8% SDS, 0.4% v/v β-Mercaptoethanol and 0.2 g bromophenol blue) for 15 minutes at 30 °C and loaded onto the gel, with PageRuler Plus prestained protein ladder (ThermoFisher) used as a molecular marker. The gels were run at 40 mA until the dye front reached the bottom of the resolving gel. Gels were stained in Coomassie brilliant blue G-250 (ThermoFisher) and imaged in a scanner (Canon Model X).

2.2.3.2 Western Blot

Samples were run on SDS-PAGE gels and protein was transferred onto PVDF membrane (Amersham) using a semi-dry blotting system (Bio-Rad), for 40 min at 10 V. The membrane was blocked with PBS blocking buffer (4 mM KH_2PO_4, 16 mM Na_2HPO_4, 115 mM NaCl, 3% Bovine Serum Albumin, 0.05% v/v Tween 20) for one hour at room temperature and washed three times with PBS-Tween buffer (4 mM KH_2PO_4, 16 mM Na_2HPO_4, 115 mM NaCl, 0.1% v/v Tween 20). The membrane was then incubated with Strep-Tactin horse radish peroxidase conjugate (IBA Lifesciences) diluted 1:10,000 in PBS-Tween buffer, and visualised with the

chemiluminescent Bio-Rad ECL system, following the manufacturer's instructions. Images were taken on a Gel Documentation system (Genesys).

2.2.3.3 Protein quantification

During purification for fast assessment, protein concentrations were determined spectrophotometrically using a NanoDrop One spectrophotometer. The extinction coefficient of *Nc*Pma1 (Abs 0.1%=1.044) was calculated by the ProtParam tool on the ExPASy server (Gasteiger et al., 2005).

The Bradford assay was used to calculate the concentration of protein when higher accuracy was required (Bradford, 1976). 20 µl BSA standards ranging from 0 to 2 mg/ml were incubated with 20 µl 1M NaOH. A range of protein sample dilutions were mixed with 20 µl NaOH, and 10 µl samples of each condition were pipetted in triplicate into a 96 well plate. 300 µl Bradford reagent was added to each well and the absorbance at 595 nm was measured. GraphPad Prism was used to analyse the data. A linear regression fit for the BSA standard would correlate protein concentration to absorbance and was used to calculate the concentration of the sample.

2.2.3.4 Baginski ATPase assay

The ATPase activity of Pma1 samples was measured by the Baginski assay (Baginski et al., 1967), which detects the amount of liberated phosphate from ATP hydrolysis. The assay was always performed in 96-well plates in reaction volumes of 50 µl. Triplicates of reaction and triplicates of negative control were run. Note that for analysis of AEX and glycerol gradient fractions, duplicates of reaction and SDS inhibition were run to conserve sample. Assays run for qualitative purposes such as

checking activity in the glycerol gradients were run at optimal pH using 50 mM MES-Tris pH 6, whilst the assays investigating E2-like inhibitors in Chapter 5 were run with 50 mM HEPES-NaOH pH 7, to promote an E2-like state in Pma1.

10 µl of sample was added to each well and 15 µl of 10% SDS was added to the negative control reactions before addition of reaction buffer. Reactions were initiated by adding 40 µl of reaction buffer: 50 mM buffer pH 6 or 7 (see above), 3 mM ATP, 1 mM $MgCl_2$, 5 mM NaN_3 (mitochondrial ATPase inhibitor), 50 mM $NaNO_3$ (vacuolar ATPase inhibitor), 0.25 mM Na_2MoO_4 (acid phosphatase inhibitor), 0.5 mg/ml Folch Fraction I lipid extract. Reactions were stopped after 40 min at room temperature (RT) with 15 µl 10% SDS. The amount of liberated phosphate was determined colorimetrically by addition of 50 µl Baginski colour reagent with a final concentration of 65 mM L-ascorbic acid, 2.2 mM ammonium heptamolybdate tetrahydrate and 189 mM HCl. The molybdenum (Mo^{VI+}) reacts with the phosphate to form $PMo_{12}O_{40}^{3-}$. The ascorbic acid reducing agent leads to the formation of the blue coloured $PMo_{12}O_{40}^{7-}$. The colour reaction was incubated for 10 minutes and the coloured complex was stabilised by addition of 75 µl of arsenite solution (3.1 mM $NaAsO_2$, 28 mM sodium citrate dihydrate, 141 mM acetic acid). Absorption was measured at 860 nm after an additional 30-minute incubation at RT.

2.2.3.5 Inhibitor dose-response curves

For the inhibitor studies, 65 µl of 0.5-1 µg Pma1, 50 mM HEPES-NaOH pH 7, 20 mM $MgCl_2$, and 10 µl of a the given inhibitor solution was preincubated for one hour. For MgF_x, BeF_x and AlF_x the $MgCl_2$/$BeCl_2$/$AlCl_2$ to NaF ratio was 1:5. For Compound 7, the positive control was incubated with 5% DMSO. The reaction was run as described in method 2.2.4.4. Raw data was imported into GraphPad Prism

and corrected for the SDS control to give a table of baseline adjusted values. The data was converted to % activity of control by calculating “Percent: 100*value/baseline”, using the positive control to represent 100% ATPase activity. The data was fitted with a nonlinear regression, using the option “[Inhibitor] vs. response – Variable slope (four parameters)”. This fit was selected because the model does not assume a standard slope but instead fits the Hill Slope from the data, making it the variable slope. The resulting analysis fitted the data with a response curve and provided IC_{50} as output.

2.2.4 Native *Neurospora crassa* Pma1 Purification

2.2.4.1 Cell culture

All native source Pma1 was purified from a cell wall-less *N. crassa* strain [Fungal Genetics Stock Center (FGSC), strain #4761] (Scarborough, 1985). Pre-cultures were grown by adding 1 ml aliquot of DMSO cell stock into 50 ml Vogel’s salts (per L: 130 g Na_3Citrate, 126 g KNO_3, 144 g $NH_4H_2PO_4$, 10 g $MgSO_4$, 5 g $CaCl_2$, 0.25 g biotin, 0.25 g $ZnSO_4$, 0.05 g $Fe(NH_4)_2(SO_4)_2$, 0.0125 g $CuSO_4$, 2.5 mg $MnSO_4$, 2.5 g H_3BO_3 and 2.5 g $NaMoO_4$) supplemented with 2% w/v mannitol, 0.75% w/v yeast extract (Difco), 0.75% w/v nutrient broth (Difco), 0.02 µg/ml and 50 µg/ml carbenicillin. This pre-culture was grown in 250 ml Ultra Yield flasks (Thomson) at 30 °C and 185 rpm (Brunswick Innova 44) for 2-3 days and cultures were continuously maintained by diluting 1 ml into 50 ml fresh medium. On the day before expression 50 ml culture were transferred into 2.5 L Ultra Yield flasks (Thomson) with AirOtop lids containing 600 ml Vogel medium supplemented as above and grown for 24 hours at 30 °C and 185 rpm. 100 ml culture is transferred

into six 2.5 L Ultra Yield flasks (Thomson) with AirOtop lids containing 600 ml Vogel medium and grown for a final 24 hours. OD_{650} of each culture was checked regularly and cells were harvested at 700 x g for 15 minutes at 4 °C, or RT for glucose-activation. In the case of glucose activation, cells were resuspended in prewarmed glucose activation buffer (50 mM Tris-HCl pH 7.5, 10 mM $MgSO_4$, 500 mM glucose) and incubated for a further 20 minutes at 30 °C and 185 rpm before being harvested at 700 x g for 15 min at 4 °C.

2.2.4.2 Membrane preparation

Membrane preparation was carried out as described previously (Scarborough, 1988), with a few modifications established by Dr. Sabine Heit. Cells were harvested and washed four times with ice-cold buffer A (50 mM Tris-HCl pH 7.5, 10 mM $MgSO_4$ and 250 mM mannitol), spinning down cells in between each wash at 700 x g for 15 min at 4 °C. Cells were resuspended in 30 °C buffer A and agglutinated with addition of concanavalin A (0.5 mg/ml) in RT buffer A for 10 min, followed by another 10 min on ice. This step is particularly temperature sensitive and determines the extent of agglutination success referred to in Chapter 4. Agglutinated cells were pelleted for 6 min at 200 x g and washed once with ice-cold buffer A. Lysis was obtained by homogenizing the cells in ice-cold lysis buffer (10 mM Tris-HCl pH 7.5, 1 mM $MgCl_2$, 1 mM $CaCl_2$, 1.5 µg/ml chymostatin and 1 µg/ml bovine deoxyribonuclease (DNase) I) containing 1.2% sodium deoxycholate (DOC) using a 50 cm^3 glass homogenizer. After centrifugation at 14,000 x g and 4 °C for 30 min the membrane pellet was washed with Buffer B (10 mM Tris-HCl pH 7.5 and 1.5 µg/ml chymostatin) containing 0.6% DOC and then with DOC-free buffer B, spinning at 14,000 x g and 4 °C for 30 min each time. Concanavalin A was

dissociated from the plasma membrane by incubation with 0.5 M α-methylmannoside in buffer B for 5 min at 30 °C. Membranes were diluted with ice-cold buffer B and pelleted at 14,000 x g at 4 °C for 30 min. The membranes were washed once with ice-cold Buffer B and resuspended in Buffer B, flash-frozen in N_2 (lq) and stored at -80 °C.

2.2.4.3 Membrane solubilisation screen

2X buffers (20 mM Tris-HCl pH 7.5, 300 mM NaCl, 2 mM Na_2ATP, 10 mM $MgSO_4$, 2X detergent) with detergents were prepared and added in equal volume to thawed membrane samples to create 200 µl reactions (3.5 mg/ml final membrane concentration for *S. cerevisiae* membranes and 2 mg/ml for *N. crassa* membranes). Samples were incubated by shaking at 600 rpm at RT for 15 min followed by 30 min of agitation at 4 °C. Samples were ultracentrifuged at 100,000 x g for 1 hr at 4 °C and supernatant was analysed by SDS-PAGE.

2.2.4.4 Purification in DDM

The protein concentration in the harvested membranes was determined by Bradford assay. Membranes were thawed in a RT water bath and spun down for 30 min at 14,000 x g and 4 °C. Membranes were resuspended to 4 mg/ml total protein concentration in ice-cold solubilisation buffer without detergent (10 mM Tris-HCl pH 7.5, 150 mM NaCl, 1 mM Na_2ATP, 5 mM $MgSO_4$, 0.1 mM Na_3VO_4 and 2 µg/ml chymostatin). The same volume of solubilisation buffer containing 4.5 mg/ml DDM (for agglutinated membranes) or 10 mg/ml LPC16 (for non-agglutinated membranes) was added to the membranes and solubilised for 1 h at RT followed by 1 h at 4 °C with constant agitation. Unsolubilised membranes were removed by

centrifugation at 17,500 x g and 4 °C for 1 h and supernatant was filtered through a 0.45 µm nylon membrane.

The protein solution was diluted 3.75-fold with anion exchange (AEX) dilution buffer [50 mM MES-Tris pH 6.8, 5 mM $MgSO_4$, 200 g/L glycerol, 1 mM dithiothreitol (DTT), 2 mM ethylenediaminetetraacetic acid (EDTA), 0.015% DDM and 2 µg/ml chymostatin] to lower the NaCl concentration below 40 mM. The diluted sample was loaded onto a pre-equilibrated 5 ml HiTrap Q HP AEX column (GE Healthcare) using a peristaltic pump. The column was attached to an AKTA PURE 25 FPLC system and washed with 10 column volumes (CV) of AEX wash buffer (50 mM MES-Tris pH 6.8, 50 mM KCl, 5 mM $MgSO_4$, 1 mM DTT, 2 mM EDTA, 0.015% DDM and 2 µg/ml chymostatin). Protein was eluted with a linear gradient to 500 mM KCl over 20 CV. Elution fractions were analysed by SDS-PAGE and Baginski assay.

Peak elution fractions were defined as the AEX fractions with peak ATPase activity and purity whereas the secondary elution fractions were defined as the fractions flanking the peak fractions that still contained ATPase activity but at a lesser purity. Peak and secondary elution fractions were pooled separately and diluted 1:10 with gradient dilution buffer (50 mM MES-Tris pH 6, 5 mM $MgSO_4$, 1 mM DTT, 2 mM EDTA, 0.015% DDM and 2 µg/ml chymostatin) and concentrated to 2 ml with Amicon Ultra centrifugal filters [100 kDa molecular weight cut-off (MWCO)]. The concentrated samples were loaded onto glycerol density gradients from 20 to 40% w/v (5% steps) in 50 mM MES-Tris pH 6.8, 50 mM KCl, 5 mM $MgSO_4$, 1 mM DTT, 2 mM EDTA, 0.015% DDM and 2 µg/ml chymostatin and ultracentrifuged for 16 hours at 34,400 x g (Optima L-100 XP, Ti70 rotor, acceleration 2, no brake). The gradients were harvested in 1 ml fractions from

bottom to top using a peristaltic pump and flash frozen in N_2 (lq). Samples of all fractions were analysed by SDS-PAGE and Baginski assay.

The purest fractions of the peak glycerol gradient were pooled and diluted in glycerol-free gradient buffer down to 15% w/v glycerol. A PD10 purification column (GE Healthcare) was washed 4 times with gradient dilution buffer and 4 times with cryoEM buffer (25 mM HEPES pH 7.0, 20 mM KCl, 5 mM MgCl2, 1 mM DTT, 2 µg/ml chymostatin and 0.015% DDM). The protein sample was loaded onto the column and the flow through was collected as waste. According to the supplier protocol, the cryoEM buffer was used to elute the sample. Using a Vivaspin 100 kDa MWCO concentrator, the buffer-exchanged protein sample was to the desired concentration for cryo-EM.

2.2.4.5 Purification in LMNG

At the beginning of this project, a sample of Pma1 purified in LMNG was provided by Dr. Sabine Heit. For this sample, cells had been grown up, as described above, in glucose-starving conditions to obtain autoinhibited Pma1. Membranes had been solubilised with 0.225% w/v DDM at 2 mg/ml and solubilised sample was concentrated pressure dialysis with a stirred cell (Amicon) and a 300-kDa MWCO filter membrane. The concentrated solution was run on two consecutive 20-40% glycerol gradients, in LMNG. After pooling the peak fractions of each gradient based on the SDS-PAGE analysis, the sample had been concentrated and purified further using SEC. Fractions had been analysed by negative stain electron microscopy and showed mixed micelles and excessive impurities. This is where the author took over.

It was rationalised, that an additional AEX purification step in LMNG could render this sample suitable for further EM analysis, Therefore, available SEC fractions were pooled and diluted using AEX dilution buffer and loaded onto a 1 ml HiTrap Q HP AEX column (GE Healthcare). The column was washed with 20 CV AEX wash buffer containing 20 mM KCl and 0.0015% LMNG followed by elution with a linear gradient to 500 mM KCl across 20 CV. Elution fractions were analysed by SDS-PAGE analysis. Peak fractions were pooled and concentrated to 0.5 ml using 100 kDa MWCO Amicon ultracentrifugal filters. The sample was loaded onto a pre-equilibrated Superose 6 Increase 10/300 (GE Healthcare) SEC column and eluted with SEC buffer (50 mM MES-Tris pH 6.5, 20% glycerol, 50 mM $MgSO_4$, 1 mM DTT, 2 mM EDTA, 0.0015% LMNG and 2 µg/ml chymostatin). Peak fractions were evaluated by SDS-PAGE, Baginski and negative stain EM.

Samples were diluted to 0.015 mg/ml [determined with NanoDrop One (see section 2.2.3.2) with glycerol-free SEC buffer and imaged by negative stain electron microscopy as described in section 2.2.6.1.

2.2.5 Recombinant expression and purification of *Nc*Pma1 in *Saccharomyces cerevisiae*

2.2.5.1 Yeast transformation

A single colony of *S. cerevisiae* strain W303 was grown overnight in 5 ml YPD media (20 g/l Bacto peptone, 10 g/l yeast extract, 20 g/l dextrose) at 30 ˚C, shaking at 225 rpm and diluted to OD_{600}=0.1 the next morning by spinning down the calculated volume at 8000 x g for 30 sec and topping up with 40 ml of fresh YPD media. Cells were incubated at 30 ˚C, shaking at 225 rpm until OD_{600} reached 0.5. Cells were pelleted by spinning at 3000 x g and 4 ˚C for 5 min and washed with

sterile water to remove excess media. Pellets were resuspended in 100 mM LiAc, split into 100 µl aliquots in Eppendorf tubes and incubated at 30 ˚C, shaking at 1000 rpm for 30 minutes. Cells were pelleted by spinning at 8000 x g and 4 ˚C for 15 seconds and supernatant was aspirated. To each cell aliquot, the following was added, in order, to the given final concentration; 35% PEG 3350, 100 mM LiAc, 0.28 mg/ml salmon sperm DNA and 2.7 µg/ml plasmid DNA. Solutions were incubated at 30 ˚C for 30 min followed by heat shock at 42 ˚C for 20 min and plating on selective MM –URA agar plates (6.9 g/l Yeast Nitogren Base without amino acids, 0.15 g/l Minimal Media -URA supplement, 12 g/l Agar).

2.2.5.2 Small scale expression

Glycerol stocks of *Nc*Pma1-X transformed *S. cerevisiae* W303 (MATα ura3-1 leu2-3,112 his3-11 trp1-1 ade2-1 can1-100), ΔPep4 (leu2-3 his3-11,15 ura3-1 ade2-1 canr,cir+ ΔPep4 MAT), Gal4ΔPep4 (leu2-3 his3-11,15 trp1-1::TRP1-GAL10-GAL4 ura3-1 ade2-1 canr,cir+ ΔPep4 MAT) or BJ5460 (MATa ura3-52 trp1 lys2-801 leu2-Δ1 his3-Δ200 pep4::HIS3 prb1-Δ1.6R can1 GAL) were streaked out onto MM –URA agar plates. Single colonies were picked and grown up in minimal media (MM) –URA 2% w/v glucose overnight at 30 ˚C, shaking at 225 rpm. The overnight culture was diluted 1/50 in MM –LEU 2% w/v glucose, growing for 48 hours at 30 ˚C, shaking at 225 rpm. On the day of expression, cells were spun down and resuspended at OD_{600}=0.05 in a 100 ml culture of MM –LEU 0.5% w/v glucose, 3% v/v glycerol for glucose starvation. At OD_{600}=1.0, the timepoint is defined as t_0 and 10 OD units of cells were spun down at 4000 x g for 5 min at 4 ˚C, supernatant was removed, and pellets were frozen in N_2 (lq) and stored at -80 ˚C. Expression was induced at t_0 by either 2% w/v lactate or 2% w/v galactose by adding 20% w/v

stock in MM –LEU. The temperature during expression was changed to 20 ˚C to favour protein expression over growth. Samples of 10OD units were taken at five timepoints: t_1=8 h, t_2=12 h, t_3=16 h, t_4=20 h and t_5=24 h.

Cell pellets from small scale expression were thawed and resuspended in lysis buffer (50 mM Tris-HCl pH 7.6, 5 mM EDTA, 10% v/v glycerol, protease inhibitor and topped up with 0.5 mm glass beads. Cells were lysed using a Fastprep machine (MPBio) by shaking tubes for three repeats of 40 sec with 5 min incubations on ice between repeats. Tubes were spun at 20,000 x g for 30 sec at 4 ˚C to separate the whole cells, debris membrane fraction and beads from the membrane fraction in the supernatant. The membranes in the supernatant were isolated by spinning the supernatant at 100,000 x g for 90 min at 4 ˚C. The pellet was resuspended in lysis buffer and homogenised for SDS-PAGE analysis. Lysis buffer was added to the pellet from the cell disruption containing the beads and debris and resuspended. Using a gel loading tip, sample was aspirated for SDS-PAGE analysis.

2.2.5.3 Large scale recombinant expression

The given *S. cerevisiae* strain transformed with *Nc*Pma1-x was plated on MM –URA plates. Single colonies were grown overnight into stock solution in MM –URA 2% w/v glucose at 30 °C, shaking at 225 rpm. Stocks were diluted 1/50 in MM –LEU 2% w/v glucose to 100 ml in baffled flasks and grown for 48 hours. The change to –LEU media would cause an increase in the copy number of the expression plasmid. Cells were spun down at 4000 x g and dissolved in 750 ml glucose-starvation media (MM –LEU), 0.5% w/v glucose, 3% v/v glycerol) to OD_{600}=0.05. At ~OD_{600}=1.25 expression was induced with 250 ml MM –LEU 8% galactose at 20

°C, shaking at 225 rpm for 12 hours. Cells were harvested by spinning at 1000 x g for 10 minutes. Pellets were resuspended in lysis buffer (50 mM Tris pH 7.6, 5mM EDTA, 10% v/v glycerol, protease inhibitor) at 5 ml/g, flash frozen in N_2 (lq) and stored at -80 °C.

2.2.5.4 Yeast membrane preparation

1 µg/ml DNAse I was added to thawed cells. Cells were disrupted three times using a high-pressure cell disrupter (Constant Systems) at 39 kPSI. Lysate was adjusted to pH 7.0-7.5 and spun at 2000 x g for 20 min to remove unlysed cells. The supernatant was spun at 20,000 x g for 30 min and the pellet was resuspended in solubilisation buffer (50 mM Tris pH 7.5, 20% v/v glycerol, 3 mM $MgCl_2$, 5 mM β-mercaptoethanol, 50 µM ATP, 100 mM KCl, protease inhibitor) to analyse as heavy membrane sample. The supernatant was ultracentrifuged at 234,000 x g for 2 h and its pellet was homogenized in salt wash buffer (50 mM Tris pH 7.5, 1 mM EDTA, 0.1 M KCl, 0.6 M sorbitol). The ultracentrifuge step was repeated followed by homogenizing with inhibitor wash buffer (50 mM Tris pH 7.5, 1 mM EDTA, 0.6 M sorbitol, 1 mM phenylmethylsolfonyl (PMSF)). Finally, membranes were ultracentrifuged and resuspended in solubilisation buffer (50 mM Tris-HCl pH 7.5, 20% w/v glycerol, 3 mM $MgCl_2$, 5 mM β-mercaptoethanol, 50 µM Na_2ATP, 100 mM KCl, 1 mM PMSF) at 5 ml/g pellet, flash frozen and stored at -80 °C. The protein concentration was determined by the Bradford assay (see section 2.2.3.2).

2.2.5.5 Recombinant Pma1 purification

Membranes were diluted to 4 mg/ml and solubilised in solubilisation buffer with 1% w/v Lysophosphatidylcholine-16, rolling for 30 min at RT followed by 1 h at 4 °C. Solubilised membranes were spun at 234,000 x g, 1.5 h at 4 °C to pellet unsolubilised membranes. Supernatant was passed over a pre-equilibrated 5 ml Strep-Tactin Superflow cartridge (IBA Lifesciences). The resin was washed with 20 CVs of wash buffer. Protein was eluted with 3 CV of elution buffer. Eluates were pooled and concentrated using a 100 kDa centrifugal concentrator to 0.7 mg/ml, spinning at 20,000 x g. The protein was loaded onto a Superose 6 10/300 column equilibrated in SEC buffer and eluted at 0.15 ml/min. Fractions were collected and analysed by SDS-PAGE and silver-stained using Bio-Rad system. ATPase activity of fractions was measured using the Baginski assay (see section 2.2.3.4).

2.2.6 Electron Microscopy

2.2.6.1 Negative stain electron microscopy

Carbon-coated 300 mesh 3mm copper grids (C267/050 TAAB Scientific) were glow-discharged (15 mA, 45 sec). Protein samples were loaded onto the grids by pipetting 4 µl sample diluted to 0.015 mg/ml (determined with NanoDrop) with glycerol-free buffer, incubating for 1 min and blotted with filter paper. 3 µl 2% uranyl acetate was applied onto the grid and incubated for 30 sec followed by blotting with Whatman filter paper. This was repeated another two times and the grid was subsequently dried at RT for 5 min. Micrographs were collected using a FEI Tecnai 12 TEM (Thermofisher Scientific) at the COSMIC facility in the Dunn School of Pathology.

2.2.6.2 CryoEM sample and grid preparation

Pma1-GA, purified in Chapter 4, was eluted in cryoEM buffer (20 mM HEPES-NaOH pH 7, 25 mM KCl, 1 mM $MgCl_2$, 1 mM DTT, 1 µg/ml chymostatin and 0.015% DDM) from the PD-10 desalting column and concentrated to 2.49 mg/ml with Vivaspin centrifugal filters (100 kDa MWCO). The protein was incubated for 2 hours on ice with 2 mM AMP-PCP and either 10 mM MgF_x or 10 mM BeF_x, at a final protein concentration of 1.7 mg/ml. CryoEM grids were prepared by applying 3 µl of sample to glow-discharged (15 mA, 75 s) UltraFoil R1.2/1.3 300-mesh gold grids, which were blotted for 7.5 s (5 °C, 100% humidity, blotting force -10) and plunge-frozen in liquid ethane using Vitribot Mark IV (Thermo Fisher Scientific).

2.2.6.3 CryoEM data acquisition

Data were collected with a Talos Glacios TEM 200 kV (Thermo Fisher Scientific) equipped with a Falcon III direct electron detector at the Oxford Particle Imagine Centre (OPIC). Micrographs were recorded automatically in linear mode at 92,000X magnification with a nominal pixel size of 1.55 Å. The defocus range was set from -0.8 to -2.6 µm, and each micrograph was dose-fractionated to 20 frames with a total dose of ~50.02 $e^-/Å^2$.

2.2.6.4 CryoEM data processing

Movies (1404 for the MgF_x sample and 1638 for the BeF_x sample) were imported into cryoSPARC (Punjani et al., 2017) and patch motion corrected (maximum alignment resolution of 5 Å and B-factor 500) followed by patch CTF corrected (4 Å minimum resolution and 25 Å maximum resolution) to give the processed micrographs. The MgF_x micrographs were curated to 1247 micrographs

on the basis of CTF alignment resolution. CryoSPARC blob picker was used to generate templates for picking. The minimum diameter was set to 120 Å and maximum diameter was set to 200 Å using a circular blob. Initial template picking was used to extract particles that were curated using the local power threshold to find the balance between genuine particles and background noise. For MgF_x, two rounds of successive 2D classification followed, selecting 100 classes in the first round and 50 in the second. 25 of the final 50 were selected for 3D-classification. For BeF_x, three rounds of successive 2D classification were run, selecting 100 classes in the first round and 50 in the second and third round. 25 of the final 50 classes were selected for 3D-classification.

The MgF_x and BeF_x inhibited particles were 3D-processed by the same protocol with a basic pipeline as the purpose was for screening the samples. *Ab initio* 3D reconstruction using the stochastic gradient descent method yielded two 3D classes (Punjani et al., 2017), all parameters were kept as default, with a maximum possible resolution of 12 Å. Heterogeneous refinement on all particles was run based on the initial *ab initio* models. The Pma1 model was further refined by non-uniform refinement for C1 and C6-selected symmetry (Punjani et al., 2020). All other parameters were left as default. Densities were analysed using ChimeraX (Pettersen et al., 2021).

2.3 Methods specific to SERCA

2.3.1 All-atom MD simulation setup

Simulations were built using the coordinates from PDB 3N8G (WT) and 6RB2 (E340A). The protein atoms were described using the CHARMM 36 force field (Best et al., 2012), and were built into a lipid bilayer composed of POPC molecules solvated with TIP3P water and Na^+ and Cl^- to 150 mM in a 120 x 120 x120 Å box. Systems were built using CHARMM-GUI (Jo et al., 2007; J. Lee et al., 2016). Generation of the *in silico* mutant E340A$_{is}$ was done with CHARMM-GUI.

The systems were energy minimized using the steepest descent method, then equilibrated with positional restraints on heavy atoms for 100 ps in the NPT ensemble at 310 K with the V-rescale thermostat and semi-isotropic Parrinello-Rahman pressure coupling (Bussi et al., 2007; Parrinello & Rahman, 1981). Production simulations were run in triplicate without positional restraints, with 2 fs time steps for a minimum of 200 ns.

All simulations were run using Gromacs 2019 (Berendsen et al., 1995). Simulations were analysed using Gromacs tools and images were made using VMD (Humphrey et al., 1996). Graphs were plotted using Matplotlib (Hunter, 2007).

Results Part I

Chapter 3: Coarse-grained simulations of Pma1 in a native-like membrane

Data up to section 3.7 are from Heit, S., Geurts, M.M.G., *et al* “Structure of the hexameric fungal plasma membrane proton pump in its autoinhibited state” Science Advances (2021), vol 7, no. 46. Any work conducted by collaborators is clearly stated in the text and figure legends.

3.1 Chapter 3 Introduction

The first section of this work sets out to explore the structure and function link between hexameric *Neurospora crassa* Pma1 and the lipid environment. Specifically, the aim is to understand how Pma1’s activity is linked to the known anionic lipids and long-chain ceramides it requires for correct membrane trafficking and function (Addison & Scarborough, 1981; Gaigg et al., 2005, 2006). As described in detail in Chapter 1, lysolecithin-solubilised Pma1 requires the addition of the Folch fraction I lipids to obtain maximal *in vitro* activity in the Baginski assay. This crude bovine brain lipid extract contains phosphatidylinositols, phosphatidylserines and cerebrosides, suggesting that Pma1 requires anionic lipids for function. Moreover, successful surface transport and raft association of Pma1 is dependent on the synthesis of sphingolipids with C26 long-chain fatty acids. However, the recent first high-resolution cryo-EM structure of *N. crassa* Pma1 resolved by Dr. Sabine Heit, as part of ongoing research with the author, did not resolve any bound lipids and thus did not address Pma1’s lipid requirements.

To probe the interaction between Pma1 and a complex lipid environment, CG MD simulations of the novel Pma1 model were run in a native-like *N. crassa* membrane.

3.2 Setting up simulations of Pma1

To run simulations of Pma1 in a lipid environment, a native-like membrane composition was constructed. The composition was based on work conducted in the 1980s investigating the structure of the N. crassa membrane and on preliminary data from a Master's student in the lab running lipidomics analysis of N. crassa

Table 3.1. Membrane composition of the coarse-grain Pma1MD simulations

Lipid name	Head group	Tails	Net charge	Inner leaflet content (%)	Outer leaflet content (%)
PIPC	Phosphatidylcholine	C16:0/18:2	0	11	28
DIPC	Phosphatidylcholine	di-C16:2-C18:2	0	5	14
PIPE	Phosphatidylethanolamine	C16:0/18:2	0	8	13
DIPE	Phosphatidylethanolamine	di-C16:2-C18:2	0	4	7
PIPA	Phosphatidic acid	C16:0/18:2	-2	11	11
DIPA	Phosphatidic acid	di-C16:2-C18:2	-2	5	5
PIPS	Phosphatidylserine	C16:0/18:2	-1	17	0
DIPS	Phosphatidylserine	di-C16:2-C18:2	-1	9	0
PIPI	Phosphatidylinositol	C16:0/18:2	-1	8	0
XNSM	Sphingomyelin (no head group)	C(d24:1/24:1)	0	2	2
PVSM	Sphingomyelin (no head group)	C(d18:1/18:1)	0	4	4
DPCE	Ceramide (no head group)	C(d18:1/18:0)	0	3	3
PNCE	Ceramide (no head group)	C(d18:1/24:1)	0	8	8
ERGO	Ergosterol	-	0	5	5

samples. The membrane was created with the available coarse-grained lipid models from Martini (Table 3.1 and Figure 3.1) (Aaronson & Martin, 1983; Friedman & Glick, 1980; SJ et al., 2007).

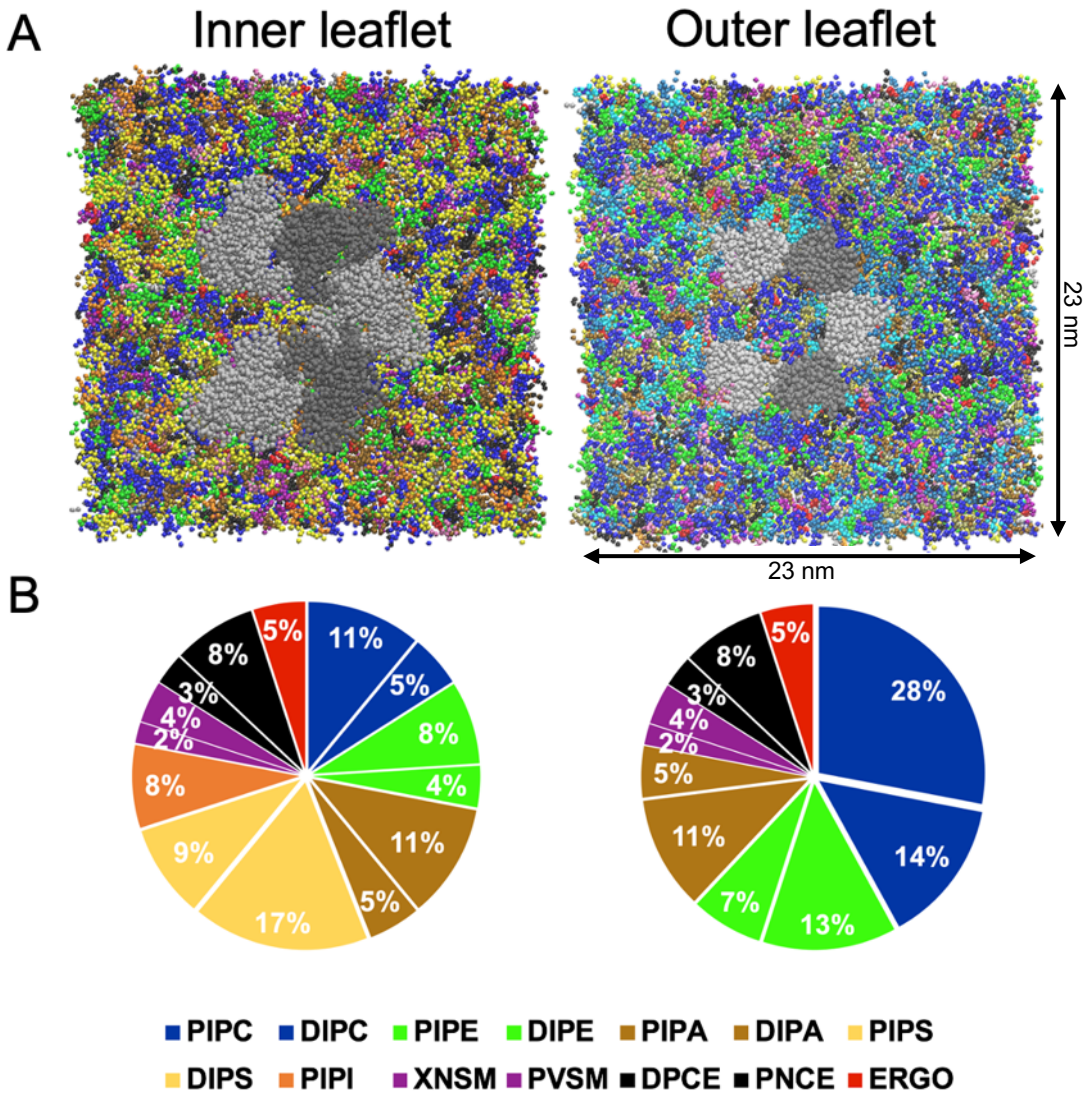

Figure 3.1: Membrane lipid composition of the pentamer simulations in a native-like Neurospora crassa membrane. *The lipid colour key at the bottom refers both to (A) and (B). A) Top view of the inner-leaflet (left) and outer-leaflet (right). B) Pie chart showing the lipid composition. For lipids of the same head group, the single-unsaturated variant is the more concentrated species.*

The membrane consists of a range of neutral lipids including PC and PE, anionic lipids PS, PI and PA, as well as the fungal sterol, ergosterol, and long-chain sphingolipids sphingomyelin and ceramides. To closely match the fatty acid composition of the fungal plasma membrane, a combination of double-unsaturated (DI-) and single-tail unsaturated (PI-) phospholipids were used. Note that for PI, DIPI was not available in Martini at the time. For sphingomyelins and ceramides, the available models did not contain any head groups.

Using the Insane membrane builder script, a membrane was built around the coarse-grained Pma1 structure (Wassenaar et al., 2015). To prevent any positional bias of lipids placed inside the ring, one monomer was omitted from the hexamer to allow a free lipid exchange during the simulations (Figure 3.1 A). By omitting a monomer, the core could also equilibrate, allowing the formation of specific protein-lipid interactions that might occur during hexamer formation in the ER.

To ensure that the pentamer system would be the best system to run, simulations of the hexamer were tested as well. 5x10μs simulations set up as per the pentamer were analysed. Figure 3.2 illustrates that the hexameric system is unstable. The calculated density of PO_4 beads in simulation show the inner leaflet of the lipid core bulges outwards and contains a hole. This is likely a result of the lipid core not equilibrating its composition or lateral pressures on the membrane. Hence, all Pma1 simulations were carried out with the pentamer, where no such artifacts occurred due to the free exchange of lipids between the protein core and the bulk membrane environment.

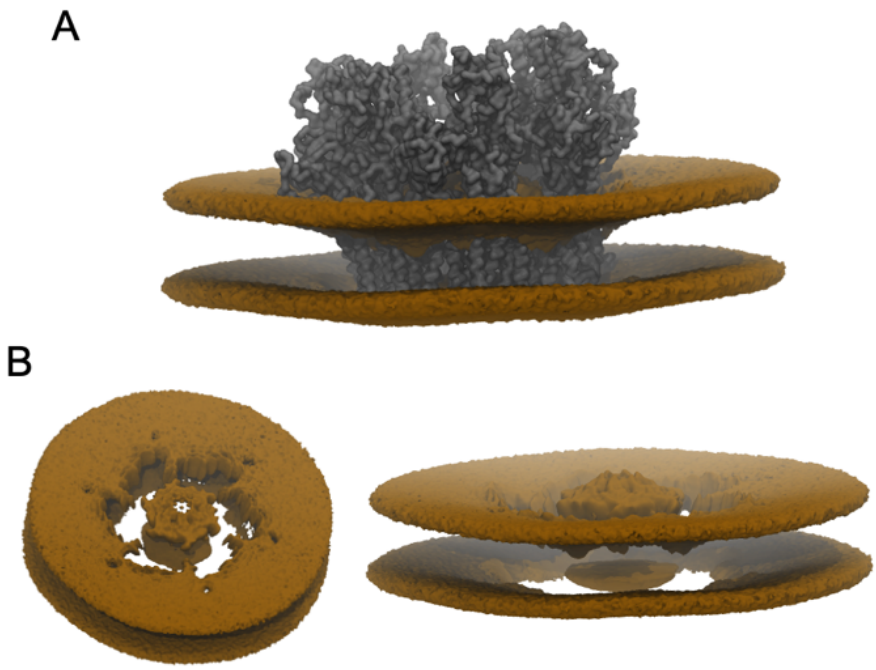

Figure 3.2: Membrane analysis of hexameric Pma1 simulations. *A) Averaged volume density of PO4 beads calculated using VMD Volmap tool. B) Tilted top view (left) and side view (right) of the average PO_4 density showing the strained inner leaflet of the plug forms a hole in the membrane.*

3.3 Pma1 preferentially interacts with double-unsaturated phospholipids

Radial distribution function (RDF) analysis initially performed on the original pentamer simulations to investigate Pma1s lipid annulus show that Pma1 preferentially interacts with the double-unsaturated 16:2/18:2 (DI-) tail of each lipid type. (Figure 3.3A). The analysis further demonstrates that anionic lipids PIPI and DIPS are most populous in the annulus, whilst the long chain sphingolipids XNSM, PVSM, DPCE and PNCE interact least with the protein.

To validate the hypothesis that Pma1 preferentially interacts with double-unsaturated lipids, and that the observation is not being driven by another factor, 3 x 3μs simulations of Pma1 in a 50% PIPC:50% DIPC membrane were analysed.

RDF analysis of this system (Figure 3.3B) confirms that Pma1 interacts with roughly twice as many DIPC molecules as compared with PIPC.

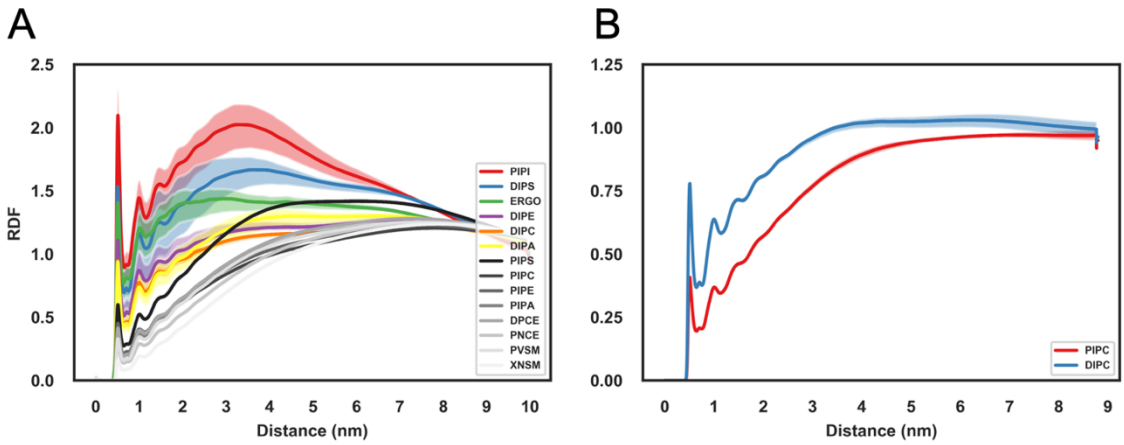

Figure 3.3: Radial distribution functions of the Pentamer in a complex membrane (A) and simplified PC membrane (B).

3.4 Local lipid accumulation at the Pma1 monomer interface suggest a role for anionic lipids

As mentioned previously, proper Pma1 hexamer formation, trafficking and function *in vivo* depends on an intact lipid biosynthesis pathway (Gaigg et al., 2005, 2006; M. C. S. Lee et al., 2002). Moreover, Dr. Heit found that the hexamer is sensitive to treatment with detergents such as octyl glucose neopentyl glycol (OGNG) *in vitro.* For lipids to influence the hexameric integrity, they are likely to interact specifically with the Pma1 monomer interface. Lipid densities across the bilayer plane were calculated using Gromacs densmap (Figure 3.4) to investigate particular lipid localisations. It is important to note that the analysis does not distinguish between the leaflets and is an average across the two. Figure 3.4 shows DIPS binds at the monomer interface, with a significantly increased density compared to the rest of the membrane. Moreover, other anionic lipids including PIPA and DIPA form distinct interactions at the same position on each monomer,

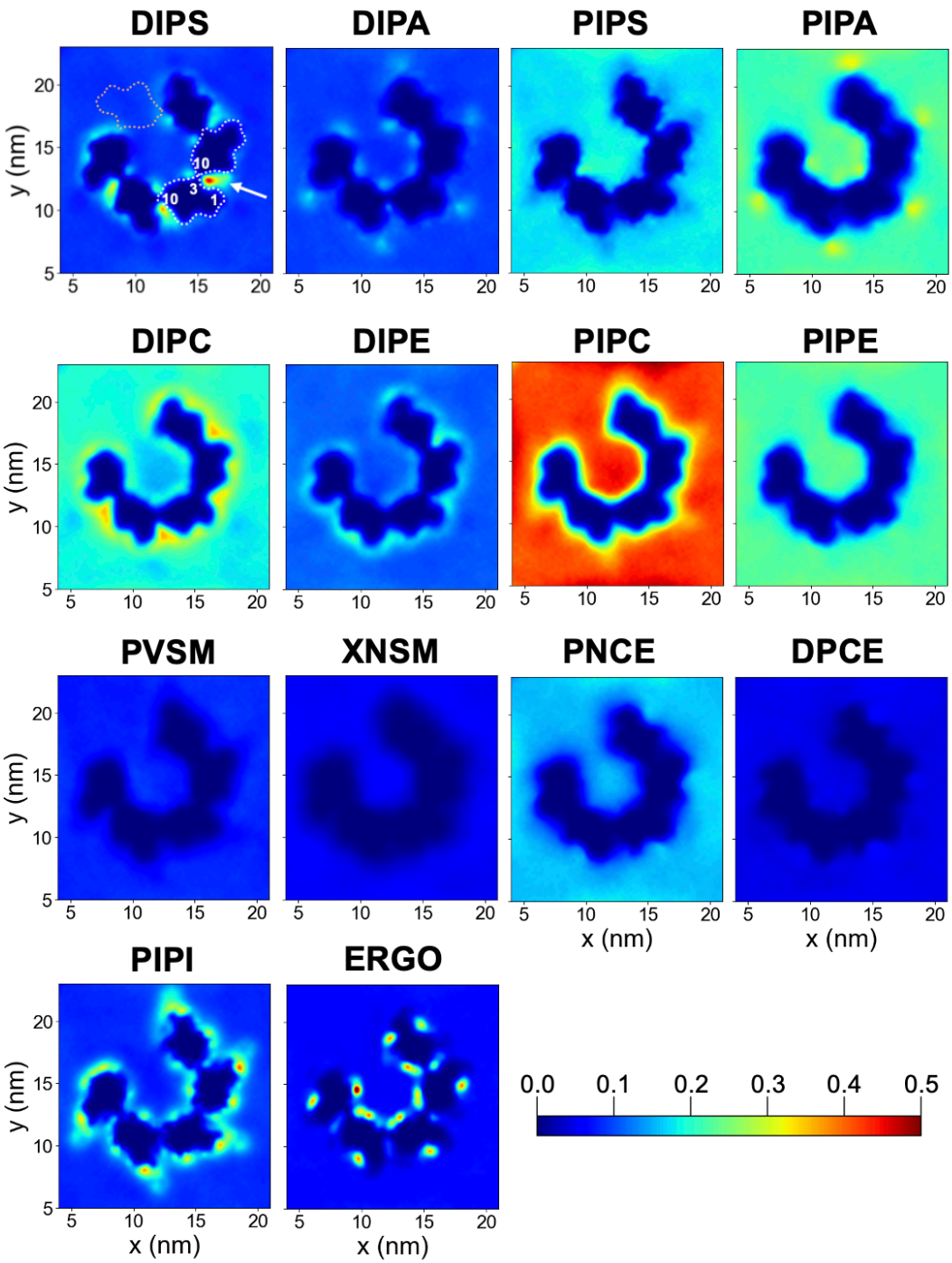

Figure 3.4: Lipid density maps averaged across the leaflets for all lipids in the membrane. *Values correspond to the average number of molecules per* nm^3 *and do not account for the respective membrane composition fraction. Dotted white lines and numbers shown in DIPS indicate monomer outlines and transmembrane helix positions, respectively. The orange dotted line denotes the omitted sixth monomer. The white arrow in DIPS points at the pool clustering outside the monomer interface. For details of the lipids, refer to Table 3.1. Modified from* Heit et al., 2021.

on both the inner and outer ring. The analysis further suggests that PIPI more generally interacts with Pma1 as an annular lipid. Similarly, DIPC and DIPE generally interact with Pma1 in its annulus and on the inside of the ring. DIPC also accumulates at the monomer interface similar to DIPS. Ergosterol accumulates in a symmetric fashion on the outer side of the protein as well as at several sites on the inside ring. The long chain sphingolipids do not, however, interact with Pma1 nor accumulate in the core.

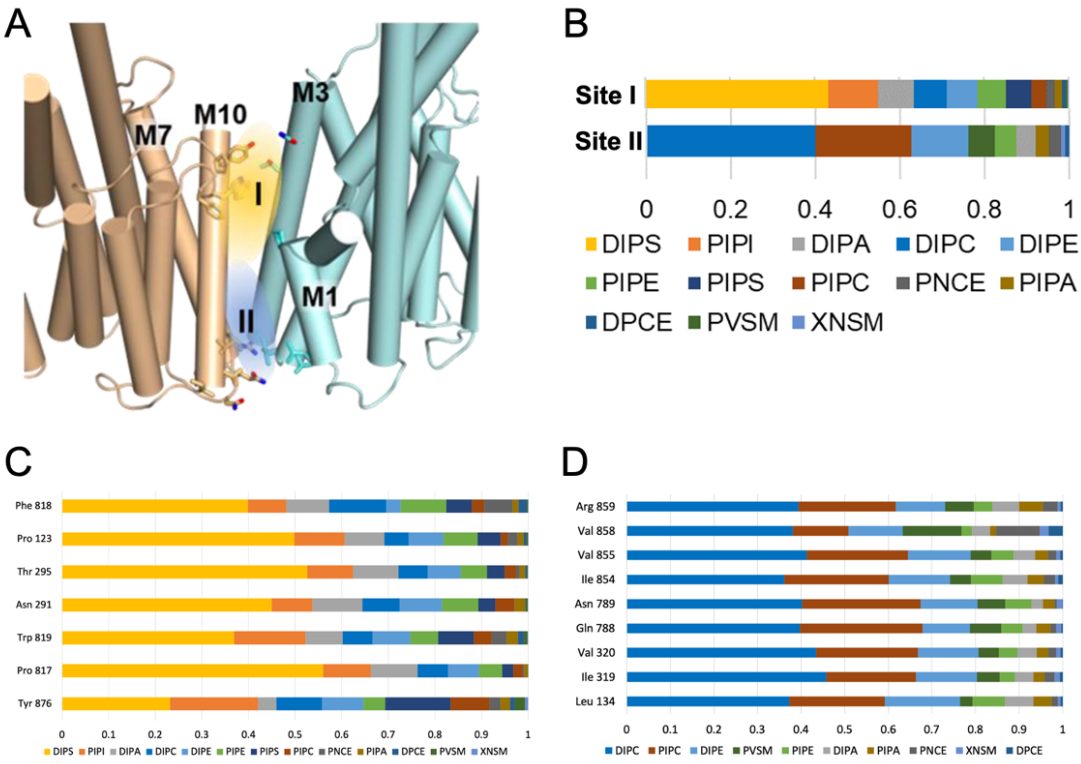

Figure 3.5: Fractional interaction times of all lipids with Pma1 residues surrounding interface Site I and Site II. *Interaction was defined as the fraction of total frames in which a lipid is within 0.6 nm of a given residue. A) Putative lipid binding sites at the monomer interface, suggested by MD simulations. Site I is located in the inner leaflet and Site II in the outer leaflet. B) Fractional interaction times of lipids in Site I and II averaged across all residues from (C) and (D). C) Fractional interaction times for Site I for each of the residues, averaged across five repeats. C) Fractional interaction times for Site II for each of the residues involved, averaged across five repeats. Modified from* Heit et al., 2021.

Fractional interaction times between each lipid's head group and all protein residues were calculated. An interaction was defined as the fraction of total frames in which a lipid is within 0.6 nm of a given residue. The fractional interactions at the interface suggest two binding sites (Figure 3.5A), Site I in the inner leaflet (involving M1, M3 and M10' of the other monomer) and Site II in the outer leaflet (involving M4 and M10' of the other monomer). Within these sites, key residues were selected based on their ability to interact with a lipid at that site, and the fractional occupancy of each lipid was averaged across the five repeats (Figure 3.5C and D).

The residue-specific data were then averaged together to generate interaction plots for the two sites (Figure 3.5B). DIPS is the predominant lipid that binds at Site I in over 40% of the frames. Aside from DIPS, the other anionic lipids PIPI and DIPA bind and together with DIPS are bound in over 60% of the frames. Site II, on the other hand, is predominantly occupied by DIPC and other neutral lipids in over 80% of the frames. Not only do individual lipid molecules bind to their respective site, the densities in Figure 3.4 indicate that DIPS and DIPC also accumulate in a pool outside the site. This accumulation could be driven by localized clustering of lipids with unsaturated tails, which could explain the presence of both DIPS and DIPC. However, this would mean that other DI- lipids like DIPE and DIPA should equally accumulate there. Alternatively, accumulation could be driven by the clustering of the acidic PS head group, a feature previously observed for phosphatidylserines (Matsunaga et al., 2015). DIPS binding to Site I aligns with the fact that the ATPase activity *in vitro* is dependent on the addition of acidic phospholipids and is a key lipid component of Folch Fraction I used in the Baginski assays (Addison & Scarborough, 1981). Moreover, a recent study also found a threefold enrichment of PS in styrene-maleic acid-solubilized *S. cerevisiae* Pma1

compared to the average plasma membrane composition (van ’t Klooster et al., 2020).

3.5 Pma1 induces a considerable membrane deformation to create a cation funnel

The simulations further demonstrate that Pma1 not only forms lipid specific contacts, but also has a considerable impact on the local membrane structure. MD has previously illustrated for other proteins that they are capable of deforming the membrane and this is often evolutionarily linked to their function (see Coupland et al., 2021; Liaci et al., 2021; Zhou et al., 2019).

To analyse the membrane morphology, the average z-height position of phosphates at each x-, y-coordinate in each frame was calculated across the concatenated 50 μs of simulation, the results of which are shown in Figure 3.6 and 3.7. The z-height values of the phosphates were graphed in Figure 3.6 for the inner and outer leaflet. Values were standardised relative to the z-height of the phosphate at coordinate -70, 110, as this most likely represents a region that is least perturbed by the protein or boundary effects. In the inner leaflet, disregarding the boundaries, the height of the phosphates varied by as much as ~20 Å. A sort of wall, or dip, exists around the monomer interface, where there is a sudden height change from 14 Å above the reference at the monomer to 2 Å above the reference in the core (Figure 3.6B). In the outer leaflet, the phosphates vary by up to 35 Å in an area that is just a few nm apart (Figure 3.6D).

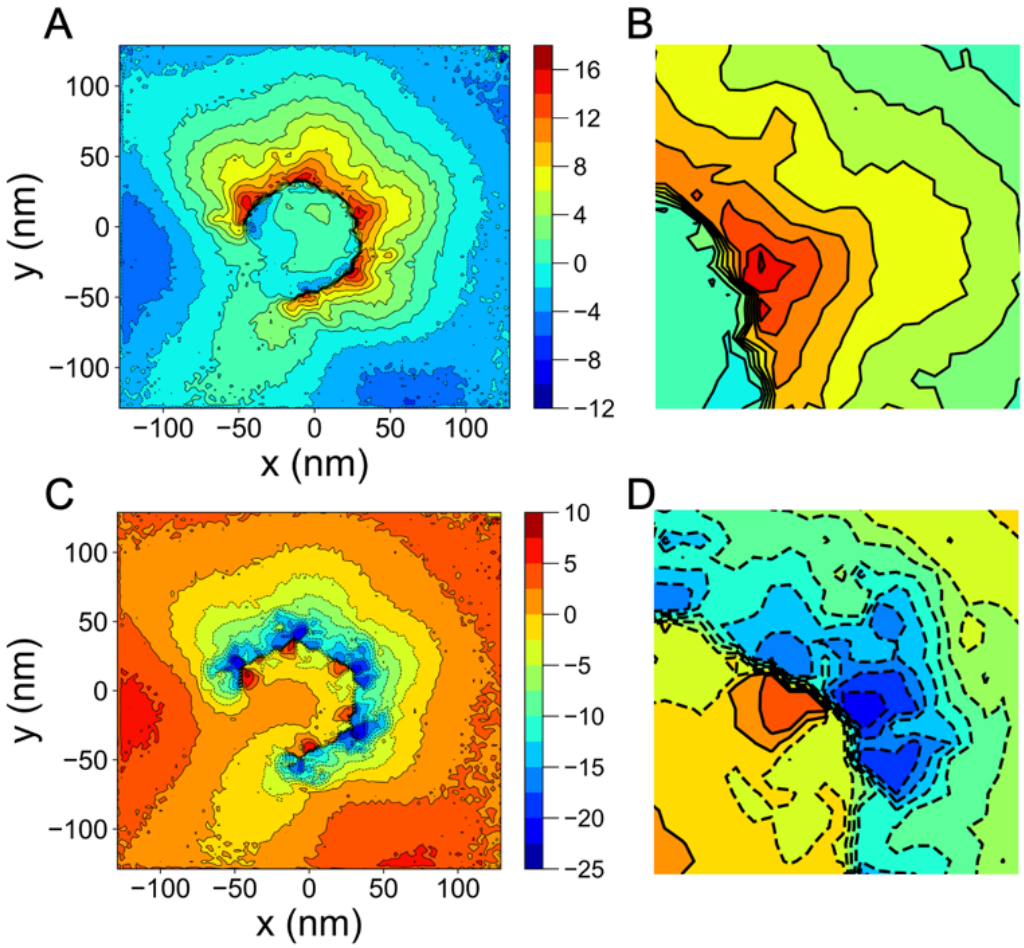

Figure 3.6: Quantitative analysis of leaflet deformation. *Values represent the z-height in Å relative to the value at coordinate -50, 110. A) Averaged z-height position of lipid head group-phosphates in the outer leaflet. B) Zoom of (A) on the region of the central Pma1 monomer. C) Averaged z-height position in the inner leaflet. D) Zoom of (C) on the region of the central Pma1 monomer.*

To put this into further context, the average membrane thickness across the simulation was calculated by subtracting the inner leaflet from the outer leaflet (Figure 3.7A). The membrane thickness ranges from 18 to 63 Å. Figure 3.7B shows a zoom on the central monomer, which most closely represents a hexameric monomer as the other monomers in the pentamer experience the edge effects of an incomplete hexamer. The zoom shows that the membrane thickness in fact ranges from ~24 Å to ~56 Å and that the recorded extremes could be an artifact

from the end monomers. Furthermore, the pentamer core as well as the belt around the pentamer is on average ~4 Å thicker than the average membrane thickness further away from the protein. This is in line with the fact that Pma1 associates with the MCP, and lipid microdomains tend to be thicker (Simons & Ikonen, 1997). Figure 3.7C illustrates this deformation qualitatively by zooming in on the central monomer of the atomistic Pma1 model aligned with the average phosphate position in 3D. The inner membrane leaflet is thinned locally around the M1-M4 helical bundle, at the interface between monomers and crucially, near the proton-accepting Asp730. This “chute”-like arrangement of the negatively charged lipids in Site I could facilitate the attraction of protons from the cytosol. Opposite the dip, on the inside of the ring, the inner membrane bulges up toward the P1-helix in the P-domain. This attraction is possibly mediated by the positive charge at the N-terminal end of M3 and by Lys749 in the L6-7 loop. Dr. Heit processed the cryo-EM density of the Pma1 structure to analyse the micelle surrounding the hexamer and there, too, the dip and bulge are evident (Figure 3.7D).

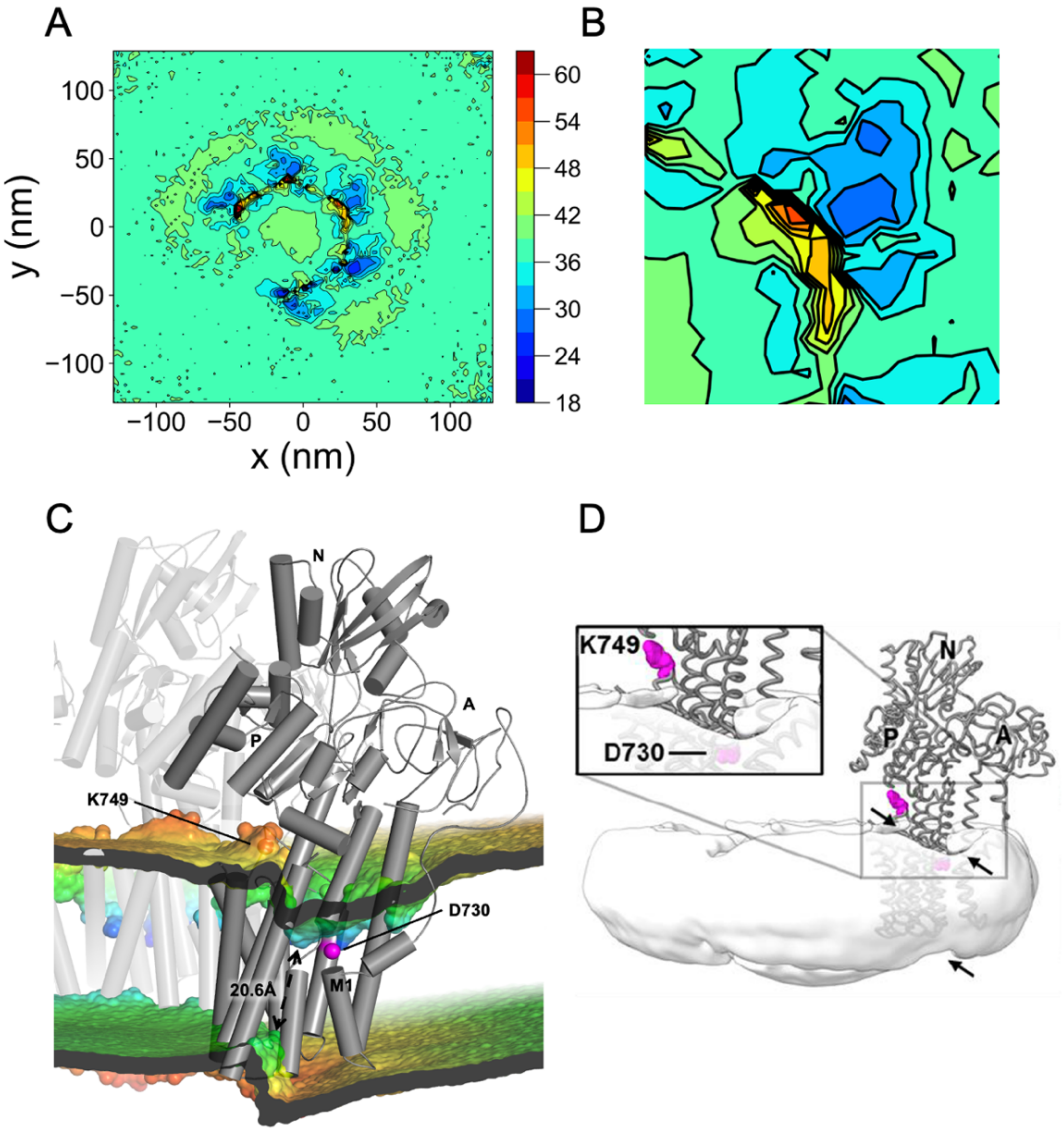

Figure 3.7: 3D analysis of the bilayer deformation. *A) Average bilayer thickness between phosphates calculated by subtracting the inner leaflet from the outer leaflet (shown in Figure 3.6). Scale is in Å. B) Zoom of (A) on the region of the central monomer. C) Side view of the bilayer deformation at the monomer interface, aligned to the atomistic Pma1 structure. The Cα positions of residue D730 and K749 are shown in magenta. The arrow marks the shortest measured distance. D) Cryo-EM map of hexameric Pma1, filtered to 12 Å, showing only the micelle after masking the protein map in Coot. The Cα trace of one monomer is shown for reference, with side chains of D730 and K749 highlighted in magenta. The micelle is locally distorted near the monomer interface (arrows). Figure (D) was prepared by Dr. Heit.*

3.6 The Chute-like membrane deformation attracts cations

As described in section 3.5, Pma1 engages with its annular lipids to create a "chute"-like membrane deformation around the proton entry site that is proposed to funnel protons down towards Asp730. In line with this, the accumulation of a pool of anionic lipids around Site I might aid in attracting these protons. To assess whether the simulations provide any evidence for this hypothesis, the cation distributions were analysed. Whilst there are no protons in a coarse-grain molecular dynamics simulation, the Na^+ ions can act as a proxy for the behaviour for other cations including H^+. The Na^+ accumulation in the concatenated 50 μs of simulation was calculated through the density function of VMD Volmap tool and shows an increased local density of cations near Site I and the position of the "chute" (Figure 3.8). The shape suggests that the Na^+ ions accumulate in a funnel-like shape, with a single Na^+ binding to the proposed DIPS in Site I.

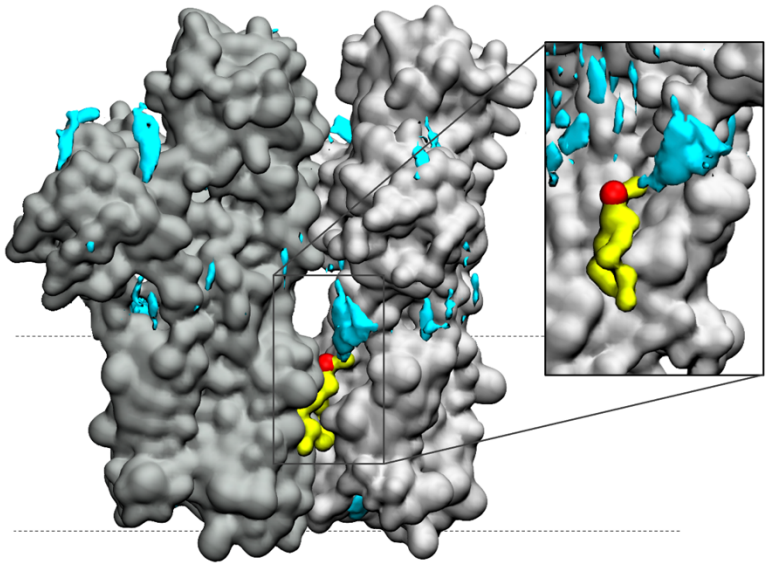

Figure 3.8: Locally increased density of Na^+ ions (cyan) around the monomer interface, as calculated by the Volmap tool of VMD. A representative DIPS molecule in Site I is shown in yellow, with the phosphate group highlighted in red. *Modified from* Heit et al., 2021.

3.7 Simulations of Pma1 with a phosphatidylinositol ceramide

Whilst the simulation results above provided an explanation for Pma1s anionic lipid dependency and uncovered significant changes to membrane morphology that could aid proton transport, it did not explain why Pma1 requires C26 long-chain sphingolipids for hexamer formation and correct trafficking to the plasma membrane. Previous studies note that specifically phosphatidylinositol ceramide is required for correct Pma1 trafficking (Bagnat et al., 2001; Eisenkolb et al., 2002; Gaigg et al., 2005; Gong & Chang, 2001; M. C. S. Lee et al., 2002). By inhibiting a series of enzymes in the phosphatidylinositol ceramide synthesis pathway, Gaigg *et al.* discovered that it was the inhibition of all steps up to and including the conversion of ceramide to phosphatidylinositol ceramide prevented proper Pma1 biogenesis. Moreover, initial lipidomics data of a Masters student in the group showed a 10-fold enrichment of a 42:0 (corresponding to C26/C16 tails) phosphatidylinositol ceramide in solubilised Pma1 compared to the plasma membrane. Hence, the role of phosphatidylinositol ceramide was probed by CG MD.

As the Martini database of available coarse-grained and verified lipids only contains ceramides without head groups, a phosphatidylinositol ceramide model (PICE) was generated by adding the atoms of the phosphatidyl head group of PIPI to the existing topology of the PNCE ceramide. Figure 3.9 shows a pictorial representation of this method using the bead models available from Martini. Beads 1-4 from the PIPI topology file were added to the topology file of PNCE and the beads were renumbered. The C3 beads 3 and 9 in PNCE were converted to C1 to fully saturate the fatty acid tails. The bond angle was changed from 120° to 180° and the force constant was changed from 45 to 25 to reflect the single bond. Other

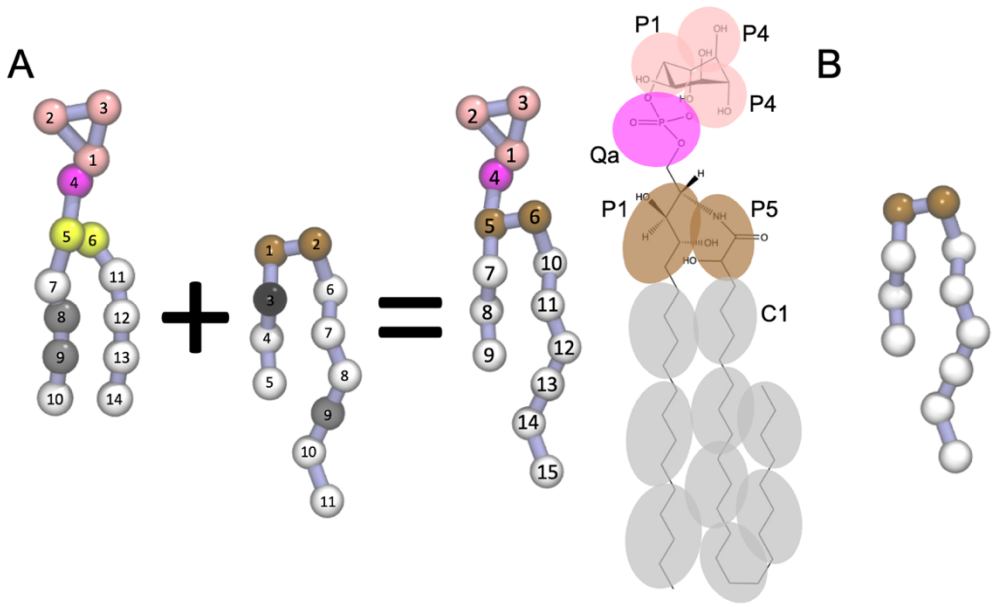

Figure 3.9: Pictorial representation of the production of a coarse-grained phosphatidylinositol ceramide. *A) Synthesis of 42:0 phosphatidylinositol ceramide (PICE) by adding the itp-file beads 1-4 of PIPI (left) to beads 1-11 of PNCE (middle) and converting PNCE beads 3 and 9 to unsaturated beads, with atomistic mapping and bead types shown on the right. B) Illustration of the control ceramide made by converting PNCE (A-middle) to fully unsaturated 42:0 PPCE.*

bond lengths and force constants were kept the same and only the connection between the head group and PNCE had to be established. Based on the atomic structure of PICE, the PI head group had to be attached to the P1 (C_3-OH equivalent) bead of PNCE and not the P5 (H_2N-C_2=O equivalent) bead. The bond length and angle of the connection of the PI head group to the lipid tails in PIPI were kept for the connection between the PI head group and ceramide tails. A control ceramide (PPCE) was created by converting PNCE to a fully saturated ceramide with only C1 tail beads (Figure 3.9B). The definition of PICE and PPCE molecules were added to the Insane script to build the membrane. A test system of 45% PIPC:45% DIPC:10% PICE was built, equilibrated and assessed in VMD. The system did not have any lipids flip between leaflets, head groups entering into the bilayer or tails exiting, so it was concluded that the generated PICE molecule was

behaving well in a dynamic system. Follow up analysis might benefit from directly comparing these parameters with atomistic simulation.

5 x 10 μs simulations of pentameric Pma1 were run in the same membrane composition as described in section 3.2, with 8% PNCE replaced by 4% PICE and 4% PPCE. According to the density analysis, PPCE does not make any specific interactions with Pma1, although a very small enrichment of the ceramide can be seen in the core (Figure 3.10A). PICE, on the other hand, significantly accumulates in the protein core in a manner not recorded for the densities in any of the lipids in section 3.4. This accumulation could be driven by intermolecular interactions between the PI head group. The unsaturated tails could further allow it to accumulate at a greater density in the spatially restrained lipid core. PICE also accumulates on the outside ring at the same position for each monomer, but not at the interface between monomers where it may have been expected. Instead, the 3D density analysis shown in Figure 3.10C highlights the density is a clump of PICE molecules in the inner leaflet that are attracted to the A-domain of Pma1. Multiple PICE molecules can simultaneously contact the A-domain in a single frame (Figure 3.10B). Additionally, a single, inner-leaflet PICE binding to the inner ring is observed.

The accumulating PICE in the centre of the pentamer in fact stems purely from the outer leaflet, as seen in Figure 3.10C. This is relevant since it coincides with a recent publication highlighting the presence of a liquid-crystalline membrane domain in the core of the first high resolution structure of the *S. cerevisiae* Pma1 (P. Zhao et al., 2021). They report the core consists of 57 ordered unsaturated lipid densities and suggest these are a combination of phospholipids, ceramides and ergosterol. Better resolved map density corresponding to phospholipids binding to

the monomers was also found between the protein and the crystalline core and they predict this to be PC. Interestingly the simulation also shows a local accumulation of DIPC wedging between Pma1 and the lipid core (Figure 3.10D). A crystalline packing of lipids in the outer leaflet was not reported in the simulation.

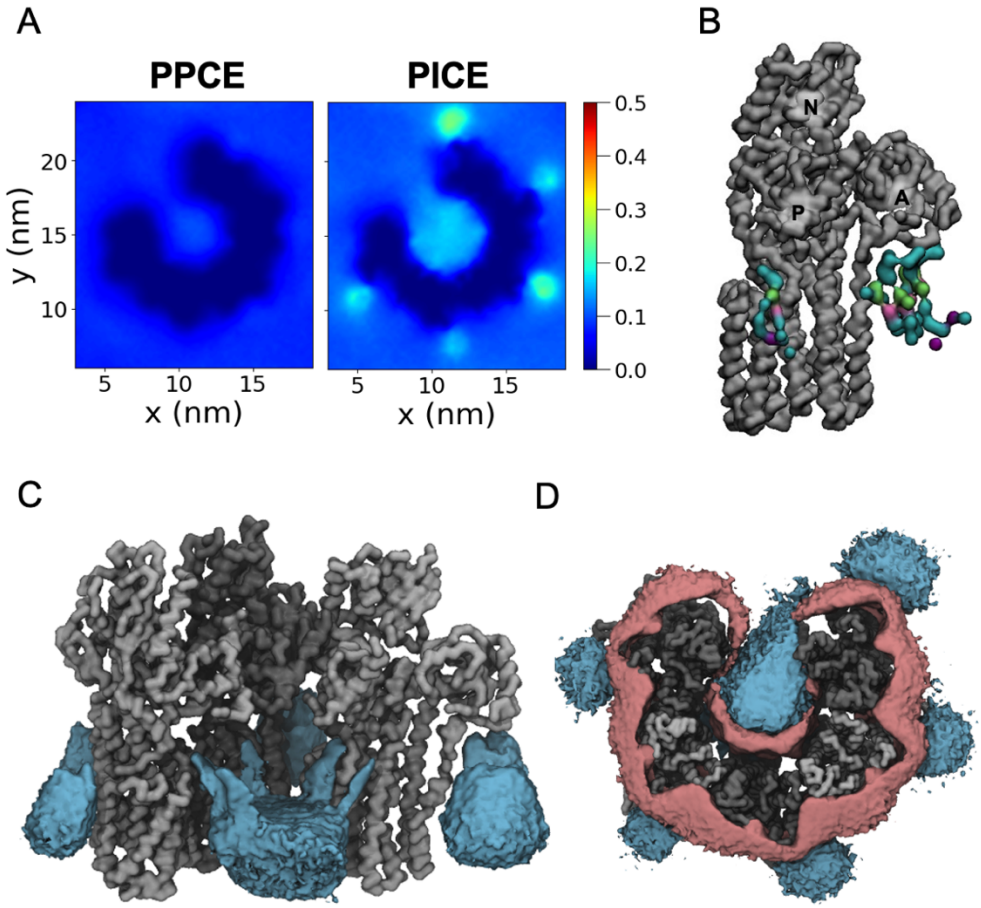

Figure 3.10: Density analysis of PICE vs PPCE in a complex membrane. *A) Lipid densities averaged across the two leaflets for PPCE (left) and PICE (right) as calculated by Gromacs densmap tool. Values correspond to the average number of molecules per cubic nanometer. B) A single simulation frame showing PICE molecules within 5 Å of a highlighted Pma1 monomer clustering onto the A-domain. C) Locally increased density of PICE molecules (blue) in the outer leaflet plug and on repeating distinct sites in the inner leaflet. Measured as the average density across the concatenated five repeats using VMD Volmap. D) Bottom view of Pma1 highlighting the locally increased density of DPCE (pink) surrounding the locally increased density of PICE (blue).*

3.8 A conserved set of Arginine residues in the Pma1 A-domain are important for supporting the membrane deformation

Simulations with PICE highlighted an interesting lipid interaction site on the soluble A-domain. The positively charged residues Arg96-98 and Lys99 in the *N. crassa* Pma1 A-domain bind the negatively charged PICE cluster (Figure 3.11A). Alignment of *N. crassa* Pma1 to 78 other fungal plasma membrane proton pumps reveals this region is highly conserved (Figure 3.11B) (full alignment shown in Appendix 10.2). Arg96 is perfectly conserved whilst the other three residues are predominantly either arginine or lysine. The functional relevance of the conserved region was investigated by mutating residues 96-99 to alanine and running 5 x 10 μs CG simulations.

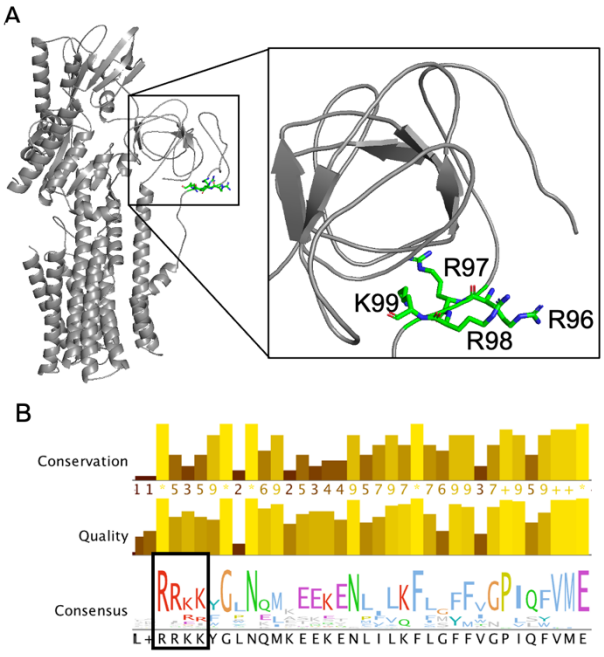

Figure 3.11: Conserved Arginine-rich region in Pma1. *A) Structural illustration of the RRRK region in N. crassa Pma1 (PDB 7NXF). Inset shows a zoom of the region. B) Multiple sequence alignment between N. crassa Pma1 and 78 other fungal plasma membrane proton pumps focussed on this segment. Box highlights the conserved RRRK region. Full alignment shown in the supplementary.*

The RRRK –> AAAA mutations eliminated the interaction with PICE, as seen from the density plot in Figure 3.12A. Close analysis of the other densities highlighted that in the original simulations, the anionic lipids PIPI and PIPA also interacted with the A-domain and in the mutant simulation, this contact was also lost

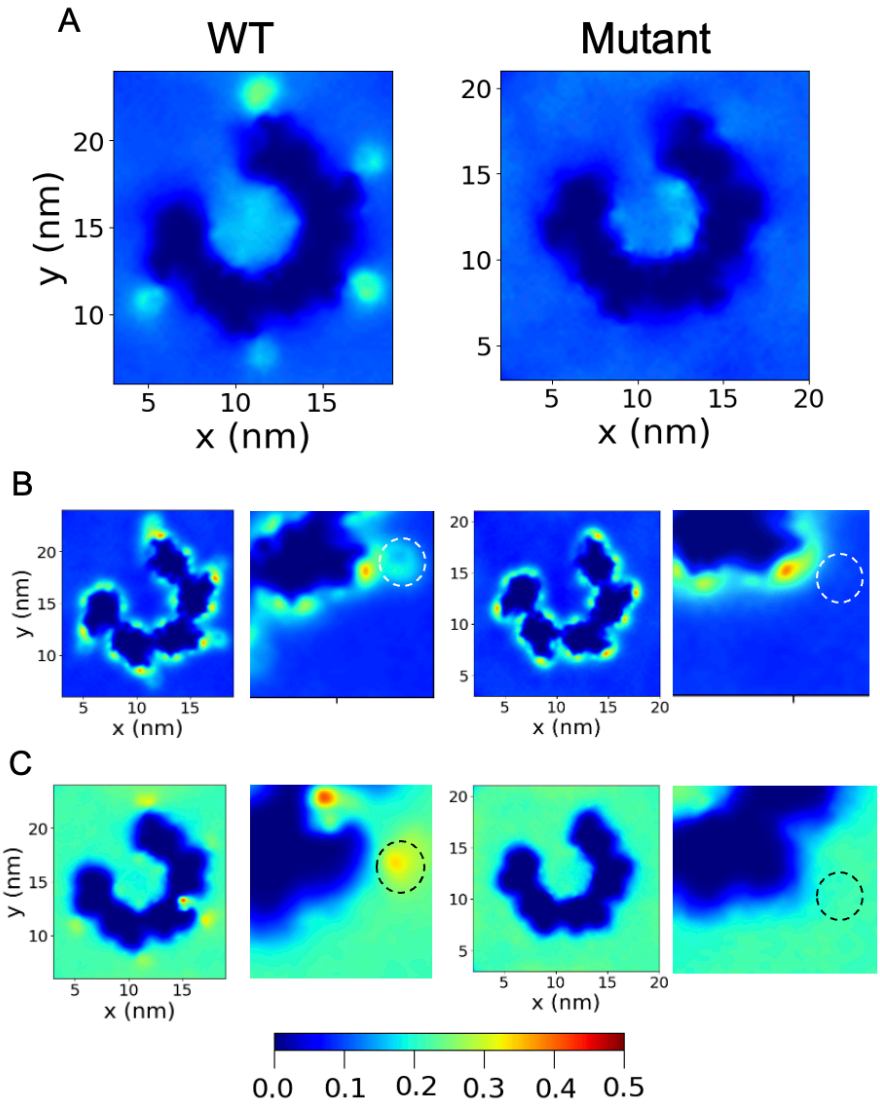

Figure 3.12: Lipid density maps of anionic lipids comparing the WT to the RRRK->AAAA mutant. *Values correspond to the average number of molecules per cubic nanometer and do not account for the respective membrane composition fraction. A) PICE density for the WT (left) and RRRK -> AAAA mutant (right). B) Lipid densities for PIPI in the WT (left) and mutant (right) with a zoom showing the loss of contact. C) Lipid densities for PIPA in the WT (left) and mutant (right) with a zoom showing the loss of contact.*

(Figure 3.12B and C). The conserved nature of the residues and their interaction with anionic lipids suggests they might play a role in the protein's activity.

The impact of the mutations on the membrane morphology was considered by calculating the average PO_4 position. Figure 3.13A-C show the calculated bilayer thickness for the WT (A), WT with PICE (B) and the mutant (C) simulation. The bilayer deformation between the WT and WT PICE simulation is roughly the same, displayed by the same thickness range and overall deformation pattern. The mutations however cause a loss of the thicker membrane around the pentamer. The extent of deformation around the central monomer is also less drastic, ranging from 28Å to 52Å (compared to 24Å to 56Å in the WT). More so, the qualitative analysis in Figure 3.13D illustrates how the WT membrane is angled in a V-shape and climbs up towards the A-domain whereas the mutant bilayer is flat. The WT bilayer also has a greater distortion around the M1 helix and creates a greater "chute"-like shape than in the mutant, suggesting the conserved region is functionally relevant.

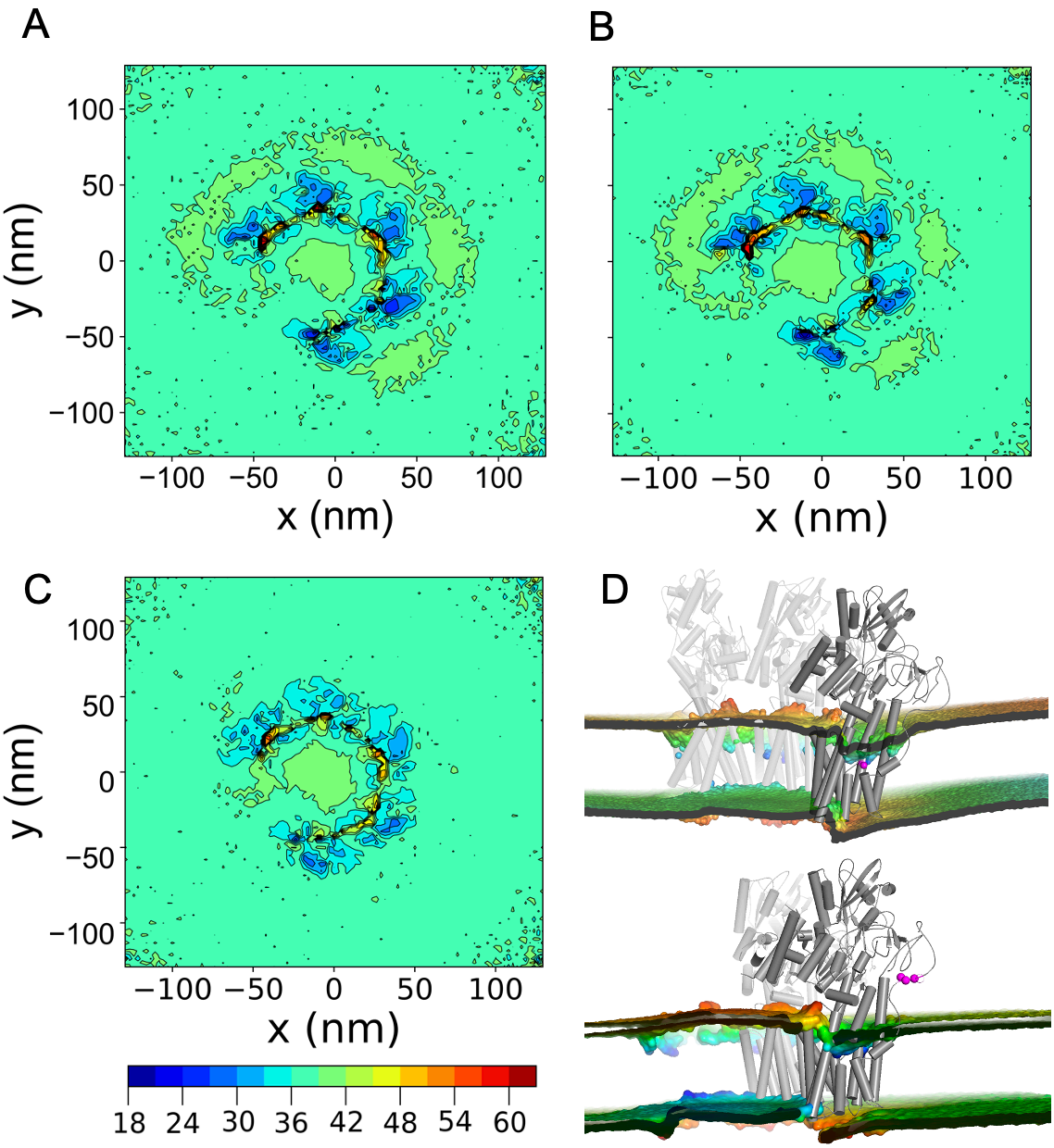

Figure 3.13: Bilayer analysis of the three different systems. *Quantitative analysis of the bilayer thickness calculated by subtracting the average z-height of the inner leaflet from the outer leaflet for WT (A), PICE (B) and RRRK->AAAA mutant (C) simulations. Values are in Å D) Side view of the coarse-grained bilayer deformation at the monomer interface for the WT system (top) and mutant system (bottom). Position of the mutations are shown as magenta spheres.*

3.9 Chapter 3 discussion

CG MD simulations were successfully employed to investigate the protein-lipid interactions between Pma1 in a native-like membrane. Evidence is provided for specific association with anionic lipids accumulating at the proton-entry site, as well as accumulating CIPs in the core and below the A-domain. The simulations further suggested significant membrane deformations that may play a role regulating the protein's function.

The fractional occupancy of each lipid was calculated between each lipid head group and all residues of the protein to define lipid binding sites and, in particular, to address the monomer interface. The results show that predominantly DIPS and other anionic lipids occupy Site I in the inner leaflet. Follow-up studies should address this further by calculating the kinetics of binding. By using a method such as a potential of mean force (PMF) simulation, the binding energy of various lipids can be estimated to get a better understanding of the driving forces for binding. By placing the protein with various lipids bound at Site I in a generic PC membrane, the umbrella sampling method can be used to calculate the ΔG for the lipid and the PC lipid and estimate $\Delta\Delta G$ between two lipid species. The PC lipid can be considered the equivalent of a water molecule binding to an apo binding site in a soluble protein domain. Another potentially useful follow-up study could be to take the coordinates of a frame where particular lipids of interest are bound to Pma1 and convert the system to atomistic scale. By running a series of repeat simulations in atomistic detail, we would be able to see whether the bound lipids remain bound and if the membrane deformation remains.

Additional simulations with a newly generated CG model for CIP were run and provided interesting insights into lipid accumulation in the protein core, as well

as localised binding to the A-domain. However, the method for producing CIP by stitching two parts of existing lipid models together has not been thoroughly validated. After running these simulations, I discovered that the PyCGTool has been developed to create novel CG models of molecules through a systematic parameterization approach (Graham et al., 2017). The tool uses atomistic simulations of the given molecule and provides the added benefit of using a more accurate representation of the bond lengths and angles from the atomistic reference model. Following work should create a model for CIP using the PyCGTool and repeat the simulations to confirm the results.

Due to the biological relevance of the results presented, a further discussion in the wider context of the field is presented in Chapter 7.

Chapter 4: Optimising native source purification of *Neurospora crassa* Pma1

4.1 Chapter 4 Introduction

Chapter 3 investigated the role of lipids in Pma1 activity through CG MD simulations, functionally established the protein's dependency on anionic lipids and provided a possible explanation for the published interaction with phosphoinositol ceramides. To further investigate the structure and function of Pma1, including by MD, structures of Pma1 in various catalytic states are required. In the early 1980s, Randolph Addison and Gene Scarborough developed a protocol for purifying *N. crassa* Pma1 from native source, using a cell wall-less mutant (Addison & Scarborough, 1981b). This method was adopted by the Bublitz lab and in part developed further by Dr. Sabine Heit. Pma1 is particularly well-suited to native source purification due to naturally high expression levels, around 10% of total membrane proteins (Bowman et al., 1981). However, the purification protocol remained somewhat inconsistent, with low yields and no visible lipids in cryoEM, possibly due to excessive purification steps. This chapter is therefore dedicated to improving the purification of Pma1 through following up on a series of samples taken over from Dr. Sabine Heit, as well as working up glucose-activated membranes with a newly established protocol. The resulting protocol can purify Pma1 to cryoEM-suitable purity through a single AEX chromatography and glycerol gradient purification step, significantly reducing the number of purification steps required. The protocol was tested three times and provided consistent results as well as yielding the first glucose-activated sample used for structural analysis in Chapter 5.

4.2 Purification of Pma1 in LMNG

One of the samples taken over from Dr. Sabine Heit at the start of this project was a partially purified sample of Pma1 in LMNG. Cells were grown up and harvested without glucose activation. Membranes were solubilised with DDM and Pma1 was purified through two rounds of glycerol gradient centrifugation, exchanging for LMNG in the buffer. The sample was purified one final round by SEC and samples were assessed by negative stain EM (data not shown). The micrographs showed that the sample was still impure and had micelles of mixed sizes. The author took over purification from this point onwards.

To attempt removal of mixed micelles and protein impurities, the peak fractions from SEC were pooled together and separated by AEX chromatography with a linear gradient to 500 mM KCl and collected in 1 mL fractions (Figure 4.1A). The eluted fractions were analysed by SDS-PAGE (Figure 4.1B). In the first few fractions, protein contaminants other than monomeric Pma1, above 100 kDa, are eluting. This highlighted an opportunity to improve the purification protocol by increasing the concentration of salt in the wash step. The conductivity of fraction D9, before Pma1 elutes, was measured at 5.5 mS/cm. This conductivity was calculated back to correspond to 50 mM KCl. The purification protocol for AEX was updated to reflect this by washing with 50 mM KCl instead of 20 mM, to increase contaminant elution in the wash step. After fraction D9, Pma1 elutes across the remainder of the fractions analysed. Fractions D10-E6 were pooled and separated by SEC using a Superose 6 10/300 column (Figure 4.1C). The chromatogram has two major peaks, one at 8.5 mL and the other at 12.5 mL. The first peak is the void volume of the column. The second peak contains a shoulder to the left and an additional small peak around 15 mL. Based on work previously conducted by Dr.

Sabine Heit, hexameric Pma1 is expected to elute around 12.5 mL and this is therefore likely to be predominantly Pma1. The fractionated elution was analysed

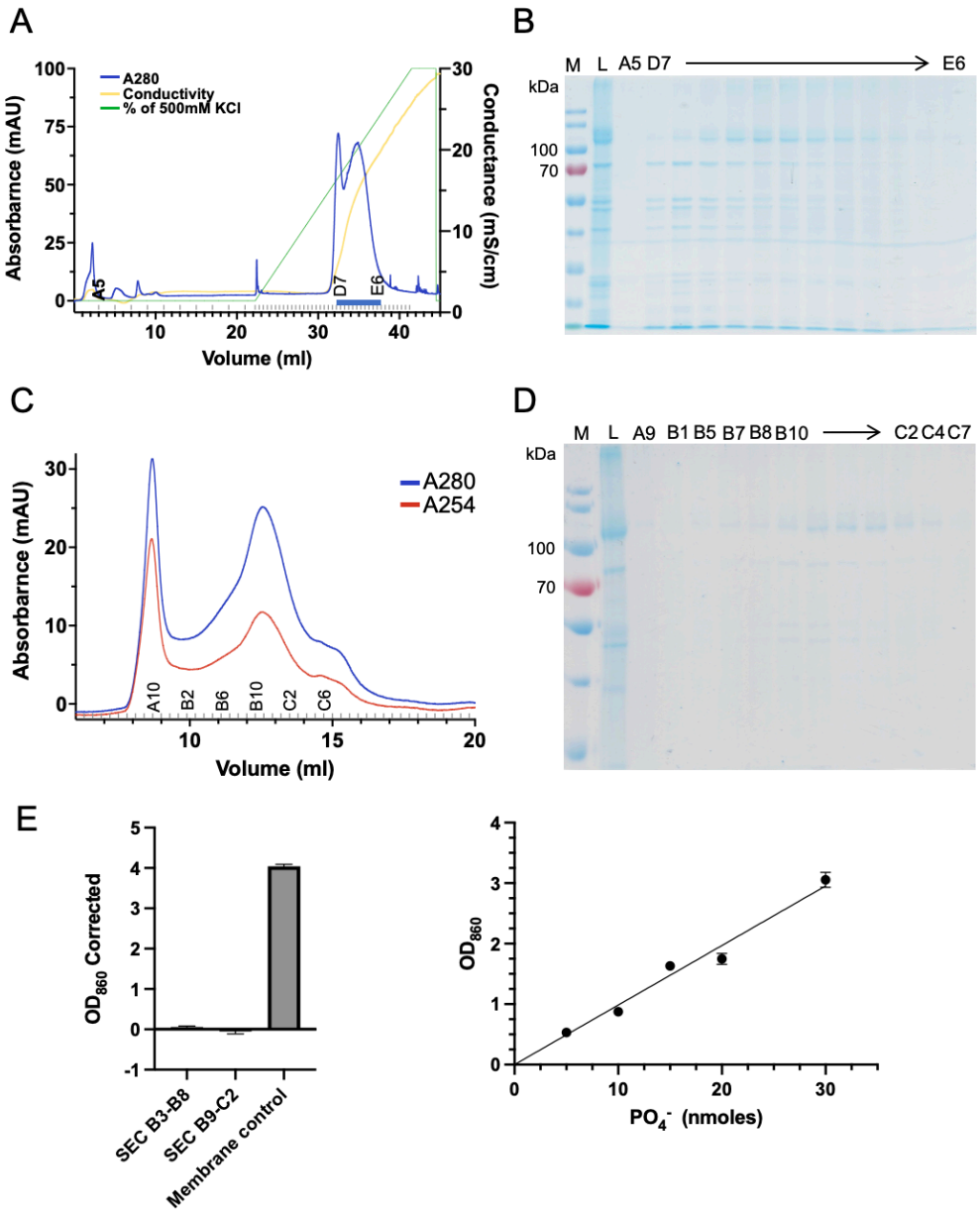

Figure 4.1: Purification of Pma1 in LMNG. A) AEX chromatogram of Pma1 elution with a linear gradient to 500 mM KCl. The blue bar represents fractions D7 to E6 shown in the SDS-PAGE analysis in (B). The percentage of 500 mM solution is shown in green and is relevant to the left y-axis values. B) SDS-PAGE gel of the fractions from (A). Labels refer to the following: M: protein marker, L: Load sample, A5-E6: fractions from the chromatogram. C) SEC chromatogram of the peak fractions pooled from (B). D) SDS-PAGE

gel of the fractions from (C). Labels refer to the following: M: protein marker, L: Load sample, A9-C7: fractions from the chromatogram. E) Left: Baginski ATPase activity assay of SEC fractions and a membrane control. Right: Phosphate standard for the Baginski showing the correlation between the amount of phosphates and OD_{860}. Error bars refer to the standard deviation from the mean calculated by Graphpad Prism (n=3).

by SDS-PAGE (Figure 4.1D) and shows that SEC did not purify the protein much more than AEX had in the previous step, suggesting there is no added benefit of SEC purification on the final sample. When comparing the load samples on the gels shown in Figures 4.1B and D, the load in D contains fewer contaminants. Fractions B3-B8 were pooled to capture the shoulder of the peak and fractions B9-C2 to capture the peak of the elution profile. Neither of the pools showed ATPase activity (Figure 4.1E), suggesting that LMNG inactivates the protein. One possibility is that the high binding affinity of LMNG prevents Folch Fraction I lipids from binding during the ATPase assay. As a result, the activity of LMNG-purified Pma1 against inhibitors discussed in Chapter 5 could not be tested.

Aliquots from the peak and shoulder fraction were prepared for negative stain EM. The shoulder peak did not contain any identifiable protein and is not shown. Two micrographs from the peak fraction are shown in Figure 4.2. The micrographs demonstrate a good density of particles, confirming that 0.015 mg/mL is a suitable protein concentration for Pma1 samples analysed by negative stain EM. Furthermore, the sample appears to be stable as the particles are not aggregated. Clear hexameric Pma1 particles are highlighted in orange circles with their zoom-in shown on the right. Top views of Pma1 appear as doughnut-like densities whilst side-views appear as E-shaped densities. Some contaminants are present, including example number 6 of the bottom micrograph. This L-shaped particle could

be Complex I from the mitochondrial respiratory chain. Nonetheless, although contaminants were visible in the SDS-PAGE analysis of the SEC peak, negative stain EM showed that this level of contamination should not prohibit successful structural determination with EM.

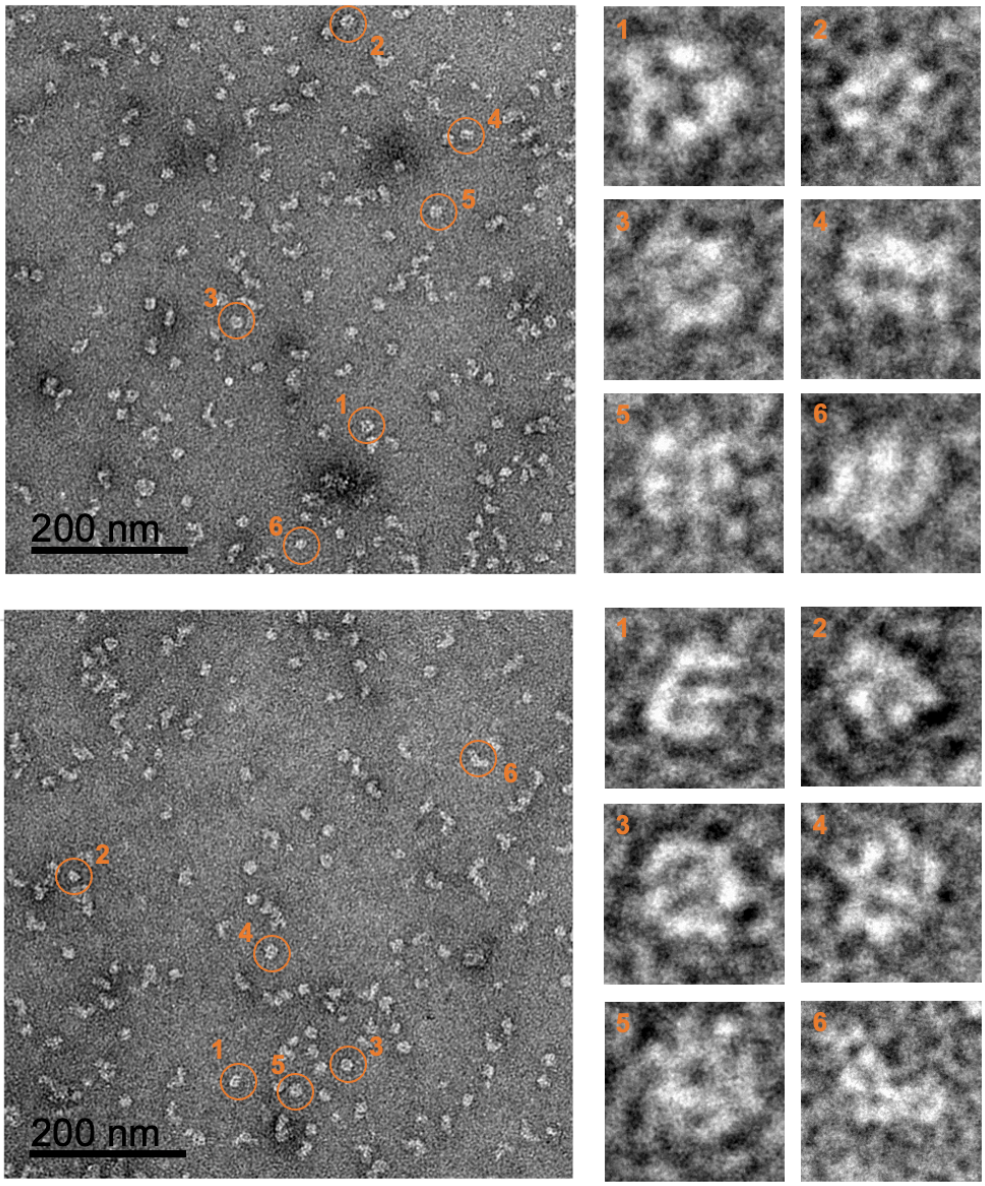

Figure 4.2: Negative stain electron microscopy of Pma1 in LMNG. *Two micrographs are shown with examples of potential hexameric Pma1 circled in orange and a zoom shown to the right, labelled with the same number. Example 6 of the bottom micrograph illustrates a contaminant protein thought to be Complex I from the mitochondrial respiratory chain.*

The SEC peak fraction was concentrated to 2.17 mg/mL for cryoEM. However, because the sample was later shown to have no ATPase activity, focus was shifted on further optimising the purification in order to obtain functionally active Pma1.

4.3 Improving the AEX purification by greater fractionation volume and a systematic approach to pooling

Based on the separation of proteins seen in the AEX chromatography of Pma1 in LMNG, membranes prepared by Dr. Sabine Heit were solubilised and purified using AEX to improve the purification protocol. Firstly, the sample was not concentrated after solubilisation for a 1 mL Q HP column but instead loaded overnight onto a 5 mL HiTrap Q HP column and washed with 50 mM KCl AEX wash buffer. The aim was to elute over a larger column volume to achieve greater separation and avoid an aggregation-prone concentration step. Elution was run over 20 CV that spread over 100 mL instead of 20 mL for the smaller column previously used. The result was an improved separation of the eluting proteins across a greater volume (Figure 4.3).

In the original protocol, fractions were pooled purely based on the SDS-PAGE analysis and typically the region of E10-F7 (relative to the chromatogram shown in Figure 4.3A and zoom-in B) was pooled for gradient centrifugation. Considering the gel in Figure 4.3C, a Pma1-like band, above the 100 kDa marker, runs across the whole elution profile, whilst the contaminant proteins across this region vary. The elution region of Pma1 was split into three separate regions, as displayed by the purple (E9-F8), orange (F9-G7) and green (G8-H7) boxes, and

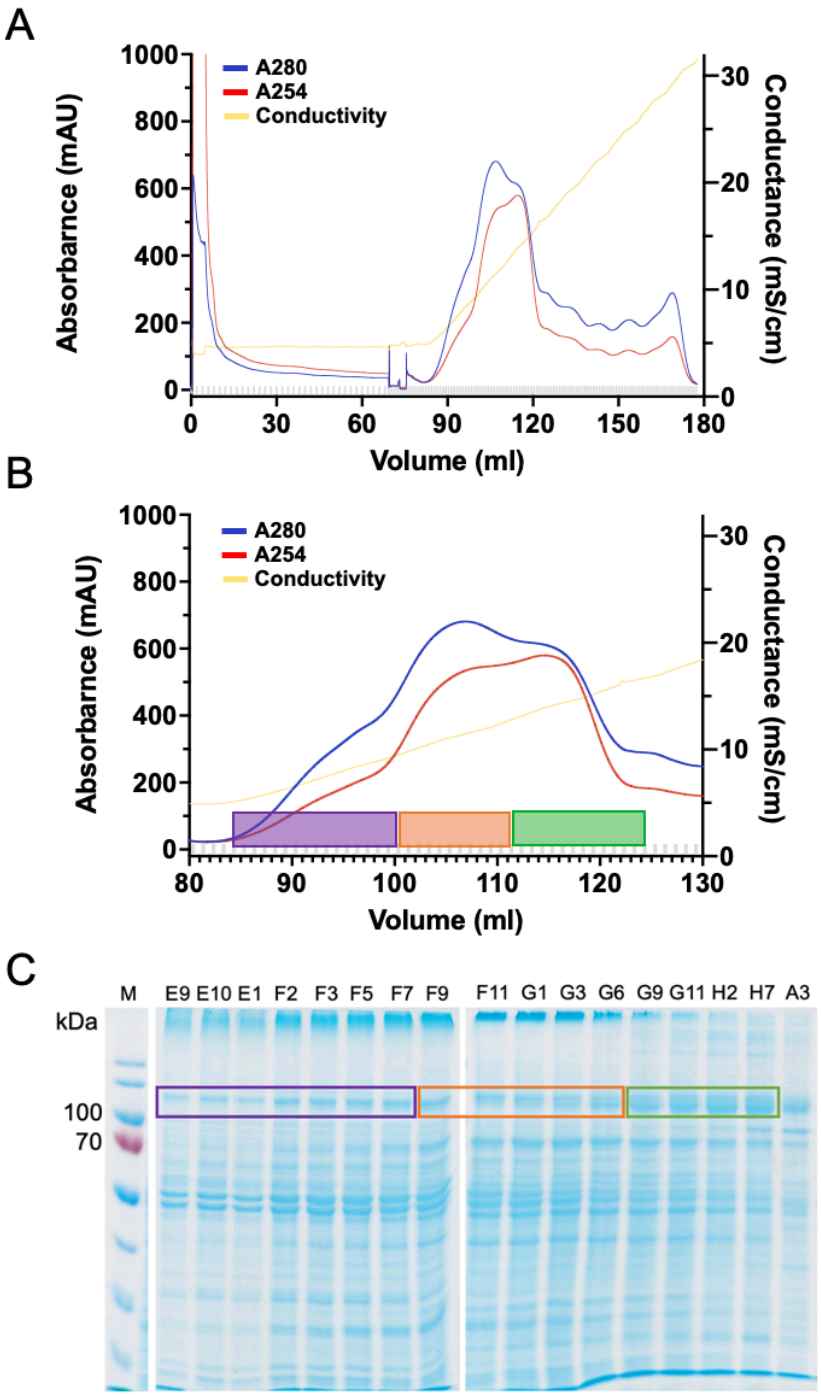

Figure 4.3: Purification of Pma1 by AEX. *A) Full AEX chromatogram illustrating the wash from 0 to 75 mL followed by linear elution with 500 mM KCl for 20 column volumes. B) Zoom on the elution region of the AEX chromatogram. The purple (E9-F8), orange (F9-G7) and green (G8-H7) boxes refer to the three pooled samples for downstream glycerol gradient purification. C) SDS-PAGE analysis of the AEX fractions. The purple, orange and green boxes surround the Pma1 monomer band and refer to the elution regions in (B).*

pooled accordingly to see the effect of glycerol gradient purification on the regions separately. These gradients were harvested and fractionated into 1 mL fractions. SDS-PAGE and Baginski assaying of the fractions show a significant difference

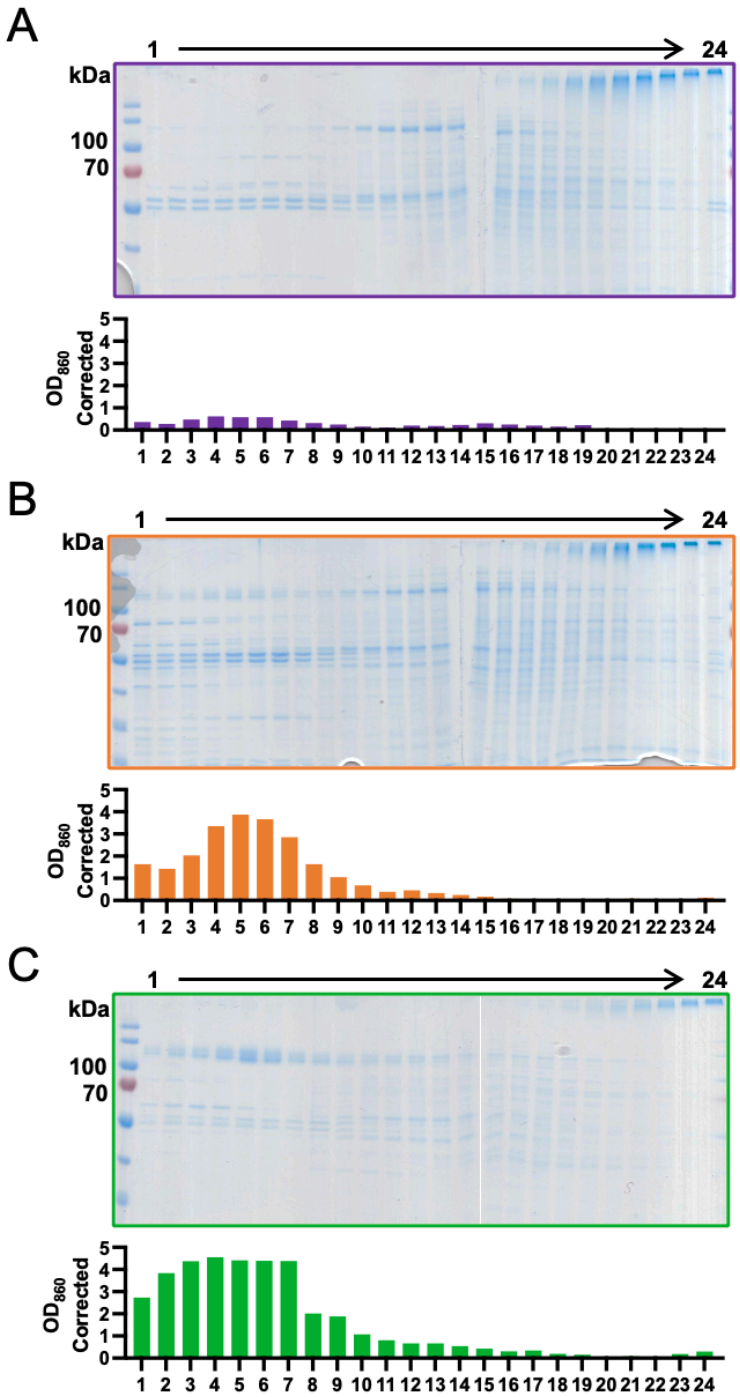

Figure 4.4: SDS-PAGE and Baginski analysis of glycerol gradient purification *of Pma1 AEX fractions E8 to F9 (A), F9 to G7 (B) and G8 to H7 (C). Colours refer to the coding in Figure 4.3. The* OD_{860} *corrected was measured by subtracting the SDS-inhibited measurement from the reaction measurement.*

between the three pools (Figure 4.4). In the purple pool (which was typically pooled in the original protocol), little hexameric Pma1 appears to be present. Since the Pma1 band runs further down the gradient, this is likely non-hexameric Pma1 due to the size-filtering effect of the glycerol gradient. This is corroborated by the low levels of ATPase activity measured in fractions 2-8. In the orange and green pool, there is a notable increase in the amount of functional and perhaps hexameric Pma1 present, marked by a significant increase in the protein band in fractions 2-8 of the SDS-PAGE gel, supported by the activity in these fractions. Most strikingly, the green pool highlights a significant step up in purity, with just a few contaminant bands present in the peak fractions 4-7. Taken together this experiment has found that active, hexameric Pma1 with limited contaminants elutes between 180 and 250 mM KCl in AEX chromatography. Considering the variation of activity recorded across the gradient (Figure 4.4A-C), future purifications included a Baginski assay on AEX fractions to assist pooling of functionally active Pma1. Figure 4.5 shows an example purification with a Baginski assay on AEX fractions to aid selection. The peak Pma1 activity lies between fractions F10 and H8 and can be combined with the SDS-PAGE analysis to pool the fractions with the greatest activity and purity.

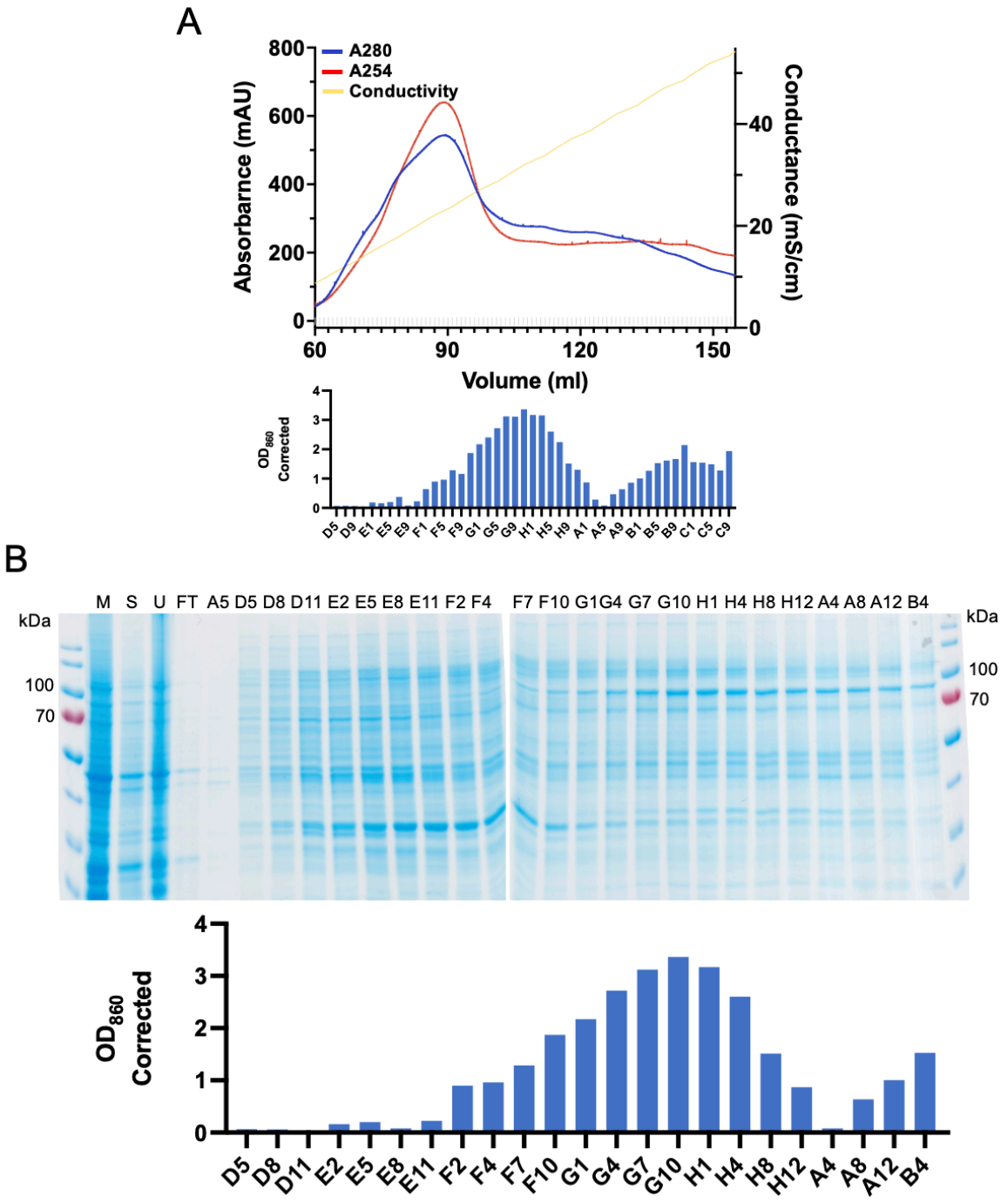

Figure 4.5: Using Baginski assays on AEX samples to pool functionally active Pma1.

A) AEX chromatogram across the elution with a linear gradient of 500 mM KCl. The activity of fractions is shown below and aligned against the fractions in the chromatogram. B) SDS PAGE analysis of the AEX elution fractions with the activity of the given fractions aligned below.

4.4 Expression and purification of glucose-activated Pma1 for functional and structural studies

To get the first glucose-activated Pma1 structure, *N. crassa* cells were grown and activated by resuspending the cells in an isotonic glucose-containing solution. Membrane preparation followed as previously established. Pma1 obtained from glucose-activated membranes will be referred to as Pma1-GA.

Membrane protein concentration was assessed by Bradford assay (Figure 4.6A) and calculated to be 11.63 mg/mL. A solubilisation screen at 2 mg/mL final

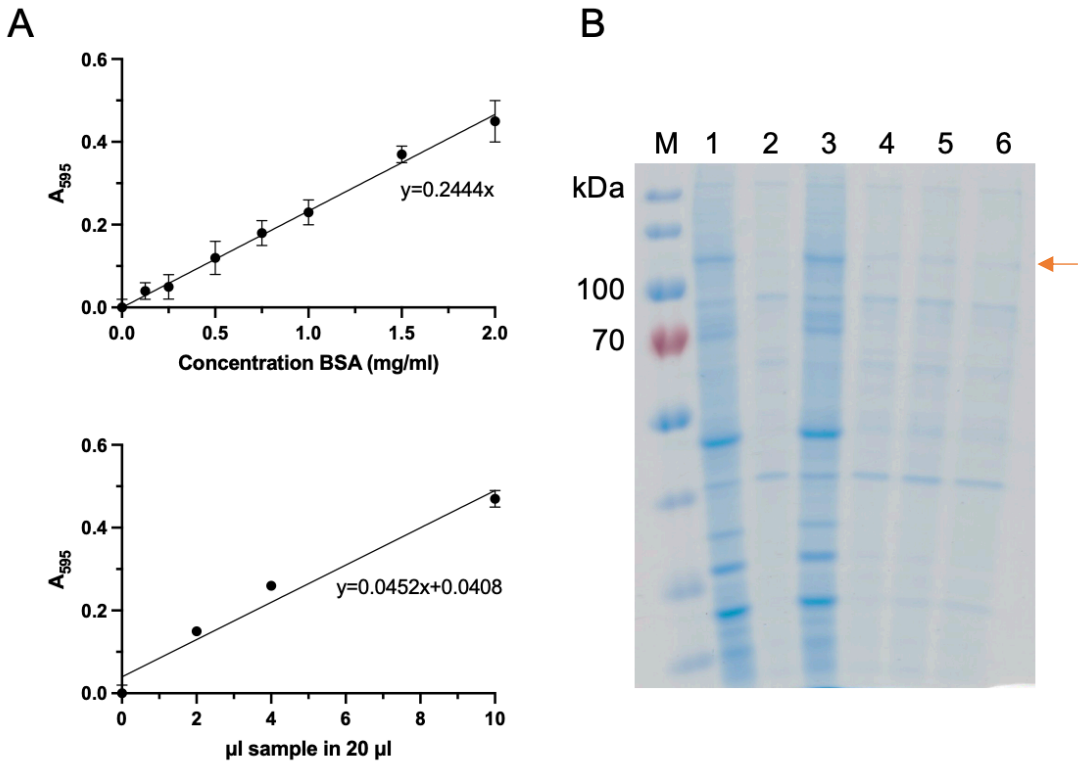

Figure 4.6: Analysis of harvested glucose activated N. crassa membranes. *A) Bradford assay of the harvested membranes to calculate the protein concentration. Top graph corresponds to the BSA standard and the bottom the dilution series of membrane sample. Error bars represent standard deviation from the mean calculated by GraphPad Prism (n=3). B) Samples of a solubilisation screen assessed by SDS-PAGE. Lane numbering refers to the following: M: protein marker 1: membrane sample, 2: buffer wash, 3: 2% SDS, 4: 0.1% DDM, 5: 0.225%, DDM 6:0.3% DDM.*

protein concentration was run and 0.225% DDM was determined optimal for solubilisation (Figure 4.6B). The buffer wash in lane 2 shows additional proteins releasing from the membranes and so an additional wash step was included before solubilisation of membranes.

AEX chromatography was used for the first round of purification and the fractionated eluate was assessed for ATPase activity and by SDS-PAGE (Figure 4.7). Under these conditions, the Baginski assay was impaired by the formation of insoluble potassium dodecylsulfate. It is unclear why the precipitation did not occur in the ATPase assay shown in Figure 4.5. Based on the SDS-PAGE analysis, fractions G3-H5 were pooled as peak fractions. F4-G2 and H6-A6 were pooled as secondary fractions.

The peak and secondary fractions from AEX were run on separate 20-40% glycerol gradients and harvested in 1 mL fractions. The fractions were analysed by SDS-PAGE and tested for ATPase activity. Very pure Pma1-GA was found in fractions 5-6 of the peak gradient (Figure 4.8A), running at the expected fractions for functional, hexameric Pma1. The ATPase activity corroborates functionally active Pma1-GA is present. The gradient of the secondary fraction shows greater contamination and a lower concentration of the Pma1 band compared to the peak gradient (Figure 4.8B). Due to the measurable activity, these fractions were considered optimal for functional studies and were stored at -80 °C, despite the lack of purity. Remarkably, there are no further (significant) lower molecular weight contaminants in fractions 5-7 of the peak gradient and therefore the sample was not subjected to further purification steps.

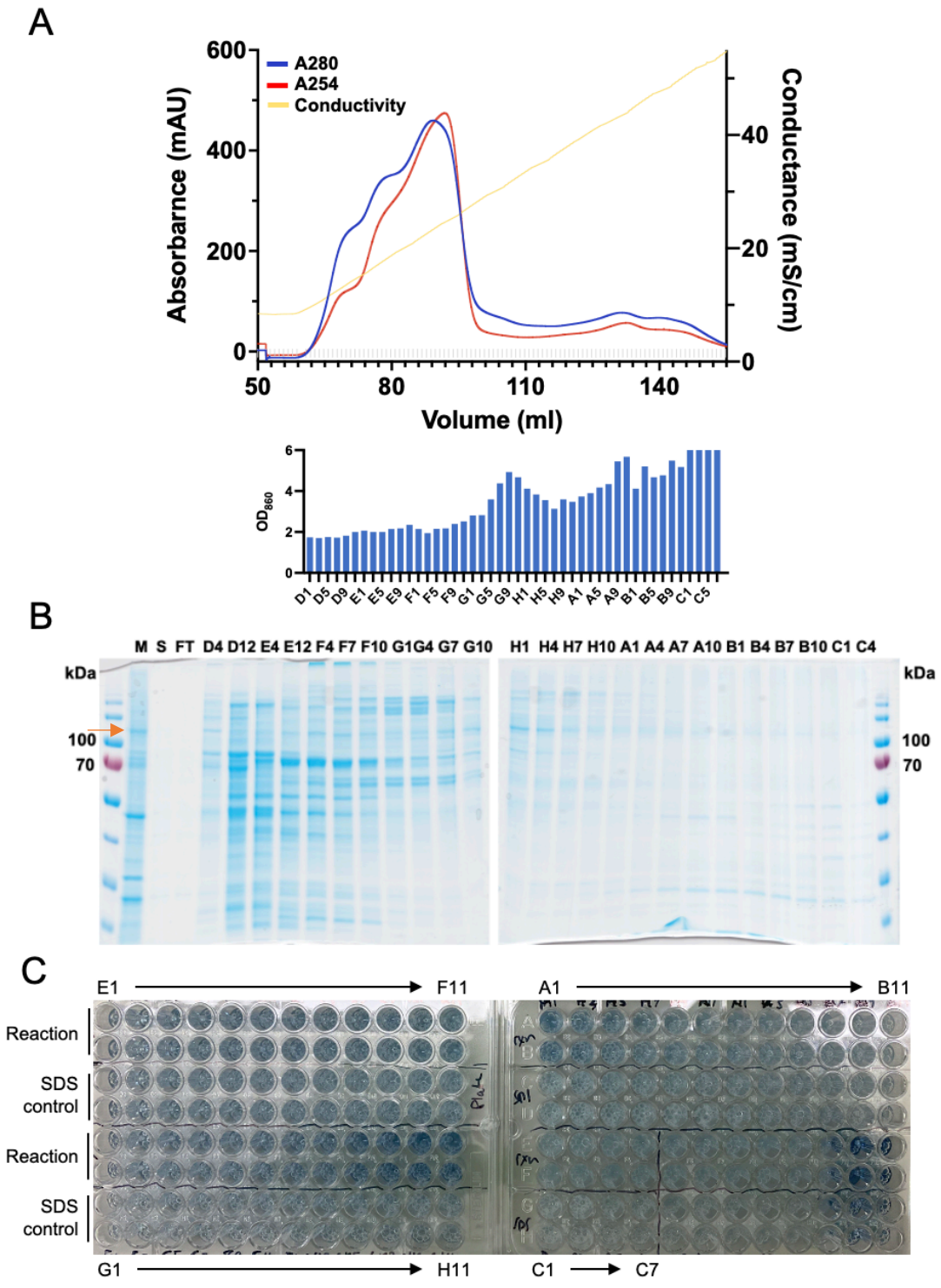

Figure 4.7: AEX of solubilised glucose-activated N. crassa membranes. *A) AEX chromatogram zoomed-in on the elution. The ATPase activity is aligned to the fractions in the chromatogram. B) SDS-PAGE analysis of fractions of the AEX elution. C) Photograph of the ATPase assay to show the difference between the colour reaction and the measured absorbance in the Baginski assay (A) due to precipitation effects.*

The purest protein in peak glycerol gradient fractions 5-7 was exchanged into cryoEM buffer using a PD-10 desalting column, followed by concentrating to 2.49 mg/mL. SDS-PAGE analysis of the PD-10 load, eluate and concentrated Pma1 sample are shown in Figure 4.9. Note that the sample is diluted upon elution from the PD-10 column. The final concentrated sample was diluted to 0.5 mg/mL and run

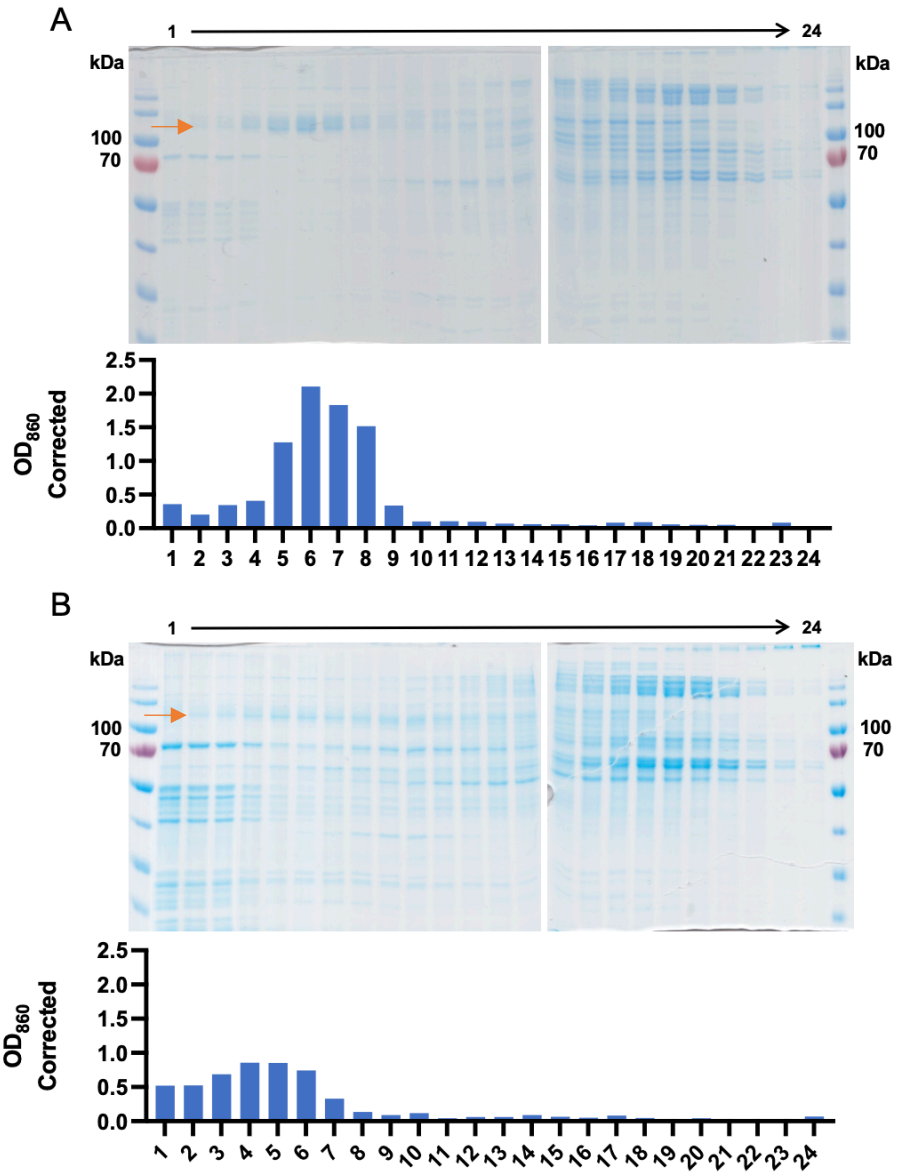

Figure 4.8: SDS-PAGE and ATPase activity Glycerol gradient fractions. *A) Glycerol gradient of AEX peak fractions G3-H5. B) Glycerol gradient of AEX secondary fractions F4-G2 and H6-A6. Refer to Figure 4.7 for the AEX chromatogram.*

on SDS-PAGE to assess the purity for cryoEM purposes. Overall, the purity of the sample is high, with a few lower molecular weight bands appearing at this higher concentration. Additionally, a more intense very high molecular weight band appears on the gel, above the highest marker band. This is believed to be a higher order oligomer of Pma1-GA that did not fully denature since its intensity is close to that of the Pma1 monomer band and is a band not observed in the other two lanes. This optimised purification had a final yield after concentration of 76.8 µg of Pma1 per L of cell culture. The Pma1 yield that produced the cryoEM structure from Dr. Sabine Heit was around 30 µg of Pma1 per L of culture, so overall, improvement in the methodology has led to a ~2.5-fold increase in yield.

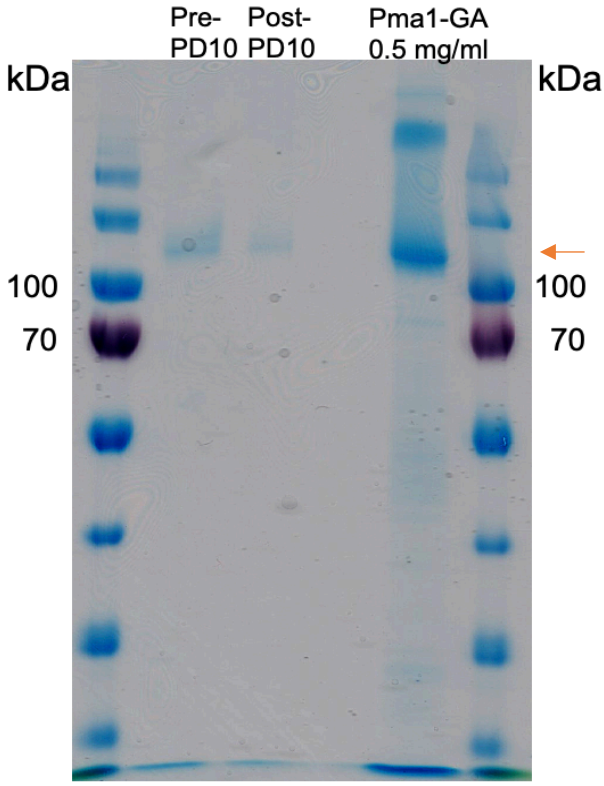

Figure 4.9: Buffer exchange of purified Pma1-GA *to cryo electron microscopy buffer using a PD-10 desalting column. SDS-PAGE analysis of the sample loaded onto (pre) and eluted from (post) as well as the final concentrated cryoEM sample of Pma1-GA diluted to 0.5 mg/mL. The orange arrow points at the Pma1 band.*

4.5 Chapter 4 discussion

Significant improvements in the purification of Pma1 from native source have been established. Through a systematic approach of testing various regions of the AEX eluate and using the ATPase assay throughout, the purification is now able to pool functionally active Pma1 from a more pure region. Due to this major improvement, Pma1 can now be purified for structural analysis within a single glycerol gradient and a 2.5-fold higher yield. Because the number of purification steps is drastically lowered, this lowers the number of stripped lipids and increases the chance that they are resolved in cryoEM analysis - this could corroborate the lipids that bind at Sites I and II proposed in Chapter 3 as well as possibly identify a lipid plug as noted for the *S. cerevisiae* Pma1 (P. Zhao et al., 2021). The updated protocol has been tested on three independent batches of cell culture and gave the same purity and yield each time, proving this is now a consistent method for obtaining high quality Pma1.

Regarding the activated state of Pma1, the cells were glucose activated to try to phosphorylate the R-domain and relieve autoinhibition. The ATPase activity measured at various stages of purification is not higher than that recorded for the non-glucose-activated samples. This is likely because the concentration of ATP lies at the V_{max} of both the 'activated' and autoinhibited states. Although metal fluoride inhibition was studied on both the activated and autoinhibited state of Pma1, Pedersen *et al.,* who have published activity assays on *ScPma1*, presented their data in terms of relative activity as a percentage of positive control (J. T. Pedersen et al., 2015). They also do not comment on whether the activated protein had an overall higher activity in the Baginski assay than the autoinhibited sample. A future

experiment should therefore investigate this by simultaneously testing the activity of equal quantities of purified activated and autoinhibited Pma1.

Lastly, another explanation for the same measured activity is that the phosphatase activity in the cell lysate could have reversed the phosphorylation of the R-domain before purification. Future membrane preparations should therefore include phosphatase inhibitors to prevent this. Finally, to test for phosphorylation, cryoEM will give an indication, however, it can be more accurately verified by mass spectroscopy analysis or phospho-specific antibodies to identify phosphorylation of the R-domain.

Chapter 5: Structural and functional studies of glucose-activated Pma1

5.1 Chapter 5 Introduction

Work presented in Chapter 3 and 4 investigated the relationship between Pma1 and lipids in a native-like membrane using CG MD and made significant improvements to the purification of hexameric Pma1. Using the newly improved method, the first sample of Pma1-GA was purified for structural and functional studies, to build on the MD results and initial *N. crassa* Pma1 structure. This first structure captured autoinhibited Pma1 in an E1 state, in the presence of ADP and AlF_4^- and provided an understanding of how the R-domain regulates autoinhibition and a possible explanation for proton transport. As we published the first structure of Pma1 from *N. crassa*, Zhao *et al.* published the first structure from *S. cerevisiae* in both an autoinhibited and 'activated' state, bound to BeF_x (P. Zhao et al., 2021). They claim to have activated Pma1 not by inducing with glucose but by lowering the pH to 6, so this structure might not represent a physiologically active state of Pma1. Whilst both papers have provided some understanding of how Pma1 functions, the glucose-induced activation and catalytic cycle require further investigation. The work presented in this chapter uses the glucose-activated Pma1 purified in Chapter 4 to conduct inhibitor assays to establish the inhibitor constants for a series of metal fluorides. These inform the conditions necessary for inhibiting E2-like states for investigation by cryoEM. Moreover, assays are conducted with Pma1-GA inhibited by a tetrahydrocarbazole shown to have antifungal activity (Bublitz et al., 2018). Finally, these conditions are used to set up cryoEM screening of Pma1-GA inhibited with BeF_x and MgF_x at pH 7.

5.2 Establishing optimal ATPase conditions for inhibitor studies at pH 7

To run the inhibitor assays of Pma1-GA with various proposed inhibitors, optimal conditions needed to be established. Since the inhibitors tested (metal fluorides MgF_x, BeF_x and AlF_x and the tetrahydrocarbazole compound '7') all aim to inhibit E2-like states, assays were run at pH 7. By increasing the pH (lowering the concentration of protons in solution), the Pma1 state equilibrium is pushed towards E2 as this is associated with proton release. The drawback to running experiments at pH 7 compared to pH 6 optimum is that it reduces the activity of Pma1 to ~30% (previously determined by Dr. Maike Bublitz) and therefore the activity of Pma1 at various concentrations was tested to establish the ideal conditions for assaying.

The sample used for testing was prepared by Dr. Sabine Heit and contains autoinhibited Pma1. An SDS PAGE gel of the glycerol gradient fractions, done by Dr. Heit, is shown in Figure 5.1B. Fractions 5, 6 and 7 were used to measure the ATPase activity at pH 7, testing 1, 2 and 5 µL of the fraction in 50 µL total reaction volume (Figure 5.1A). Fraction 7 had the highest activity and the equation of the linear regression fit is shown. For inhibitor assays, readings should ideally be above 2 absorbance units after SDS-control correction. To correlate this to the total amount of Pma1 in each well the image of the gel was loaded into ImageJ (Schneider et al., 2012) and the intensity of the bands in lane 8 (corresponding to fraction 7) was measured to calculate what fraction of total protein constitutes Pma1. The Pma1 peak corresponds to 2610 out of 12,672 units total (with the sharp jump at the end of the plot omitted from the calculation. Pma1 makes up 20.6% of the protein. A Bradford assay (Figure 5.1C) calculated the total protein concentration in fraction 7 to be 0.084 mg/mL and thus 0.084, 0.168 and 0.420 µg

of Pma1 per well were tested. Based on this, ~0.5-1 µg of Pma1 was used per well for future inhibitor assays.

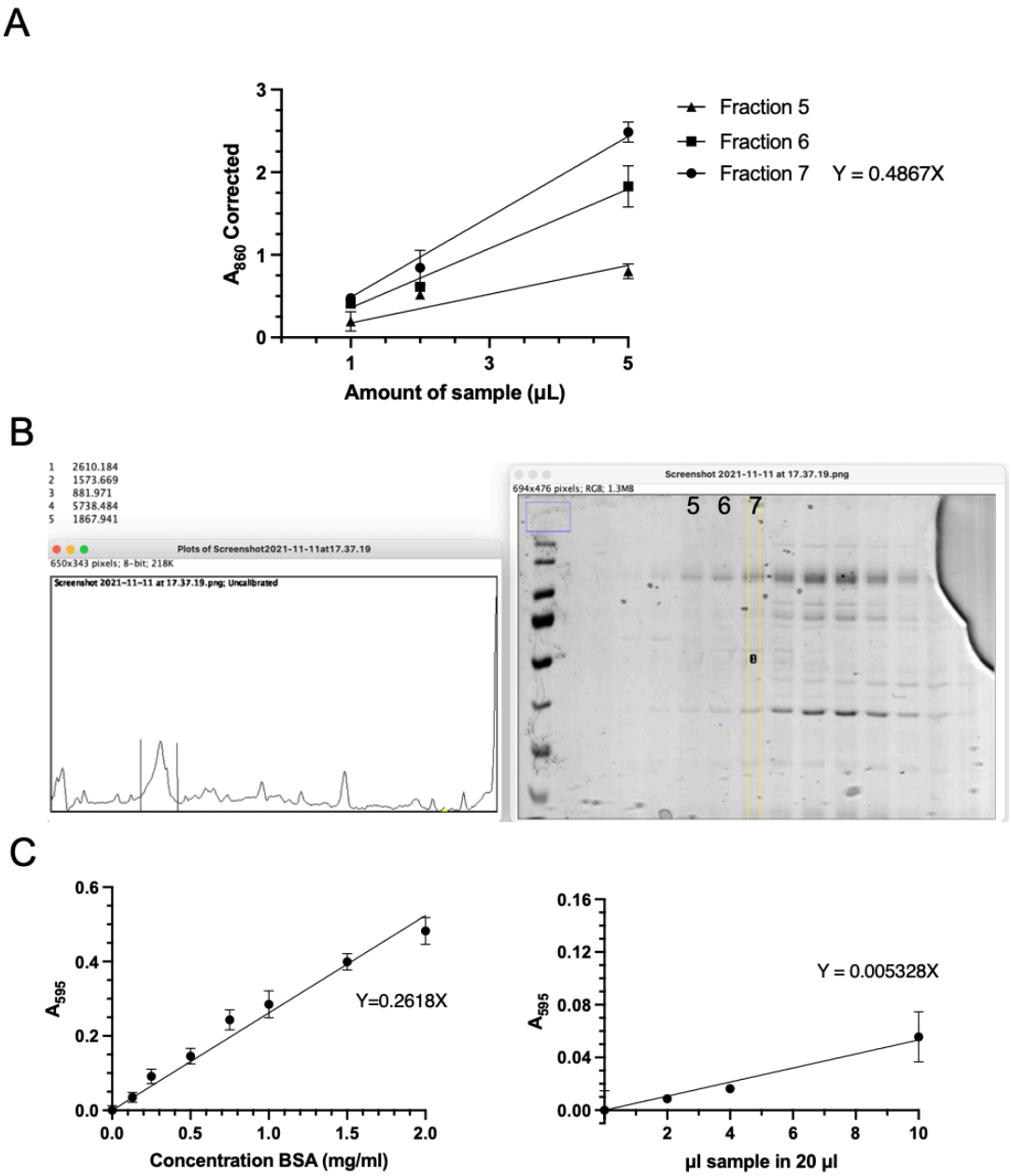

Figure 5.1: Determining the optimal concentration of Pma1 for conducting inhibition assays. *Error bars represent standard deviation from the mean, calculated by GraphPad Prism (n=3). A) ATPase assay comparing the activity of different amounts of glycerol gradient fractions 5, 6 and 7. B) ImageJ analysis of the gel of fraction 7 to calculate the percent of band intensity contributed by Pma1. C) Bradford assay of a BSA standard (left) and the fraction (right) to calculate the concentration of protein.*

5.3 Inhibition studies with a proposed antifungal

Bublitz *et al.* identified a series of tetrahydrocarbazoles as novel P-Type ATPase inhibitors that showed antifungal activity and tested their functionality against Pma1 amongst other P-Type ATPases (Bublitz et al., 2018). A total of 12 inhibitors were designed with varying inhibitory and antifungal properties, of which compound **7** (Figure 5.2B) was one of the most potent. Since Pma1 had not been resolved at high resolution at the time and the purification was not as established as presented in the previous chapter, the structure of SERCA bound to compound 7 was elucidated. It is almost identical to that of E2 SERCA, with the soluble domains adopting a conformation between Ca^{2+}-free E2 and Ca^{2+}-bound E1. Due to this observation, compound 7 is believed to stabilise an E2-like state in P-type ATPases, meaning a high pH could promote binding of compound 7 to Pma1. Inhibitor assays were first tested on samples of purified autoinhibited Pma1 (fraction 7 discussed above) since this was before the purification protocol had been further optimised and Pma1-GA had not yet been produced. Two Baginski assays with compound 7 were tested. The first tested four concentrations ranging from 0.1 to 100 μM, pushing inhibition to just below 50% of positive control's activity (Figure 5.2A). The assay was repeated, adding 1mM compound 7, which resulted in 20% activity and did not fully inhibit the protein. The data for these two repeats are not very consistent, since the first measures activity above the control sample, and the second shows too much fluctuation at the low end. The assays did indicate that the right concentration range was being tested.

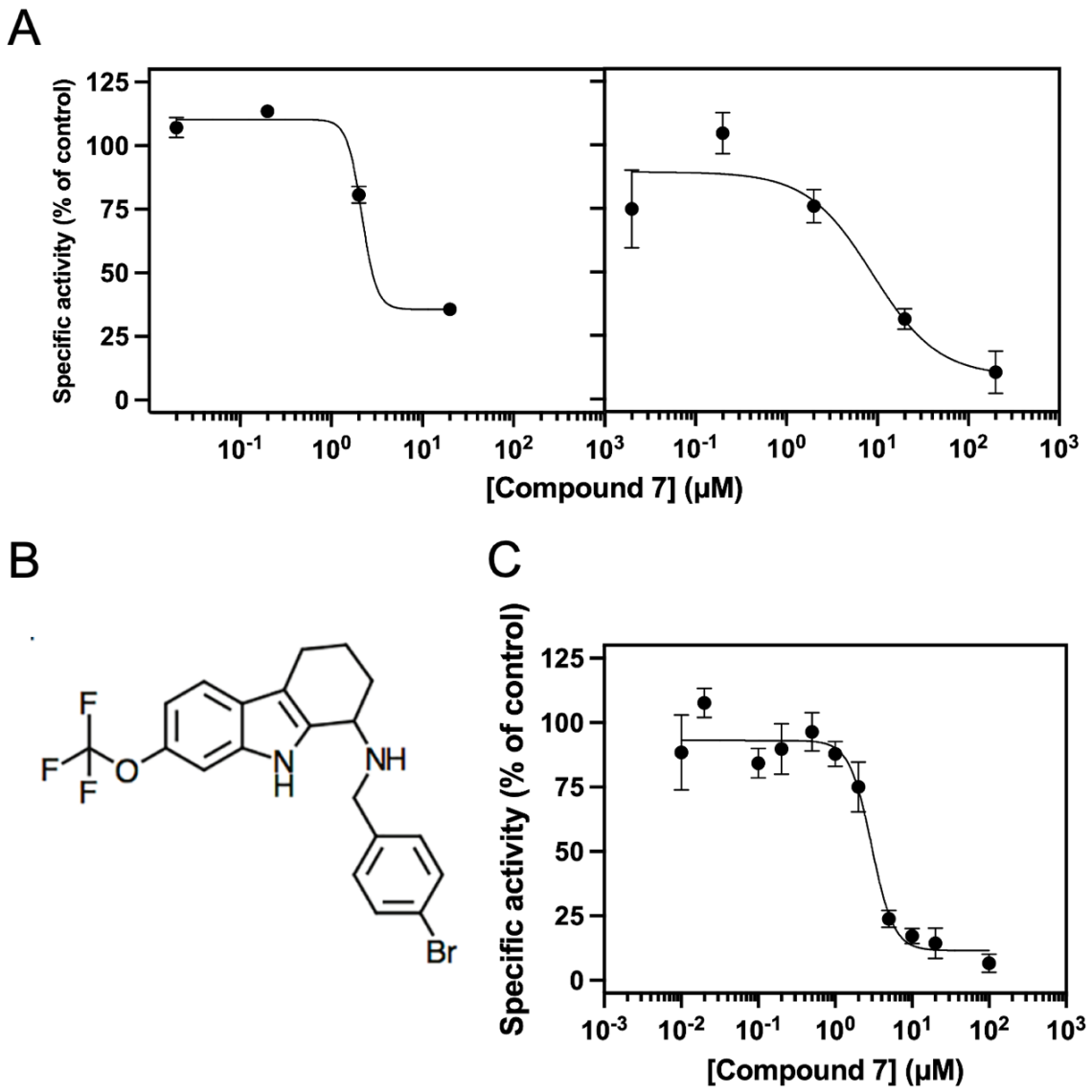

Figure 5.2: Antifungal tetrahydrocarbazole Compound 7 inhibition of Pma1 using the Baginski assay. *Error bars represent standard deviation from the mean, calculated by GraphPad Prism (n=3). Nonlinear regression of [inhibitor] vs response - variable slope was used to fit the data using GraphPad Prism. A) Two independently run range finding assays of autoinhibited Pma1 with Compound 7 to understand the activity range. B) Chemical structure of the tetrahydrocarbazole Compound 7 taken from Bublitz et al. 2018 C) Inhibition assay of Compound 7 on Pma1-GA.*

The assay was conducted on Pma1-GA with 11 conditions ranging from 0.02 to 100 μM, the results of which are shown in Figure 5.2C. The data closely matches the fitted nonlinear regression calculated by GraphPad Prism. The fit measures the IC_{50} at 2.96 μM (R^2=0.948). This is similar to the IC_{50} of compound 7 inhibiting *S. cerevisiae* Pma1 (2.43 μM) reported by Bublitz *et al*. However, the study does not show the binding curves, so no comparison to the quality of the fit of data and the shape of the binding curve can be made. Interestingly, however, comparing the data from Figure 5.2C to 5.2A, the data shows a tighter, more vertical binding curve and comes closer to full inhibition, suggesting that the glucose activation of the cells resulted in phosphorylated and thus activated Pma1.

5.4 Inhibition studies with metal fluorides that mimic phospho-intermediate states

To capture the structure of activated Pma1 in various catalytic states, a series of heavy metal fluorides can be used to mimic the stereochemistry of phosphate as it transitions to and from the enzyme (see Introduction 1.2.2.1). Pedersen *et al*. tested the inhibition of *S. cerevisiae* Pma1 in isolated membranes. To compare the inhibition to the published *S. cerevisiae* Pma1 (*Sc*Pma1) data and to inform the conditions needed for cryoEM, Pma1-GA inhibition assays with MgF_x, BeF_x and AlF_x were run (Figure 5.3). The assays were conducted at pH 7 to push the equilibrium towards the E2 state. At low concentrations, the MgF_x-inhibited protein is active at around 100% of positive control activity whilst the BeF_x-inhibited protein is only 80% active at the same concentrations. Although the error for MgF_x

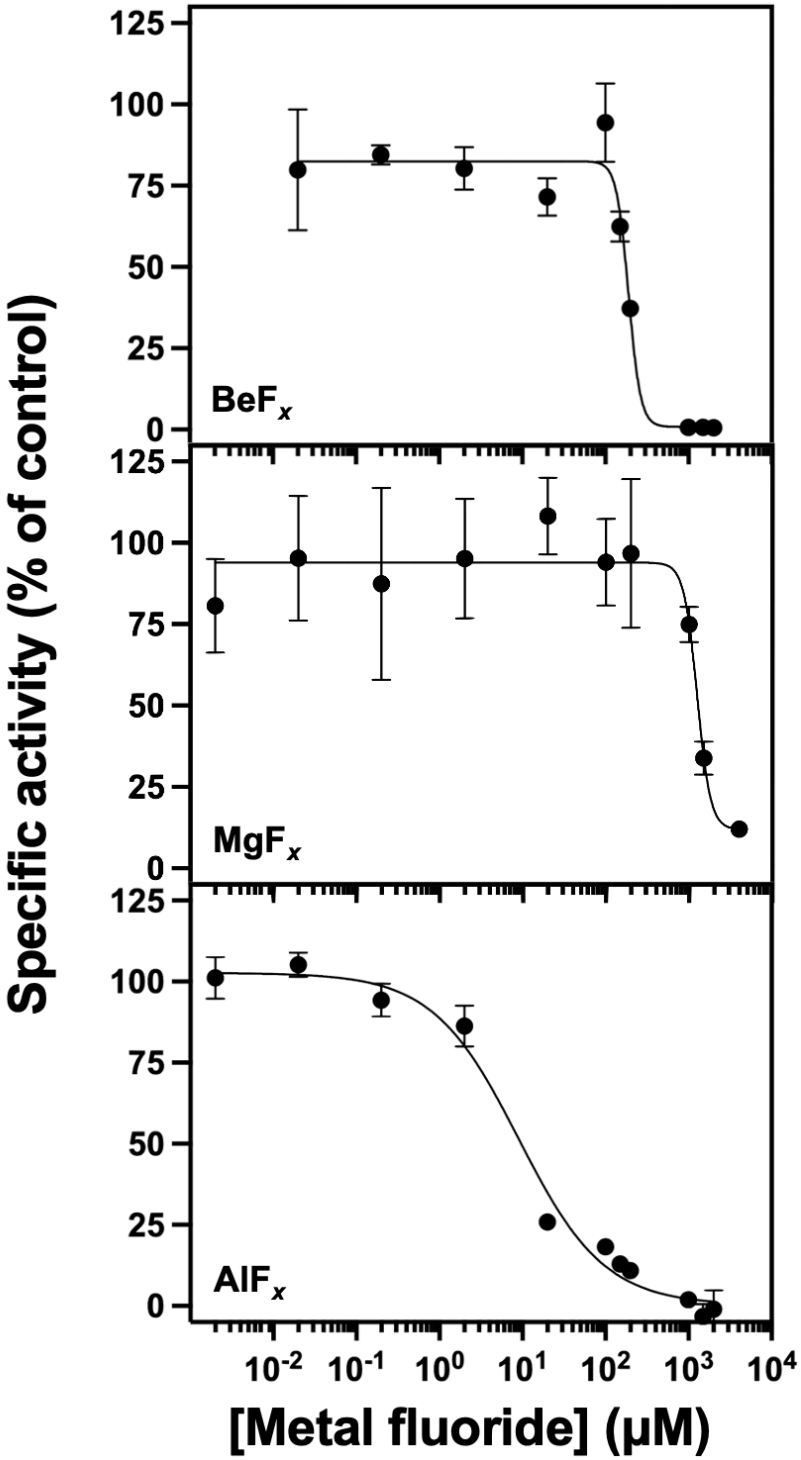

Figure 5.3: Metal fluoride inhibition of Pma1-GA. *Metal fluoride inhibition was tested using the Baginski assay at pH 7. Metal fluoride concentrations were as indicated. The error shown represents the standard error from the mean and was calculated by GraphPad Prism (n=3). Nonlinear regression of [inhibitor] vs response - variable slope was used to fit the data using GraphPad Prism.*

is fairly high, it is important to consider that Pedersen *et al.* study the reversibility of binding of the metal fluorides and find that MgF_x can be reversed more rapidly than BeF_x (J. T. Pedersen et al., 2015). After the 1-hour preincubation, the reaction buffer is added and for MgF_x this could directly dilute the inhibitor 5-fold and cause unbinding whilst for BeF_x it may remain bound and thus lower the measurable activity to 80%.

The error for MgF_x and BeF_x is a lot higher than for AlF_x possibly due to precipitation of arsenite solution. Due to time limitations, MgF_x and BeF_x experiments could not be repeated. Whilst AlF_x inhibits with a significantly lower IC_{50} (discussed below), the slope of the linear regression fit is shallower than for MgF_x and BeF_x. In all three cases, inhibition reaches almost 0% of control activity, suggesting full inhibition occurs. As Pedersen *et al* note that the basal auntoinhibited state cannot be inhibited to the extent of the activated Pma1 in *S. cerevisiae*, this suggests that purified Pma1-GA's R-domain is indeed phosphorylated.

The IC_{50} data is shown in Table 5.1 below, along with the equivalent data from the work by Pedersen *et al* for comparison. The data taken from Pedersen *et al*. refers to their indirect assays at pH 6.7 following a 1-hour incubation, which most closely matches the assay used here. The IC_{50} values calculated for Pma1-GA lie higher than for *Sc*Pma1. However, the slopes of the linear regression fits are much steeper than they are for *Sc*Pma1 in the study, and the assays reach closer to full inhibition of the sample. Another interesting comparison is that Pedersen *et al.* were unable to determine IC_{50} values for MgF_x, with inhibition going no lower than 50% specific activity.

Table 5.1: IC_{50} values of metal fluoride inhibitors against ATP hydrolysis activity of N. crassa and S. cerevisiae Pma1. *Values for S. cerevisiae Pma1 were obtained from Pedersen et al. (2015). n=3*

	ATPase hydrolysis IC_{50} [μM]		
	MgF_x	BeF_x	AlF_x
*Nc*Pma1-GA	1246.6	189.9	9.0
*Sc*Pma1	ND	26	17

5.5 CryoEM screening of Pma1-GA

In order to obtain the structure of Pma1-GA E2 states, the purified protein was separately incubated with MgF_x and BeF_x and the non-hydrolysable ATP analogue AMP-PCP for screening by cryoEM. The protein concentration and buffer conditions were kept the same as the conditions used for the autoinhibited ADP-AlF_x structure (Heit et al., 2021). However, as a means of optimising one of the conditions, UltrAuFoil R1.2/1.3 300-mesh gold grids were used. Ultrastable gold grids were initially developed in 2014 to reduce the radiation-induced movement of the ice-imbedded specimen during imaging (Russo & Passmore, 2014). The gold grids benefit from being highly conductive, inert and radiation-hard. Moreover, since both the support and mesh are gold, the entire grid has the same electrical conductivity, which prevents differential thermal contraction during the cooling process. This also typically produces more uniform ice across the grid squares.

5.5.1 CryoEM screening of MgF_x-inhibited Pma1-GA

The cryoEM work presented below was done with Dr. Margaret Young, Bublitz laboratory. Pma1-GA (at 1.7 mg/ml) inhibited with 10 mM MgF_x and 2 mM AMP-PCP was imaged at 92,000 X magnification with a nominal pixel size of 1.55

Å. A total of 1404 movies were collected and imported into CryoSPARC for evaluation.

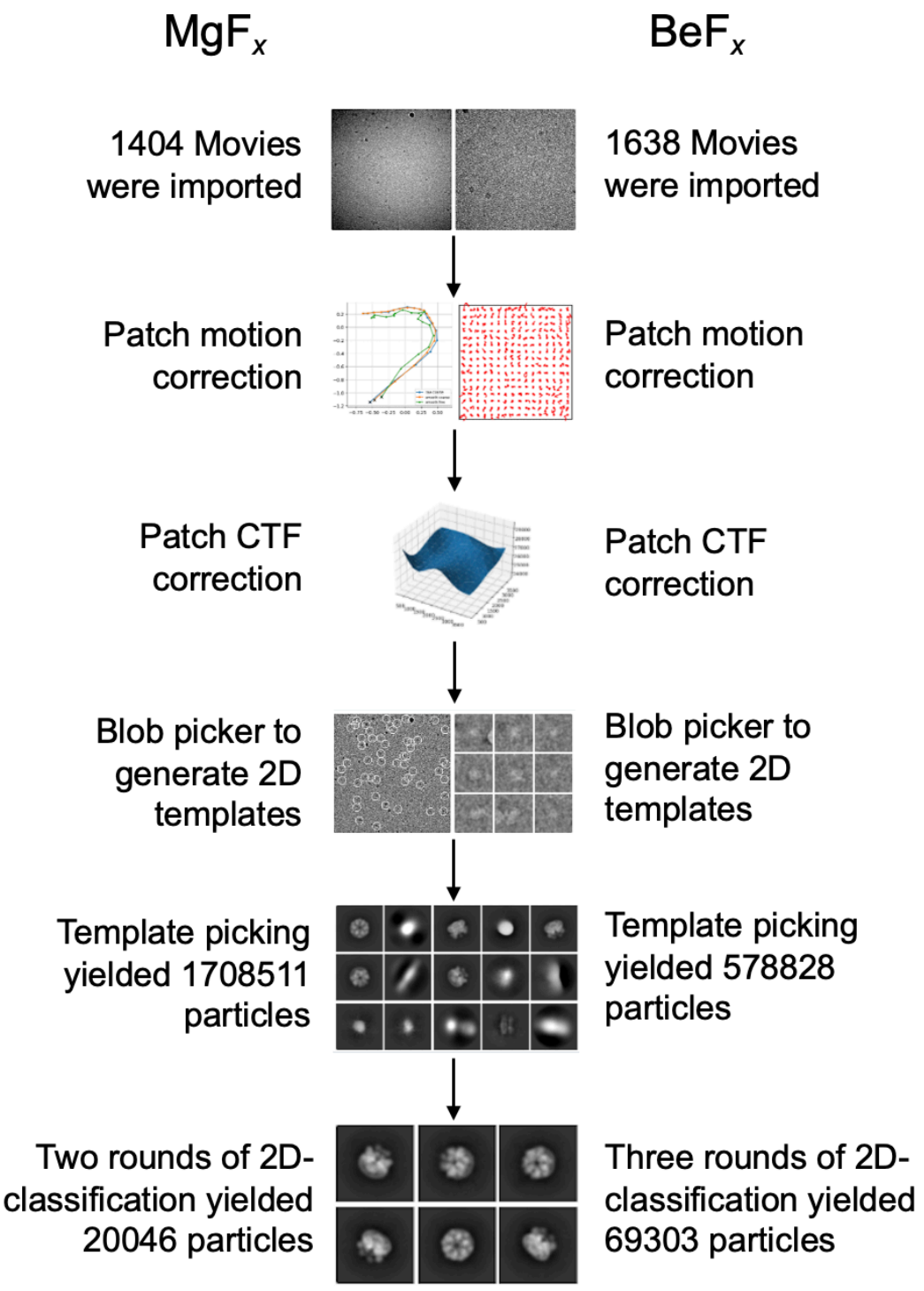

Figure 5.4: Workflow of movie correction and 2D-processing of the MgF_x (left) and BeF_x (right) inhibited Pma1-GA sample. *Images were taken from the CryoSPARC interface.*

The overall workflow for 2D classification is shown in Figure 5.4. The movies were patch motion corrected and patch CTF corrected to produce 1404 micrographs. Representative micrographs at low and high defocus are shown in Figure 5.5A. The ice thickness was consistent across the grid holes, apparent by an equal distribution of particles across without particular clustering near the edge or the centre. Moreover, the thickness was also sufficient to contain Pma1 particles but was not so thick that it added background noise to the data. The particle density was sufficient for picking with a good number of particles available per hole and limited overlapping. If repeated, the protein concentration could be increased slightly to obtain more particles per hole. On the basis of CTF alignment resolution calculated by CryoSPARC, 157 micrographs were removed to produce a curated set of 1247 for picking. Templates for picking generated by CryoSPARC blob picker showed a good distribution of particles from various angles, seen as a doughnut-like density for the top view, a circular density for the bottom view, and an E-shaped density for side views. A significant number of junk classes also formed. Based on 10 selected templates covering a range of angles of Pma1, a total of 1,708,511 particles were picked by template picking. The initial 2D-classification of 100 classes shows a good variety of angles of Pma1, as well as several junk classes (Figure 5.5B). Through two rounds of 2D classification, 50 classes were generated. Of these 50, 25 classes, containing 20,046 particles, were selected for 3D-classification based on angle distributions, with examples shown in Figure 5.5C. Within the 2D classes, it is possible to distinguish the soluble domains and helices within the micelle, suggesting the data is of good quality.

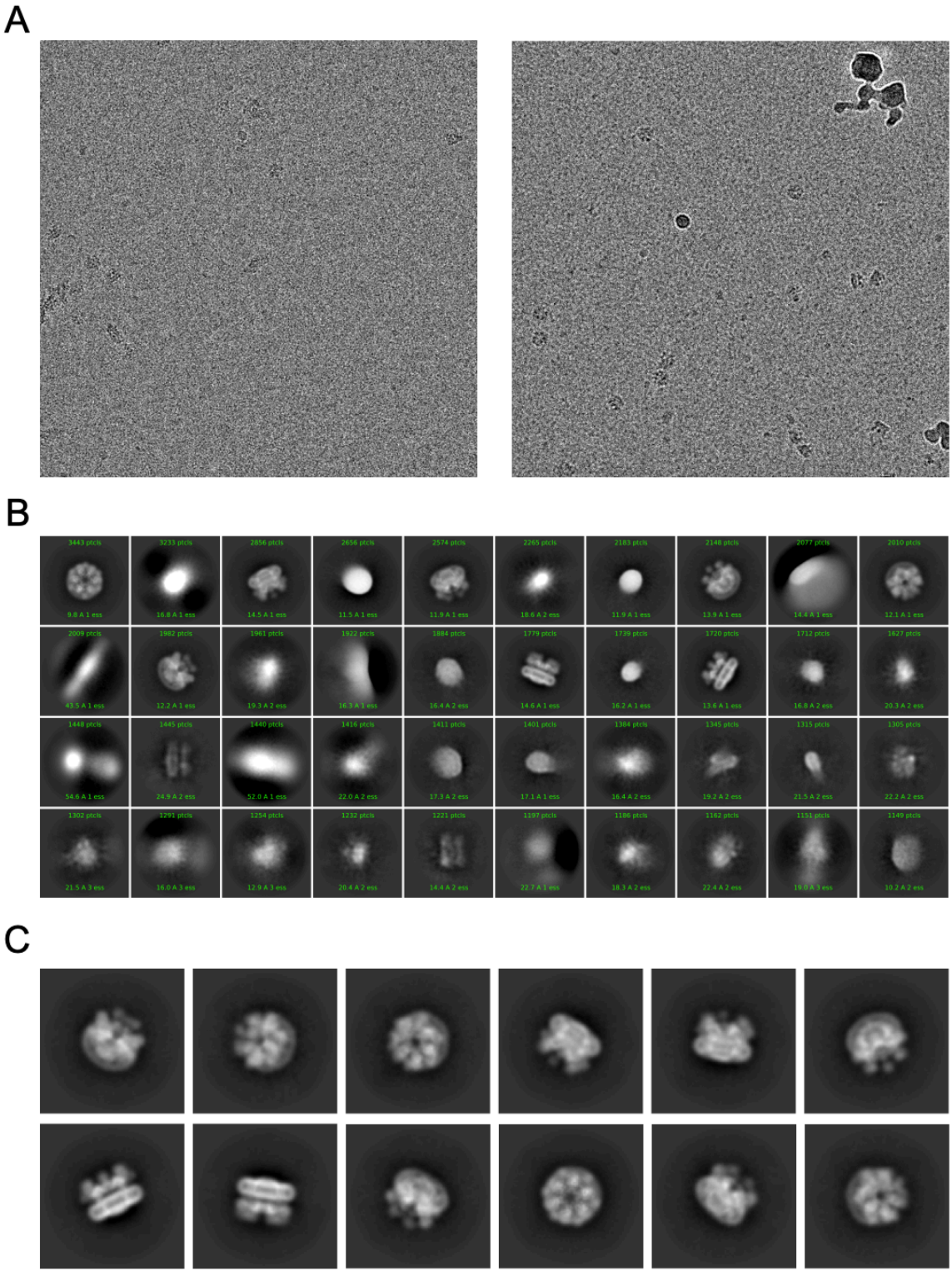

Figure 5.5: Micrographs and 2D class averages of Pma1-GA MgF_x. *A) Low (left) and high (right) defocus examples of motion and patch CTF corrected micrographs. B) Initial 2D-class averages after picking, showing the first 40 of 100 classes. C) Final 2D-class averages that were selected for 3D-classification.*

The process of 3D-classification is presented in Figure 5.6A. *Ab initio* classification of two classes created a clear Pma1-like map, and one junk map. Decent particles could still be found in the junk class, so the complete set was taken forward to heterogeneous refinement. Of the 2213 particles in the *ab initio* junk class, 1342 particles were used to improve the Pma1 map. Inspection of the data did not provide any obvious variations in the dataset. *Ab initio* classification into three classes formed two junk classes, hence no obvious alternate confirmations were found. The processing was not tested further to separate out various possible confirmations, as for example was done by Hofmann *et al.* for the ABC transporter (Hofmann et al., 2019). Finally, the Pma1 class was refined using non-uniform refinement with either C1 or C6-imposed symmetry. The purpose of the imposed symmetry is to define existing symmetry in the sample to therefore obtain six times more data for each particle. One downside to imposing symmetry is that this averages across all monomers in the hexamer and removes monomer-specific variations that may exist due to factors such as cooperativity. Non-uniform refinement with C1 symmetry produced a 6.62 Å resolution map as calculated by GSFSC after auto-tightening. The C6 refinement produced a significantly improved 4.62 Å resolution map, illustrating the benefit of using the symmetry-imposed refinement (Figure 5.6A). The overall improvement in resolution across the map is illustrated in Figures 5.7A and C. In the C1 map, the resolution varies across the monomers and is particularly visible in the N- and A-domain. This is a likely result of the alignment process, with the most stable monomer as the basis for alignment. Variation in the stability throughout the monomer could be due to partial inhibition of some of the monomers in the structure or cooperativity. Alignment of the two models in Figure 5.6B shows particular improvement in the density of the N- and A-

soluble domains of Pma1 when C6 symmetry is imposed, suggesting that these are most mobile, a feature also recorded for the initial high-resolution structure of

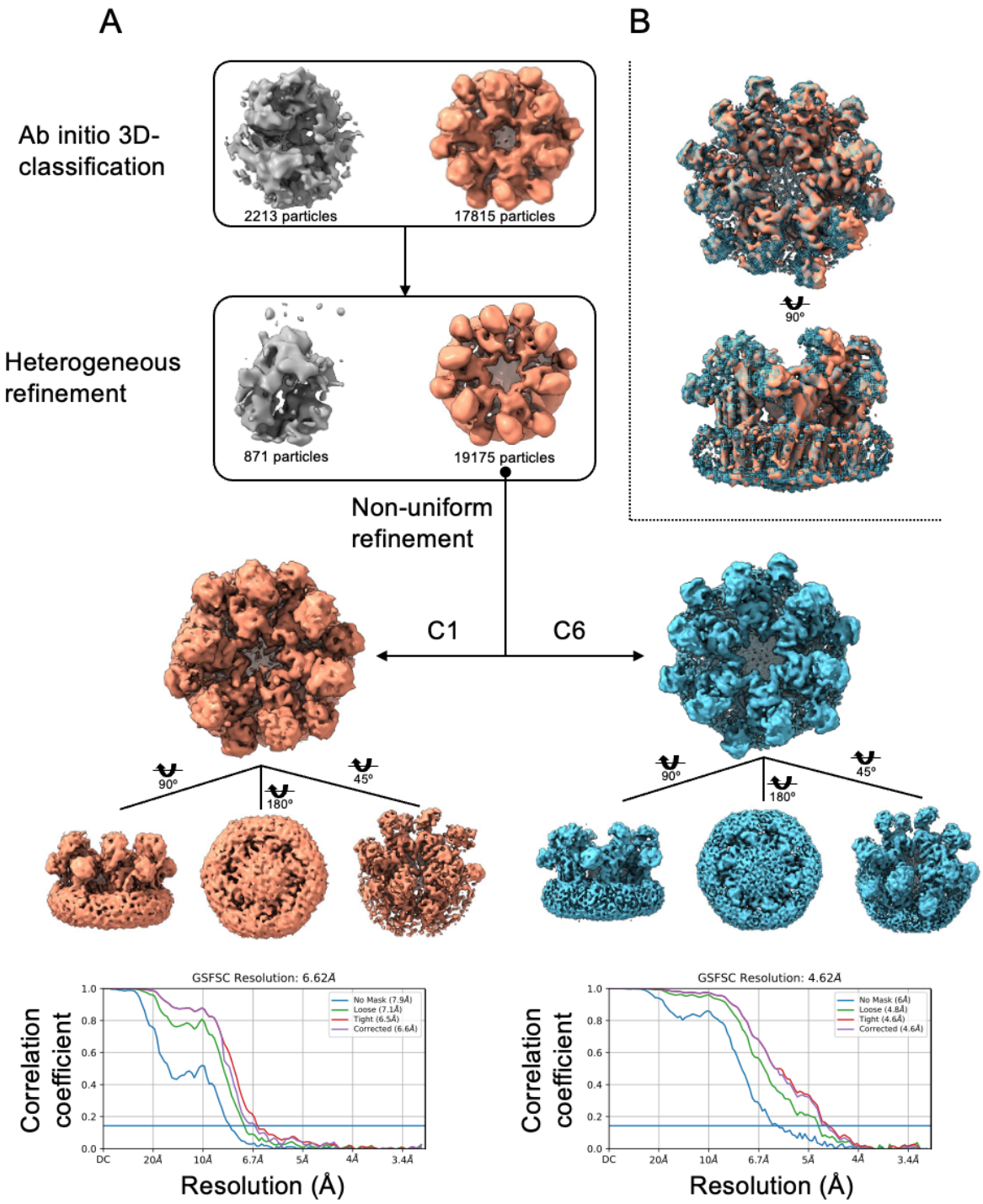

Figure 5.6: Processing of the MgF_x-inhibited Pma1-GA. *A) Workflow for 3D-classification by cryoSPARC. B) Overlay of the C1 map (salmon solid volume) against the C6 map (blue wiremesh volume) showing the top and side view.*

*Nc*Pma1 (Heit et al., 2021). The resolution improvement is corroborated by the GSFSC curves of the two maps, with enhancement in the correlation value in the 6.7-20 Å range (the range in which we expect to see the details of domains and secondary structure). The particle angles are fairly well distributed and there are no missing angles (Figure 5.7B and D). There is however a slight over-representation of top and bottom views, which, at high-resolution, may cause anisotropic effects. Now that this is noted, potential anisotropy can be accounted for.

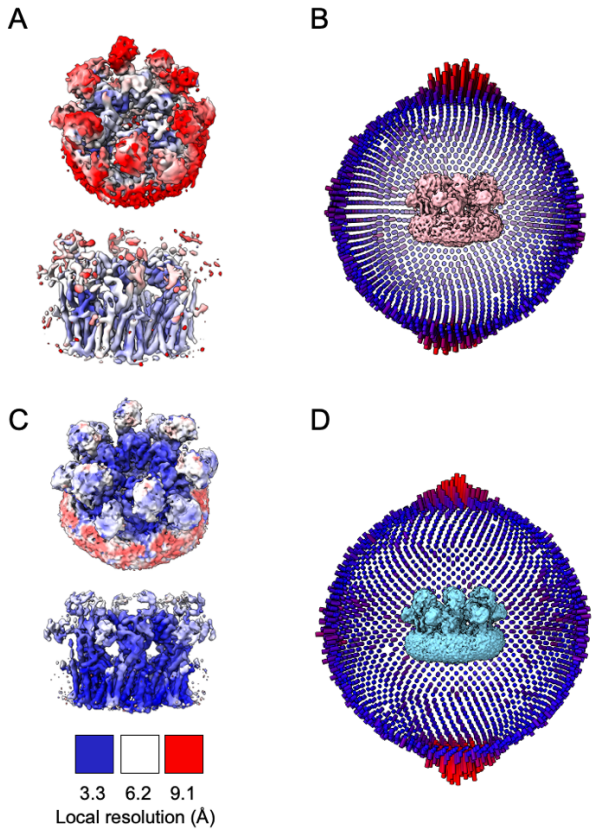

Figure 5.7: Quality overview of the C1- and C6-refined maps of MgF_x-inhibited Pma1-GA. (A and C) Local resolution estimation of the Fourier densities for the C1-refined (A) and C6-refined (C) maps, as estimated by CryoSPARC. (B and D) Angular assignment for the C1-refined (B) and C6-refined (D) map. The height of individual cylinder bars is proportional to the number of particles in each view. The most frequent views are coloured in red.

In the alignment of C1 vs C6 (Figure 5.6B), four of six soluble domains align well, however, two of the soluble domains seem to be shifted outwards compared to the rest for the C1 structure. The overall 4.6 Å resolution of the C6-map from a screening data set (compared to 3.21 Å obtained in the published structure) suggests that these conditions are suited for taking forward for full data collection.

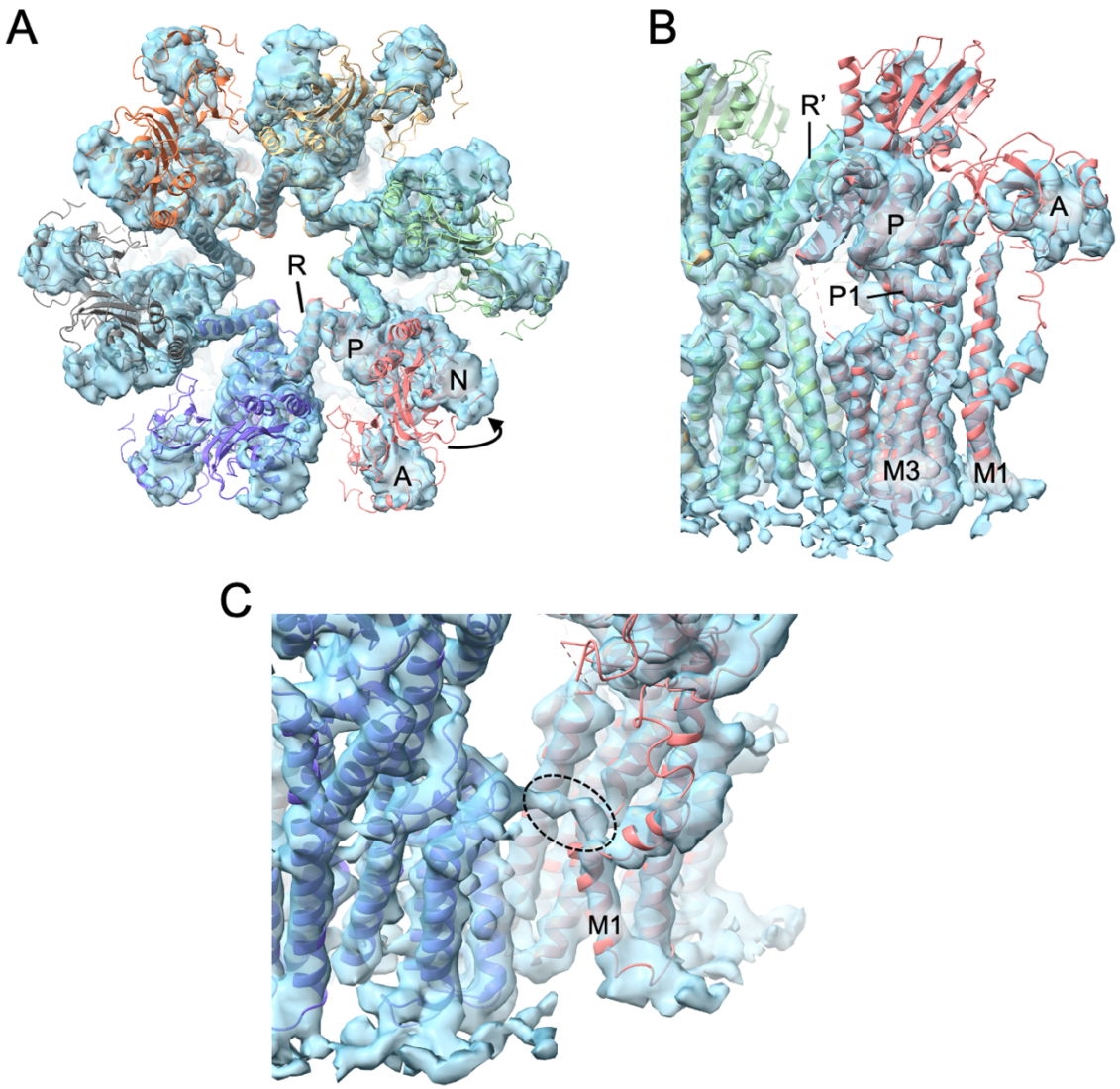

Figure 5.8: Analysis of the C6-refined map of MgF_x-inhibited Pma1-GA compared to the Pma1 E1-inhibted structure, aligned by ChimeraX*. A) Top view of the alignment. Domain positions are labelled on the red monomer, and the arrow illustrating the observed shift in the N-domain. B) Zoom-in side view of the alignment showing the overall fit. C) Zoom-in view of the interface between monomers with putative lipid density highlighted. PDB used: 7NY1.*

Inhibition with MgF_x at pH 7 is expected to inhibit Pma1-GA in an E2-P_i state. Close inspection of the C6-map however suggests that the protein behaves more like the E1-inhibited state solved by the Bublitz lab (Heit et al., 2021). Aligning the

E1 ADP inhibited *Nc*Pma1 structure to the map has an overall good fit in the TM region and shows that the soluble domain adopts an E1-like confirmation (Figure 5.8A and B). However, closer inspection highlights a critical difference. Firstly, whilst the A-domain matches the density well, the N-domain of the map is further outwards (Figure 5.8A). Moreover, whilst the sample is expected to be in an activated state, the R-domain appears to still be attached to the P-domain. Analysis of the density at the interface between monomers reveals additional density just above the M1-helix (Figure 5.8C). Even at low contour levels, the density is observed and the local resolution map suggests it is resolved to around 4 Å. The location of the density is in Site I defined in Chapter 3 and is possibly a co-purified lipid.

Altogether, the data suggest that a quasi-state has been captured. Since functional data presented in Figure 5.3 suggests MgF_x is the weakest inhibitor tested, Pma1-GA should be incubated with a higher MgF_x concentration and a higher pH to push the protein further into an E2-P_i state.

5.5.2 CryoEM screening of BeF_x-inhibited Pma1-Ga

Pma1-GA (at 1.7 mg/ml) inhibited with 10 mM BeF_x and 2 mM AMP-PCP was imaged at 92,000 X magnification with a nominal pixel size of 1.55 Å. Much of the 2D- and 3D-processing was the same as for the MgF_x data and therefore only variations are described. A total of 1638 movies were collected and imported into CryoSPARC for evaluation. The estimated CTF resolutions were not as high as for MgF_x, limiting the possible resolution of subsequent maps. The overall workflow for 2D-classification is shown in Figure 5.4. Representative micrographs at low and high defocus are shown in Figure 5.9A, presenting good particle density and distribution. The particles at both high and low defocus appeared better defined

compared to the MgF_x data. Template picking yielded 578,828 particles. Three rounds of 2D-classification were run to obtain 50 classes. Of the 50, 25 classes, containing 69,303 particles, were selected for 3D-classification, with examples shown in Figure 5.9C.

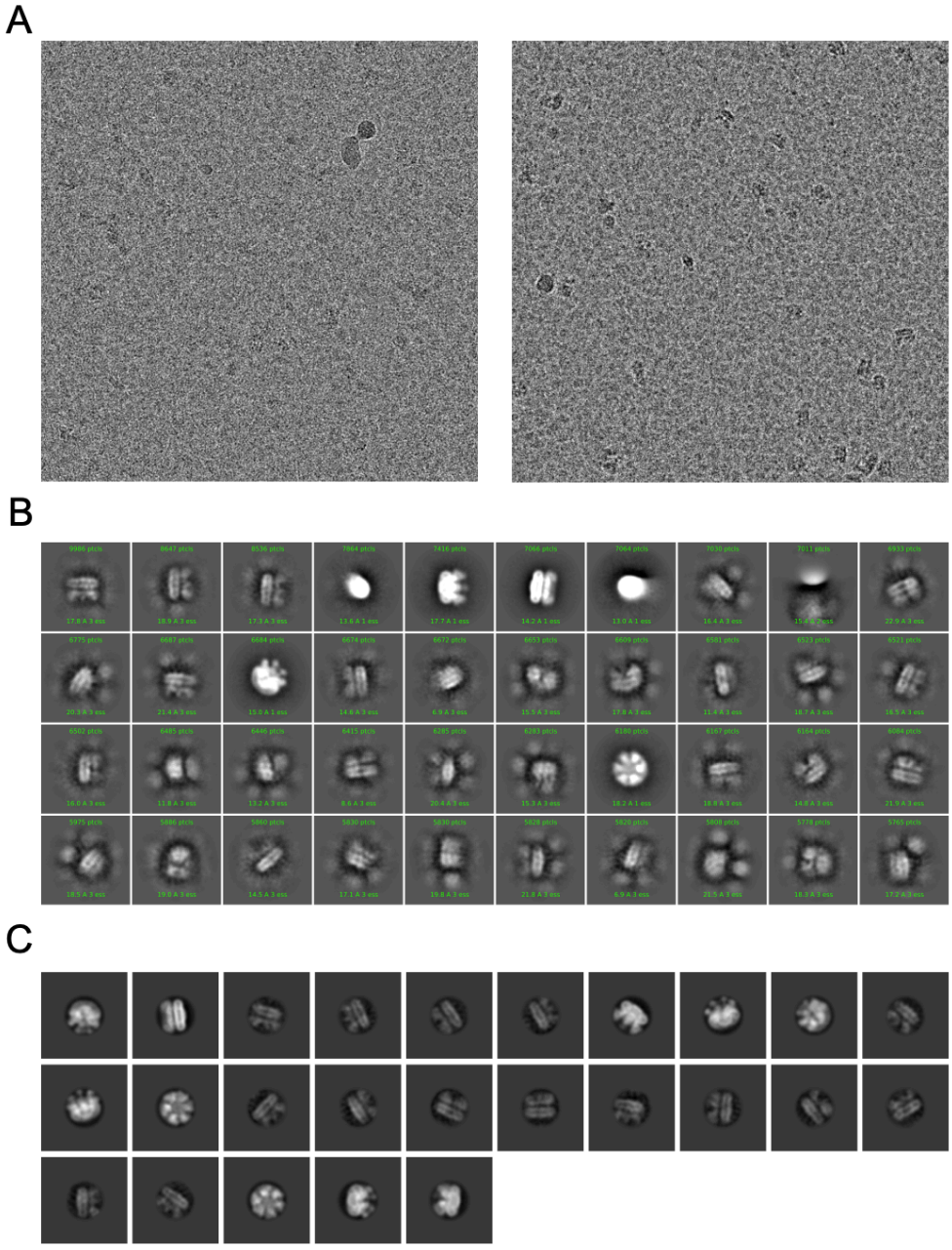

Figure 5.9: **Micrographs and 2D class averages of Pma1-GA *BeF$_x$*.** *A) Low (left) and high (right) decofus examples of motion and patch CTF corrected micrographs. B) Initial 2D-class averages after picking, showing the first 40 of 100 classes. C) Final 2D-class averages that went on to 3D-classification.*

The 3D-classification workflow is presented in Figure 5.10A. *Ab initio* classification of two classes created a clear Pma1 class and one junk class. Around 50% of the particles were classed into the junk pile, significantly higher than for MgF_x.

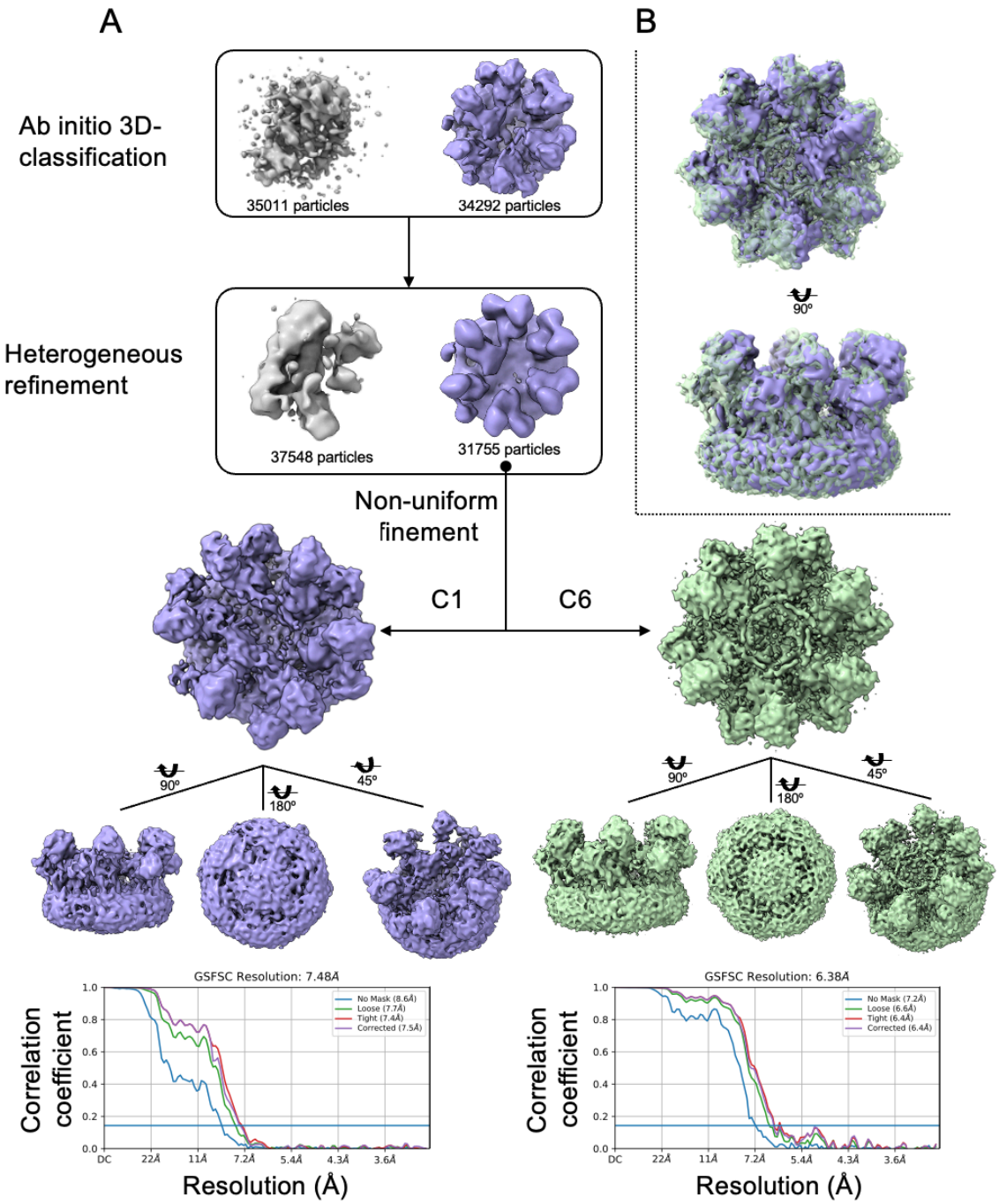

Figure 5.10: Processing of the BeF_x-inhibited Pma1-GA map. *A) Workflow for 3D-classification by cryoSPARC. B) Overlay of the C1 map (purple volume) against the C6 map (green volume) showing the top and side view.*

The particles from the junk class were used to repeat *ab initio* classification, followed by heterogeneous refinement. One of the resulting maps resembled Pma1 at very low resolution, but further processing did not yield better maps. The Pma1 class was improved by heterogeneous refinement, which removed 2537 particles from the *ab initio* Pma1 class. The C1 map was refined to 7.48 Å as calculated by GSFSC after auto-tightening. In comparison, the C6 refinement produced a significantly improved 6.38 Å resolution map (Figure 5.10A). Overall, the resolution of the map is lower than that of the MgF_x map.

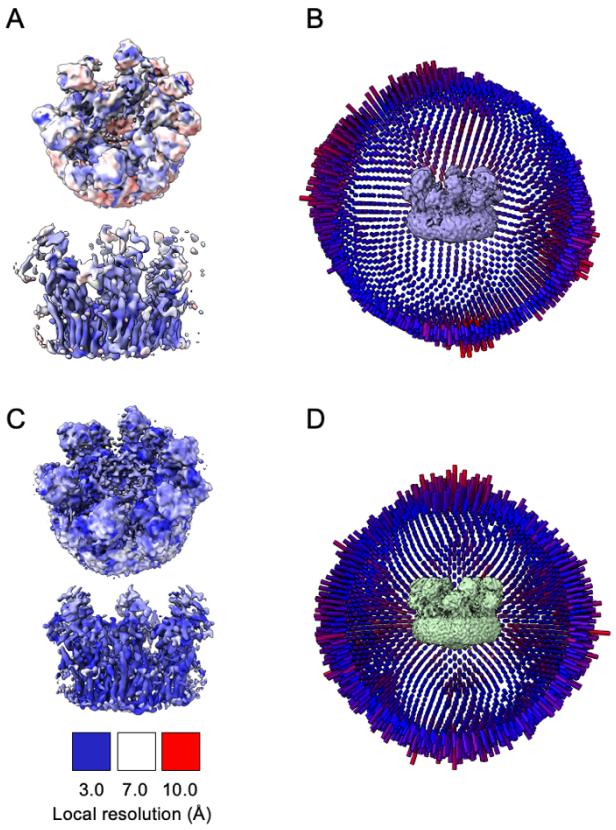

Figure 5.11: Quality overview of the C1- and C6-refined maps of BeF_x-inhibited Pma1-GA. (A and C) Local resolution estimation of the Fourier densities for the C1-refined (A) and C6-refined (C) maps, as estimated by CryoSPARC. (B and D) Angular assignment for the C1-refined (B) and C6-refined (D) map. The height of individual cylinder bars is proportional to the number of particles in each view. The most frequent views are coloured in red.

Again in the C1 map, the density quality varies per monomer (Figure 5.11A). Since this is observed for both of the inhibited maps, it is possible that this occurs due to potential cooperativity, which Zhao *et al.* propose (P. Zhao et al., 2021). The alignment of the C6-model to the C1 model shows again that the process significantly improves the quality of the map across all monomers, in particular for

the N- and A-domain (Figure 5.10B and 5.11A and C). This improvement can again be seen in the GSFSC curves as well, with an improvement in resolution in the 7.2-22 Å range. Interestingly, whilst the MgF_x map refines to higher resolution, the particles that make up the BeF_x map display a greater angular distribution (Figure 5.11B and D). The overall quality of the data suggests the conditions are suitable to go forward for data collection on a high-resolution electron microscope.

Inhibition of Pma1-GA with BeF_x is expected to arrest the protein in an E2P state. Zhao *et al*, previously published the structure of *Saccharomyces cerevisiae* Pma1 with BeF_x at pH 6 (P. Zhao et al., 2021). Firstly, Zhao *et al* indicate to have activated the protein by dropping the pH to 6, where it is expected to stabilise more of an E1-like state. They report that the R-domain becomes released by pH-induction and therefore they state there is no discernible density for it. For analysis of our C6-map, it was aligned to the available structure (PDB 7VH6). Firstly, the overall alignment against the map is strong (Figure 5.12 A and E). The helices align well to the tubular densities and the P-, N- and A-domain all align well too. Potentially, a slight rotation of the A-domain in the map is noted compared to the structure (Figure 5.12A). Whilst the *Sc*Pma1 E2P has no density and no built structure for the R-domain, this map contains novel density at the core of the protein where the R-domain is expected. It however appears to be in a disengaged state, suggesting that the Pma1-GA purified protein, in fact, has an untethered R-domain (Figure 5.12A and B). Moreover, the *Nc*Pma1 E1-inhibited structure only resolved part of the R-domain. The *Sc*Pma1 structure resolved more, including a short horizontal α-helix that is also visible in the C6-map (Figure 5.12C). Regarding the *Sc*Pma1 E2P structure, it might be activated non-physiologically through pH and therefore this map would therefore provide a novel state and further the

understanding of the function of the R-domain. Like the MgF_x map, the additional density found at lipid binding site I at the interface between monomers is also seen in the BeF_x map (Figure 5.12D). Finally, density for the linker between M1 and the A-domain was found, which was not seen in any of the published Pma1 structures (Figure 5.12E).

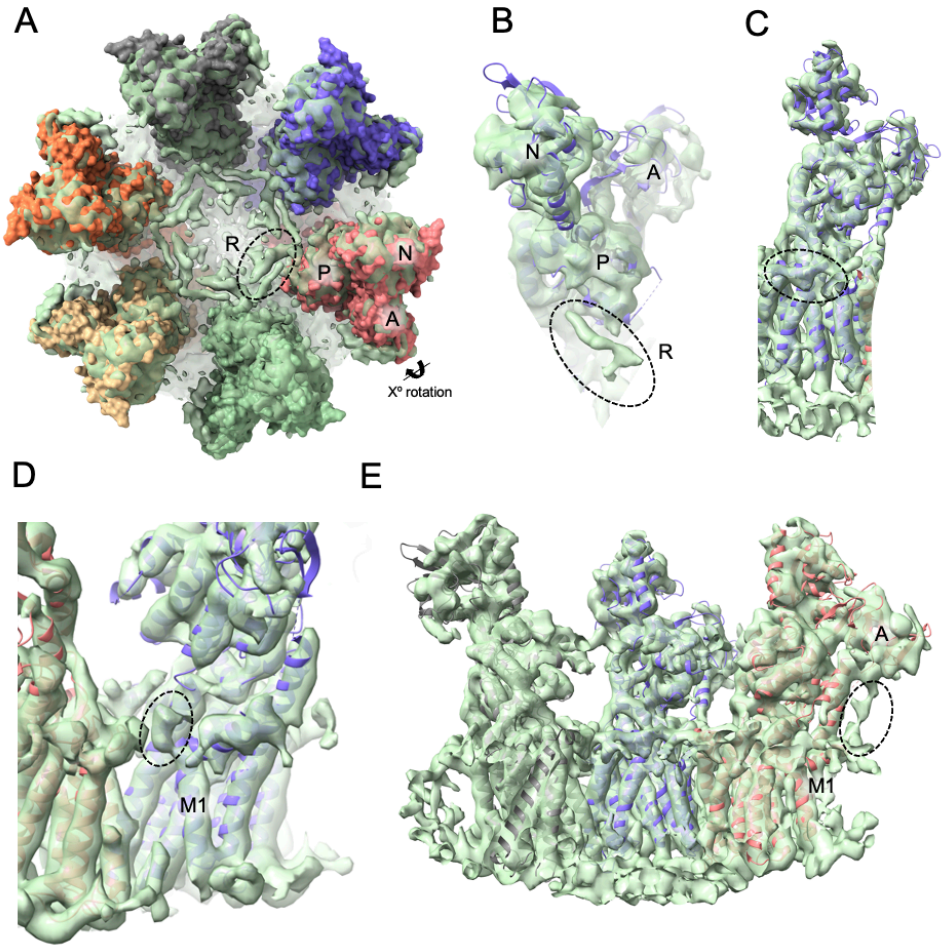

Figure 5.12: Analysis of the C6-refined map of BeF_x-inhibited Pma1-GA compared to the ScPma1 E2 BeF_x structure, aligned by ChimeraX. *A) Top view of the alignment. Domain positions are labelled on the red monomer. The putative R-domain is circled. B) Zoom-in of a single monomer to highlight the putative R-domain C) Zoom-in on a monomer with circle highlighting additional helix-density not previously seen in the NcPma1 ADP-AlF_4^- structure. D) Zoom-in view of the interface between monomers with putative lipid density highlighted. E) Middle view of the overall alignment of the structure to the map. Circle highlights possible M1-A-domain linker density*

5.6 Chapter 5 discussion

Functional studies of glucose-activated Pma1 inhibited by a series of metal fluorides and a tetrahydrocarbazole provided initial inhibitory data to inform structural studies by cryoEM. The calculated IC_{50} for AlF_x-inhibition at pH 7 is significantly lower than for BeF_x and MgF_x, which does not match the findings reported for *Sc*Pma1, where the values fall within the same range (J. T. Pedersen et al., 2015). AlF_x is capable of inhibiting both an E1 state (with ADP) and an E2 state. During the Baginski assay, as the reaction progresses, ADP is released and therefore the alternative complex could form. Inhibition with ADP-AlF_x (capturing the E1 phosphoryl transfer state) may be stronger than with AlF_x alone leading to the ADP-AlF_x complex comprising the majority of Pma1. Additionally, in case Pma1 exhibits cooperativity, AlF_x and ADP-AlF_x could inhibit monomers within the same hexamer in a potentially sterically favourable manner. In other words, the same hexamer would contain both E1 and E2 inhibited states that cooperatively could further lower the measured IC_{50}. Regardless of this result, the E2 state captured by AlF_x can still be resolved by cryoEM by excluding ADP from the inhibition mixture. Since the conditions used for BeF_x cryoEM screening were suitable and the IC_{50} value measured for AlF_x is almost 20-fold stronger when compared to BeF_x, the same cryoEM conditions should be used for AlF_x.

The metal fluoride inhibitors caused almost full inhibition of Pma1-GA, as measured by the Baginski assay, suggesting indirectly that the sample had been successfully glucose-activated by phosphorylation of the R-domain. BeF_x, as well as AlF_x, inhibit to 0% of positive control activity, which is lower than Pedersen *et al*. report for activated *Sc*Pma1. MgF_x on the other hand only inhibited to ~10% of positive control activity, which matches the cryoEM screening data that suggests

Pma1-GA might not be fully inhibited in the expected E2-P_i state. To further investigate this, samples of non-activated *Nc*Pma1 should in future be purified to use as control and further research the role of the R-domain in autoinhibition. Pedersen *et al*. report that the metal fluorides are able to inhibit basal (autoinhibited) *Sc*Pma1, however only to a lesser extent. To truly corroborate that a phosphorylated Pma1-GA has been purified, the sample should be tested for phosphorylation. Firstly, one would expect that by high-resolution cryoEM, the phosphates are visible on the R-domain. However, that depends on the R-domains adopting a rigid, regular structure. In the case that their release from the protein causes instability or increased flexibility, as previously reported (P. Zhao et al., 2021), the phosphates would not be resolvable. Mass spectrometry methods have been developed to assess phosphorylation and should be straightforward using a sample separated by SDS-PAGE (Breitkopf & Asara, 2012).

The screened samples demonstrated that they were of good quality, displaying sufficient concentration on the grids and established the conditions are right to use for high resolution data acquisition. Whilst the overall resolution obtained for the BeF_x-inhibited sample was lower than for MgF_x, the overall map closely matched the *Sc*Pma1 BeF_x structure solved at pH 6. Due to the unexpected E1-like fold the MgF_x map displays, the concentration of MgF_x and the pH might need to be increased to obtain the true E2-P_i structure. An interesting observation for the E1-like state inhibited by MgF_x is that the N-domain was disengaged from the P-A domain body, whilst the R-domain seemed to be engaged in an autoinhibited like conformation. This poses the question whether, if the protein is indeed autoinhibited, whether the flexibility displayed by the N-domain means that Pma1

can in fact cycle through its catalytic cycle, albeit at a much lower, "autoinhibited" rate.

The UltrAuFoil grids used for the first time on a Pma1 sample worked well. The particles showed a good range of angle orientations, were well distributed across the holes and the ice-thickness across grid squares was good. These grids therefore should be used in future cryoEM studies of Pma1.

Strikingly, additional density was found at the site corresponding to lipid-binding Site I identified by MD in Chapter 3. A ~3-fold increase of PS has been reported for *S. cerevisiae* grown on glucose compared to glycerol (Klose et al., 2012). Since the sample was obtained from glucose-activated cells that might have increased PS production, there is certainly a likelihood that this density might shed light on the lipid binding at Site I and could explain why no density was observed in the published structure from glucose-starved cells. Similarly, growth in glucose reportedly caused a 3-fold increase of CIP, as well. As Chapter 3 illustrated significant accumulation of PICE in the core, this could potentially be resolved in the *Nc*Pma1 structure as was found in the *Sc*Pma1 structure.

Future experiments of this Pma1-GA sample should aim to obtain full high-resolution data sets on a high-end electron microscope. Moreover, inhibitor data for both AlF_x and the tetrahydrocarbazole compound 7 were compelling and should be screened in the same way as for the MgF_x and BeF_x samples presented here. Resolving the structure of Pma1 bound to compound 7 will be of particular interest as docking studies presented by Heit *et al.* suggest a different binding site compared to the published structure with SERCA (Bublitz et al., 2018; Heit et al., 2021). The structure will also confirm or reject this finding. Further experimentation could also make use of cryoEM's ability to resolve multiple states from a single grid by

capturing Pma1 under turnover conditions. This could then be correlated with the metal fluoride inhibited states, however it is likely that varying maps from turnover conditions will be poorer quality compared to an inhibited sample and might therefore require following up with mutations to capture at a higher resolution.

Chapter 6: Establishing a recombinant expression system for *Neurospora crassa* Pma1

6.1 Chapter 6 Introduction

The previous three chapters investigated both the structure and function of *N. crassa* Pma1 through MD simulations, native source purification, inhibitor assays and cryoEM. Whilst the work presented here has advanced the understanding of the protein, to investigate Pma1 structure and function further, a recombinant expression system that will allow expression and purification of functionally relevant mutations and truncations must be established. This system would allow us to investigate mutations such as the conserved arginine residues in the A-domain, known mutations that impact function and truncations of the N- and C- terminal extensions, to develop both our structural and functional understanding of these.

Previous work in the Bublitz lab conducted by Dr. Focht focused on establishing a recombinant Pma1 expression system. A series of constructs of *N. crassa* Pma1 were designed in the pEMBLyex4 expression vector for expression in *S. cerevisiae.* The pEMBLyex4 vector contains a defective LEU2d gene that can increase the plasmid copy levels from 20 to 80-100 per cell and expression levels by as much as 5.7-fold (Erhart & Hollenberg, 1983; Parker & Newstead, 2014). Previous trials conducted in the lab concluded that C- and N-terminal His-tagged Pma1 did express recombinantly, but did not purify well. Therefore, seven constructs were designed using a single STREPII-tag at the N-terminus or inserted in the extracellular loops that connect transmembrane helices (Table 6.1). Three constructs contained truncations of the C-terminal and/or N-terminal regulatory extensions. When I started this work, four of the seven constructs had been

produced (*Nc*Pma1-1, -3, -5, and -6). Initial expression tests of these four constructs found that the loop-STREPII constructs gave the best levels of recombinant expression. This chapter details the results from expressing and purifying *Nc*Pma1-6 and synthesising and expressing construct *Nc*Pma1-7.

Table 6.1: Full list of constructs for expression of *N. crassa* Pma1 in *S. cerevisiae*

Construct name	*Pma1 sequence length*	*STREPII location*	*Previously synthesised*
NcPma1-1	Full length	N-terminus	Yes
NcPma1-2	ΔN37	N-terminus	No
NcPma1-3	ΔC34	N-terminus	Yes
NcPma1-4	ΔN37 ΔC34	N-terminus	No
NcPma1-5	Full length	TM loop 3-4 (pos. 315)	Yes
NcPma1-6	Full length	TM loop 7-8 (pos. 784)	Yes
NcPma1-7	Full length	TM loop 9-10 (pos. 850)	No

6.2 Small scale expression of *Nc*Pma1-6

Small scale expression of *Nc*Pma1-6 was set up to assess induction with lactate vs. galactose and to identify the ideal expression window for optimising yield vs. degradation. *S. cerevisiae* Gal4Δpep4 cells (peptidase 4 deletion and low constitutive expression of the GAL4p transactivation factor) were transformed with the *Nc*Pma1-6 expression plasmid and selected for growth in –Ura and –Leu media. Expression of the construct was induced with lactate or galactose at t_0 and samples were collected after 8 hours (t_1) and every four hours thereafter (t_2-t_5) (Figure 6.1). The gel of lactate-induced samples shows no increased intensity for a band at the expected 100kDa molecular weight in either the membrane or debris fraction. The western blot detects STREPII-tagged peptides at apparent degradation bands in both the membrane and debris fraction.

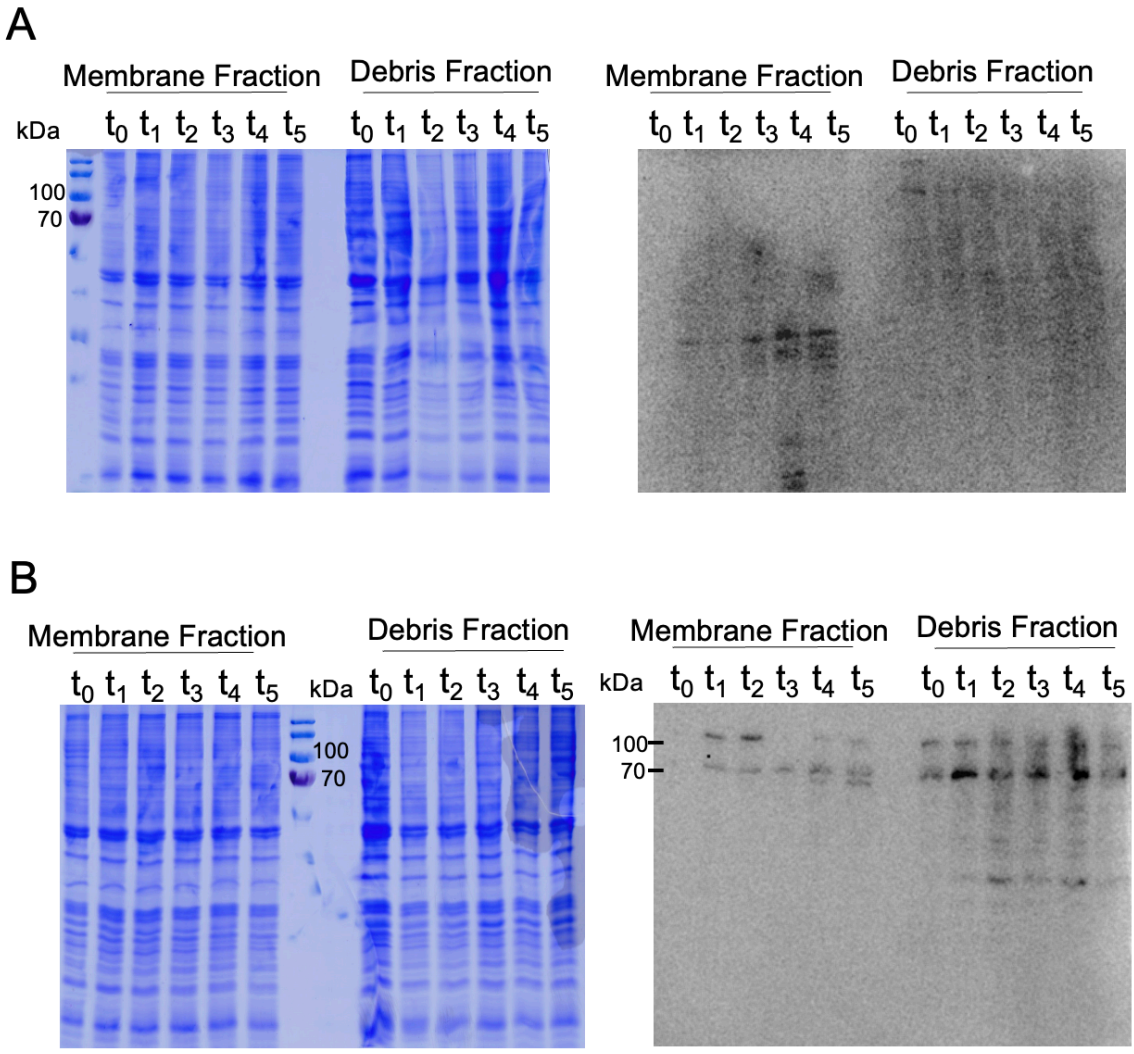

Figure 6.1: Small scale expression of NcPma1-6 in S. cerevisiae Gal4Δpep4. *Analysis of lactate-induced expression (A) and galactose-induced expression (B) of NcPma1-6 analysed by SDS-PAGE (left) and anti-STREPII Western blot (right). Cell samples were processed to separate the membrane fraction from a debris fraction. Timepoints refer to the following; t_0:0 hours, t_1: 8 hours, t_2: 12 hours, t_3: 16 hours, t_4: 20 hours, t_5: 24 hours.*

Limited yet successful expression of full-length *Nc*Pma1-6 was found in galactose-induced cells after 12 hours (Figure 6.1B). Whilst the western blot shows optimal expression of full-length *Nc*Pma1-6 in the membrane fraction after 12 hours, no gel-band intensity change can be seen between t_0 and t_2, therefore the expression of *Nc*Pma1-6 is low. Low expression levels and instability are further

confirmed when compared to the intensity of western blot bands in the debris fractions. Nonetheless, large-scale expression of *Nc*Pma1-6 was tested using galactose induction and a 12-hour expression period.

6.3 Large-scale expression and purification of *Nc*Pma1-6

Having established the optimal expression window for *Nc*Pma1-6, 6L cultures of *S. cerevisiae* were grown, and membranes were harvested according to an established protocol. The protocol includes a slow spin to remove heavy membranes/debris and fast spins for several wash steps of the harvested membranes containing *Nc*Pma1-6. Samples were analysed by SDS-PAGE and Western blot (Figure 6.2A). The final membrane sample contains a Strep-tagged protein at ~100 kDa, corresponding to the Pma1 monomer. The gel stained inconsistently across the gel as the light membrane fraction does not show much band intensity in the 70+ kDa molecular weight range. However, the final membrane sample stained well and the Western blot shows a clear band for Pma1.

A solubilisation screen shows that LPC16 solubilised Pma1 best (Figure 6.2B). There was no difference in solubilisation efficiency between 1% and 1.5% LPC16. The SDS positive control and Foscholine-16 also solubilised *Nc*Pma1-6. Interestingly, DDM solubilised membrane proteins less efficiently than LPC16 and did not solubilise any *Nc*Pma1-6. This could mean that NcPma1-6 is embedded in the *S. cerevisiae* membrane with different lipids compared to NcPma1 in *N.* crassa, which does solubilise with DDM.

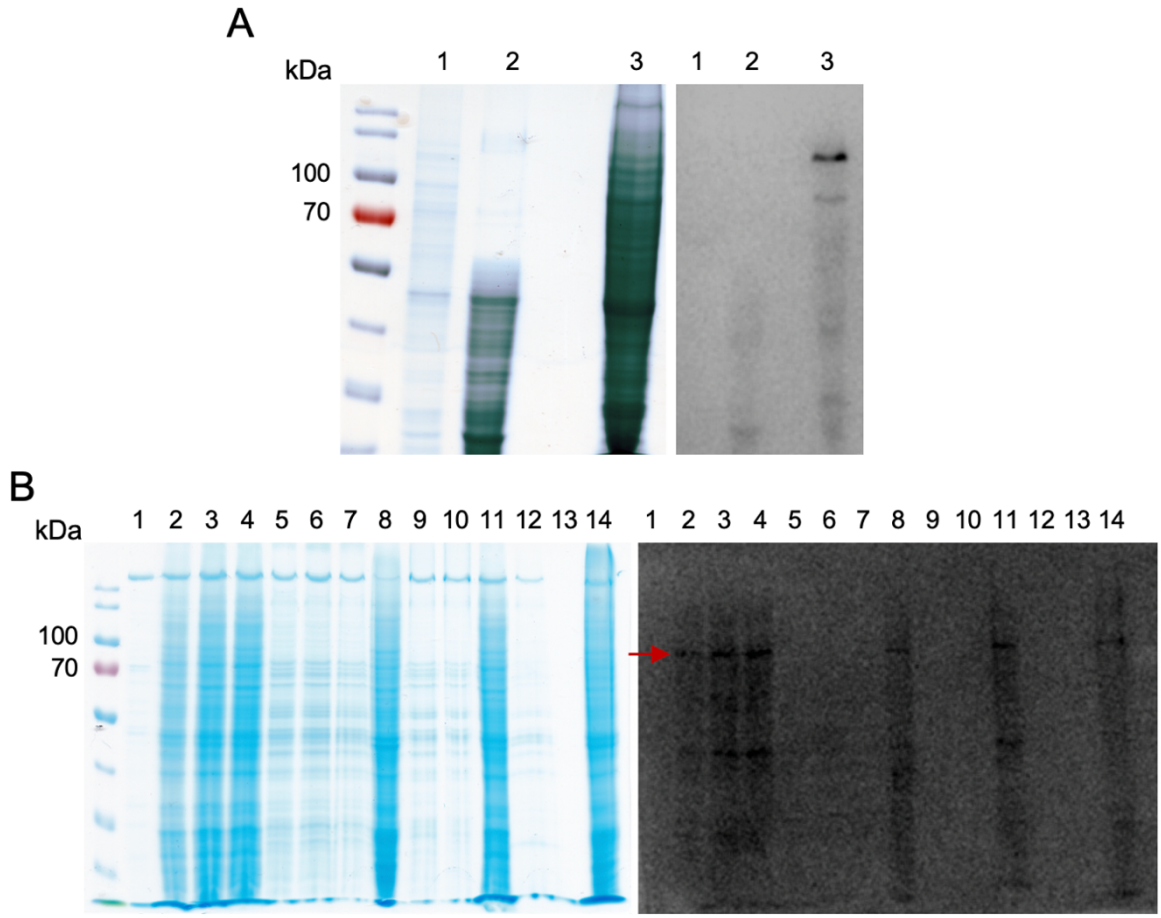

Figure 6.2: Large-scale expression and purification of NcPma1-6 in S. cerevisiae Gal4ΔPep4. *A) SDS-PAGE analysis of the membrane harvest. Sample numbers refer to the following samples, 1: heavy membrane fraction, 2: light membrane fraction, 3: final membrane at 5mg/ml. B) Solubilisation screen of S. cerevisiae membranes. SDS-PAGE gel of samples (left) and anti-STREPII western blot of the gel (right). Red arrow points at the intact monomer band. Sample numbers refer to the following detergent conditions, 1: H_2O negative control, 2: 0.5% Lysofos Choline-16, 3: 1.0% Lysofos Choline-16, 4: 1.5% Lysofos Choline-16, 5: 0.5% DDM, 6: 1.0% DDM, 7: 1.5% DDM, 8: 1% SDS positive control, 9: 1% C12E8, 10: 3% C12E8, 11: 1% FosCholine-16, 12: 3.5% Octylglucoside, 13: Buffer, 14: Untreated membrane sample.*

The protein was purified by STREP-Tactin affinity chromatography. It was eluted using 2.5mM D-desthiobiotin and analysed by SDS-PAGE (Figure 6.3). Washing steps effectively removed contaminants. The second elution pool collected

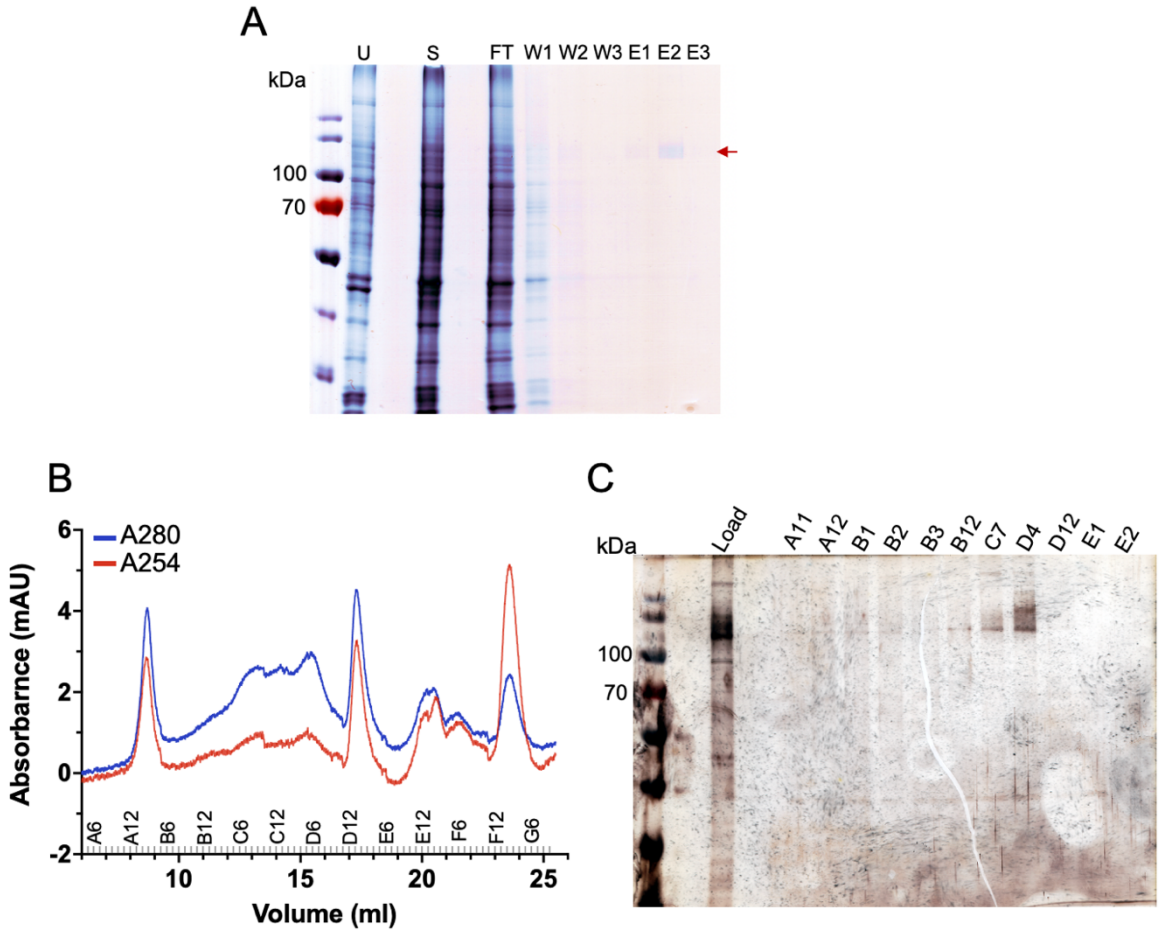

Figure 6.3: Purification of NcPma1-6 by affinity and size exclusion chromatography. *A) Analysis of NcPma1-6 purification on a Strep-Tactin affinity chromatography column. Samples were run on an SDS-PAGE gel. U: Unsolubilised protein, S: solubilised protein, FT: flow through. W1-3: wash fractions 1-3 and E1-3: elution fractions 1-3. B) Size exclusion chromatography chromatogram of the eluate from (A) on a GE Superose 6 10/300 increase column. C) Silver-stained SDS-PAGE analysis of SEC fractions and the load sample.*

(E2) has a faint band at the expected molecular weight of the Pma1 monomer, as shown by the red arrow, although the protein is very dilute. The sample was concentrated for size exclusion chromatography on a Superose 6 10/300 column

(Cytiva). The chromatogram shows a hexamer peak at 13 ml consistent with the SEC profile of native *Nc*Pma1, and another at ~15 ml, which could correspond to a lower order oligomer. Other peaks correspond to the void volume (at 8.5 ml), a potential monomer peak at 17 mL and lipids at 24 ml (as A_{254}>A_{280}). SDS-PAGE shows the protein in both the 13 ml and 17 ml peaks correspond to Pma1 at the expected molecular weight, only detectable by silver staining. The low yield from 6L of culture highlights the need to further optimise the expression of recombinant Pma1. Samples from fraction C5 (corresponding to the 13 ml peak) and D4 (corresponding to the 15 ml peak) were analysed by negative stain EM. A Baginski assay showed no detectable ATPase activity in the SEC fractions of the final pooled sample of fractions B11-D6, indicating the protein is either inactive or too dilute to produce measurable amounts of P_i under the given conditions (results not shown).

6.4 Negative stain electron microscopy of *Nc*Pma1-6

Negative stain EM was used to assess the quality and contents of SEC fractions C5 and D4 (see Figure 6.3 B and C). Figure 6.4 shows two micrographs taken at 49,000X magnification. In the C5 sample, large circular bodies indicate the presence of excess glycerol. No particles stand out as potential Pma1 hexamers. In the D4 sample, however, the bulk of the particles look smaller than in C5 – these could be protein contaminants or monomeric/oligomeric forms of Pma1. Importantly, several particles from the micrographs of fraction D4 were picked that match the expected size and shape of Pma1 (Figure 6.4B). These particles are similar to those from native source Pma1 in Chapter 5. The size of these particles lies between 153 and 167 Å, matching the 165 Å diameter (Figure 6.4C) of the

structure published along with the data from Chapter 1 (Heit et al., 2021). There were not enough particles to generate class averages.

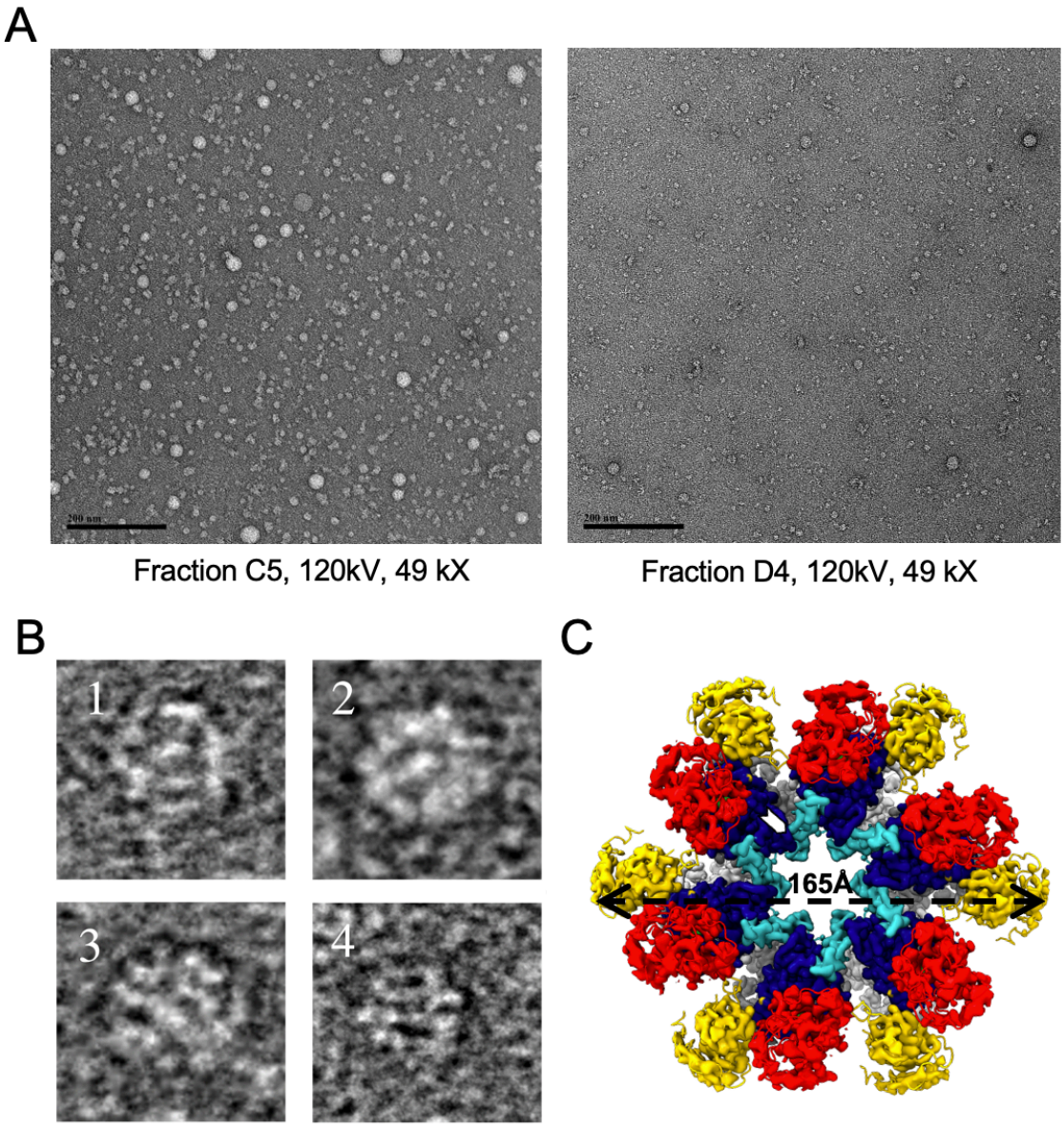

Figure 6.4: Micrographs of NcPma1-6 SEC fractions. *A) Left: sample micrograph of SEC fraction C5 (see Figure 4.3B). Right: Sample micrograph of SEC fraction D4. The size bar represents 200nm. B) Sample particles picked from the D4 micrograph. Particles 1 and 2 show possible top/bottom views of hexameric Pma1 and particles 3 and 4 show possible side views. C) Top view of the overlay of the cryo-EM map and structural model of N. crassa Pma1 from native source illustrating a diameter of 165Å. Figure created by Sabine Heit* (Heit et al., 2021)

Expression and purification of hexameric *Nc*Pma1-6 was successful, albeit in too little yield to obtain meaningful structural data or deem the system good enough for future mutational work. Therefore, the expression system and construct design need to be revisited.

6.5 Redesigning and restriction cloning of *Nc*Pma1-7

Analysis of the structural position of designed Strep-tag constructs indicated the limitation of the tested *Nc*Pma1-6 design and highlighted *Nc*Pma1-7 as the potential solution to the issues with expression yield. Furthermore, previously used constructs contained an additional N-terminal STREPII-TEV tag. Since previous expression testing of *Nc*Pma1-1 failed, there was no reason to retain this tag on any of the other constructs. Therefore, *Nc*Pma1-7 was redesigned to remove the N-terminal tag and insert a Twin-STREPII tag at position 850 in the loop between TM 9 and 10. The Twin-STREPII-tag has been developed to reduce the off-rate of binding to tetrameric STREP-Tactin to achieve more steady binding compared to the original STREPII-tag (Schmidt et al., 2013).

*Nc*Pma1-7 was successfully cloned according to classical cloning protocols described in section 2.2.2.1. This was verified by both restriction digestion and by sequencing, however the results are not shown.

6.6 Expression testing of *Nc*Pma1-7

The *Nc*Pma1-7 construct was transformed into four *S. cerevisiae* strains for expression testing: W303, ΔPep4, Gal4ΔPep4 and BJ5460 and plated on –URA plates followed by secondary selection in –LEU media culture. Each transformed strain was grown up and expression was induced using galactose, testing

expression over 20 hours. *Nc*Pma1-6 in Gal4ΔPep4 was used as a positive control for expression. Figure 6.5 shows the SDS-PAGE and Western blot analysis of the samples taken at each time point. There was no detectable expression of *Nc*Pma1-7 in any of the strains – the SDS-PAGE gels did not show a marked increase in band intensity around the 100 kDa marker, nor were any Pma1 noticeable on the Western blot. Due to time restraints, establishing a recombinant expression system for *Nc*Pma1 could not be investigated further.

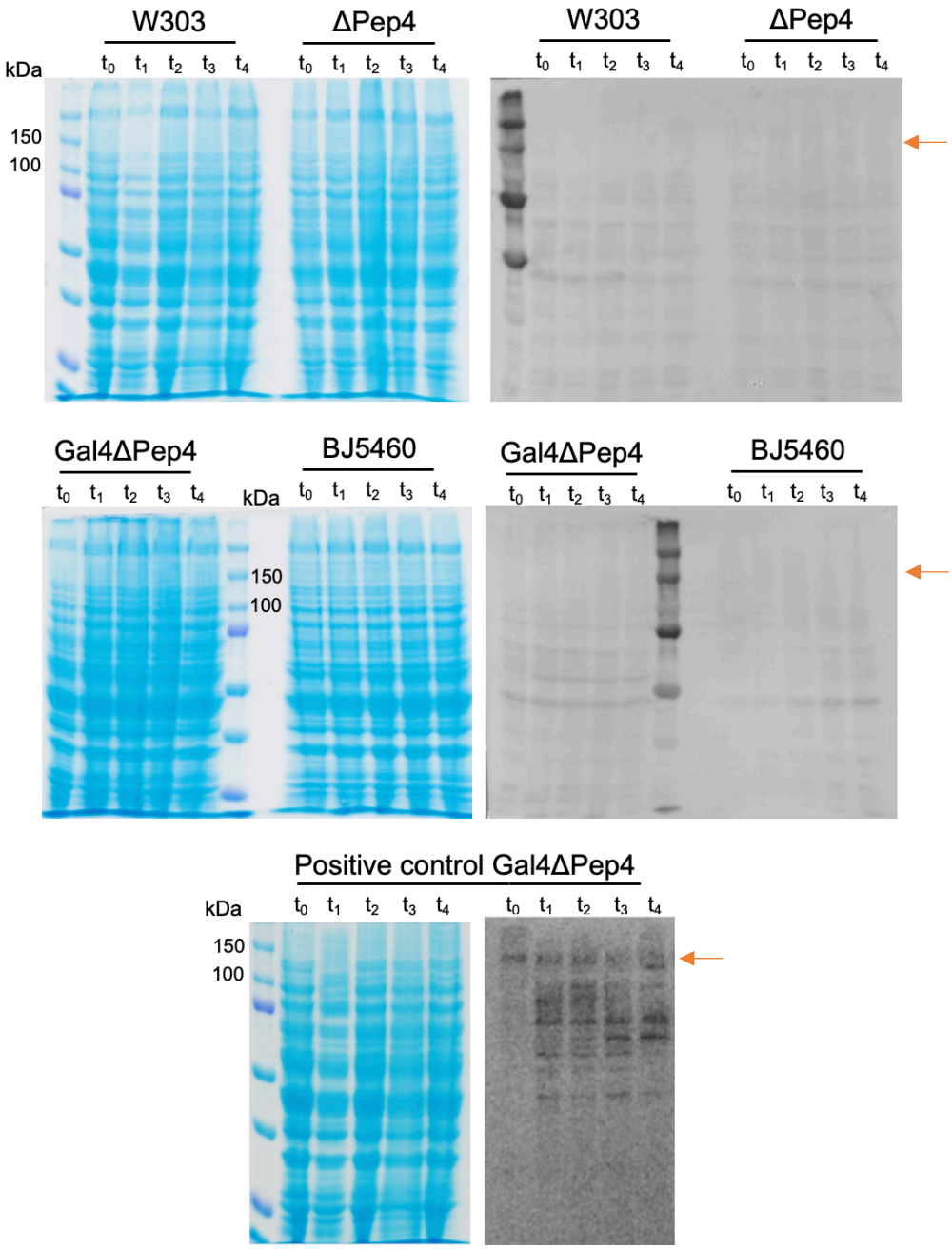

Figure 6.5 Analysis of NcPma1-7 expression in S. cerevisiae strains. *Samples were taken at induction (t_0) and every four hours starting after the first 8 hours (t_1-t_4) and analysed by SDS-PAGE and Western blotting. Expression of NcPma1-6 in Gal4ΔPep4 was used as a positive control. PageRuler marker bands are indicated.*

6.7 Chapter 6 discussion

Recent progress in the lab yielded the first high-resolution cryo-EM structure of native Pma1. Furthermore, molecular dynamics studies of the Pma1 structure in a complex lipid membrane illustrated the potential role of lipids in its function. To characterise other conformational states and probe structure-guided mutations in functional analysis, a recombinant system for expression and purification of active protein is required. Small-scale trials showed successful expression and purification of a Strep-tagged protein, however, the resulting sample was too dilute for structural studies. Negative stain EM of *Nc*Pma1-6 samples after SEC indicates the presence of hexameric Pma1 but further optimisation is required.

The original construct design was based on a SERCA-derived homology model of Pma1. Taking into account the now available structural data, consideration of the positions of the Strep-tags in relation to the monomer contacts highlights that the original designs were flawed (Figure 6.6): the Strep tags for both *Nc*Pma1-5 and *Nc*Pma1-6, in L3-4 and L7-8 respectively, lie at the interface between monomers in the hexamer. These positions are likely to affect the expression and stability of *Nc*Pma1 in *S. cerevisiae*. Moreover, the function is likely also impaired, owing to no measurable activity. Mutagenic studies of residues in loop 5-6 found a temperature-sensitive defect in Pma1 biogenesis (Chang & Fink, 1995). Therefore, the Strep-tags could prevent proper trafficking to the plasma membrane and cause degradation, explaining the low expression yields. Additionally, both the

multimerization and activity of Pma1 are lipid dependent (Bagnat et al., 2001), as supported by the MD work in Chapter 3. The CG MD simulations of Pma1 showed that this site binds PC lipids. If the binding of these lipids at this site is important for hexamer stability and/or function, then the polar residues in the Strep-tag could destabilise that contact and as a result cause the protein to be signalled for degradation. The *Nc*Pma1-7 construct Strep-tag in L9-10, however, does not lie at an interface and was therefore hypothesised to express well in the recombinant system.

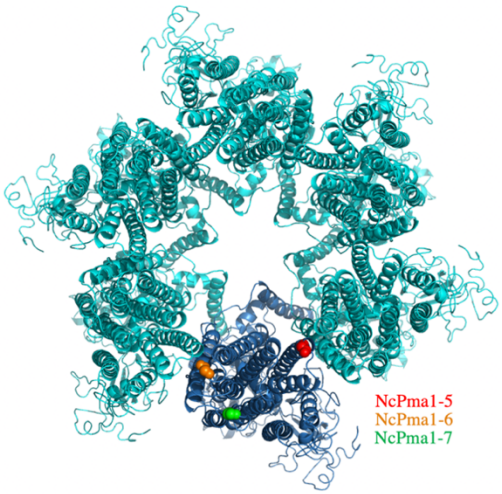

Figure 6.6 Structural evaluation of the NcPma1-5, -6 and -7 constructs. *High-resolution structure of Pma1 shown in cyan, with one monomer highlighted in blue (PDB 7NY1). Spheres represent the sites of STREPII-tag insert.*

Restriction cloning was used to generate a Pma1 sequence with a Twin-STREPII tag embedded in loop 9-10. However, surprisingly, expression trials showed no expression of this construct. Most likely, this lack of expression could be down to an issue in the promoter region. The construct design was altered to contain a polyA site in *Nc*Pma1-7 as this is required in yeast. Since this is the only alteration

around the promoter, future experiments should remove this addition from *Nc*Pma1-7 and repeat the expression trials.

One of the potential issues with the overall experimental design is that ScPma1 constitutes up to 30% of *S. cerevisiae* membrane proteins, significantly more than reported in *N. crassa* (Fajardo-Somera et al., 2013). Since the native Pma1 is already expressed at high levels and essential for cellular function, any Pma1 that is not optimised for its host might be directed for vacuolar degradation. Moreover, Pma1 sorts into the fungal MCP. Variations in the MCP could mean that *Nc*Pma1 is not compatible with the *S. cerevisiae* MCP lipid composition, especially if there are variations in the acyl chain lengths, particularly with the native Pma1 present. Future experimentation to establish the recombinant expression of *Nc*Pma1 should focus on experimenting with the RS-72 Pma1 knock-out strain of *S. cerevisiae* that would only conditionally grow on recombinant expression of *Nc*Pma1 (Cid et al., 1987). Moreover, the recent structure of *Sc*Pma1 from Zhao *et al*, was obtained using C-terminally FLAG-tagged Pma1 that was tagged through genome editing instead of plasmid-based expression (P. Zhao et al., 2021). Previous expression testing of *Nc*Pma1 with a C-terminal STREPII-tag was unsuccessful, so considering the FLAG-tag worked, there may be an issue with the biochemical nature of the STREPII-tag and the tag should be switched to test this. Testing in both the Gal4ΔPep4 and Pma1 knock-out strain will give the highest likelihood of generating a successful expression system.

Chapter 7: Discussion and conclusion Part I

Ongoing work in the lab resolved the high-resolution cryoEM structure of Pma1 in an autoinhibited E1 ADP-bound state. The structure addressed several questions in the field regarding the molecular basis for hexamer formation and autoinhibition via the R-domain. However, it did not shed any light on Pma1s specific lipid dependencies. Namely, Pma1 requires the presence of anionic lipids for function *in vitro* and association with these lipids and long-chain sphingolipids for hexamer formation, correct trafficking to the PM and function (Addison & Scarborough, 1981b; Gaigg et al., 2005). Hence, CG MD simulations of Pma1 in a complex *N. crassa* native-like membrane were run to investigate these potential interactions.

The simulations revealed that Pma1s dependence on anionic lipids is based on a preferential interaction with these lipids, namely DIPS, in the inner leaflet at the monomer interface. Lipidomics studies of the PM of *S. cerevisiae* grown on various carbon sources showed a significantly higher level of PS in cells grown on glucose compared to glycerol (Klose et al., 2012). Since glucose sensing causes activation of Pma1, this further corroborates the role PS might have. To date, no research has investigated the signalling pathway by which glucose sensing increases PS synthesis. However, it is possible that the process involves expression of a protein like a kinase that is directly involved in a signalling cascade that causes increased PS production. It is likely that the anionic lipid in this binding site not only mediates the inter-monomer contacts and stability of the hexamer, but is also involved in attracting protons to the acceptor binding site, helping Pma1 pump maintain the -180 mV membrane potential. The cryoEM studies of Pma1 inhibited with MgF_x and

BeF_x presented in Chapter 5 found additional density at this same site, although no identification of lipid species has been possible. As a following step, high resolution structure determination of these states combined with lipidomics analysis on the same purified sample of Pma1 could confirm the nature of the lipid binding at this site.

The additional role of anionic lipids in attracting protons is in line with the finding that Pma1 induces significant local membrane deformations with a concomitant clustering of cations in a simulated environment. The thickened membrane within the core and surrounding the hexamer (Figure 3.7A) might be aided by the high density of ergosterol binding sites on the protein (Figure 3.4). This would cause a local increased concentration in ergosterol within and around Pma1. Cholesterol (and by extension ergosterol) concentrations have been correlated with formation of a thicker membrane and therefore the concentration of ergosterol binding sites may have evolved to accommodate the thicker membrane and plasma membrane microdomains that Pma1 localises to (Cornell et al., 2020; de Meyer & Smit, 2009; Heberle et al., 2020; Kaiser et al., 2011; Rukmini et al., 2001). It is however worth pointing out that another recent study using SMALPs to isolate MCPs from *S. cerevisiae* found depletion of ergosterol (van 't Klooster et al., 2020), and so there are still discrepancies in the currently available studies. Pma1s interaction with the bilayer also causes a considerable distortion of the overall morphology. At the monomer interface, the membrane is thinned to around 20 Å right beside the proton transport pathway (Figure 3.7A and C). Not only is the deformation and lipid attraction proposed to attract protons to the binding site, the significantly thinner bilayer at the monomer interface could also prove to be an evolutionary benefit by lowering the energetic penalty of transporting a proton

through the hydrophobic barrier. This theory is further supported by the inward deformation of the outer leaflet around the proposed proton exit site (Figure 3.7C).

The fact that membrane proteins can influence the membrane structure is becoming increasingly recognised and has been reported in other MD studies. Whilst proteins are much more rigid than membranes, it has been shown, based on the energetics, that membranes will adapt to the protein and not vice versa (O. S. Andersen & Koeppe, 2007; Cornelius et al., 2015). Simulations of the Signal Peptidase Complex showed that it induced local membrane thinning to accommodate signal peptides based on the length of their hydrophobic segment (Liaci et al., 2021). The recent structure of Hedgehog acyltransferase (HHAT) was simulated to find that HHAT adapts the membrane environment to transfer an acyl chain across the ER more efficiently (Coupland et al., 2021). Finally, CG MD simulations of the Na^+-aspartate symporter, Glt_{Ph}, in various catalytic states demonstrated that the protein significantly modulates the membrane morphology to different degrees for the various states and using novel simulation methods, the authors could estimate the free-energy cost of the membrane perturbation (Zhou et al., 2019). The authors suggest that it might be more important to consider variations in the extent and free-energy cost of these deformations among different functional states of the protein and how they might contribute significantly to defining the catalytic mechanism.

Local attractions between the lipid bilayer and the protein may also facilitate or accelerate conformational changes in the protein. For example, this study found that a conserved region of arginine and lysine residues in the A-domain binds to anionic lipids on the outside of the ring. Not only does this help thicken the membrane, it may also play a role in regulating the motion of the A-domain. The A-

domain of P-type ATPases is the most mobile domain, capable of flipping in and out of contact with the N-, P-domain body. The mechanism of flipping could be impacted by the interaction with lipids in the bilayer. Moreover, the PM is crowded with other proteins, especially as Pma1 is thought to form a quasi-crystalline lattice under starving conditions. In a crowded membrane there will be additional tensions on the bilayer that may not allow it to curve up onto the protein and instead the A-domain's motility could be altered by an attraction toward the membrane. Another interaction noted between the bilayer and Pma1 is that in the inner ring of the protein, the leaflet thickens and climbs up towards the P-domain, possibly mediated by Lys749 (Figure 3.7C). This could impact the motility of M1 as L6-7 and the P1-helix are both closely involved in the gating of substrate (see Chapter 8). These mutual adaptations between protein and membrane, as well as membrane deformations assisting cytosolic ion entry have already been suggested for SERCA and might be a common feature of P-type ATPase function (Sonntag et al., 2011; Winther et al., 2013).

A recent study investigating the structure of the P_{VA}-ATPase, Spf1, found an arm domain protruding from the P-domain. This arm consists of an α-helix and positions its distal portion on the detergent micelle in the cryoEM structure. The authors state that whilst the atomic model for this region could not be built, the micelle around the contact was noticeably pulled up toward the arm domain. They suggest that the arm might affect local membrane structure (McKenna et al., 2020). Interestingly, the arm domain roughly wraps around the A-domain and draws the membrane up in a similar location as for Pma1, near the M1 substrate entry site. Local membrane deformation towards the A-domain point toward a widespread feature of P-type ATPases.

Finally, simulating Pma1 in a bilayer with PICE highlighted that this specific ceramide only found in fungi interacts with Pma1 both directly through contact with the A-domain and indirectly by clustering in the lipid core. A possible explanation for a pure PICE core could be that the synthesis of the ceramide localises in the ER near Pma1 synthesis and multimerization. The final step in phosphatidylinositol ceramide synthesis is the transfer of the phosphatidylinositol from a PI lipid onto a ceramide base by inositol phosphorylceramide synthase, a membrane protein (Aur1p in *S. cerevisiae)* (Nagiec et al., 1997; Sugimoto et al., 2004). To date, studies have only focussed on the antifungal activity of aureobasidin A on this protein and have not investigated its subcellular localisation or if it interacts with any other proteins.

As has been shown for PS lipids (Matsunaga et al., 2015), headgroups of the same species can interact with each other to promote accumulation. This interaction could exist between CIPs too and could drive their accumulation in the protein core, however it has not been investigated. This is supported by the fact that PICE accumulates in the protein core, whilst PPCE does not (Figure 3.10), the only difference being the head group. Moreover, the fully unsaturated, long fatty acid chains of CIP would allow it to tightly pack in these microdomains. In line with this finding, lipidomics studies of *S. cerevisiae* grown on glucose compared to glycerol reported a 3-fold increase in CIP levels (Klose et al., 2012). Since Pma1 oligomerisation and trafficking requires CIP and glucose activates Pma1, CIP is likely densely populated in the Pma1 core.

Zhao *et al.* demonstrated that the outer leaflet could contain a liquid crystalline lipid core in Pma1 that prevents back leakage of protons. They also suggest that the inner leaflet lipids in the core are free to exchange with the bulk

bilayer by travelling through the space between monomers. The movement of lipids in the inner leaflet through the monomer interface was assessed in this study's simulations and no lipids were noted exiting through this pathway. Of course, lipids might require the energetic strain of the hexamer to exchange via the interface, but due to the instable nature of the hexamer simulation, this was not analysed in that system. The pool of DIPS accumulating at the suggested exchange site also points outwards and from the inside of the core to the position of DIPS, there is a significant drop in height, all suggesting that lipids would not transfer through this site. Moreover, if lipids could move between this space, then the hexamer simulations might not have had the instability shown in Figure 3.2B. This could be due to a limitation in the CG methodology, as *in vivo*, the hexamer cycles through its transport mechanism and the possible structural rearrangement of helices in a different state might accommodate exchange of lipids through this site, even though a proton-tight seal must always be maintained.

To address some of the questions raised above, I propose several follow up studies to investigate Pma1s intricate relationship with the plasma membrane. Results from Chapter 5 indicate that high-resolution structures of *N. crassa* Pma1 inhibited in an E2 state will soon be available. Simulating the different catalytic states of Pma1 could provide useful insights into whether the bilayer deformation is permanent throughout the Post-Albers cycle or whether this deformation fluctuates between an E1-induced and E2-induced shape. As was considered by Zhou *et al* for Glt_{Ph}, it would be interesting to consider the energetics of the membrane deformation of different catalytic states and the extent to which this might define the mechanism of Pma1 (Zhou et al., 2019). Moreover, a membrane dip surrounding P-type ATPases' M1 helix has been proposed before. For example, in the study

presented by Sonntag *et al.* close inspection of their hydrophobic matching data shows membrane thinning near M1 in SERCA (Sonntag et al., 2011). With the setup designed here, other P-type ATPases can be simulated to address the membrane deformation, lipid binding and ion attraction around the substrate entry site.

Altogether, the work presented in this thesis has developed our understanding of the interactions between Pma1 and a complex lipid bilayer. It has also made significant improvements to the expression and purification of the enzyme, with successful initial cryoEM testing. This high throughput pipeline for structure resolving suggests it is now possible to address the myriad of follow up questions regarding lipid interactions and the catalytic mechanism.

Results Part II

Chapter 8: The role of E340 in SERCA

Most of the data presented here are from Geurts, M.M.G., Clausen, J.D., Arnou, B., *et al* "The SERCA residue Glu340 mediates interdomain communication that guides Ca^{2+} transport" PNAS (2020), vol 117, no. 49. Any work conducted by collaborators is clearly stated in the text and figure legends.

8.1 Chapter 8 Introduction

This final chapter moves away from the focus on Pma1 and sets out to investigate the role of the P-type ATPase family-wide conserved Glu340 in SERCA. This is done through the use of all-atom MD simulations to probe the dynamics of the mutant E340A.

SERCA has been used as a model P-type ATPase for a long time to study the conserved transport mechanism of this family of enzymes. A large body of mutational data coupled with structural studies of SERCA inhibited in various catalytic states has aimed to uncover the intricacies of substrate transport in P-type ATPases. Now that there is a general consensus on the overall catalytic cycle of P-type ATPases, it is important to investigate the role that key conserved residues play in transporting substrate, focussing on understanding the remaining questions, including how communication between the substrate binding site and the ATPase site is mediated. There are several strictly conserved residues across all P-type ATPases that can provide such insight.

Glu340 is a residue that is almost perfectly conserved across P-type ATPases, with the exception of the P_V-subfamily and some bacterial representatives

that have either a glutamine or asparagine. This residue is centrally positioned on the P1-helix that sits at the interface between the membrane-facing side of the P-domain and the cytosolic ends of M3 through M7. The original study investing the role of Glu340 found that mutating it to alanine lowered ATP turnover to 13% of WT and reduced calcium transport to 34% (Clausen & Andersen, 2004). They note that the mutation causes little to no increase in the $K_{0.5}$ compared to WT suggesting there is little impact on Ca^{2+} affinity. In the same publication, by running functional assays of E340A in COS cell microsomes, the authors found that the mutation not only slows Ca^{2+} binding, it also slows the reverse reaction ($Ca_2E1 \rightarrow E1$). This is an important point to note as the action that occurs between binding and unbinding of substrate is the process of substrate occlusion. The mutation was moreover found not to affect SERCA's apparent vanadate affinity (which is typically affected by E2 to E1 shifts), suggesting that the slowing of $H_nE2 \rightarrow E1 \rightarrow Ca_2E1$ is due to inhibition of the latter part of this reaction sequence. Crucially, the authors also note that the mutation had no significant effect on the other partial reactions of the P-type ATPase reaction cycle. These findings are in line with E340A impacting substrate occlusion, although this was not commented on at the time.

Through functional studies and X-ray crystallography of the mutant E340A (trapped in the Ca_2E1 state with AMP-PCP), collaborators of the study presented here discovered the structural differences between the mutant and WT enzyme. However, these methods failed to provide a clear understanding for why the mutation caused impairment of Ca^{2+} binding and unbinding (shown in section 8.2) and what the conserved role of the Glutamate is.

This chapter addresses this question by running all-atom MD simulations of SERCA E1 WT, E340A and, as a control, *in silico* E340A ($E340A_{is}$), where the WT

structure was used to mutate Glu340 to an alanine. The analysis aimed to corroborate the structural differences observed between the WT and E340A and to investigate the dynamics of important protein regions during catalysis. Taken together, the simulations, along with the structural and functional work, provide a deeper understanding of the role the conserved Glutamate plays in the P-type ATPase superfamily.

8.2 Structure of SERCA E340A and Functional assay

The data shown in this section were collected by collaborators. Dr. Clausen grew the crystals, Dr. Bublitz solved the structure and Dr. Lenoir obtained the functional data. This data is used to provide the background information to the work shown in section 8.3 to 8.6.

Collaborators expressed and purified functional *Oryctolagus cuniculus* SERCA1a E340A from *Saccharomyces cerevisiae* alongside WT *O. cuniculus* SERCA. Through an enzyme-coupled assay, the ATPase activity of E340A measured 4 times lower than that of the WT (0.86 vs. 3.45 µmoles ATP/mg/min) (Figure 8.1A). This indicates a lowered catalytic turnover. Using intrinsic tryptophan fluorescence measurements, the transition from E2 to E1 upon Ca^{2+} addition showed a reduced rate of Ca^{2+} binding. Fig 8.1B and C illustrate that the for E340A, the transition from E2 to Ca_2E1 has a 3-times slower half-time, suggesting the mutation impacts Ca^{2+} occlusion. The impact of the mutation on the Vmax was not tested and has not been tested in other studies.

Dr. Bublitz solved the structure of E1 AMP-PCP SERCA E340A at 3.2 Å resolution and compared it to the WT structure (PDB 3N8G). The key results found are displayed in Figure 8.2 and will be referenced from section 8.3 onwards. When

WT and E340A are superposed across all main chain atoms, the two structures deviate by an RMSD of 2.3 Å. However, when the structures are aligned across M5-M10 (the least mobile region of the protein), M1-4 align almost perfectly.

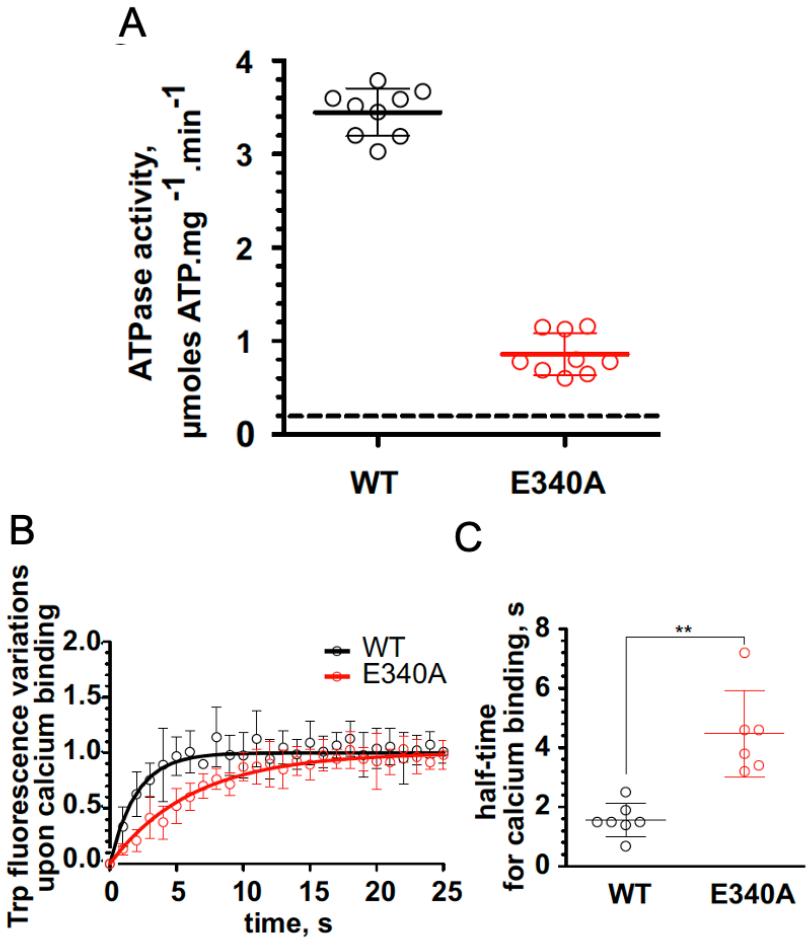

Figure 8.1 – SERCA WT and E340A activity measurements. *A) Steady-state ATPase activity of purified WT SERCA (black) and E340A SERCA (red) in an enzyme-coupled assay at 50 μM free Ca^{2+}. B) Magnified view of the tryptophan fluorescence time course measurements of Ca^{2+} binding transition. The official time course continued to 120s. C) Half-time for Ca^{2+} binding to WT and E340A SERCA. Reactions were run with at 50 μM free Ca^{2+}. Data was collected by collaborators and taken from Geurts et al., 2020.*

The M1 kink is slightly more acute (105° in E340A vs 109° in WT) and there is a 1.6 Å inward shift of M3 (Figure 8.2A). More noteworthy is the pronounced shift of the soluble domain of E340A down towards the membrane by 10 Å. This shift seems to pivot at the cytosolic ends of M2, M4 and M5, initiating around the P1-helix, where the mutation is found. The direction of this shift follows the trajectory that empty MgE1 SERCA takes upon binding Ca^{2+} and shifting to Ca_2E1 (Winther et al., 2013), albeit that the E340A shift is extended further. A loss in the connectivity between the N-domain and the A-domain is observed (Figure 8.2B and C) as an increase in the distance between the N- and A-domain. This is possibly driven by the noted loss of six out of eight polar contacts between the N- and A-domain, leaving only the contact between Thr171 to Glu486 and Arg134 to Asp426. The contacts between the P-domain and the A-domain remain the same.

Finally, the structure illustrates a local change in the hydrogen bond network surrounding residue 340 (Figure 8.2 D and E). In the WT structure, Glu340 makes a bond with the tip of M3 and engages is a water-mediated hydrogen bond contact to Arg822 in loop 6-7. Through the loss of the carboxylate group in E340A, these bonds disappear. However, the local confirmation of residues does not alter much, aside from a slight decrease in the distance from P1 to the tip of M3. Importantly, the contact to Arg822 is also lost and L6-7 is displaced outwards by about 3 Å.

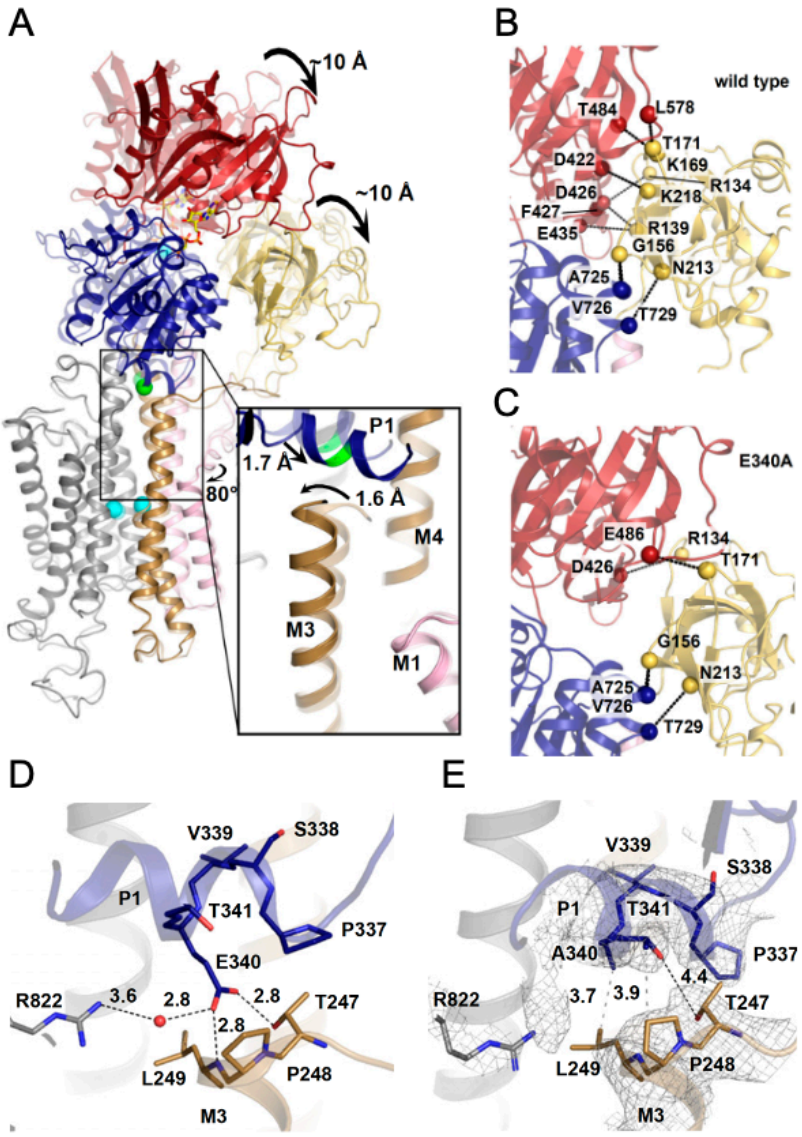

Figure 8.2: Comparison of the SERCA WT E1 AMPPCP (PDB 3N8G) and E340A crystal structures. *A) Superposition of E340A onto WT (transparent), aligned across TM7-10. (Inset) Local changes in tertiary structure near residue 340. B and C) Polar contacts between the N (red) and P (blue) domains and the A (yellow) domain for WT (B) and E340A (C) SERCA. D) and E) Local structural changes in the hydrogen bond network (black dashes) around residue 340 in WT (D) and E340A (E), with proposed hydrophobic contacts around E340A shown in grey dashes. Grey mesh represents the 2mFo-DFc electron density map contoured at 1.0σ. Data collected by collaborators and taken from Geurts et al., 2020.*

8.3 The structural deviations of E340A from WT are stable in MD simulations

Initially, molecular dynamics simulations of WT and E340A SERCA were run and compared. The objective was to test whether the shifted headpiece and loosened A-domain would stay in place during the simulation, or whether the system would relax to the same state as the WT. As an internal control, an *in silico* mutant was generated by truncating the side chain of Glu340 in the WT Ca_2E1-AMP-PCP structure. 3 X 200 ns all-atom simulations of each structure in a POPC lipid bilayer were constructed (Figure 8.3), containing the same starting positions but varying

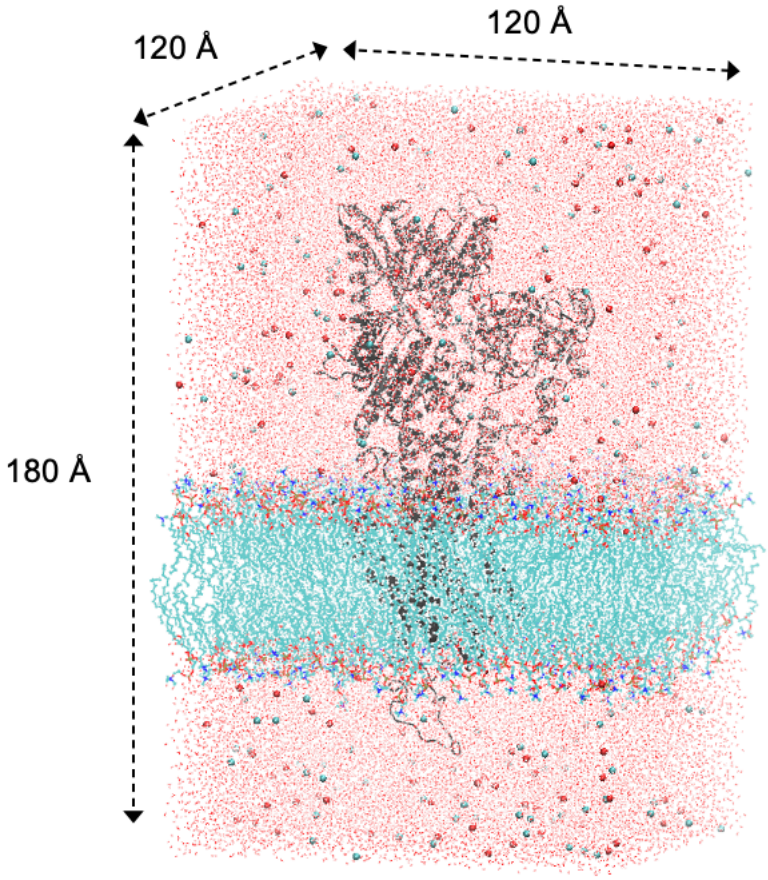

Figure 8.3: Example all-atom molecular dynamics setup box of SERCA E340A *(grey cartoon) in a POPC membrane (cyan), solvated with water (small red spheres) and* Na^+ *(blue spheres) and* Cl^- *(red spheres).*

starting velocities. Simulations reached structural equilibration, tested by checking the RMSD, shown in Appendix 10.3. It is worth noting that these simulations, unlike those presented in Chapter 3, are all-atom, meaning the protein is not rigidified by the elastic network of CG simulations. It is therefore the appropriate method to study the structural observations noted above.

To quantify and parametrise the headpiece tilt observed in the crystal structure, a set of three residues were chosen to define the angle of the headpiece: Vectors between the three residues were used to measure the angle between them in each frame of the simulation. Importantly, the set of residues needed to lie in the same plane as the trajectory of the headpiece tilt. Firstly, the central point was defined by picking Thr86 as a point of pivot. Then, sets of two further residues were tested and whilst several showed similar results, the greatest resolution in the tilt was found with Leu13 in the A-domain, presumably because the further movement occurs at the extremity of the tilting object. The angle measured between Leu13,

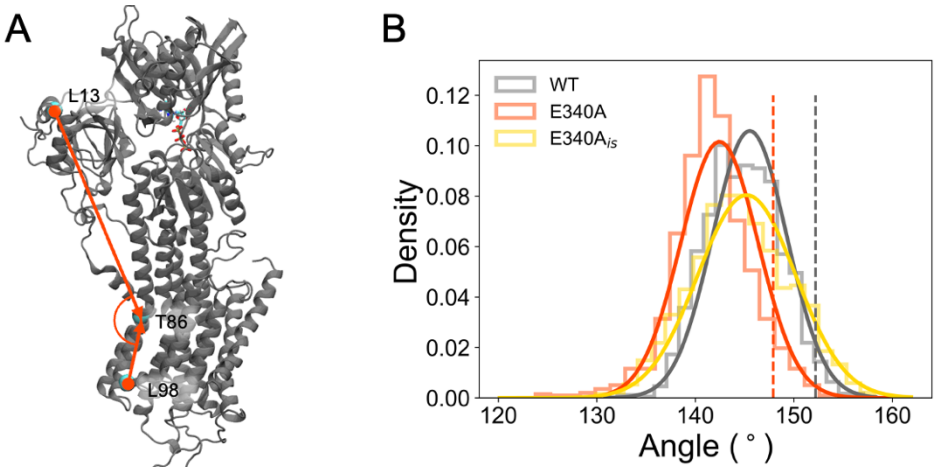

Figure 8.4: Molecular dynamics analysis of the head tilt in WT (grey), E340A (orange) and E340A$_{is}$ (yellow). *Dotted lines correspond to reference values in respective crystal structures. A) Structural illustration of the angle measured in SERCA, measuring the angle between Leu13 in the A-domain and Thr86 and Leu98 in M2. B) Angle histogram between the soluble headpiece and the transmembrane domain. Density is given as an arbitrary unit on the Y-axis.*

Thr86 and Leu98 in M2 (Figure 8.4A) provided a suitable plane for the measurement when compared to the morph of the E340A and WT structures. The histogram plot of the data (Figure 8.4B) shows that the two crystal structure angles (147° for E340A and 152° for WT) are both more obtuse than the median angles in the simulations of E340A and WT. Both structures therefore relax toward more acute angles, but the difference stays at 5°. This confirms that the greater headpiece tilt in E340A is

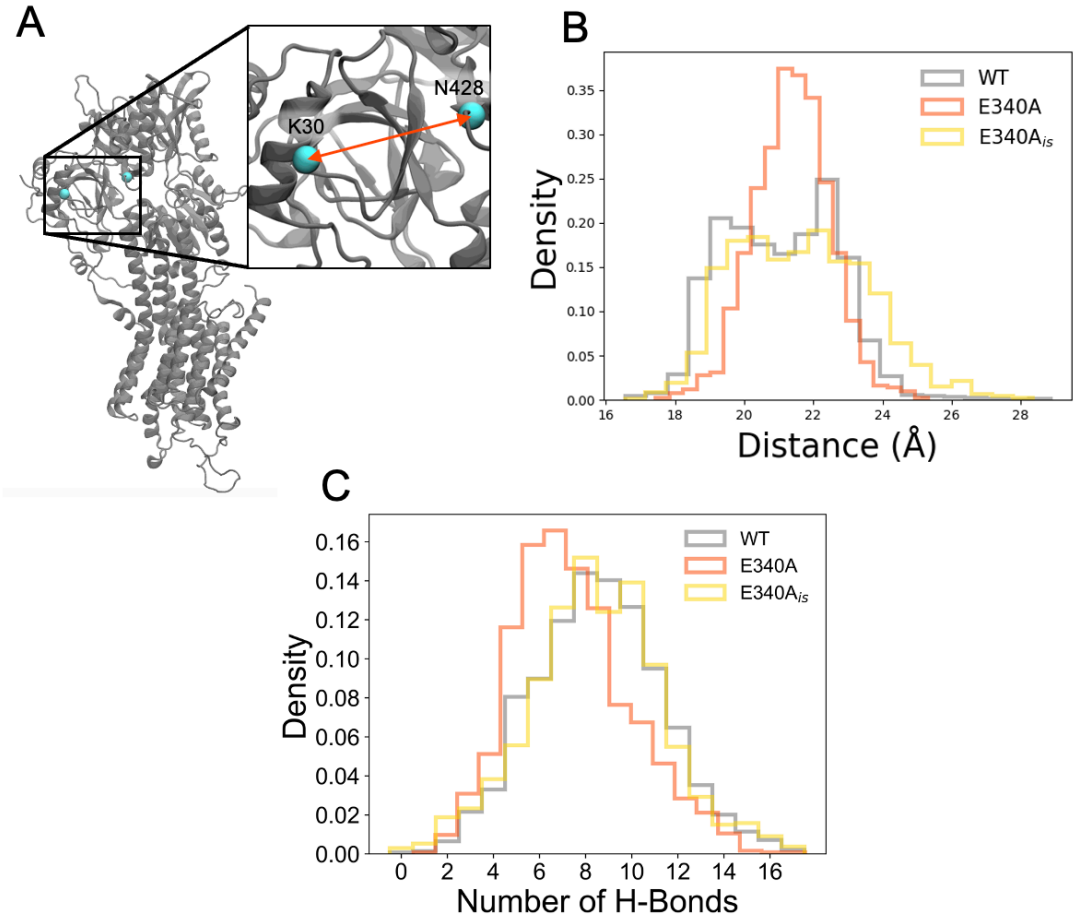

Figure 8.5: Molecular dynamics analysis of the connectivity between the A domain and the N and P domain of WT (grey), E340A (orange) and E340A$_{is}$ (yellow). *A) Structural illustration of the distance measured between Lys30 in the A domain and Asn428 in the N domain. (inset) Focus view of the measurement. B) Histogram of the distance between the C_α of Lys30 and Asn428. C) Histogram of the number of hydrogen bonds between the A domain and N/P domain in a given frame of the simulation.*

a small but true phenotype of the mutation. Since this motion is associated with Ca^{2+} binding and occlusion in WT SERCA, the overshoot in the E340A mutant could be linked to an altered occlusion of Ca^{2+}.

The connectivity between the A-domain and the N/P-domain body remained looser in the E340A simulation (Figure 8.5). The distance between C_α of Lys30 in the A-domain and Asn428 in the N-domain displays a bimodal split for the WT (medians at 19 Å and 22 Å), whilst E340A behaves within a single distribution with a median of 22 Å. Moreover, the histogram of measured hydrogen bonds between the A-domain and the N/P domain body (Figure 8.5C) show E340A on average has 3 to 4 fewer hydrogen bonds in any given frame, illustrating that the A-domain is less tightly tethered in the mutant. In this analysis $E340A_{is}$ behaved more akin to WT than E340A suggesting it is still traversing the energy landscape of transition towards E340A or is stuck in an energy minimum.

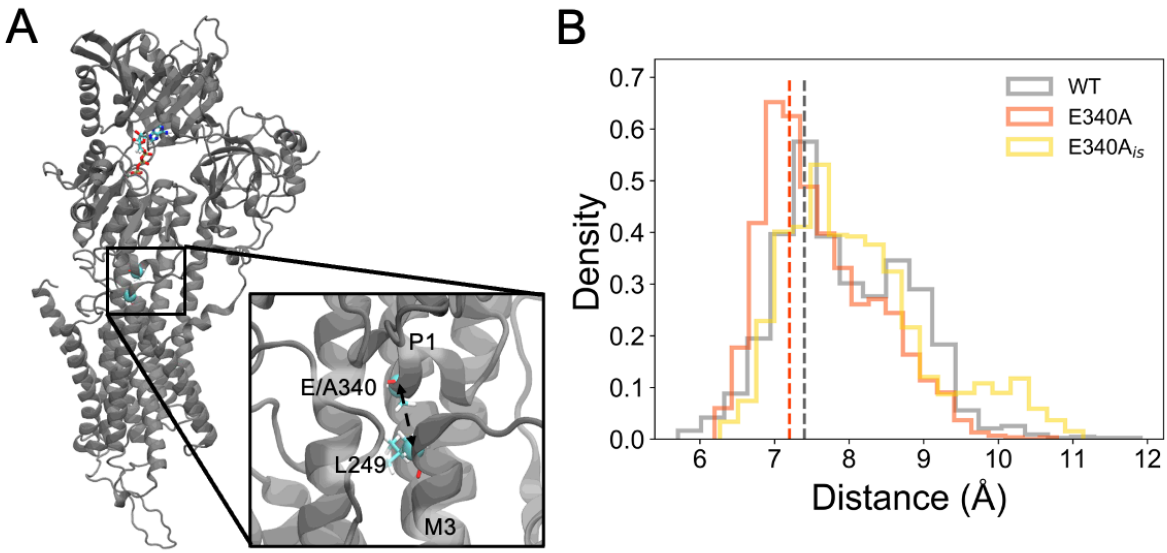

Figure 8.6: Molecular dynamics analysis of the P1-helix association with M3 in WT (grey), E340A (orange) and E340A$_{is}$ (yellow). *Dotted lines correspond to the reference values in respective crystal structures. A) Structural illustration of the measurement between the C_α of residue 340 and Leu249, with the inset showing a zoom on the P1 and M3 helices. B) Distance histogram of the measurement shown in (A).*

The distance between the P1 helix and the tip of M3 was measured in the simulations (Figure 8.6). The decreased distance noted in the E340A crystal structure is maintained in the simulation, and interestingly the WT protein relaxes to form two states, in which one has an even greater distance between the P1 helix and tip of M3.

Altogether, the analyses described above corroborate the observed deviations of the crystal structure of SERCA E340A from WT. However, they do not yet directly address why the mutant displays slowed kinetics of Ca^{2+} binding.

8.4 E340A stabilises occluding behaviour in Loop 6-7 and M3

As the crystal structure has suggested, E340A might alter the binding kinetics of Ca^{2+} by stabilising a more occluded state. In line with this, other factors involved in P-type ATPase substrate occlusion were analysed.

Arg822 has previously been proposed to play a role in ion binding (Clausen & Andersen, 2004). Simulations show a noticeable difference between WT vs. E340A. Through the loss of the sidechain in E340A, direct interaction to Arg822 is no longer possible, and thus the arginine is no longer constrained to the interaction with the P1-helix and tip of M3. This observation was confirmed by analysing the distance between the N_ε of Arg822 and C_β of residue 340 (Figure 8.7B). In the WT simulations, the arginine remains within 6 to 8 Å from the C_β whilst in E340A and E340A$_{is}$ it can flip to an 'out' position at a distance of 13 Å and 15 Å, respectively.

In the structure of WT Ca_2E1 SERCA, a water molecule is connected within the hydrogen bond network between Arg822 and Glu340. However, in the simulations the water molecule leaves the interaction in all three repeats and Arg822 adopts two possible 'in' states (Figure 8.7D). In one state, the arginine is in

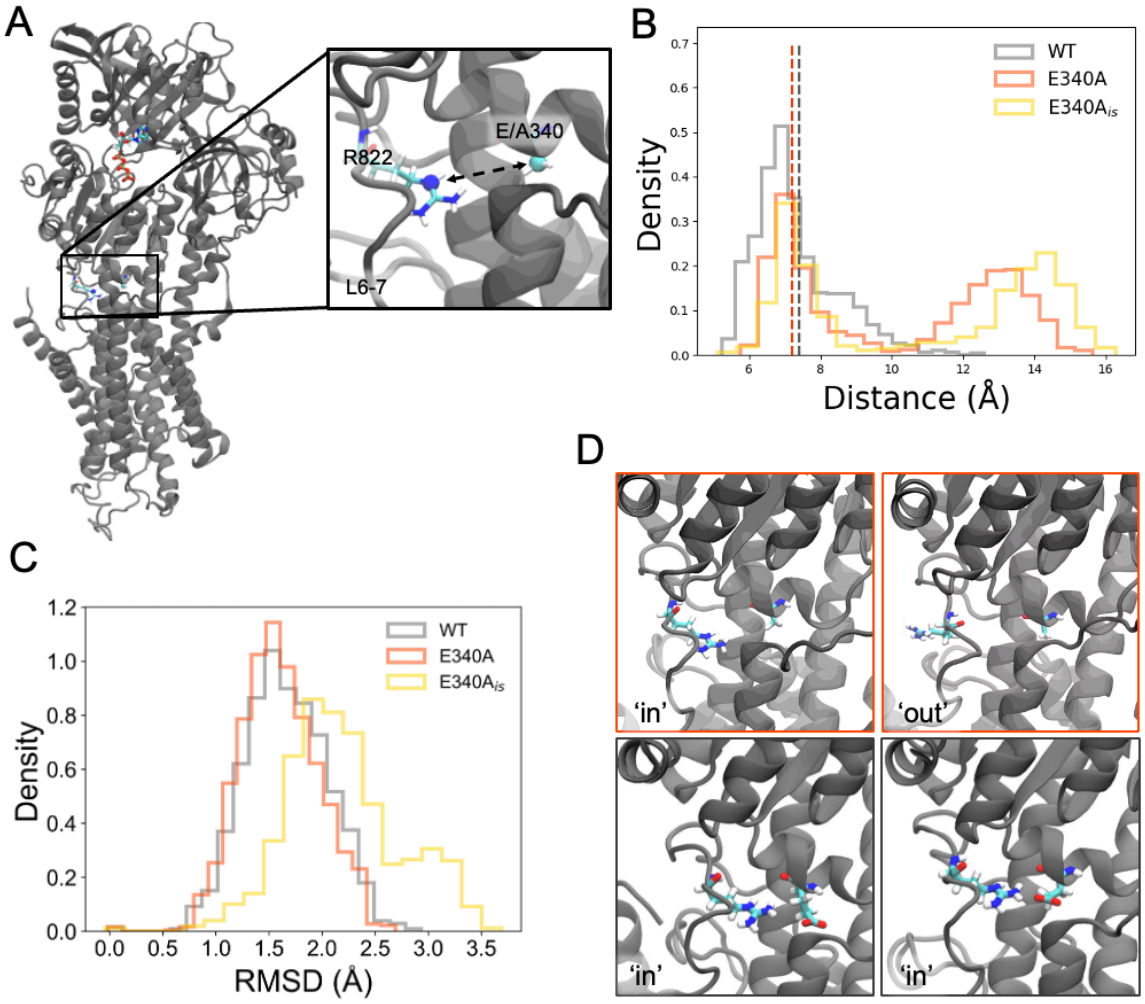

Figure 8.7: Analysis of the interaction between loop 6-7 and its Arg822 and residue 340 in WT (grey), E340A (orange) and E340A$_{is}$ (yellow). *Dotted lines correspond to the reference values in respective crystal structures. A) Structural illustration of Arg822 and residue 340. (Inset) zoom of loop 6-7 and the distance measurement between the N_ε of Arg822 and the C_β of residue 340 shown in (B). B) Histogram of the distance between the N_ε of Arg822 and the C_β of residue 340. C) RMSD histogram of loop 6-7 over the course of the simulation. D) Visualisation of the possible states of Arg822 in E340A (top) illustrating the 'in' (left) and 'out' (right) state and in WT (bottom) illustrating the 'in' disengaged (left) and 'in' engaged (right). Figure published in Geurts et al., 2020.*

a disengaged 'in' state where it is pointed towards the carboxylate group of E340, however it does not make a hydrogen bond contact, similar to the 'in' state of E340A.

It is likely held in place through electrostatic attraction. In the alternate state, Arg822 is in an engaged 'in' state where it maintains a direct hydrogen bond with the carboxylate of E340.

Due to the loss of contact with Arg822, and its consequent flipping outwards in E340A, the L6-7 loop could become more mobile. To assess this flexibility, the RMSD of L6-7, with reference to the crystal structure coordinates, was measured. The result, shown in Figure 8.7C, shows no particular variation in the dynamics of the loop for WT and E340A. However, there is a higher RMSD for the loop in E340A$_{is}$ and this could be linked to the slightly higher 'out' distance of Arg822 in E340A$_{is}$. This difference suggests that the *in silico* mutant might still be undergoing further equilibration.

On closer inspection of the interaction site between Arg822, residue 340 and the tip of M3, a noticeable change can be seen when the arginine flips out: as Arg822 flips out, there is a concomitant decrease in the distance between Pro814 in L6-7 and Leu249 at the tip of M3 (Figure 8.8). This motion represents a tightening of the helical bundle as the M3 helix moves inwards on the core of the structure and increases occlusion of Ca^{2+}, an observation not seen in the WT simulations. The flipping out and concomitant tightening of the helical bundle is observed in two out of three simulation runs for both E340A and E340A$_{is}$. Importantly, once flipped to the out position, the arginine does not flip back during any of the simulation runs and the decreased distance between Pro814 and Leu249 remains stably low (Figure 8.8B). With the outward swing of Arg822 one might expect the soluble domain to lose affinity for M3 and L6-7. However, contrary to the expectation, this motion results in Leu249 taking up the empty space, driving the inward motion of M3. Leu249 has previously been mutated to alanine, which impacted Ca^{2+} binding

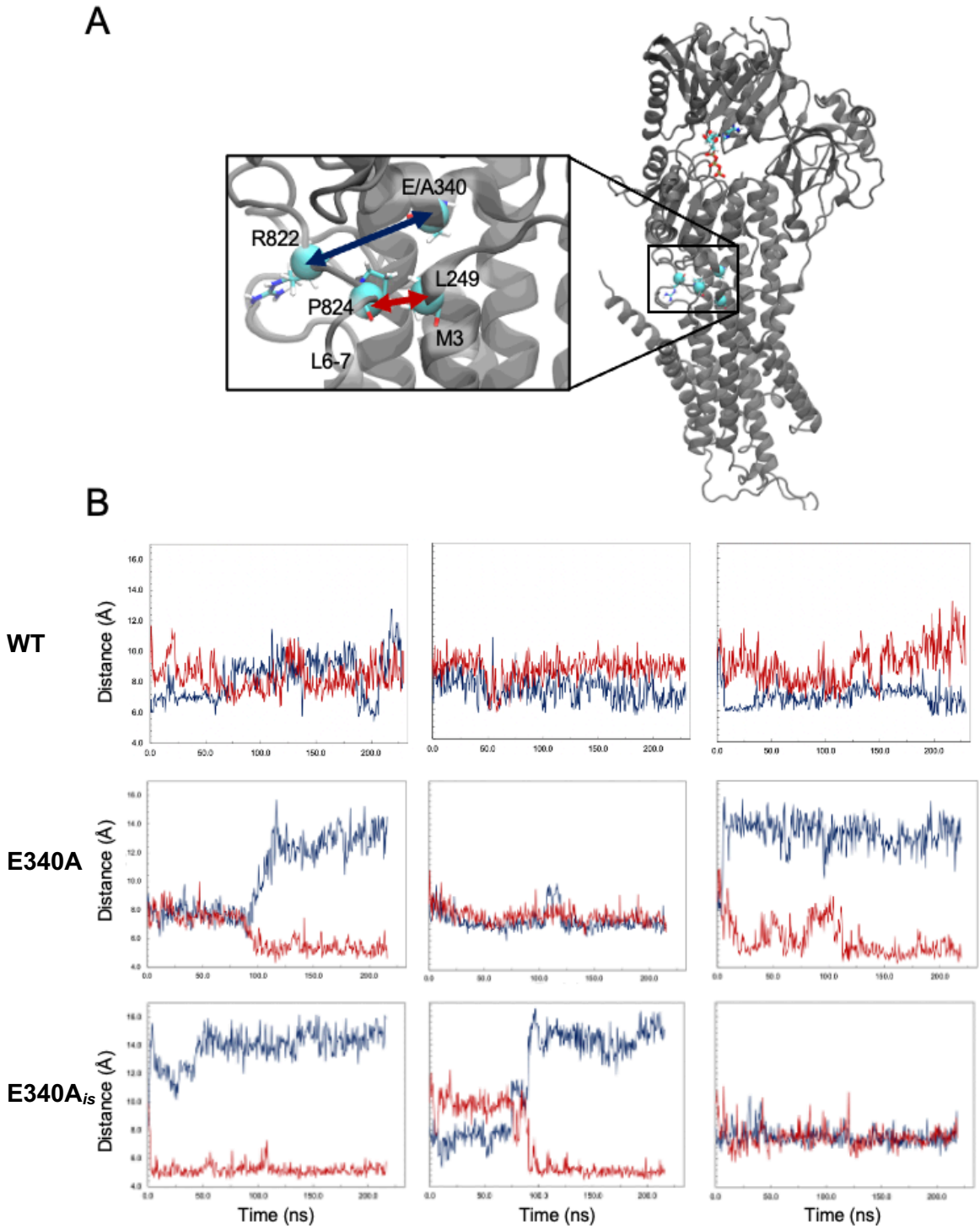

Figure 8.8: Measuring the occluding motion in M3 in WT, E340A and E340A$_{is}$. *A) Visualisation of the distance measurements between Glu/Ala 340 and Arg822 and Leu249 and Pro824. B) Distance traces throughout the course of the simulation between the N_ε of Arg822 and the C_α of residue 340 (blue) and between the C_α of Leu249 and the C_α of Pro824 (red). Left to right: Simulation repeats 1 to 3.*

(Clausen & Andersen, 2003). This result suggests that the changes in the hydrogen bond network around P1 resulting from the mutation play a role in defining the observed structural changes.

8.5 E340A rigidifies the mobility of the M1 kink

To further understand the influence of the mutation on the occlusion of Ca^{2+}, the transmembrane helices were closely analysed. An interesting difference between WT and E340A was noted in the kinked region of M1. The M1 helix has previously been shown to straighten out in the E309Q mutant that lacks the ability to occlude Ca^{2+}, thereby theorising that the M1 kink is mobile and involved in the stable binding and occlusion of Ca^{2+} (Clausen et al., 2013). To quantify the behaviour of the kink, the angle between Trp50, Arg63 and Val74 was measured (Figure 8.9A and B). The WT structure exhibits a bimodal split in the confirmations it adopts; a more acute M1 of 108° in one conformation (example shown in Figure 8.9C – middle panel) and a more obtuse M1 of 124° in the other (Figure 8.9C – right panel). This bimodal distribution highlights the WT M1 is mobile and alternates between a more and less kinked conformation, suggesting it regulates the binding and unbinding of Ca^{2+}. In both E340A and E340A$_{is}$, the M1 kink is more rigid, as seen by the unimodal distribution. The mutant kink averages at 108° (shown in Figure 8.9C-left panel). This finding is particularly interesting due to the previously mentioned role of M1 in Ca^{2+} binding and occlusion and suggests that the E340A mutation impacts M1 mobility to favour Ca^{2+} occlusion. Conversely, this suggests Glu340 plays a role in the mobility of M1 which is key for efficient catalytic turnover.

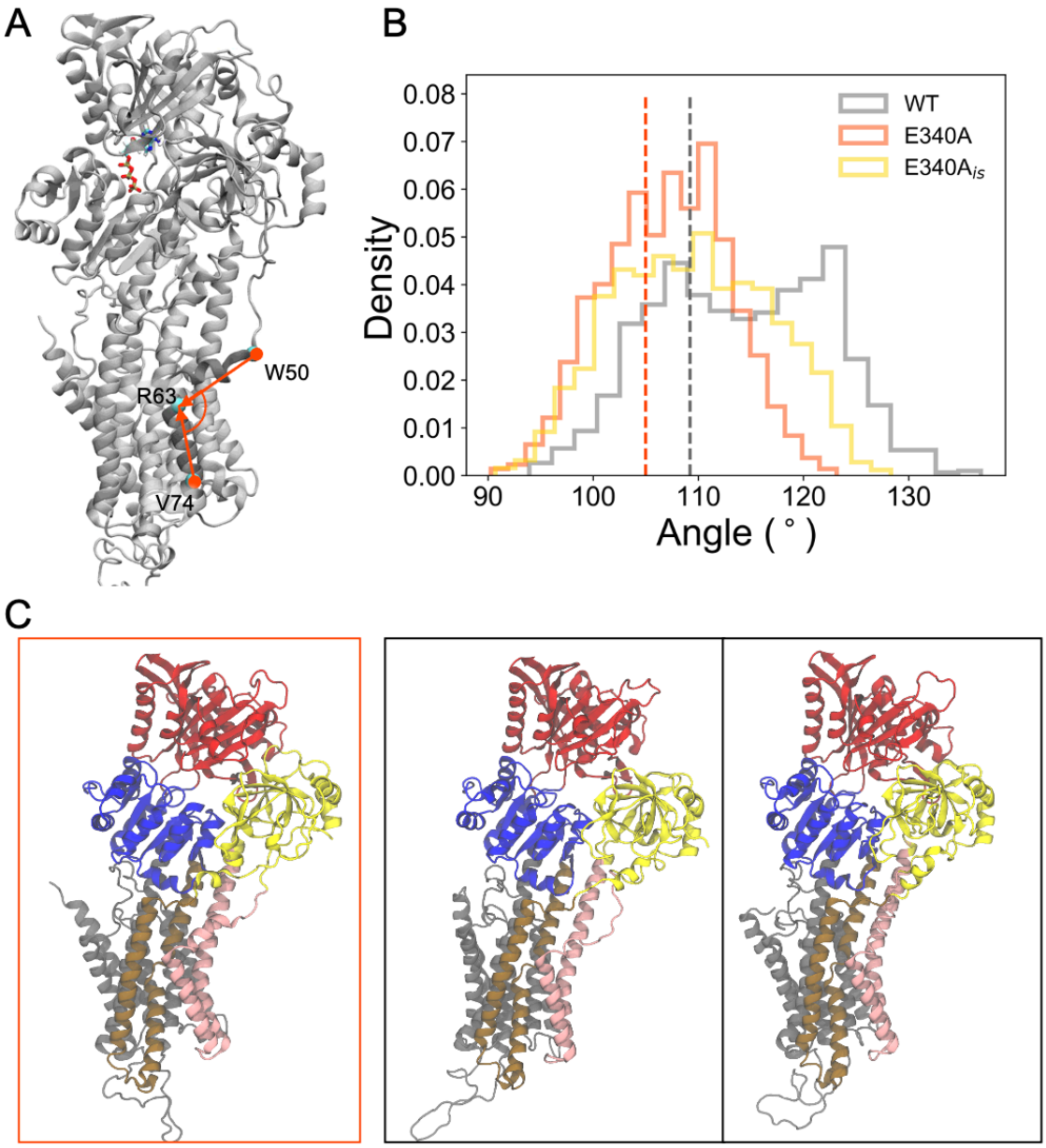

Figure 8.9: Analysis of the behaviour of the M1 kink in WT (grey), E340A (orange) and E340A$_{is}$ (yellow). *Dotted lines correspond to the reference values in respective crystal structures. A) Visualisation of the angle measurement between Trp50, Arg63 and Val74 with the corresponding M1 helix highlighted in darker grey. B) Angle histogram over the course of the simulation. C) Representative states of the single angle in E340A (left) and two angles in WT (right two panels), coloured according to classical P-Type annotation: M1-2 are shown in pink, M3-4 are shown in brown, M5-10 are shown in grey, P-domain is shown in blue, N-domain in red and A-domain in yellow.*

8.6 E340A stabilises the phosphorylation site in a more occluded state

To complete the picture of E340A's role in Ca^{2+} occlusion, the behaviour of the nucleotide-binding site was analysed. The transport of Ca^{2+} is inherently linked to the ATPase site of the protein, as the binding and phosphoryl transfer onto and off of the protein drives the ion transport cycle. Interdomain communication is required for this. Hence, a more stabilised ion-occluded conformation of SERCA should be more prone to phosphorylation by ATP. This was investigated by attempting to analyse the likelihood of Asp351 phosphorylation.

In the AMP-PCP inhibited E1 state, SERCA has bound nonhydrolyseable ATP and Ca^{2+} and the next step will be phosphoryl transfer of the Pγ of ATP to Asp351. A favourable reaction site geometry must be adopted to allow for an in-line nucleophilic attack: the carboxyl oxygen of Asp351 must be sufficiently close to Pγ, and positioned at the right angle with regard to the $O_{3\beta}$-P_γ phosphoanhydride bond of the nucleotide. The distance from Asp351-O_δ to the P_γ of ATP as well as the angle was measured for both $O_{\delta1}$ and $O_{\delta2}$ (which are regarded as equivalent in the deprotonated state) (Figure 8.10A).

Values for $O_{\delta1}$ and $O_{\delta2}$ had to be measured as the delocalised electrons in the carboxyl group would allow either oxygen to catalyse the reaction depending on which was closest. For each frame, the distance and the angle were paired up and plotted in Figure 8.10B. For both O_δs, two clusters for each simulation were noted - one at a shorter and one at a longer distance. Either of the O_δ's can be the catalytically primed oxygen and when one O_δ is close, the other will be further away.

To improve the analysis, the respective closer of the two pairs was selected for each frame (Figure 8.10C). For reference, the distance and angle of the fully occluded transition state AlF_x crystal structure are 2.1 Å and 159° respectively

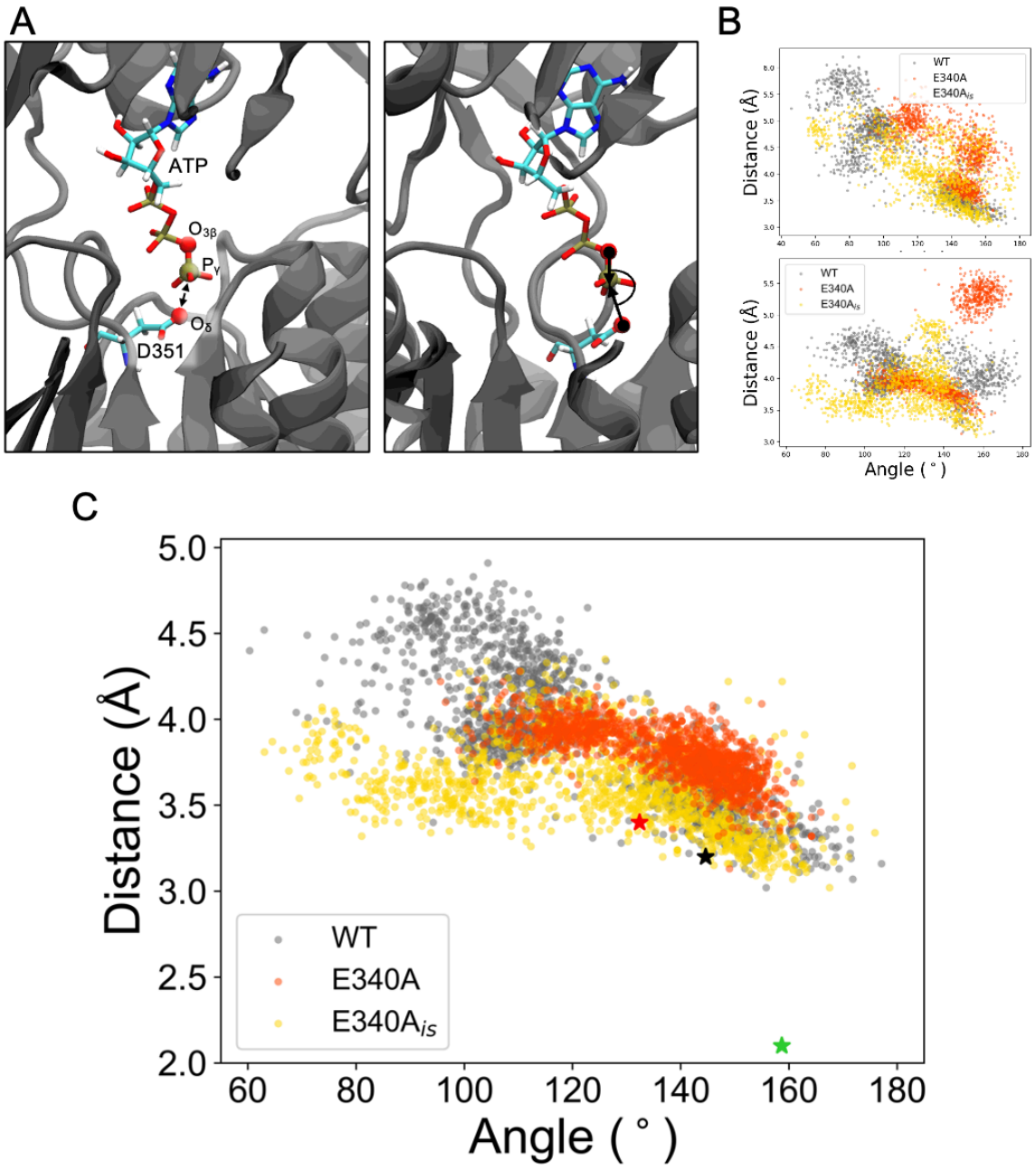

Figure 8.10: Analysis of the ATPase site in the N-P domains of WT (grey), E340A (orange) and E340A$_{is}$ (yellow). *Stars correspond to the reference values in respective crystal structures. Green star: 1T5T* (T. L. M. Sørensen et al., 2004)*, ADP-AlF$_x$ complex. A) Visualisation of the phosphorylation site atoms and distance measurement between the O_δ of Asp351 and P_γ of ATP (left) and angle between the O_δ of Asp351 and $O_{3\beta}$ and P_γ of ATP (right). B) Geometry at the catalytic site as angles and distances between the $O_{3\beta}$ and P_γ of ATP and $O_{\delta1}$ of Asp351 (top) and $O_{\delta2}$ of Asp351 (bottom). C) Geometry of the catalytic site for the optimal O_δ for catalysis in each frame.*

(T. L. M. Sørensen et al., 2004). As seen in Figure 8.10C, the WT E1-AMP-PCP structure displays a large spread of angles (60° to 180°) and distances (3 Å to 5 Å), many of which are not compatible with an in-line associative attack. In E340A, the distances are more narrowly spread, mostly between 3.5 Å and 4Å, and the angles are more restricted toward the catalytically relevant obtuse angle, between 110° and 170°. However, E340A does not manage to adopt the values of the transition state, which WT does. E340A$_{is}$ displays an intermediate distribution, once again hinting that the system is still undergoing transition. The dynamics of the E340A phosphorylation site support the hypothesis that it stabilises a more occluded state and conversely the glutamate might ensure greater dynamics to retain catalytic efficiency.

Chapter 9: Discussion and conclusion Part II

In this collaborative study, the Bublitz laboratory established that the E340A mutation in SERCA shows impaired Ca^{2+} binding and unbinding - a process that involves ion occlusion. The crystal structure of E340A revealed a less connected A-domain and a lowered headpiece and yet there was no observable difference in the geometry and structure of the Ca^{2+} binding site or ATPase site in the E340A crystal structure. Clearly, the structural data could not assess the effect of this mutation on the protein dynamics in a membrane context. Hence, all-atom MD simulations of both WT and E340A SERCA in an all-POPC membrane provided crucial insight into the effects of the mutation and thereby into the role of the conserved Glu340.

The crystal structure revealed a loss of electrostatic interactions between Glu340 and the tip of M3 and Arg822. With no perturbation of the Ca^{2+} binding site in the TM domain of the structure, an alteration in the kinetics of binding induced by the mutation could explain the impaired activity and this is discussed below. It is worth noting that the geometry and dynamics of the Ca^{2+} binding site in the simulation were analysed by considering the RMSD of Ca^{2+}, however this showed that the ions remain tightly bound in both WT and E340A and corroborates that the functional impairment must in fact lie in altered occlusion behaviour of other regions of the protein.

The downward movement of the headpiece observed in the crystal structure was also observed in the dynamics of the mutant (Figure 8.4). The trajectory of this movement is identical to that when WT SERCA binds and occludes Ca^{2+} and shifts from empty MgE1 to Ca_2E1. In E340A, the loss of the glutamate accommodates an overshoot of this tilt, stabilising a more occluded state of SERCA that slows down

the binding and unbinding dynamics of Ca^{2+}. If this overshoot is accommodated by the greater space available between P1 and the top of M3, then the glutamate may be conserved to act as a spacer to retain the structural integrity of the soluble domain.

The A-domain loses a significant number of contacts with the N/P domain body (Figure 8.5), suggesting that this would increase its flexibility. The functional implication of this is not yet clear, although it could impair the A-domain's ability to engage with the N/P body to promote catalytic turnover. Crystal structures, X-ray solution scattering and our MD simulations show that the A-domain is the most mobile and flexible domain in P-type ATPases and is known to ‘flip’ in and out of contact with the N- and P-domains (Clausen et al., 2013; Olesen et al., 2007; Ravishankar et al., 2020; Toyoshima et al., 2004). Moreover, it directly interacts and impacts the behaviour of M1 and M3 through its linkage and this could explain the rigidification of M1 (Figure 8.9).

The loss of interaction of residue 340 with Arg822 is particularly prevalent as there was no immediate consequence noted in the crystal structure. However, previous studies have shown that the adjacent loop 6-7 plays an important role in catalysis (Clausen & Andersen, 2004; Lenoir et al., 2004). For example, there is a notable similarity between the recorded behaviour of E340A and some L6-7 mutants, including R822A. Furthering this interesting link, a recent study on SERCA3b found that conformational changes in the L6-7–P1 interaction, induced by long-range effects through the luminal region of the TM domain, cause changes to the structural arrangement of the headpiece (Zhang et al., 2020). Taken together, the simulation data suggests that loss of contact with Arg822 and its consequent irreversible swinging out of the P1-M3 interface plays an immediate role in impairing

WT Ca^{2+} occlusion and conversely suggests that Glu340 is required to maintain these interactions and the proper kinetics for substrate occlusion.

Concomitant with Arg822 swinging out, a small inward shift of the tip of M3 in E340A is observed in the simulation, possibly due to the loss of the carboxylate group, allowing Leu249 to shift inwards. Interestingly, a mutation of Leu249 at the tip of M3 to alanine leads to an increased rate of Ca^{2+} binding and unbinding (Clausen & Andersen, 2003), suggesting it plays a role in the process of occlusion. Furthermore, in the SERCA E309Q occlusion-deficient mutant, the tip of M3 is outward shifted (Clausen et al., 2013), this could mean that the tip of M3 acts like a fine-tuning regulatory element in the kinetics of Ca^{2+} occlusion.

Finally, two unique observations to come out of the simulation are that the M1 kink is seemingly rigidified by E340A and the ATPase site geometry clusters towards a more catalytically competent state. A structural and functional study of inhibited ADP-AlF_x SERCA illustrated that the Ca^{2+}-occluded SERCA structure did not deviate from the unoccluded AMP-PCP structure, suggesting that the difference lies in the altered dynamics between the two states (T. L. M. Sørensen et al., 2004). Furthermore, they uncovered that the inhibited state's M1 kink at Leu60 allows Phe57 to engage in a hydrophobic lock, which is involved in occluding calcium by preventing the helix to slide up and down [as is suggested by the straight M1 helix in the nucleotide-free structures (Toyoshima et al., 2001)]. Taken together, by being more rigid, this hydrophobic lock is less likely to open and close which would slow down the process of Ca^{2+} exchange with the cytoplasm.

Finally, the geometry of the ATPase site clearly illustrated that the mutant state was sampling geometries closer to a catalytically competent state defined by the bond lengths and angles (Figure 8.10). As was noted in the ADP-AlF_x transition

state structure publication (T. L. M. Sørensen et al., 2004), the altered geometry in the phosphorylation site can directly impact the binding kinetics without showing a noticeable difference in the static structure when compared to AMP-PCP-bound SERCA.

A component of this study worth commenting on is the behaviour of the E340A$_{is}$ simulations. The aim was to convert WT Glu340 to alanine by deleting the carboxylate coordinates and run the simulations as an internal control. The expectation was that by removing the functional group, the structure would alter and behaviour would converge to that of the experimentally determined E340A system. Instead, E340A$_{is}$ behaved like a hybrid state between WT and E340A. Whilst the Arg822, M3 motion and M1 kink behaved like E340A, the headpiece tilt, connectivity of the A-domain and to a certain extent the phosphorylation geometry closely matched the WT simulation. On the one hand, this could be because E340A$_{is}$ is still undergoing a transition from WT to E340A, as Figure 8.7C illustrates with a much greater RMSD in L6-7 compared to WT and E340A. However, extension of the simulation length of E340A$_{is}$ to 400 ns did not alter the results (data not shown). Alternatively, E340A$_{is}$ may have equilibrated to a hybrid state between WT and E340A. It is conceivable that the impact Glu/Ala340 has on the structure is induced during the folding of the protein or only manifests itself upon cycling through larger-scale conformational changes. The *in silico* mutant might, therefore, be stuck in a local energy minimum in the energy landscape, representing a transition from WT to E340A (Figure 9.1).

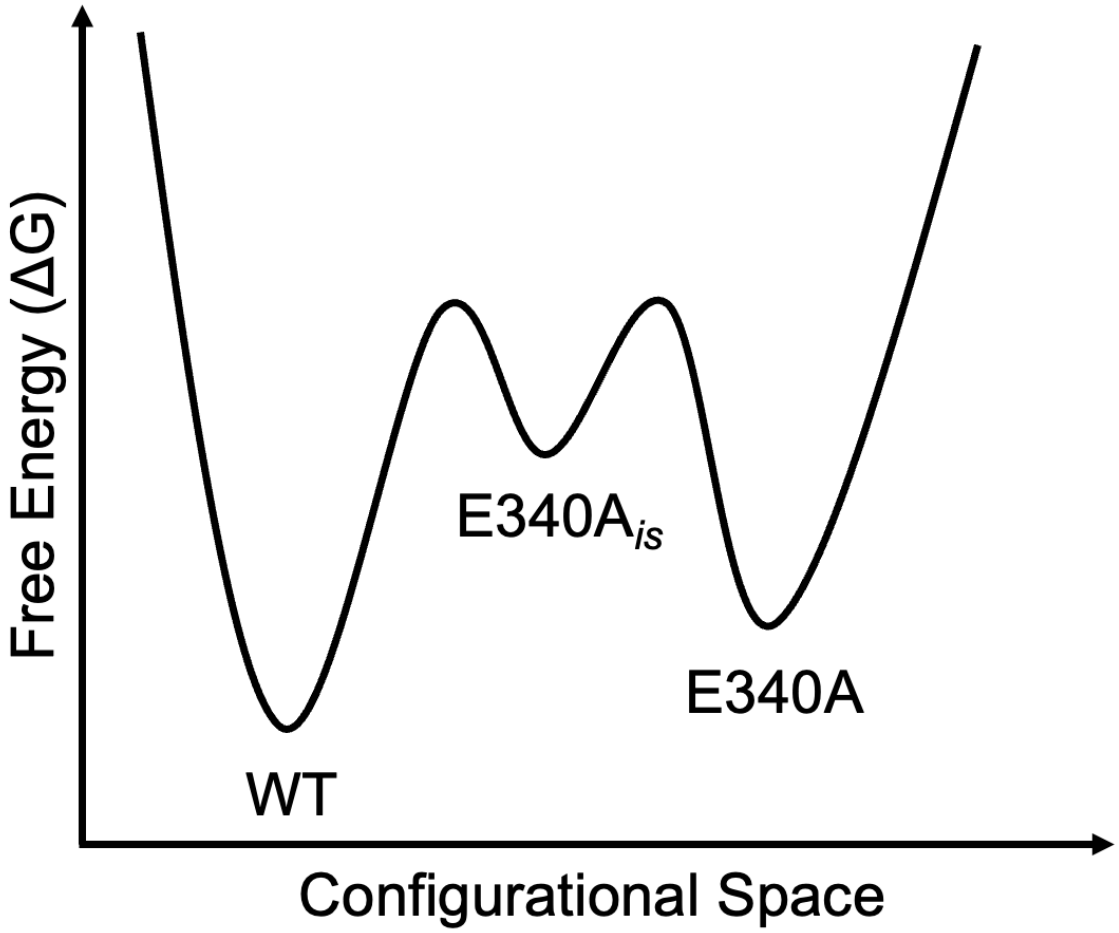

Figure 9.1: Proposed potential free energy landscape for WT, E340A and E340A$_{is}$ Ca_2E1 SERCA.

Whilst this study culminated in the referenced publication (Geurts et al., 2020), given more time, several follow up studies would be interesting to consider. Firstly, the study suggests that E340A stabilises a more occluded state. A possible limitation to this is that the study only considered the dynamics of the mutant on the E1 AMP-PCP stabilised state and that this might not represent the entire picture. Although the first functional study of E340A finds that the slowing of the $H_nE2 \rightarrow E1 \rightarrow Ca_2E1$ reaction is due to inhibition of the latter part of this reaction sequence and not the remaining partial reaction steps of the transport cycle (Clausen & Andersen, 2004), the study should be extended to consider the role of the mutant on the dynamics of E2 states of SERCA as this may be hidden within the dynamics.

Secondly, the ADP-AlF_x transition state that has fully occluded Ca^{2+}, but does not deviate structurally from the Ca_2E1 AMP-PCP structure, is said to differ in its dynamics. Therefore, to further understand what constitutes the dynamics of a fully occluded SERCA, running the same simulations on the ADP-AlF_x structure (PDB 1T5T) could provide further information and confirm whether the reduced M1 dynamics is a feature of an occluded SERCA.

Further insight into occlusion could be gained from simulating other known mutations of SERCA that influence the occlusion of calcium, such as the mutation R822A. However, the drawback in this is that such simulations require crystal structures, as *in silico* mutants may not equilibrate to their native state. However, heterologous expression and purification of functional SERCA mutants has been a challenge to date.

Finally, this study illustrates the value in using MD to investigate P-Type ATPases. Given the ability to gain atomic-level detail into the dynamics of a given catalytic state, the field could benefit from a wider study using MD to investigate the dynamics of each of the structurally resolved catalytic states to address some of the open questions remaining in the field. For example, this would be able to further investigate the cross-talk between the substrate and phosphorylation domains in P-type ATPases at the different stages of the catalytic cycle, and further probe the M1-kink and formation of the hydrophobic lock. Even more so, Chapter 3 illustrated that the M1 of Pma1 may interact with anionic lipids, and so investigating the catalytic cycle in a complex, native-like membrane could shed further light on the TM dynamics and interaction with individual lipids. Having said that, there are a few limitations to atomistic MD simulations that are worth mentioning. Firstly, the quality of the results heavily depends on the reliance of the input models. As can be seen

in this study, E340A$_{is}$ behaves unlike both WT and E340A. The crystal structure of a protein might be that of an artifact and therefore by extension, the results obtained from simulating such a structure need to be carefully considered. Moreover, certain approximations are made that limit the potential use of MD. For example, according to the Born-Oppenheimer approximation, MD simulations consider the nuclei only and therefore force fields are incapable of describing processes that include electron transfer and therefore the dynamics of SERCA phosphorylation and full catalysis mechanism cannot be studied. This underpins the importance of combining simulation data with experiment wherever possible.

To conclude, the above findings illustrate how MD simulations can provide key insights not captured by static structures obtained through traditional techniques such as X-ray crystallography and cryoEM. The results led to the proposal that SERCA E340A exhibits a more occluded confirmation and that the conserved E340 acts as a spacer between the soluble domain and TM domain, aiding retention of the dynamic flexibility required for efficient turnover.

References

Aaronson, L. R., & Martin, C. E. (1983). Temperature-induced modifications of glycosphingolipids in plasma membranes of Neurospora crassa. *BBA - Biomembranes*, *735*(2), 252–258. https://doi.org/10.1016/0005-2736(83)90300-0

Abraham, M. J., Murtola, T., Schulz, R., Páll, S., Smith, J. C., Hess, B., & Lindah, E. (2015). Gromacs: High performance molecular simulations through multi-level parallelism from laptops to supercomputers. *SoftwareX*, *1–2*, 19–25. https://doi.org/10.1016/j.softx.2015.06.001

Addison, R., & Scarborough, G. A. (1981a). Solubilization and Purification of the. *Reactions*, *256*(24), 13165–13171.

Addison, R., & Scarborough, G. A. (1981b). Solubilization and purification of the Neurospora plasma membrane H+-ATPase. *Journal of Biological Chemistry*, *256*(24), 13165–13171. https://doi.org/10.1016/s0021-9258(18)43022-0

Albers, R. W. (1967). Biochemical aspects of active transport. *Annual Review of Biochemistry*, *36*(44), 727–756. https://doi.org/10.1146/annurev.bi.36.070167.003455

Andersen, H. C. (1980). Molecular dynamics simulations at constant pressure and/or temperature. *The Journal of Chemical Physics*, *72*(4), 2384–2393. https://doi.org/10.1063/1.439486

Andersen, O. S., & Koeppe, R. E. (2007). Bilayer thickness and membrane protein function: An energetic perspective. *Annual Review of Biophysics and Biomolecular Structure*, *36*, 107–130. https://doi.org/10.1146/annurev.biophys.36.040306.132643

Anger, M., Samuel, J. L., Marotte, F., Wuytack, F., Rappaport, L., & Lompré, A. M. (1993). The sarco(endo)plasmic reticulum Ca(2+)-ATPase mRNA isoform, SERCA 3, is expressed in endothelial and epithelial cells in various organs. *FEBS Letters*, *334*(1), 45–48. https://doi.org/10.1016/0014-5793(93)81677-r

Athanasopoulos, A., André, B., Sophianopoulou, V., & Gournas, C. (2019). Fungal plasma membrane domains. *FEMS Microbiology Reviews*, *43*(6), 642–673. https://doi.org/10.1093/femsre/fuz022

Autzen, H. E., Siuda, I., Sonntag, Y., Nissen, P., Møller, J. V., & Thøgersen, L. (2015). Regulation of the Ca2+-ATPase by cholesterol: A specific or non-specific effect? *Molecular Membrane Biology*, *32*(3), 75–87. https://doi.org/10.3109/09687688.2015.1073382

Axelsen, K. B., & Palmgren, M. G. (1998). Evolution of substrate specificities in the P-type ATPase superfamily. *Journal of Molecular Evolution*, *46*(1), 84–101. https://doi.org/10.1007/PL00006286

Baginski, E. S., Foà, P. P., & Zak, B. (1967). Microdetermination of inorganic phosphate, phospholipids, and total phosphate in biologic materials. *Clinical Chemistry*, *13*(4), 326–332. https://doi.org/10.1093/clinchem/13.4.326

Bagnat, M., Chang, A., & Simons, K. (2001). Plasma membrane proton ATPase Pma1p requires raft association for surface delivery in yeast. *Molecular Biology of the Cell*, *12*(12), 4129–4138. https://doi.org/10.1091/mbc.12.12.4129

Bagshaw, C. R. (2001). ATP analogues at a glance. *Journal of Cell Science*, *114*(3), 459–460.

Berendsen, H. J. C., Postma, J. P. M., van Gunsteren, W. F., Dinola, A., & Haak, J. R. (1984). Molecular dynamics with coupling to an external bath. *The Journal of Chemical Physics*, *81*(8), 3684–3690. https://doi.org/10.1063/1.448118

Berendsen, H. J. C., van der Spoel, D., & van Drunen, R. (1995). GROMACS: A message-passing parallel molecular dynamics implementation. *Computer Physics Communications*, *91*(1–3), 43–56. https://doi.org/10.1016/0010-4655(95)00042-E

Best, R. B., Zhu, X., Shim, J., Lopes, P. E. M., Mittal, J., Feig, M., & MacKerell, A. D. (2012). Optimization of the additive CHARMM all-atom protein force field targeting improved sampling of the backbone φ, ψ and side-chain χ1 and χ2 Dihedral Angles. *Journal of Chemical Theory and Computation*, *8*(9), 3257–3273. https://doi.org/10.1021/ct300400x

Bond, P. J., Holyoake, J., Ivetac, A., Khalid, S., & Sansom, M. S. P. (2007). Coarse-grained molecular dynamics simulations of membrane proteins and peptides. *Journal of Structural Biology*, *157*(3), 593–605. https://doi.org/10.1016/j.jsb.2006.10.004

Bowman, B. J., Blasco, F., & Slayman, C. W. (1981). Purification and characterization of the plasma membrane ATPase of Neurospora crassa. *The Journal of Biological Chemistry*, *256*(23), 12343–12349.

Bradford, M. M. (1976). A rapid and sensitive method for the quantitation of microgram quantities of protein utilizing the principle of protein-dye binding. *Analytical Biochemistry*, *72*, 248–254. https://doi.org/10.1006/abio.1976.9999

Breitkopf, S. B., & Asara, J. M. (2012). Determining in vivo phosphorylation sites using mass spectrometry. *Current Protocols in Molecular Biology*, *1*(SUPPL.98). https://doi.org/10.1002/0471142727.mb1819s98

Bublitz, M., Kjellerup, L., Cohrt, K. O. H., Gordon, S., Mortensen, A. L., Clausen, J. D., Pallin, T. D., Hansen, J. B., Fuglsang, A. T., Dalby-Brown, W., & Winther, A. M. L. (2018). Tetrahydrocarbazoles are a novel class of potent P-type ATPase inhibitors with antifungal activity. *PLoS ONE*, *13*(1), 1–21. https://doi.org/10.1371/journal.pone.0188620

Bublitz, M., Morth, J. P., & Nissen, P. (2011). P-type ATPases at a glance. *Journal of Cell Science*, *124*(15), 2515–2519. https://doi.org/10.1242/jcs.088716

Bublitz, M., Poulsen, H., Morth, J. P., & Nissen, P. (2010). In and out of the cation pumps: P-Type ATPase structure revisited. *Current Opinion in Structural Biology*, *20*(4), 431–439. https://doi.org/10.1016/j.sbi.2010.06.007

Bussi, G., Donadio, D., & Parrinello, M. (2007). Canonical sampling through velocity rescaling. *Journal of Chemical Physics*, *126*(1). https://doi.org/10.1063/1.2408420

Camley, B. A., Lerner, M. G., Pastor, R. W., & Brown, F. L. H. (2015). Strong influence of periodic boundary conditions on lateral diffusion in lipid bilayer membranes. *Journal of Chemical Physics*, *143*(24). https://doi.org/10.1063/1.4932980

Chadwick, C. C., Goormaghtigh, E., & Scarborough, G. A. (1987). A hexameric form of the Neurospora crassa plasma membrane H+-ATPase. *Archives of Biochemistry and Biophysics*, *252*(2), 348–356. https://doi.org/10.1016/0003-9861(87)90041-5

Champeil, P., Riollet, S., Orlowski, S., Guillain, F., Seebregts, C. J., & McIntosh, D. B. (1988). ATP regulation of sarcoplasmic reticulum Ca2+-ATPase. Metal-free ATP and 8-bromo-ATP bind with high affinity to the catalytic site of phosphorylated ATPase and accelerate dephosphorylation. *The Journal of Biological Chemistry*, *263*(25), 12288–12294.

Chang, A., & Fink, G. R. (1995). Targeting of the yeast plasma membrane [H+]ATPase: A novel gene AST1 prevents mislocalization of mutant ATPase to the vacuole. *Journal of Cell Biology*, *128*(1–2), 39–49. https://doi.org/10.1083/jcb.128.1.39

Cid, A., Perona, R., & Serrano, R. (1987). Replacement of the promoter of the yeast plasma membrane ATPase gene by a galactose-dependent promoter and its physiological consequences. *Current Genetics*, *12*(2), 105–110. https://doi.org/10.1007/BF00434664

Clausen, J. D., & Andersen, J. P. (2003). Roles of Leu249, Lys252, and Leu253 in membrane segment M3 of sarcoplasmic reticulum Ca2+-ATPase in control of Ca2+ migration and long-range intramolecular communication. *Biochemistry*, *42*(9), 2585–2594. https://doi.org/10.1021/bi0271897

Clausen, J. D., & Andersen, J. P. (2004). Functional consequences of alterations to Thr247, Pro 248, Glu340, Asp813, Arg819, and Arg822 at the interfaces between domain P, M3, and L6-7 of sarcoplasmic reticulum Ca2+-ATPase: Roles in Ca2+ interaction and phosphoenzyme processing. *Journal of Biological Chemistry*, *279*(52), 54426–54437. https://doi.org/10.1074/jbc.M410204200

Clausen, J. D., Bublitz, M., Arnou, B., Montigny, C., Jaxel, C., Møller, J. V., Nissen, P., Andersen, J. P., & le Maire, M. (2013). SERCA mutant E309Q binds two Ca 2+ ions but adopts a catalytically incompetent conformation. *EMBO Journal*, *32*(24), 3231–3243. https://doi.org/10.1038/emboj.2013.250

Cornelius, F., Habeck, M., Kanai, R., Toyoshima, C., & Karlish, S. J. D. (2015). General and specific lipid-protein interactions in Na,K-ATPase. *Biochimica et Biophysica Acta - Biomembranes*, *1848*(9), 1729–1743. https://doi.org/10.1016/j.bbamem.2015.03.012

Cornell, C. E., Mileant, A., Thakkar, N., Lee, K. K., & Keller, S. L. (2020). Direct imaging of liquid domains in membranes by cryo-electron tomography. *Proceedings of the National Academy of Sciences of the United States of America*, *117*(33), 19713–19719. https://doi.org/10.1073/PNAS.2002245117

Coupland, C. E., Andrei, S. A., Ansell, T. B., Carrique, L., Kumar, P., Sefer, L., Schwab, R. A., Byrne, E. F. X., Pardon, E., Steyaert, J., Magee, A. I., Lanyon-Hogg, T., Sansom, M. S. P., Tate, E. W., & Siebold, C. (2021). Structure, mechanism, and inhibition of Hedgehog acyltransferase. *Molecular Cell*, *81*(24), 5025-5038.e10. https://doi.org/10.1016/j.molcel.2021.11.018

Cyrklaff, M., Auer, M., Kühlbrandt, W., & Scarborough, G. A. (1995). 2-D structure of the Neurospora crassa plasma membrane ATPase as determined by electron cryomicroscopy. *EMBO Journal*, *14*(9), 1854–1857. https://doi.org/10.1002/j.1460-2075.1995.tb07177.x

Daiho, T., Danko, S., Yamasaki, K., & Suzuki, H. (2010). Stable structural analog of Ca2+-ATPase ADP-insensitive phosphoenzyme with occluded Ca2+ formed by elongation of A-domain/M1′-linker and beryllium fluoride binding. *Journal of Biological Chemistry*, *285*(32), 24538–24547. https://doi.org/10.1074/jbc.M110.144535

Danko, S., Yamasaki, K., Daiho, T., & Suzuki, H. (2004). Distinct natures of beryllium fluoride-bound, aluminum fluoride-bound, and magnesium fluoride-bound stable analogues of an ADP-insensitive phosphoenzyme intermediate of sarcoplasmic reticulum Ca2+-ATPase: Changes in catalytic and transport sites during ph. *Journal of Biological Chemistry*, *279*(15), 14991–14998. https://doi.org/10.1074/jbc.M313363200

Darden, T., York, D., & Pedersen, L. (1993). Particle mesh Ewald: An N·log(N) method for Ewald sums in large systems. *The Journal of Chemical Physics*, *98*(12), 10089–10092. https://doi.org/10.1063/1.464397

de Jong, D. H., Singh, G., Bennett, W. F. D., Arnarez, C., Wassenaar, T. A., Schäfer, L. v., Periole, X., Tieleman, D. P., & Marrink, S. J. (2013). Improved parameters for the martini coarse-grained protein force field. *Journal of Chemical Theory and Computation*, *9*(1), 687–697. https://doi.org/10.1021/ct300646g

de Meyer, F., & Smit, B. (2009). Effect of cholesterol on the structure of a phospholipid bilayer. *Proceedings of the National Academy of Sciences of the United States of America*, *106*(10), 3654–3658. https://doi.org/10.1073/pnas.0809959106

Dehay, B., Ramirez, A., Martinez-Vicente, M., Perier, C., Canron, M. H., Doudnikoff, E., Vital, A., Vila, M., Klein, C., & Bezard, E. (2012). Loss of P-type ATPase ATP13A2/PARK9 function induces general lysosomal deficiency and leads to Parkinson disease neurodegeneration. *Proceedings of the National Academy of Sciences of the United States of America*, *109*(24), 9611–9616. https://doi.org/10.1073/pnas.1112368109

Dieudonné, T., Herrera, S. A., Laursen, M. J., Lejeune, M., Stock, C., Slimani, K., Jaxel, C., Lyons, J. A., Montigny, C., Pomorski, T. G., Nissen, P., & Lenoir, G. (2022). Autoinhibition and regulation by phosphoinositides of ATP8B1, a human lipid flippase associated with intrahepatic cholestatic disorders. *ELife*, *11*, 1–33. https://doi.org/10.7554/eLife.75272

Drachmann, N. D., Olesen, C., Møller, J. v., Guo, Z., Nissen, P., & Bublitz, M. (2014). Comparing crystal structures of Ca(2+) -ATPase in the presence of

different lipids. *The FEBS Journal*, *281*(18), 4249–4262. https://doi.org/10.1111/febs.12957

Dufour, J., & Goffeau, A. (1980). Molecular and Kinetic Properties of the Purified Plasma Membrane ATPase of the Yeast Schizosaccharomyces pombe. *European Journal of Biochemistry*, *105*(1), 145–154. https://doi.org/10.1111/j.1432-1033.1980.tb04484.x

Dupont, S., Lemetais, G., Ferreira, T., Cayot, P., Gervais, P., & Beney, L. (2012). Ergosterol biosynthesis: a fungal pathway for life on land? *Evolution; International Journal of Organic Evolution*, *66*(9), 2961–2968. https://doi.org/10.1111/j.1558-5646.2012.01667.x

Eisenkolb, M., Zenzmaier, C., Leitner, E., & Schneiter, R. (2002). A Specific Structural Requirement for Ergosterol in Long-chain Fatty Acid Synthesis Mutants Important for Maintaining Raft Domains in Yeast. *Molecular Biology of the Cell*, *13*, 4414–4428. https://doi.org/10.1091/mbc.E02

Eraso, P., & Gancedo, C. (1987). Activation of yeast plasma membrane ATPase by acid pH during growth. *FEBS Letters*, *224*(1), 187–192. https://doi.org/10.1016/0014-5793(87)80445-3

Eraso, P., Mazón, M. J., & Portillo, F. (2006). Yeast protein kinase Ptk2 localizes at the plasma membrane and phosphorylates in vitro the C-terminal peptide of the H+-ATPase. *Biochimica et Biophysica Acta*, *1758*(2), 164–170. https://doi.org/10.1016/j.bbamem.2006.01.010

Erhart, E., & Hollenberg, C. P. (1983). The presence of a defective LEU2 gene on 2μ DNA recombinant plasmids of Saccharomyces cerevisiae is responsible for curing and high copy number. *Journal of Bacteriology*, *156*(2), 625–635. https://doi.org/10.1128/jb.156.2.625-635.1983

Ewald, P. P. (1921). Die Berechnung optischer und elektrostatischer Gitterpotentiale. *Annalen Der Physik*, *369*(3), 253–287. https://doi.org/https://doi.org/10.1002/andp.19213690304

Fajardo-Somera, R. A., Bowman, B., & Riquelme, M. (2013). The plasma membrane proton pump PMA-1 is incorporated into distal parts of the hyphae independently of the spitzenkörper in Neurospora crassa. *Eukaryotic Cell*, *12*(8), 1097–1105. https://doi.org/10.1128/EC.00328-12

Falson, P., Menguy, T., Corre, F., Bouneau, L., de Gracia, A. G., Soulié, S., Centeno, F., Moller, J. v, Champeil, P., & le Maire, M. (1997). The cytoplasmic loop between putative transmembrane segments 6 and 7 in sarcoplasmic reticulum Ca2+-ATPase binds Ca2+ and is functionally important. *The Journal of Biological Chemistry*, *272*(28), 17258—17262. https://doi.org/10.1074/jbc.272.28.17258

Fernandes, A. R., & Sá-Correia, I. (2003). Transcription patterns of PMA1 and PMA2 genes and activity of plasma membrane H+-ATPase in Saccharomyces cerevisiae during diauxic growth and stationary phase. *Yeast*, *20*(3), 207–219. https://doi.org/10.1002/yea.957

Ferreira, T., Mason, A. B., & Slayman, C. W. (2001). The Yeast Pma1 Proton Pump: A Model for Understanding the Biogenesis of Plasma Membrane Proteins.

Journal of Biological Chemistry, *276*(32), 29613–29616. https://doi.org/10.1074/jbc.R100022200

Focht, D., Croll, T. I., Pedersen, B. P., & Nissen, P. (2017). Improved model of proton pump crystal structure obtained by interactive molecular dynamics flexible fitting expands the mechanistic model for proton translocation in P-type ATPases. *Frontiers in Physiology*, *8*(APR). https://doi.org/10.3389/fphys.2017.00202

Friedman, K. J., & Glick, D. (1980). Role of lipids in the Neurospora crassa membrane: III. Lipid composition and phase transition properties of the plasma membrane, and its components. *The Journal of Membrane Biology*, *54*(3), 183–190. https://doi.org/10.1007/BF01870234

Gaigg, B., Timischl, B., Corbino, L., & Schneiter, R. (2005). Synthesis of sphingolipids with very long chain fatty acids but not ergosterol is required for routing of newly synthesized plasma membrane ATPase to the cell surface of yeast. *Journal of Biological Chemistry*, *280*(23), 22515–22522. https://doi.org/10.1074/jbc.M413472200

Gaigg, B., Toulmay, A., & Schneiter, R. (2006). Very long-chain fatty acid-containing lipids rather than sphingolipids per se are required for raft association and stable surface transport of newly synthesized plasma membrane ATPase in yeast. *Journal of Biological Chemistry*, *281*(45), 34135–34145. https://doi.org/10.1074/jbc.M603791200

Gasteiger, E., Hoogland, C., Gattiker, A., Duvaud, S., Wilkins, M. R., Appel, R. D., & Bairoch, A. (2005). Protein Identification and Analysis Tools on the ExPASy Server. In J. M. Walker (Ed.), *The Proteomics Protocols Handbook* (pp. 571–607). Humana Press. https://doi.org/10.1385/1-59259-890-0:571

Geurts, M. M. G., Clausen, J. D., Arnou, B., Montigny, C., Lenoir, G., Corey, R. A., Jaxel, C., Møller, J. v., Nissen, P., Andersen, J. P., le Maire, M., & Bublitz, M. (2020). The SERCA residue Glu340 mediates interdomain communication that guides Ca2+transport. *Proceedings of the National Academy of Sciences of the United States of America*, *117*(49), 31114–31122. https://doi.org/10.1073/pnas.2014896117

Geva, Y., Crissman, J., Arakel, E. C., Gómez-Navarro, N., Chuartzman, S. G., Stahmer, K. R., Schwappach, B., Miller, E. A., & Schuldiner, M. (2017). Two novel effectors of trafficking and maturation of the yeast plasma membrane H(+) -ATPase. *Traffic (Copenhagen, Denmark)*, *18*(10), 672–682. https://doi.org/10.1111/tra.12503

Gong, X., & Chang, A. (2001). A mutant plasma membrane ATPase, Pma1-10, is defective in stability at the yeast cell surface. *Proceedings of the National Academy of Sciences of the United States of America*, *98*(16), 9104–9109. https://doi.org/10.1073/pnas.161282998

Goormaghtigh, E., Chadwick, C., & Scarborough, G. A. (1986). Monomers of the Neurospora plasma membrane H+-ATPase catalyze efficient proton translocation. *The Journal of Biological Chemistry*, *261*(16), 7466–7471.

Graham, J. A., Essex, J. W., & Khalid, S. (2017). PyCGTOOL: Automated Generation of Coarse-Grained Molecular Dynamics Models from Atomistic Trajectories. *Journal of Chemical Information and Modeling*, *57*(4), 650–656. https://doi.org/10.1021/acs.jcim.7b00096

Gross, H., Kuebler, O., Bas, E., & Moor, H. (1978). Decoration of specific sites on freeze-fractured membranes. *Journal of Cell Biology*, *79*, 646–656.

Grossmann, G., Opekarová, M., Malinsky, J., Weig-Meckl, I., & Tanner, W. (2007). Membrane potential governs lateral segregation of plasma membrane proteins and lipids in yeast. *The EMBO Journal*, *26*(1), 1–8. https://doi.org/10.1038/sj.emboj.7601466

Habeck, M., Kapri-Pardes, E., Sharon, M., & Karlish, S. J. D. (2017). Specific phospholipid binding to Na,K-ATPase at two distinct sites. *Proceedings of the National Academy of Sciences*, 201620799. https://doi.org/10.1073/pnas.1620799114

Heberle, F. A., Doktorova, M., Scott, L., Skinkle, A. D., Waxham, M. N., Levental, I., Heberle, F. A., Doktorova, M., Scott, H. L., Skinkle, A. D., & Waxham, M. N. (2020). Direct label-free imaging of nanodomains in biomimetic and biological membranes by cryogenic electron microscopy. *Proceedings of the National Academy of Sciences of the United States of America*, *117*(41), 25944. https://doi.org/10.1073/pnas.2018746117

Heit, S., Geurts, M. M. G., Murphy, B. J., Corey, R. A., Mills, D. J., Kühlbrandt, W., & Bublitz, M. (2021). Structure of the hexameric fungal plasma membrane proton pump in its autoinhibited state. *Science Advances*, *7*(46), 1–13. https://doi.org/10.1126/sciadv.abj5255

Hofmann, S., Januliene, D., Mehdipour, A. R., Thomas, C., Stefan, E., Brüchert, S., Kuhn, B. T., Geertsma, E. R., Hummer, G., Tampé, R., & Moeller, A. (2019). Conformation space of a heterodimeric ABC exporter under turnover conditions. *Nature*, *571*(7766), 580–583. https://doi.org/10.1038/s41586-019-1391-0

Hoover, W. G. (1985). Canonical dynamics: Equilibrium phase-space distributions. *Phys. Rev. A*, *31*(3), 1695–1697. https://doi.org/10.1103/PhysRevA.31.1695

Humphrey, W., Dalke, A., & Schulten, K. (1996). VMD: visual molecular dynamics. *Journal of Molecular Graphics*, *14*(1), 27-28,33-38. https://doi.org/10.1016/0263-7855(96)00018-5

Hunter, J. D. (2007). Matplotlib: A 2D Graphics Environment. *Computing in Science & Engineering*, *9*(3), 90–95. https://doi.org/10.1109/MCSE.2007.55

Ingólfsson, H. I., Arnarez, C., Periole, X., & Marrink, S. J. (2016). Computational “microscopy” of cellular membranes. *Journal of Cell Science*, *129*(2), 257–268. https://doi.org/10.1242/jcs.176040

Jahn, T., Fuglsang, A. T., Olsson, A., Brüntrup, I. M., Collinge, D. B., Volkmann, D., Sommarin, M., Palmgren, M. G., & Larsson, C. (1997). The 14-3-3 protein interacts directly with the C-terminal region of the plant plasma membrane H+-ATPase. *The Plant Cell*, *9*(10), 1805–1814. https://doi.org/10.1105/tpc.9.10.1805

Jardetzky, O. (1966). Simple Allosteric Model for Membrane Pumps. *Nature*, *211*(5052), 969–970. https://doi.org/10.1038/211969a0

Jefferies, D., & Khalid, S. (2021). Atomistic and coarse-grained simulations of membrane proteins: A practical guide. *Methods*, *185*(February 2020), 15–27. https://doi.org/10.1016/j.ymeth.2020.02.007

Jensen, A. M. L., Sørensen, T. L. M., Olesen, C., Møller, J. V., & Nissen, P. (2006). Modulatory and catalytic modes of ATP binding by the calcium pump. *EMBO Journal*, *25*(11), 2305–2314. https://doi.org/10.1038/sj.emboj.7601135

Jo, S., Kim, T., & Im, W. (2007). Automated builder and database of protein/membrane complexes for molecular dynamics simulations. *PLoS ONE*, *2*(9). https://doi.org/10.1371/journal.pone.0000880

Jones, J. E. (1924). On the Determination o f Molecular Fields.—II. From the Equation of State of a Gas. *Proceedings of the Royal Society of London A: Mathematical, Physical and Engineering Sciences*, 463–477.

Jumper, J., Evans, R., Pritzel, A., Green, T., Figurnov, M., Ronneberger, O., Tunyasuvunakool, K., Bates, R., Žídek, A., Potapenko, A., Bridgland, A., Meyer, C., Kohl, S. A. A., Ballard, A. J., Cowie, A., Romera-Paredes, B., Nikolov, S., Jain, R., Adler, J., … Hassabis, D. (2021). Highly accurate protein structure prediction with AlphaFold. *Nature*, *596*(7873), 583–589. https://doi.org/10.1038/s41586-021-03819-2

Kabsch, W., & Sander, C. (1983). Dictionary of protein secondary structure: pattern recognition of hydrogen-bonded and geometrical features. *Biopolymers*, *22*(12), 2577–2637. https://doi.org/10.1002/bip.360221211

Kaiser, H. J., Orłowski, A., Róg, T., Nyholm, T. K. M., Chai, W., Feizi, T., Lingwood, D., Vattulainen, I., & Simons, K. (2011). Lateral sorting in model membranes by cholesterol-mediated hydrophobic matching. *Proceedings of the National Academy of Sciences of the United States of America*, *108*(40), 16628–16633. https://doi.org/10.1073/pnas.1103742108

Kandt, C., Ash, W. L., & Peter Tieleman, D. (2007). Setting up and running molecular dynamics simulations of membrane proteins. *Methods*, *41*(4), 475–488. https://doi.org/10.1016/j.ymeth.2006.08.006

Klose, C., Surma, M. A., Gerl, M. J., Meyenhofer, F., Shevchenko, A., & Simons, K. (2012). Flexibility of a eukaryotic lipidome--insights from yeast lipidomics. *PloS One*, *7*(4), e35063. https://doi.org/10.1371/journal.pone.0035063

Kühlbrandt, W. (2004). Biology, structure and mechanism of P-type ATPases. *Nature Reviews Molecular Cell Biology*, *5*(4), 282–295. https://doi.org/10.1038/nrm1354

Kühlbrandt, W., Zeelen, J., & Dietrich, J. (2002). Structure, mechanism, and regulation of the Neurospora plasma membrane H+-ATpase. *Science*, *297*(5587), 1692–1696. https://doi.org/10.1126/science.1072574

Leach, A. R. (2001). *Molecular modelling: principles and applications* (Second Edi). Pearson education.

Lecchi, S., Allen, K. E., Pardo, J. P., Mason, A. B., & Slayman, C. W. (2005). Conformational changes of yeast plasma membrane H(+)-ATPase during

activation by glucose: role of threonine-912 in the carboxy-terminal tail. *Biochemistry*, *44*(50), 16624–16632. https://doi.org/10.1021/bi051555f

Lecchi, S., Nelson, C. J., Allen, K. E., Swaney, D. L., Thompson, K. L., Coon, J. J., Sussman, M. R., & Slayman, C. W. (2007). Tandem phosphorylation of Ser-911 and Thr-912 at the C terminus of yeast plasma membrane H+-ATPase leads to glucose-dependent activation. *The Journal of Biological Chemistry*, *282*(49), 35471–35481. https://doi.org/10.1074/jbc.M706094200

Lee, J., Cheng, X., Swails, J. M., Yeom, M. S., Eastman, P. K., Lemkul, J. A., Wei, S., Buckner, J., Jeong, J. C., Qi, Y., Jo, S., Pande, V. S., Case, D. A., Brooks, C. L., MacKerell, A. D., Klauda, J. B., & Im, W. (2016). CHARMM-GUI Input Generator for NAMD, GROMACS, AMBER, OpenMM, and CHARMM/OpenMM Simulations Using the CHARMM36 Additive Force Field. *Journal of Chemical Theory and Computation*, *12*(1), 405–413. https://doi.org/10.1021/acs.jctc.5b00935

Lee, M. C. S., Hamamoto, S., & Schekman, R. (2002). Ceramide biosynthesis is required for the formation of the oligomeric H+-ATPase Pma1p in the yeast endoplasmic reticulum. *Journal of Biological Chemistry*, *277*(25), 22395–22401. https://doi.org/10.1074/jbc.M200450200

Lenoir, G., Picard, M., Møller, J. v., le Maire, M., Champeil, P., & Falson, P. (2004). Involvement of the L6-7 loop in SERCA1a Ca2+-ATPase activation by Ca2+ (or Sr2+) and ATP. *Journal of Biological Chemistry*, *279*(31), 32125–32133. https://doi.org/10.1074/jbc.M402934200

Levental, I., Grzybek, M., & Simons, K. (2011). Raft domains of variable properties and compositions in plasma membrane vesicles. *Proceedings of the National Academy of Sciences*, *108*(28), 11411–11416. https://doi.org/10.1073/pnas.1105996108

Levental, I., Levental, K. R., & Heberle, F. A. (2020). Lipid Rafts: Controversies Resolved, Mysteries Remain. *Trends in Cell Biology*, *30*(5), 341–353. https://doi.org/10.1016/j.tcb.2020.01.009

Li, P., Wang, K., Salustros, N., Grønberg, C., & Gourdon, P. (2021). Structure and transport mechanism of P5B-ATPases. *Nature Communications*, *12*(1), 2–9. https://doi.org/10.1038/s41467-021-24148-y

Liaci, A. M., Steigenberger, B., Telles de Souza, P. C., Tamara, S., Gröllers-Mulderij, M., Ogrissek, P., Marrink, S. J., Scheltema, R. A., & Förster, F. (2021). Structure of the human signal peptidase complex reveals the determinants for signal peptide cleavage. *Molecular Cell*, *81*(19), 3934-3948.e11. https://doi.org/10.1016/j.molcel.2021.07.031

Lindahl, E., & Sansom, M. S. (2008). Membrane proteins: molecular dynamics simulations. *Current Opinion in Structural Biology*, *18*(4), 425–431. https://doi.org/10.1016/j.sbi.2008.02.003

López, C. A., Rzepiela, A. J., de Vries, A. H., Dijkhuizen, L., Hünenberger, P. H., & Marrink, S. J. (2009). Martini Coarse-Grained Force Field: Extension to Carbohydrates. *Journal of Chemical Theory and Computation*, *5*(12), 3195–3210. https://doi.org/10.1021/ct900313w

Lund, S., & Møller, J. v. (1988). Biphasic kinetics of sarcoplasmic reticulum Ca2+-ATPase and the detergent-solubilized monomer. *The Journal of Biological Chemistry*, *263*(4), 1654–1664.

Malínská, K., Malínský, J., Opekarová, M., & Tanner, W. (2003). Visualization of protein compartmentation within the plasma membrane of living yeast cells. *Molecular Biology of the Cell*, *14*(11), 4427–4436. https://doi.org/10.1091/mbc.e03-04-0221

Malinska, K., Malinsky, J., Opekarova, M., & Tanner, W. (2004). Distribution of Can1p into stable domains reflects lateral protein segregation within the plasma membrane of living S. cerevisiae cells. *Journal of Cell Science*, *117*(Pt 25), 6031–6041. https://doi.org/10.1242/jcs.01493

Malinsky, J., Tanner, W., & Opekarova, M. (2016). Transmembrane voltage: Potential to induce lateral microdomains. *Biochimica et Biophysica Acta - Molecular and Cell Biology of Lipids*, *1861*(8), 806–811. https://doi.org/10.1016/j.bbalip.2016.02.012

Marrink, S. J., de Vries, A. H., & Mark, A. E. (2004). Coarse Grained Model for Semiquantitative Lipid Simulations. *Journal of Physical Chemistry B*, *108*(2), 750–760. https://doi.org/10.1021/jp036508g

Marrink, S. J., Risselada, H. J., Yefimov, S., Tieleman, D. P., & de Vries, A. H. (2007). The MARTINI force field: Coarse grained model for biomolecular simulations. *Journal of Physical Chemistry B*, *111*(27), 7812–7824. https://doi.org/10.1021/jp071097f

Marrink, S. J., & Tieleman, D. P. (2013). Perspective on the martini model. *Chemical Society Reviews*, *42*(16), 6801–6822. https://doi.org/10.1039/c3cs60093a

Mason, A. B., Kardos, T. B., & Monk, B. C. (1998). Regulation and pH-dependent expression of a bilaterally truncated yeast plasma membrane H+-ATPase. *Biochimica et Biophysica Acta*, *1372*(2), 261–271. https://doi.org/10.1016/s0005-2736(98)00065-0

Matsunaga, S., Yamada, T., Kobayashi, T., & Kawai, M. (2015). Scanning tunneling microscope observation of the phosphatidylserine domains in the phosphatidylcholine monolayer. *Langmuir*, *31*(19), 5449–5455. https://doi.org/10.1021/acs.langmuir.5b00859

Mazón, M. J., Eraso, P., & Portillo, F. (2015). Specific phosphoantibodies reveal two phosphorylation sites in yeast Pma1 in response to glucose. *FEMS Yeast Research*, *15*(5). https://doi.org/10.1093/femsyr/fov030

McKenna, M. J., Sim, S. I., Ordureau, A., Wei, L., Wade Harper, J., Shao, S., & Park, E. (2020). The endoplasmic reticulum P5A-ATPase is a transmembrane helix dislocase. *Science*, *369*(6511). https://doi.org/10.1126/science.abc5809

Menguy, T., Corre, F., Bouneau, L., Deschamps, S., Møller, J. V., Champeil, P., Maire, M. le, & Falson, P. (1998). The cytoplasmic loop located between transmembrane segments 6 and 7 controls activation by Ca2+ of sarcoplasmic reticulum Ca2+-ATPase. *Journal of Biological Chemistry*, *273*(32), 20134–20143. https://doi.org/10.1074/jbc.273.32.20134

Menguy, T., Corre, F., Juul, B., Bouneau, L., Lafitte, D., Derrick, P. J., Sharma, P. S., Falson, P., Levine, B. A., Møller, J. v., & le Mairea, M. (2002). Involvement of the cytoplasmic loop L6-7 in the entry mechanism for transport of Ca2+ through the sarcoplasmic reticulum Ca2+ATPase. *Journal of Biological Chemistry*, *277*(15), 13016–13028. https://doi.org/10.1074/jbc.M108899200

Michaud-Agrawal, N., Denning, E. J., Woolf, T. B., & Beckstein, O. (2011). MDAnalysis: a toolkit for the analysis of molecular dynamics simulations. *Journal of Computational Chemistry*, *32*(10), 2319–2327. https://doi.org/10.1002/jcc.21787

Mintz, E., Mata, A. M., Forge, V., Passafiume, M., & Guillain, F. (1995). The modulation of Ca2+ binding to sarcoplasmic reticulum ATPase by ATP analogues is pH-dependent. *The Journal of Biological Chemistry*, *270*(45), 27160–27164. https://doi.org/10.1074/jbc.270.45.27160

Miranda, M., Pardo, J. P., & Petrov, V. v. (2011). Structure-function relationships in membrane segment 6 of the yeast plasma membrane Pma1 H(+)-ATPase. *Biochimica et Biophysica Acta*, *1808*(7), 1781–1789. https://doi.org/10.1016/j.bbamem.2010.11.034

Møller, A. B., Asp, T., Holm, P. B., & Palmgren, M. G. (2008). Phylogenetic analysis of P5 P-type ATPases, a eukaryotic lineage of secretory pathway pumps. *Molecular Phylogenetics and Evolution*, *46*(2), 619–634. https://doi.org/10.1016/j.ympev.2007.10.023

Møller, J. v., Olesen, C., Winther, A. M. L., & Nissen, P. (2010). The sarcoplasmic Ca2+-ATPase: Design of a perfect chemi-osmotic pump. In *Quarterly Reviews of Biophysics* (Vol. 43, Issue 4). https://doi.org/10.1017/S003358351000017X

Monteiro, G. A., & Sá-Correia, I. (1998). In vivo activation of yeast plasma membrane H+-ATPase by ethanol: effect on the kinetic parameters and involvement of the carboxyl-terminus regulatory domain. *Biochimica et Biophysica Acta*, *1370*(2), 310–316. https://doi.org/10.1016/s0005-2736(97)00281-2

Monticelli, L., Kandasamy, S. K., Periole, X., Larson, R. G., Tieleman, D. P., & Marrink, S. J. (2008). The MARTINI coarse-grained force field: Extension to proteins. *Journal of Chemical Theory and Computation*, *4*(5), 819–834. https://doi.org/10.1021/ct700324x

Monticelli, L., & Tieleman, D. P. (2013). Force fields for classical molecular dynamics. *Methods in Molecular Biology (Clifton, N.J.)*, *924*, 197–213. https://doi.org/10.1007/978-1-62703-017-5_8

Moor, H., & Muhlethaler, K. (1963). Fine structure in frozen-etched yeast cells. *The Journal of Cell Biology*, *17*(3), 609–628.

Morsomme, P., Slayman, C. W., & Goffeau, A. (2000). Mutagenic study of the structure, function and biogenesis of the yeast plasma membrane H+-ATPase. *Biochimica et Biophysica Acta - Reviews on Biomembranes*, *1469*(3), 133–157. https://doi.org/10.1016/S0304-4157(00)00015-0

Nagiec, M. M., Nagiec, E. E., Baltisberger, J. A., Wells, G. B., Lester, R. L., & Dickson, R. C. (1997). Sphingolipid Synthesis as a Target for Antifungal Drugs:

COMPLEMENTATION OF THE INOSITOL PHOSPHORYLCERAMIDE SYNTHASE DEFECT IN A MUTANT STRAIN OF SACCHAROMYCES CEREVISIAE BY THE AUR1 GENE*. *Journal of Biological Chemistry*, *272*(15), 9809–9817. https://doi.org/https://doi.org/10.1074/jbc.272.15.9809

Nelson, N. (1999). Metal ion transporters and homeostasis. *EMBO Journal*, *18*(16), 4361–4371. https://doi.org/10.1093/emboj/18.16.4361

Olesen, C., Picard, M., Winther, A. M. L., Gyrup, C., Morth, J. P., Oxvig, C., Møller, J. V., & Nissen, P. (2007). The structural basis of calcium transport by the calcium pump. *Nature*, *450*(7172), 1036–1042. https://doi.org/10.1038/nature06418

Olesen, C., Sørensen, T. L. M., Nielsen, R. C., Møller, J. V., & Nissen, P. (2004). Dephosphorylation of the calcium pump coupled to counterion occlusion. *Science*, *306*(5705), 2251–2255. https://doi.org/10.1126/science.1106289

Onsager, L. (1936). Electric Moments of Molecules in Liquids. *Journal of the American Chemical Society*, *58*(8), 1486–1493. https://doi.org/10.1021/ja01299a050

Or, E., David, P., Shainskaya, A., Tal, D. M., & Karlish, S. J. (1993). Effects of competitive sodium-like antagonists on Na,K-ATPase suggest that cation occlusion from the cytoplasmic surface occurs in two steps. *The Journal of Biological Chemistry*, *268*(23), 16929–16937.

Palmgren, M. G. (2002). Plant Plasma Membrane H + -ATPases: Powerhouses for Nutrient Uptake. *Annual Review of Plant Physiology and Plant Molecular Biology*, *52*(1), 817–845. https://doi.org/10.1146/annurev.arplant.52.1.817

Parker, J. L., & Newstead, S. (2014). Method to increase the yield of eukaryotic membrane protein expression in saccharomyces cerevisiae for structural and functional studies. *Protein Science*, *23*(9), 1309–1314. https://doi.org/10.1002/pro.2507

Parrinello, M., & Rahman, A. (1981). Polymorphic transitions in single crystals: A new molecular dynamics method. *Journal of Applied Physics*, *52*(12), 7182–7190. https://doi.org/10.1063/1.328693

Pedersen, J. T., Falhof, J., Ekberg, K., Buch-Pedersen, M. J., & Palmgren, M. (2015). Metal fluoride inhibition of a P-type H+ pump stabilization of the phosphoenzyme intermediate contributes to post-translational pump activation. *Journal of Biological Chemistry*, *290*(33), 20396–20406. https://doi.org/10.1074/jbc.M115.639385

Pedersen, P. L., & Carafoli, E. (1987). Ion motive ATPases. II. Energy coupling and work output. *Trends in Biochemical Sciences*, *12*(C), 186–189. https://doi.org/10.1016/0968-0004(87)90090-9

Periasamy, M., & Kalyanasundaram, A. (2007). SERCA pump isoforms: Their role in calcium transport and disease. *Muscle and Nerve*, *35*(4), 430–442. https://doi.org/10.1002/mus.20745

Periole, X., Cavalli, M., Marrink, S. J., & Ceruso, M. A. (2009). Combining an elastic network with a coarse-grained molecular force field: Structure, dynamics, and

intermolecular recognition. *Journal of Chemical Theory and Computation*, *5*(9), 2531–2543. https://doi.org/10.1021/ct9002114

Permyakov, S., Suzina, N., & Valiakhmetov, A. (2012). Activation of H +-ATPase of the plasma membrane of saccharomyces cerevisiae by glucose: The role of sphingolipid and lateral enzyme mobility. *PLoS ONE*, *7*(2). https://doi.org/10.1371/journal.pone.0030966

Peter Mitchell. (1961). Coupling of Phosphorylation to Electron and Hydrogen Transfer by a Chemi-Osmotic type of Mechanism. *Nature*, *191*, 144–148.

Pettersen, E. F., Goddard, T. D., Huang, C. C., Meng, E. C., Couch, G. S., Croll, T. I., Morris, J. H., & Ferrin, T. E. (2021). UCSF ChimeraX: Structure visualization for researchers, educators, and developers. *Protein Science*, *30*(1), 70–82. https://doi.org/10.1002/pro.3943

Pinto, F. de T., & Adamo, H. P. (2002). Deletions in the acidic lipid-binding region of the plasma membrane Ca2+ pump. A mutant with high affinity for Ca2+ resembling the acidic lipid-activated enzyme. *The Journal of Biological Chemistry*, *277*(15), 12784–12789. https://doi.org/10.1074/jbc.M111055200

Post, R. L., Kume, S., Tobin, T., Orcutt, B., & Sen, A. K. (1969). Flexibility of an active center in sodium-plus-potassium adenosine triphosphatase. *Journal of General Physiology*, *54*(1), 306–326. https://doi.org/10.1085/jgp.54.1.306

Punjani, A., Rubinstein, J. L., Fleet, D. J., & Brubaker, M. A. (2017). CryoSPARC: Algorithms for rapid unsupervised cryo-EM structure determination. *Nature Methods*, *14*(3), 290–296. https://doi.org/10.1038/nmeth.4169

Punjani, A., Zhang, H., & Fleet, D. J. (2020). Non-uniform refinement: adaptive regularization improves single-particle cryo-EM reconstruction. *Nature Methods*, *17*(12), 1214–1221. https://doi.org/10.1038/s41592-020-00990-8

Rahman, A. (1964). Correlations in the Motion of Atoms in Liquid Argon. *Phys. Rev.*, *136*(2A), A405--A411. https://doi.org/10.1103/PhysRev.136.A405

Ravishankar, H., Pedersen, M. N., Eklund, M., Sitsel, A., Li, C., Duelli, A., Levantino, M., Wulff, M., Barth, A., Olesen, C., Nissen, P., & Andersson, M. (2020). Tracking Ca2+ ATPase intermediates in real time by x-ray solution scattering. *Science Advances*, *6*(12). https://doi.org/10.1126/sciadv.aaz0981

Rhee, K. H., Scarborough, G. A., & Henderson, R. (2002). Domain movements of plasma membrane H+-ATPase: 3D structures of two states by electron cryo-microscopy. *EMBO Journal*, *21*(14), 3582–3589. https://doi.org/10.1093/emboj/cdf385

Rosen, B. P. (2002). Transport and detoxification systems for transition metals, heavy metals and metalloids in eukaryotic and prokaryotic microbes. *Comparative Biochemistry and Physiology. Part A, Molecular & Integrative Physiology*, *133*(3), 689–693. https://doi.org/10.1016/s1095-6433(02)00201-5

Rukmini, R., Rawat, S. S., Biswas, S. C., & Chattopadhyay, A. (2001). Cholesterol organization in membranes at low concentrations: Effects of curvature stress and membrane thickness. *Biophysical Journal*, *81*(4), 2122–2134. https://doi.org/10.1016/S0006-3495(01)75860-2

Russo, C. J., & Passmore, L. A. (2014). Ultrastable gold substrates for electron cryomicroscopy. *Science*, *346*(6215), 1377–1381. https://doi.org/10.1126/science.1259530 A

Sansom, M. S. P., & Biggin, P. C. (2010). *Molecular simulations and biomembranes: from biophysics to function* (Issue 20). Royal Society of Chemistry.

Scarborough, G. A. (1975). Isolation and characterization of Neurospora crassa plasma membranes. *Journal of Biological Chemistry*, *250*(3), 1106–1111. https://doi.org/10.1016/s0021-9258(19)41896-6

Scarborough, G. A. (1985). A variant of the cell wall-less fz;sg;os-1 strain of Neurospora crassa with altered morphology and improved growth. *Experimental Mycology*, *9*(3), 5–78. https://doi.org/10.1016/0147-5975(85)90025-8

Scarborough, G. A. (1988). Large scale purification of plasma membrane H+-ATPase from a cell wall-less mutant of Neurospora crassa. *Methods in Enzymology*, *157*, 574–579.

Schlesser, A., Ulaszewski, S., Ghislain, M., & Goffeau, A. (1988). A second transport ATPase gene in Saccharomyces cerevisiae. *The Journal of Biological Chemistry*, *263*(36), 19480–19487.

Schmidt, T. G. M., Batz, L., Bonet, L., Carl, U., Holzapfel, G., Kiem, K., Matulewicz, K., Niermeier, D., Schuchardt, I., & Stanar, K. (2013). Development of the Twin-Strep-tag® and its application for purification of recombinant proteins from cell culture supernatants. *Protein Expression and Purification*, *92*(1), 54–61. https://doi.org/10.1016/j.pep.2013.08.021

Schneider, C. A., Rasband, W. S., & Eliceiri, K. W. (2012). NIH Image to ImageJ: 25 years of image analysis. *Nature Methods*, *9*(7), 671–675. https://doi.org/10.1038/nmeth.2089

Schröder, B., Wrocklage, C., Pan, C., Jäger, R., Kösters, B., Schäfer, H., Elsässer, H. P., Mann, M., & Hasilik, A. (2007). Integral and associated lysosomal membrane proteins. *Traffic*, *8*(12), 1676–1686. https://doi.org/10.1111/j.1600-0854.2007.00643.x

Shainskaya, A., Schneeberger, A., Apell, H. J., & Karlish, S. J. D. (2000). Entrance port for Na+ and K+ ions on Na+,K+-ATPase in the cytoplasmic loop between trans-membrane segments M6 and M7 of the α subunit: Proximity of the cytoplasmic segment of the β subunit. *Journal of Biological Chemistry*, *275*(3), 2019–2028. https://doi.org/10.1074/jbc.275.3.2019

Simons, K., & Ikonen, E. (1997). Functional rafts in cell membranes. *Nature*, *387*(6633), 569–572. https://doi.org/10.1038/42408

Singer, S. J., & Nicolson, G. L. (1972). The fluid mosaic model of the structure of cell membranes. *Science (New York, N.Y.)*, *175*(4023), 720–731. https://doi.org/10.1126/science.175.4023.720

SJ, M., HJ, R., S, Y., DP, T., & de Vries AH. (2007). The martini force field: coarse grained model for biomolecular simulations. *Journal of Physical Chemistry B*, *111*(27), 7812.

Skou, J. C. (1957). The influence of some cations on an adenosine triphosphatase from peripheral nerves. *BBA - Biochimica et Biophysica Acta*, *23*(C), 394–401. https://doi.org/10.1016/0006-3002(57)90343-8

Skulachev, V. P. (1994). Bioenergetics: the evolution of molecular mechanisms and the development of bioenergetic concepts. *Antonie van Leeuwenhoek*, *65*(4), 271–284. https://doi.org/10.1007/BF00872213

Slayman, C. L. (1965). Electrical Properties of Neurospora crassa : Effects of external cations on the intracellular potential. *Journal of General Physiology*, *49*(1), 69–92. https://doi.org/10.1085/jgp.49.1.69

Slayman, C. L., Long, W. S., & Lu, C. Y.-H. (1973). The relationship between ATP and an electrogenic pump in the plasma membrane ofNeurospora crassa. *The Journal of Membrane Biology*, *14*(1), 305–338. https://doi.org/10.1007/BF01868083

Sonntag, Y., Musgaard, M., Olesen, C., Schiøtt, B., Møller, J. V., Nissen, P., & Thøgersen, L. (2011). Mutual adaptation of a membrane protein and its lipid bilayer during conformational changes. *Nature Communications*, *2*(1). https://doi.org/10.1038/ncomms1307

Sørensen, D. M., Holen, H. W., Pedersen, J. T., Martens, H. J., Silvestro, D., Stanchev, L. D., Costa, S. R., Pomorski, T. G., López-Marqués, R. L., & Palmgren, M. (2019). The P5A ATPase Spf1p is stimulated by phosphatidylinositol 4-phosphate and influences cellular sterol homeostasis. *Molecular Biology of the Cell*, *30*(9), 1069–1084. https://doi.org/10.1091/mbc.E18-06-0365

Sørensen, T. L. M., Møller, J. V., & Nissen, P. (2004). Phosphoryl transfer and calcium ion occlusion in the calcium pump. *Science*, *304*(5677), 1672–1675. https://doi.org/10.1126/science.1099366

Spira, F., Mueller, N. S., Beck, G., von Olshausen, P., Beig, J., & Wedlich-Söldner, R. (2012). Patchwork organization of the yeast plasma membrane into numerous coexisting domains. *Nature Cell Biology*, *14*(6), 640–648. https://doi.org/10.1038/ncb2487

Sugimoto, Y., Sakoh, H., & Yamada, K. (2004). IPC synthase as a useful target for antifungal drugs. *Current Drug Targets. Infectious Disorders*, *4*(4), 311–322. https://doi.org/10.2174/1568005043340597

Supply, P., Wach, A., & Goffeau, A. (1993). Enzymatic properties of the PMA2 plasma membrane-bound H(+)-ATPase of Saccharomyces cerevisiae. *The Journal of Biological Chemistry*, *268*(26), 19753–19759.

Toyoshima, C., & Mizutani, T. (2004). Crystal structure of the calcium pump with a bound ATP analogue. *Nature*, *430*(6999), 529–535. https://doi.org/10.1038/nature02680

Toyoshima, C., Nakasako, M., Nomura, H., & Ogawa, H. (2001). Structure determination of the calcium pump of sarcoplasmic reticulum at 2.6 Å resolution. *Nature*, *405*(6787), 647–655.

Toyoshima, C., Nomura, H., & Tsuda, T. (2004). Lumenal gating mechanism revealed in calcium pump crystal structures with phosphate analogues. *Nature*, *432*(7015), 361–368. https://doi.org/10.1038/nature02981

Traaseth, N. J., Ha, K. N., Verardi, R., Shi, L., Buffy, J. J., Masterson, L. R., & Veglia, G. (2008). Structural and Dynamic Basis of Phospholamban and Sarcolipin Inhibition of Ca2+-ATPase. *Biochemistry*, *47*(1), 3–13. https://doi.org/10.1021/bi701668v

Uusitalo, J. J., Ingólfsson, H. I., Akhshi, P., Tieleman, D. P., & Marrink, S. J. (2015). Martini Coarse-Grained Force Field: Extension to DNA. *Journal of Chemical Theory and Computation*, *11*(8), 3932–3945. https://doi.org/10.1021/acs.jctc.5b00286

van Gunsteren, W. F., & Berendsen, H. J. C. (1988). A Leap-Frog Algorithm for Stochastic Dynamics. *Molecular Simulation*, *1*(3), 173–185. https://doi.org/10.1080/08927028808080941

van Meer, G., Voelker, D. R., & Feigenson, G. W. (2008). Membrane lipids: where they are and how they behave. *Nature Reviews. Molecular Cell Biology*, *9*(2), 112–124. https://doi.org/10.1038/nrm2330

van 't Klooster, J. S., Cheng, T.-Y., Sikkema, H. R., Jeucken, A., Moody, B., & Poolman, B. (2020). Periprotein lipidomes of saccharomyces cerevisiae provide a flexible environment for conformational changes of membrane proteins. *ELife*, *9*, 1–19. https://doi.org/10.7554/eLife.57003

van Veen, S., Martin, S., van den Haute, C., Benoy, V., Lyons, J., Vanhoutte, R., Kahler, J. P., Decuypere, J. P., Gelders, G., Lambie, E., Zielich, J., Swinnen, J. v., Annaert, W., Agostinis, P., Ghesquière, B., Verhelst, S., Baekelandt, V., Eggermont, J., & Vangheluwe, P. (2020). ATP13A2 deficiency disrupts lysosomal polyamine export. *Nature*, *578*(7795), 419–424. https://doi.org/10.1038/s41586-020-1968-7

Wassenaar, T. A., Ingólfsson, H. I., Böckmann, R. A., Tieleman, D. P., & Marrink, S. J. (2015). Computational lipidomics with insane: A versatile tool for generating custom membranes for molecular simulations. *Journal of Chemical Theory and Computation*, *11*(5), 2144–2155. https://doi.org/10.1021/acs.jctc.5b00209

Wielandt, A. G., Pedersen, J. T., Falhof, J., Kemmer, G. C., Lund, A., Ekberg, K., Fuglsang, A. T., Pomorski, T. G., Buch-Pedersen, M. J., & Palmgren, M. (2015). Specific Activation of the Plant P-type Plasma Membrane H+-ATPase by Lysophospholipids Depends on the Autoinhibitory N- and C-terminal Domains. *The Journal of Biological Chemistry*, *290*(26), 16281–16291. https://doi.org/10.1074/jbc.M114.617746

Winther, A. M. L., Bublitz, M., Karlsen, J. L., Møller, J. v., Hansen, J. B., Nissen, P., & Buch-Pedersen, M. J. (2013a). The sarcolipin-bound calcium pump stabilizes calcium sites exposed to the cytoplasm. *Nature*, *495*(7440), 265–269. https://doi.org/10.1038/nature11900

Winther, A. M. L., Bublitz, M., Karlsen, J. L., Møller, J. v., Hansen, J. B., Nissen, P., & Buch-Pedersen, M. J. (2013b). The sarcolipin-bound calcium pump stabilizes

calcium sites exposed to the cytoplasm. *Nature*, *495*(7440), 265–269. https://doi.org/10.1038/nature11900

Yang, Q., & Kempken, F. (2020). The Composition and the Structure of MCC/Eisosomes in Neurospora crassa. *Frontiers in Microbiology*, *11*(September), 1–15. https://doi.org/10.3389/fmicb.2020.02115

Yang, W.-K., Kang, C.-K., Hsu, A.-D., Lin, C.-H., & Lee, T.-H. (2016). Different Modulatory Mechanisms of Renal FXYD12 for Na(+)-K(+)-ATPase between Two Closely Related Medakas upon Salinity Challenge. *International Journal of Biological Sciences*, *12*(6), 730–745. https://doi.org/10.7150/ijbs.15066

Zhang, Y., Inoue, M., Tsutsumi, A., Watanabe, S., Nishizawa, T., Nagata, K., Kikkawa, M., & Inaba, K. (2020). Cryo-EM structures of SERCA2b reveal the mechanism of regulation by the luminal extension tail. *Science Advances*, *6*(33), 1–12. https://doi.org/10.1126/sciadv.abb0147

Zhao, P., Zhao, C., Chen, D., Yun, C., Li, H., & Bai, L. (2021a). Structure and activation mechanism of the hexameric plasma membrane H+-ATPase. *Nature Communications*, *12*(1), 1–11. https://doi.org/10.1038/s41467-021-26782-y

Zhao, P., Zhao, C., Chen, D., Yun, C., Li, H., & Bai, L. (2021b). Structure and activation mechanism of the hexameric plasma membrane H+-ATPase. *Nature Communications*, *12*(1). https://doi.org/10.1038/s41467-021-26782-y

Zhao, Y., Ogawa, H., Yonekura, S.-I., Mitsuhashi, H., Mitsuhashi, S., Nishino, I., Toyoshima, C., & Ishiura, S. (2015). Functional analysis of SERCA1b, a highly expressed SERCA1 variant in myotonic dystrophy type 1 muscle. *Biochimica et Biophysica Acta (BBA) - Molecular Basis of Disease*, *1852*(10, Part A), 2042–2047. https://doi.org/https://doi.org/10.1016/j.bbadis.2015.07.006

Zhou, W., Fiorin, G., Anselmi, C., Karimi-Varzaneh, H. A., Poblete, H., Forrest, L. R., & Faraldo-Gómez, J. D. (2019). Large-scale state-dependent membrane remodeling by a transporter protein. *ELife*, *8*, 1–20. https://doi.org/10.7554/eLife.50576

Appendices

10.1 Appendix I

PNCE ITP file

```
;;;;;; Martini lipid topology for C(d18:1/24:1) CER (PNCE), generated using:
; The Martini lipid itp generator version 0.4  Args are: -o martini_v2.0_PNCE_01.itp
-alname PNCE -alhead ' ' -allink 'A A' -altail 'TCC CCCDCC'
; WARNING: Lipids topology was generated following the Martini 2.0 guidelines but
this specific lipid type might
;         not have been tested and should therefore be used with care.
;
; Description:
;      A general model ceramide (CER) lipid corresponding to atomistic e.g.
C(d18:1/24:1) tails.
; Parameterization:
;   This topology follows the standard Martini 2.0 lipid definitions and building block
rules.
; Reference(s):
;      S.J. Marrink, A.H. de Vries, A.E. Mark. Coarse grained model for semi-
quantitative lipid simulations. JPC-B, 108:750-760,
;   2004. doi:10.1021/jp036508g
;    S.J. Marrink, H.J. Risselada, S. Yefimov, D.P. Tieleman, A.H. de Vries. The
MARTINI force field: coarse grained model for
;   biomolecular simulations. JPC-B, 111:7812-7824, 2007. doi:10.1021/jp071097f
;    T.A. Wassenaar, H.I. Ingolfsson, R.A. Bockmann, D.P. Tieleman, S.J. Marrink.
Computational lipidomics with insane: a versatile
;      tool for generating custom membranes for molecular simulations. JCTC,
150410125128004, 2015. doi:10.1021/acs.jctc.5b00209
; Created: 2015.04.20
;
;@INSANE alhead= , allink=A A, altail=TCC CCCDCC, alname=PNCE, charge=0
;@RESNTEST PNC==PNCE if: atoms[0]==AM1
;@BEADS AM1 AM2 T1A C2A C3A C1B C2B C3B D4B C5B C6B
;@BONDS AM1-AM2 AM1-T1A T1A-C2A C2A-C3A AM2-C1B C1B-C2B C2B-C3B
C3B-D4B D4B-C5B C5B-C6B
;

[moleculetype]
; molname      nrexcl
  PNCE         1



[atoms]
; id     type    resnr   residu          atom    cgnr    charge
   1     P1      1       PNCE            AM1     1       0
   2     P5      1       PNCE            AM2     2       0
   3     C3      1       PNCE            T1A     3       0
   4     C1      1       PNCE            C2A     4       0
   5     C1      1       PNCE            C3A     5       0
```

```
   6     C1      1       PNCE        C1B    6      0
   7     C1      1       PNCE        C2B    7      0
   8     C1      1       PNCE        C3B    8      0
   9     C3      1       PNCE        D4B    9      0
  10     C1      1       PNCE        C5B   10      0
  11     C1      1       PNCE        C6B   11      0

[bonds]
;  i  j    funct   length          force.c.
   1  2  1        0.37    1250
   1  3  1        0.47    1250
   3  4  1        0.47    1250
   4  5  1        0.47    1250
   2  6  1        0.47    1250
   6  7  1        0.47    1250
   7  8  1        0.47    1250
   8  9  1        0.47    1250
   9 10          1       0.47    1250
  10 11          1       0.47    1250

[angles]
;  i  j  k         funct   angle  force.c.
   1  3  4         2       180.0  45.0
   3  4  5         2       180.0  25.0
   2  6  7         2       180.0  25.0
   6  7  8         2       180.0  25.0
   7  8  9         2       180.0  25.0
   8  9 10         2       120.0  45.0
   9 10 11         2       180.0  25.0
```

PIPI ITP file

```
[atoms]
; id    type    resnr  residu        atom   cgnr    charge
   1     P1       1     PIPI    C1     1      0
   2     P4       1     PIPI    C2     2      0
   3     P4       1     PIPI    C3     3      0
   4     Qa       1     PIPI    PO4    4      -1.0    ; Name changed from CP to PO4
; Tail part (uses standar Martini v2.0 tail rules)
   5     Na       1     PIPI    GL1    5      0
   6     Na       1     PIPI    GL2    6      0
   7     C1       1     PIPI    C1A    7      0
   8     C4       1     PIPI    D2A    8      0
   9     C4       1     PIPI    D3A    9      0
  10     C1       1     PIPI    C4A    10     0
  11     C1       1     PIPI    C1B    11     0
  12     C1       1     PIPI    C2B    12     0
  13     C1       1     PIPI    C3B    13     0
  14     C1       1     PIPI    C4B    14     0

[bonds]
;  i  j    funct   length          force.c.
#ifdef FLEXIBLE
; Using bonds not constraints
   1  2  1        0.40    30000
   1  3  1        0.40    30000
   2  3  1        0.40    30000
#endif
   1  4  1        0.35    1250
   4  5  1        0.47    1250
; Tail part (uses standar Martini v2.0 tail rules)
   5  6  1        0.37    1250
   5  7  1        0.47    1250
   7  8  1        0.47    1250
   8  9  1        0.47    1250
   9 10          1        0.47    1250
   6 11          1        0.47    1250
  11 12          1        0.47    1250
  12 13          1        0.47    1250
  13 14          1        0.47    1250

[angles]
;  i  j  k         funct   angle  force.c.
   3  1  4        2        133.0  100.0
   2  1  4        2        100.0  70.0
; Orient Head
   1  4  5        2        140.0  30.0    ; link to lipid
; 4    5    6        2 120.00 25.0 ; These are part of the default lipids rules but not used
          here
; 4    5    7        2 180.00 25.0 ; These are part of the default lipids rules but not used
          here
```

```
; Tail part (uses standar Martini v2.0 tail rules)
   5  7  8        2        180.0  25.0
   7  8  9        2        100.0  10.0
   8  9 10        2        120.0  45.0
   6 11 12        2        180.0  25.0
  11 12 13        2        180.0  25.0
  12 13 14        2        180.0  25.0

[dihedrals]
;  i  j  k  l       funct   angle  force.c.
; 3  1  4  5  1  -30.0  5.0  1 ; Removed as it was unstable - WARNING has not been
          tested

[constraints]
;  i  j  k          funct   length
#ifndef FLEXIBLE
; Using constraints not bonds
   1  2  1        0.40
   1  3  1        0.40
   2  3  1        0.40
#endif
```

PICE ITP file

```
;;;;;; Martini lipid topology for C(d18:0/24:0) Phosphoinositol CER (CIPE), generated
        using:
; A combination of PIPI and PNCE was used to generate this lipid
; WARNING: Lipids topology was generated following the Martini 2.0 guidelines but
        this specific lipid type might
;       not have been tested and should therefore be used with care.
;
; Description:
;     A model phosphoinositol ceramide lipid corresponding to atomistic e.g.
        C(d18:0/24:0) tails.
; Parameterization:
;   This topology follows the standard Martini 2.0 lipid definitions and building block
        rules.
; Reference(s):
;     S.J. Marrink, A.H. de Vries, A.E. Mark. Coarse grained model for semi-
        quantitative lipid simulations. JPC-B, 108:750-760,
;   2004. doi:10.1021/jp036508g
;    S.J. Marrink, H.J. Risselada, S. Yefimov, D.P. Tieleman, A.H. de Vries. The
        MARTINI force field: coarse grained model for
;   biomolecular simulations. JPC-B, 111:7812-7824, 2007. doi:10.1021/jp071097f
;    T.A. Wassenaar, H.I. Ingolfsson, R.A. Bockmann, D.P. Tieleman, S.J. Marrink.
        Computational lipidomics with insane: a versatile
;     tool for generating custom membranes for molecular simulations. JCTC,
        150410125128004, 2015. doi:10.1021/acs.jctc.5b00209
; Created: 2021.10.05
;as
;@INSANE alhead= , allink=A A, altail=TCC CCCDCC, alname=PNCE, charge=0
;@RESNTEST PNC==PNCE if: atoms[0]==AM1
;@BEADS AM1 AM2 T1A C2A C3A C1B C2B C3B D4B C5B C6B
;@BONDS AM1-AM2 AM1-T1A T1A-C2A C2A-C3A AM2-C1B C1B-C2B C2B-C3B
        C3B-D4B D4B-C5B C5B-C6B
;

[moleculetype]
; molname      nrexcl
  PICE         1

[atoms]
; id     type    resnr   residu          atom    cgnr    charge
   1     P1      1       PICE    C1      1       0
   2     P4      1       PICE    C2      2       0
   3     P4      1       PICE    C3      3       0
   4     Qa      1       PICE    CP      4       -1.0

   5     P1      1       PICE    AM1     5       0
   6     P5      1       PICE    AM2     6       0
   7     C1      1       PICE    T1A     7       0
   8     C1      1       PICE    C2A     8       0
   9     C1      1       PICE    C3A     9       0
```

```
  10    C1      1       PICE  C1B   10      0
  11    C1      1       PICE  C2B   11      0
  12    C1      1       PICE  C3B   12      0
  13    C1      1       PICE  D4B   13      0
  14    C1      1       PICE  C5B   14      0
  15    C1      1       PICE  C6B   15      0

[bonds]
;  i  j    funct   length          force.c.
#ifdef FLEXIBLE
   1  2  1        0.40    30000
   1  3  1        0.40    30000
   2  3  1        0.40    30000
#endif
   1  4  1        0.35    1250
   4  5  1        0.47    1250
   5  6  1        0.37    1250
   5  7  1        0.47    1250
   7  8  1        0.47    1250
   8  9  1        0.47    1250
   6 10          1       0.47    1250
  10 11          1       0.47    1250
  11 12          1       0.47    1250
  12 13          1       0.47    1250
  13 14          1       0.47    1250
  14 15          1       0.47    1250

[angles]
;  i  j  k         funct   angle  force.c.
   3  1  4        2       133.0  100.0
   2  1  4        2       100.0  70.0
; Orient Head
   1  4  5        2       140.0  30.0    ; link to lipid
; 4    5    6       2 120.00 25.0 ; These are part of the default lipids rules but not used
          here
; 4    5    7       2 180.00 25.0 ; These are part of the default lipids rules but not used
          here
; Tail part (changed to C1s only so angles and constants match the change)
   5  7  8        2       180.0  25.0
   7  8  9        2       180.0  25.0
   6 10 11       2       180.0  25.0
  10 11 12       2       180.0  25.0
  11 12 13       2       180.0  25.0
  12 13 14       2       180.0  25.0
  13 14 15       2       180.0  25.0

;the following below is directly from the PIPI itp file
[dihedrals]
;  i  j  k  l       funct   angle  force.c.
```

```
; 3  1  4  5  1  -30.0  5.0  1 ; Removed as it was unstable - WARNING has not been
          tested

[constraints]
;  i  j  k          funct   length
#ifndef FLEXIBLE
; Using constraints not bonds
   1  2  1         0.40
   1  3  1         0.40
   2  3  1         0.40
#endif
```

PPCE ITP file

```
;;;;;; Martini lipid topology for C(d18:1/24:1) CER (PNCE), generated using:
; The Martini lipid itp generator version 0.4  Args are: -o martini_v2.0_PNCE_01.itp
        -alname PNCE -alhead ' ' -allink 'A A' -altail 'TCC CCCDCC'
; WARNING: Lipids topology was generated following the Martini 2.0 guidelines but
        this specific lipid type might
;       not have been tested and should therefore be used with care.
;
; Description:
;     A general model ceramide (CER) lipid corresponding to atomistic e.g.
        C(d18:1/24:1) tails.
; Parameterization:
;   This topology follows the standard Martini 2.0 lipid definitions and building block
        rules.
; Reference(s):
;     S.J. Marrink, A.H. de Vries, A.E. Mark. Coarse grained model for semi-
        quantitative lipid simulations. JPC-B, 108:750-760,
;   2004. doi:10.1021/jp036508g
;    S.J. Marrink, H.J. Risselada, S. Yefimov, D.P. Tieleman, A.H. de Vries. The
        MARTINI force field: coarse grained model for
;   biomolecular simulations. JPC-B, 111:7812-7824, 2007. doi:10.1021/jp071097f
;    T.A. Wassenaar, H.I. Ingolfsson, R.A. Bockmann, D.P. Tieleman, S.J. Marrink.
        Computational lipidomics with insane: a versatile
;     tool for generating custom membranes for molecular simulations. JCTC,
        150410125128004, 2015. doi:10.1021/acs.jctc.5b00209
; Created: 2015.04.20
;
;@INSANE alhead= , allink=A A, altail=TCC CCCDCC, alname=PNCE, charge=0
;@RESNTEST PNC==PNCE if: atoms[0]==AM1
;@BEADS AM1 AM2 T1A C2A C3A C1B C2B C3B D4B C5B C6B
;@BONDS AM1-AM2 AM1-T1A T1A-C2A C2A-C3A AM2-C1B C1B-C2B C2B-C3B
        C3B-D4B D4B-C5B C5B-C6B
;

[moleculetype]
; molname      nrexcl
  PPCE         1

[atoms]
; id     type    resnr   residu          atom    cgnr    charge
   1     P1      1       PPCE            AM1     1       0
   2     P5      1       PPCE            AM2     2       0
   3     C1      1       PPCE            T1A     3       0
   4     C1      1       PPCE            C2A     4       0
   5     C1      1       PPCE            C3A     5       0
   6     C1      1       PPCE            C1B     6       0
   7     C1      1       PPCE            C2B     7       0
   8     C1      1       PPCE            C3B     8       0
   9     C1      1       PPCE            D4B     9       0
```

```
  10    C1      1       PPCE          C5B   10      0
  11    C1      1       PPCE          C6B   11      0

[bonds]
;  i  j    funct   length          force.c.
   1  2  1        0.37    1250
   1  3  1        0.47    1250
   3  4  1        0.47    1250
   4  5  1        0.47    1250
   2  6  1        0.47    1250
   6  7  1        0.47    1250
   7  8  1        0.47    1250
   8  9  1        0.47    1250
   9 10          1       0.47    1250
  10 11          1       0.47    1250

[angles]
;  i  j  k         funct   angle  force.c.
   1  3  4        2       180.0  25.0
   3  4  5        2       180.0  25.0
   2  6  7        2       180.0  25.0
   6  7  8        2       180.0  25.0
   7  8  9        2       180.0  25.0
   8  9 10        2       180.0  25.0
   9 10 11        2       180.0  25.0
```

10.2 Appendix II

Multiple sequence alignment of Pma1 sequences from fungi.

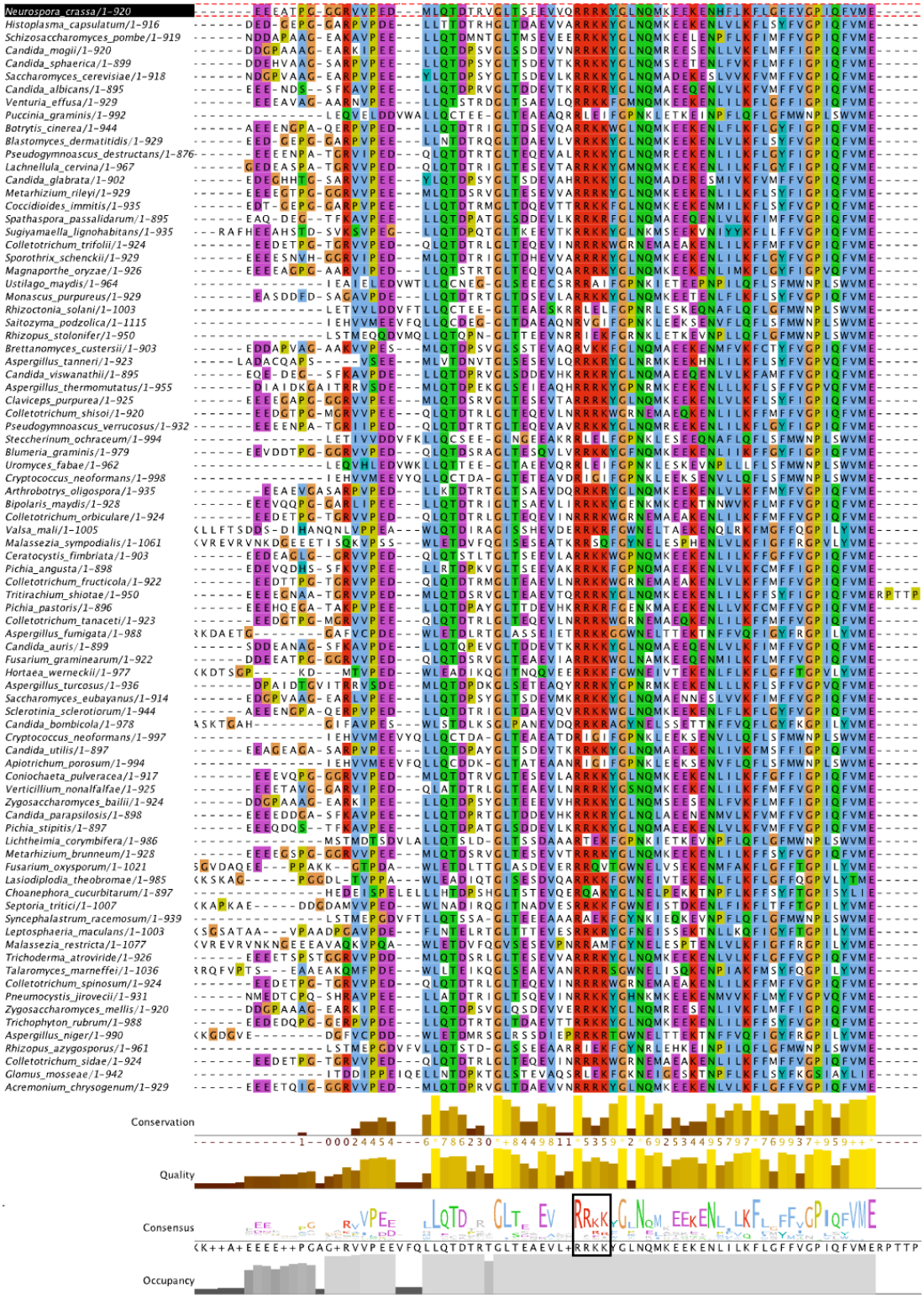

10.3 Appendix III

Equilibration of the protein mainchain atoms of the SERCA WT, E340A and E340A$_{is}$ production simulations, measured by the root mean squared deviation.

